Multiwavelength variability in active galactic nuclei jets and other VLBI studies

INAUGURAL-DISSERTATION

zur Erlangung des Doktorgrades
der Mathematisch-Naturwissenschaftlichen Fakultät
der Universität zu Köln

vorgelegt von

Benke Petra
Budapest, Magyarország

Köln, 2024

Berichterstatter: Prof. Dr. Andreas Eckart
Prof. Dr. J. Anton Zensus

Tag der letzten mündlichen Prüfung: 9. September 2024
Dissertation angenommen von der Mathematisch-Naturwissenschaftlichen Fakultät der Universität zu Köln: 9. September 2024

Erklärung

„Hiermit versichere ich an Eides statt, dass ich die vorliegende Dissertation selbstständig und ohne die Benutzung anderer als der angegebenen Hilfsmittel und Literatur angefertigt habe. Alle Stellen, die wörtlich oder sinngemäß aus veröffentlichten und nicht veröffentlichten Werken dem Wortlaut oder dem Sinn nach entnommen wurden, sind als solche kenntlich gemacht. Ich versichere an Eides statt, dass diese Dissertation noch keiner anderen Fakultät oder Universität zur Prüfung vorgelegen hat; dass sie - abgesehen von unten angegebenen Teilpublikationen und eingebundenen Artikeln und Manuskripten - noch nicht veröffentlicht worden ist sowie, dass ich eine Veröffentlichung der Dissertation vor Abschluss der Promotion nicht ohne Genehmigung des Promotionsausschusses vornehmen werde. Die Bestimmungen dieser Ordnung sind mir bekannt. Darüber hinaus erkläre ich hiermit, dass ich die Ordnung zur Sicherung guter wissenschaftlicher Praxis und zum Umgang mit wissenschaftlichem Fehlverhalten der Universität zu Köln gelesen und sie bei der Durchführung der Dissertation zugrundeliegenden Arbeiten und der schriftlich verfassten Dissertation beachtet habe und verpflichte mich hiermit, die dort genannten Vorgaben bei allen wissenschaftlichen Tätigkeiten zu beachten und umzusetzen. Ich versichere, dass die eingereichte elektronische Fassung der eingereichten Druckfassung vollständig entspricht."

Köln, 2024. Juli 01.

Benke Petra

Relevante Publikationen zur Doktorarbeit

Benke, P. et al. (2023): From binary to singular: The AGN PSO J334.2028+1.4075 under the high-resolution scope. *Astronomy and Astrophysics*, 677, A1.

Benke, P. et al. (2024): TANAMI: Tracking Active Galactic Nuclei with Austral Milliarcsecond Interferometry. III. First-epoch S band images. *Astronomy and Astrophysics*, 681, A69.

Benke, P. et al.: VLBI study of the flaring blazar TXS 1508+572 in the early Universe. Eingereicht bei *Astronomy and Astrophysics*, AA/2024/50153.

Benke, P. et al.: RadioAstron reveals a change in the jet collimation profile of 3C 84. Manuskript.

„Gorcsev Iván, a Rangoon teherhajó matróza még huszonegy éves sem volt, midőn elnyerte a fizikai Nobel-díjat. Ilyen nagy jelentőségű tudományos jutalmat e poétikusan ifjú korban megszerezni példátlan nagyszerű teljesítmény, még akkor is, ha egyesek előtt talán szépséghibának tűnik majd, hogy Gorcsev Iván a fizikai Nobel-díjat a makao nevű kártyajátékon nyerte el, Noah Bertinus professzortól, akinek ezt a kitüntetést Stockholmban, néhány nappal előbb, a svéd király nyújtotta át, de végre is a kákán csomót keresők nem számítanak; a lényeg a fő: hogy Gorcsev Iván igenis huszonegy éves korában elnyerte a Nobel-díjat."

Rejtő Jenő: A tizennégy karátos autó

Abstract

Active galactic nuclei (AGN) jets are one of the most fascinating objects in the Universe. Since their discovery by Curtis about a hundred years ago, we uncovered many of their secrets, but fundamental mechanisms related to the nature of their launching, evolution and multiwavelength variability are still not perfectly understood. In this dissertation work, I present my research on very long baseline interferometry (VLBI) observations of AGN jets, investigating the above-mentioned of topics. After the introductory chapters describing phenomena related to AGN (Ch. 3), I describe the observational method, VLBI (Ch. 4), which enables radio astronomers to reach unprecedented spatial resolutions to study the central parsec region of AGN.

AGN emit radiation throughout the entire electromagnetic spectrum, and the correlation of the activity between the different wavebands is a widely investigated topic. This includes temporal variations in brightness and polarization, ejection of new jet features in connection to elevated flux density states or detection of high-energy astroparticles associated with a given object, as well as common characteristics of astroparticle-emitter sources. In this dissertation, I research the link between the radio and the γ-ray activity in AGN jets using VLBI imaging techniques.

In Chapter 5 I present the first images from the 2.3-GHz monitoring of the TANAMI Collaboration targeting the TeV-emitter AGN of the southern sky. The goal of the study is to prove the viability of such a program, as many of the objects are extremely faint, and more importantly, to investigate the characteristics of TeV-detected objects. When analyzing this biased sample of twenty-four TeV-emitter AGN, I found that the core brightness temperatures shows an inverse relation with synchrotron peak frequency, and a direct relationship with the $0.1-100$ GeV γ-ray flux density. In addition, the median and average core brightness temperature of the sample is a magnitude lower than the value observed for samples dominated by low- and intermediate-synchrotron-peaked blazars. These results suggest that Doppler boosting is more prevalent in low-synchrotron-peaked objects than in high-synchrotron-peaked ones.

While blazars are the most common objects populating the γ-ray sky, only a handful of them were detected at high energies above $z > 2.5$, and overarching, contemporaneous multiwavelength studies are rarely focused on these high-redshift objects. For the first time to our knowledge, I present a multi-frequency VLBI follow-up analysis of the $z = 4.31$ blazar, TXS 1508+572 in Chapter 6. I aim to track the morphological changes, spectral index and opacity variations which could be associated with the preceding γ-ray flare observed in 2022 February. I find significant changes in brightness and morphology in the jet region, a feature which shows superluminal apparent motion, and was most likely

ejected during $2016 - 2019$. The position of the core with respect to the jet apex stays consistent through the observed time period of ~ 1 yr. I associated the γ-ray flare to the jet feature, and propose that the flare resulted from an interaction between the jet feature and the new plasma that was injected in this region.

As galaxy evolution in the ΛCDM Universe happens in a hierarchical manner via mergers, their central supermassive black holes form binaries (SMBHBs). SMBHBs tell us about the merger history of galaxies, the growth of black holes, as well as AGN activity related to mergers. PSO J334.2028+1.4075 (hereafter PSO J334) was one such candidate, whose periodic optical flux density variability triggered several multiwavelength observations to confirm its nature. The only remaining indication of a SMBHB residing in the center of this AGN was a 39 deg misalignment between its parsec- and kiloparsec-scale jet. In Chapter 7 I discuss my observations taken with the Karl G. Jansky Very Large Array that resolve the kiloparsec-scale jet of this PSO J334. The 6.2-GHz map shows a two-sided, lobe-dominated quasar with an asymmetric jet structure. The jets are remarkably straight until they bend, probably due to an interaction with the ambient medium, suggested by the magnetic field structure. I find no indication of jet precession, showing that PSO J334 harbors only a single black hole in its center.

In Chapter 8 I investigate the evolution of a recently ejected jet feature in the radio galaxy 3C 84, in order to learn more about jet launching and collimation. For this endeavor, I use 22-GHz data from *RadioAstron*, which takes VLBI to its extreme by utilizing space baselines, thus providing an unprecedented angular resolution, only matched by the Event Horizon Telescope. Comparing two *RadioAstron* observations, one from 2013, and the one presented in this thesis from 2016, I confirm the presence of an edge-brightened jet and counter-jet, but also find significant changes in jet morphology. These include a change in the collimation profile from a quasi-cylindrical to a parabolic shape, indicative of the decreasing pressure of the mini-cocoon inflated by the jet that cannot collimate the jet as efficiently as when it was closer to the core. This finding highlights one of the important external collimation mechanisms in AGN jets.

The works presented in this dissertation were made in anticipation of future telescope arrays and space missions, such as the Square Kilometer Array, that will revolutionize AGN surveys, especially of southern-sky sources, the Cherenkov Telescope Array which promises increased sensitivity at TeV energies, and the Laser Interferometer Space Antenna, which will open a new window to the gravitational Universe and hunt for supermassive black hole binaries. That so many upcoming instruments are focused on AGN science, tells us that these objects still present us with a plethora of open questions, many of which may be uncovered with these next generation telescopes.

Kivonat

Az aktív galaxismagok (AGN) által kibocsátott jetek az Univerzum egyik leglenyűgözőbb objektumai. A mintegy száz évvel ezelőtti felfedezésük óta számos titkukat feltártuk, viszont az eredetükkel, fejlődésükkel, és a több hullámhosszt átfogó fényességváltozásukkal kapcsolatos alapvető folyamatokat még mindig nem értjük tökéletesen. Ebben a disszertációban az AGN jetek nagyon hosszú bázisvonalas interferometriás (VLBI) megfigyeléseivel kapcsolatos kutatásaimat mutatom be, amelyek a fent említett témákat taglalják. Az aktív galaxismagokat és a velük kapcsolatos jelenségeket bemutató bevezető fejezet után (3. fejezet) a megfigyelési módszert, a hosszú bázisvonalas interferometriát ismertetem (4. fejezet), amely lehetővé teszi a rádiócsillagászok számára, hogy soha nem látott térbeli felbontást érjenek el az AGN-ek központi régiójának vizsgálata során.

Az aktív galaxismagok a teljes elektromágneses spektrumban bocsátanak ki sugárzást, és a különböző hullámsávok közötti aktivitás korrelációja széles körben vizsgált téma. Ide tartoznak a fényesség és a polarizáció időbeli változásai, a megemelkedett fluxussűrűségű állapotokhoz kapcsolódó új jet komponensek kilövellése, vagy az adott objektumhoz kapcsolódó nagyenergiájú asztrorészecskék észlelése, valamint az asztrorészecske-kibocsátó források közös jellemzőinek tanulmányozása. A disszertációmban a rádió és a γ-sugárzás változása közötti kapcsolatot kutatom AGN jetekben a VLBI képalkotó technika segítségével.

A 5. fejezetben bemutatom a TANAMI Kollaboráció által végzett, a déli égbolt TeV-sugárzást kibocsátó aktív galaxismagjaira irányzott 2.3 GHz-es megfigyelés első képeit. A vizsgálat célja egy ilyen program sikerének felmérése, mivel a mintában szereplő objektumok jelentős része rendkívül halvány, és ami még fontosabb, a TeV-sugárzó objektumok jellemzőinek vizsgálata. A huszonnégy TeV-sugárzó aktív galaxismagból álló elfogult minta elemzésekor azt találtam, hogy a mag fényességi hőmérséklete fordított összefüggést mutat a szinkrotron csúcsfrekvenciával, és közvetlen összefüggést a $0.1 - 100$ GeV-os γ-fluxussűrűséggel. Ezen kívül a források mag fényességi hőmérsékletének mediánja és átlaga egy nagyságrenddel alacsonyabb, mint az alacsony és közepes szinkrotroncsúcsú blazárok által dominált mintákban megfigyelt érték. Ezek az eredmények arra utalnak, hogy a Doppler effektus az alacsony szinkrotroncsúcsú blazárokban jobban érvényesül, mint a magas szinkrotroncsúcsú objektumokban.

Bár a blazárok a leggyakoribb γ-sugárzó objektumok, csak néhányat detektáltak közülük nagy energiatartományban $z = 2.5$ vöröseltolódás felett. Emellett átfogó, egyidejű, több hullámhosszt lefedő észlelések ritkán vizsgálják ezeket a forrásokat. Tudomásunk szerint először mutatom be a 4.31-es vöröseltolódású blazár, a TXS 1508+572 többfrekvenciás VLBI elemzését a 6. fejezetben. Az észlelések célja a forrás szerkezetének, a

spektrális index és az opacitás változásának nyomon követése, valamint annak a vizsgálata, hogy ezek összefüggésbe hozhatóak-e a 2022 februárjában megfigyelt γ-kitöréssel. A γ-felfényesedés után jelentős fényesség és morfológiai változásokat találok a jet régiójában, amely szuperluminális látszólagos mozgást mutat, és valószínűleg $2016 - 2019$ során vált ki a magból. A körülbelül egy évet lefedő észlelések alatt a központi fekete lyuk helyzete konzisztens marad a 43 GHz-es rádió maghoz képest. Következtetésképpen, a γ-tartományban észlelt felfényesedést a jet és a komponensbe injektált új plazma közötti kölcsönhatáshoz kapcsoltam.

Mivel a ΛCDM Univerzumban a galaxisok fejlődése hierarchikusan, összeolvadásokon keresztül történik, a központi szupermasszív fekete lyukak kettősöket alkothatnak (SMBHB). A kettős szupermasszív fekete lyukak a galaxisok fejlődéstörténetéről, a fekete lyukak növekedéséről, valamint az összeolvadáshoz kapcsolódó AGN-aktivitásról árulkodnak. A PSO J334.2028+1.4075 (a továbbiakban PSO J334) egy ilyen jelölt volt, amely periodikus optikai fluxussűrűség-változása számos megfigyelést indított el a különböző hullámhossztartományokban, hogy megerősítsék a forrás természetéről alkotott feltevést. Az egyetlen fennmaradt jel arra, hogy az aktív galaxismag középpontjában egy kettős található a parszek- és kiloparszek méretű jetje közötti 39 deg elhajlás volt. A 7. fejezetben a Karl G. Jansky Very Large Array-vel végzett megfigyeléseimet tárgyalom, amelyek képesek felbontani a kvazár kiloparszek skálájú jetjét. A $6,2$ GHz-es térkép egy kétoldali, lebeny-dominált kvazárt mutat aszimmetrikus jet struktúrával. A jetek feltűnően egyenesek amíg el nem hajlanak, valószínűleg a környező galaxisközi anyaggal való kölcsönhatás miatt. Erre a jet mágneses térszerkezete utal. Vizsgálataim során nem találtam a jet precessziójára utaló jelet, ami azt mutatja, hogy a PSO J334 csak egyetlen fekete lyukat rejt a középpontjában.

A 8. fejezetben a 3C 84 rádiógalaxis újonnan kibocsátott plazmanyalábját vizsgálom, hogy többet tudjak meg a jet fejlődéséről és kollimációjáról. Ehhez a vállalkozáshoz a *RadioAstron* űrtávcső 22 GHz-es adatait használtam, amely példátlan szögfelbontását csak az Eseményhorizont Távcső képes elérni. A 2013-as és 2016-os *RadioAstron* megfigyeléseket összehasonlítva megerősítem az észlelő felé és az észlelőtől távolodó jetek peremén megfigyelt fényesdést, valamint jelentős változásokat találok a jet morfológiájában. Ezek közé tartozik a jet szélességi profiljának változása, amely henger alakúról parabolává szélesedett. Ennek egy lehetséges oka, hogy a jet által felfújt úgynevezett burok csökkenő nyomása nem tudja olyan hatékonyan összenyalábolni a jetben lévő plazmát, mint amikor az közelebb volt a rádió maghoz. Ez az eredmény rávilágít a jetek egyik fontos külső kollimációs mechanizmusára.

A disszertációban bemutatott munkák a jövőbeli távcsövek és űrmissziók céljainak figyelembevételével készültek: a Square Kilometer Array forradalmasítani fogja az AGN-

felméréseket, különösen a déli égbolt forrásainak vizsgálatát; a Cherenkov Telescope Array nagyobb érzékenységet ígér a TeV-energiákon sugárzó források vizsgálatában; és a Laser Interferometer Space Antenna új ablakot nyit majd a gravitációs Univerzumra és szupermasszív fekete lyuk kettősökre vadászik majd. Az, hogy ennyi tervezett távcső összpontosít aktív galaxismagokkal kapcsolatos kutatásokra azt mutatja, hogy ezek az objektumok még mindig rengeteg érdekes kérdést vetnek fel, amelyek közül soknak a feltárására csak a következő generációs teleszkópok segítségével kerülhet sor.

Zusammenfassung

Die Jets aktiver galaktischer Kerne (AGN) sind eines der faszinierendsten Objekte im Universum. Seit ihrer Entdeckung durch Curtis vor etwa hundert Jahren haben wir viele ihrer Geheimnisse gelüftet, aber die grundlegenden Mechanismen im Zusammenhang mit der Art ihres Starts, ihrer Entwicklung und ihrer Variabilität über mehrere Wellenlängen hinweg sind immer noch nicht vollständig verstanden. In dieser Dissertation präsentiere ich meine Forschungsarbeit über die Beobachtung von AGN-Jets mit der Interferometrie mit sehr langer Basislinie (VLBI), in der ich die oben genannten Themen untersuche. Nach den einleitenden Kapiteln, in denen die Phänomene im Zusammenhang mit AGN beschrieben werden (Kap. 3), beschreibe ich die Beobachtungsmethode VLBI (Kap. 4), die es Radioastronomen ermöglicht, eine noch nie dagewesene räumliche Auflösung zu erreichen, um die zentrale Parsec-Region von AGN zu untersuchen.

AGN emittieren Strahlung über das gesamte elektromagnetische Spektrum, und die Korrelation der Aktivität zwischen den verschiedenen Wellenbändern ist ein Thema in einer Vielzahl von Studien. Dazu gehören zeitliche Schwankungen der Helligkeit und Polarisation, der Ausstoß neuer Jet-Komponenten in Verbindung mit erhöhten Flussdichtezuständen oder der Nachweis von hochenergetischen Astroteilchen, die mit einem bestimmten Objekt assoziiert sind, sowie gemeinsame Merkmale von Astroteilchen-Emitter-Quellen. In dieser Dissertation untersuche ich die Verbindung zwischen der Radio- und der γ-Strahlenaktivität in AGN-Jets mit Hilfe von VLBI-Abbildungstechniken.

In Kapitel 5 stelle ich die ersten Bilder der 2,3 GHz-Untersuchung der TANAMI-Kollaboration vor, die auf die TeV-Emitter-AGN des Südhimmels abzielt. Das Ziel der Studie ist es, die Durchführbarkeit eines solchen Programms zu beweisen, da viele der Objekte extrem schwach sind, und, was noch wichtiger ist, die Eigenschaften der TeV-entdeckten Objekte zu untersuchen. Bei der Analyse von vierundzwanzig TeV-emittierenden AGN hab ich festgestellt, dass die Kernhelligkeitstemperaturen eine umgekehrte Beziehung zur Synchrotronspitzenfrequenz und eine direkte Beziehung zur $0,1-100$ GeV γ-Strahlenflussdichte aufweisen. Darüber hinaus ist die mittlere und durchschnittliche Kernhelligkeitstemperatur der Stichprobe um eine Größenordnung niedriger als der Wert, der für Stichproben beobachtet wird, die von Blazaren mit niedrigen und mittleren Synchrotronspitzen dominiert werden. Diese Ergebnisse deuten darauf hin, dass Doppler-Boosting bei Objekten mit niedrigem Synchrotronspitzen stärker ausgeprägt ist als bei solchen mit hohem Synchrotronspitzen.

Obwohl Blazare die häufigsten Objekte am γ-Röntgenhimmel sind, wurden nur eine Handvoll von ihnen bei hohen Energien oberhalb von $z > 2,5$ entdeckt, und gleichzeitige Multiwellenlängenstudien sind selten auf diese hochverschiebten Objekte ausgerichtet. Z

um ersten Mal, soweit bekannt, präsentiere ich eine VLBI-Multifrequenz-Nachfolgeanalyse des $z = 4.31$ Blazars TXS$\dot{1}$508+572 in Kapitel 6. Mein Ziel ist es, die morphologischen Veränderungen, den Spektralindex und die optische Dichtevariationen zuverfolgen, die mit dem vorangegangenen γ-Strahlenflare, der im Februar 2022 beobachtet wurde, verbunden sein könnten. Ich finde signifikante Helligkeits- und Morphologieveränderungen in der Jet-Region, die eine superluminale scheinbare Bewegung aufweist und höchstwahrscheinlich während $2016 - 2019$ ausgestoßen wurde. Die Position des Kerns in Bezug auf die Spitze des Jets bleibt während des beobachteten Zeitraums von ~ 1 Jahr konstant. Ich habe das γ-Strahlenflare mit dem Jet-Feature in Verbindung gebracht und schlage vor, dass das Flare aus einer Wechselwirkung zwischen dem Jet-Feature und dem neuen Plasma, das in dieser Region injiziert wurde, resultiert.

Da die Entwicklung der Galaxien im ΛCDM-Universum hierarchisch über Verschmelzungen verläuft, bilden ihre zentralen supermassereichen schwarzen Löcher Doppelsysteme (SMBHBs). SMBHBs geben Aufschluss über die Fusionsgeschichte von Galaxien, das Wachstum von Schwarzen Löchern und die AGN-Aktivität im Zusammenhang mit Fusionen. PSO J334.2028+1.4075 (im Folgenden PSO J334) war ein solcher Kandidat, dessen periodische Schwankungen der optischen Flussdichte mehrere Multiwellenlängenbeobachtungen auslösten, um seine Natur zu bestätigen. Der einzige verbleibende Hinweis auf eine SMBHB im Zentrum dieses AGN war eine 39 deg-Fehlausrichtung zwischen seinem Jet auf der Parsec- und Kiloparsec-Skala. In Kapitel 7 bespreche ich meine Beobachtungen mit dem Karl G. Jansky Very Large Array, die den Jet dieses PSO J334, im Kiloparsec-Bereich auflösen. Die 6, 2-GHz-Karte zeigt einen zweiseitigen, von Keulen dominierten Quasar mit einer asymmetrischen Jet-Struktur. Die Jets sind bemerkenswert gerade, bis sie sich biegen, wahrscheinlich aufgrund einer Wechselwirkung mit dem umgebenden Medium, was durch die Struktur des Magnetfeldes nahegelegt wird. Ich finde keinen Hinweis auf eine Präzession der Jets, was zeigt, dass PSO J334 nur ein einziges Schwarzes Loch in seinem Zentrum beherbergt.

In Kapitel 8 untersuche ich die Entwicklung eines kürzlich ausgestoßenen Jets in der Radiogalaxie 3C 84, um mehr über den Start und die Kollimation von Jets zu erfahren. Für dieses Unterfangen verwende ich 22-GHz-Daten von *RadioAstron*, das VLBI auf die Spitze treibt, indem es Weltraum-Basislinien verwendet und so eine noch nie dagewesene Winkelauflösung bietet, die nur vom Event Horizon Telescope übertroffen wird. Beim Vergleich von zwei *RadioAstron*-Beobachtungen, einer aus dem Jahr 2013 und der in dieser Arbeit vorgestellten aus dem Jahr 2016, bestätige ich das Vorhandensein eines kantenaufgehellten Jets und eines Gegenjets, finde aber auch signifikante Veränderungen in der Jet-Morphologie. Dazu gehört eine Veränderung des Kollimationsprofils von einer quasi-zylindrischen zu einer parabolischen Form, was auf den abnehmenden Druck des vom

Jet aufgeblasenen Mini-Kokons hindeutet, der den Jet nicht mehr so effizient kollimieren kann, wie wenn er näher am Kern wäre. Diese Erkenntnis unterstreicht einen der wichtigen externen Kollimationsmechanismen in AGN-Jets.

Die in dieser Dissertation vorgestellten Arbeiten wurden im Vorgriff auf zukünftige Teleskopanordnungen und Weltraummissionen durchgeführt, wie z.B. das Square Kilometer Array, das die Durchmusterung von AGN, insbesondere von Quellen am Südhimmel, revolutionieren wird, das Cherenkov Telescope Array, das eine erhöhte Empfindlichkeit bei TeV-Energien verspricht, und die Laser Interferometer Space Antenna, die ein neues Fenster zum gravitativen Universum öffnen und nach supermassiven Schwarzen Löchern suchen wird. Die Tatsache, dass sich so viele neue Instrumente auf die Erforschung von AGNs konzentrieren, zeigt uns, dass diese Objekte immer noch eine Fülle offener Fragen aufwerfen, von denen viele mit diesen Teleskopen der nächsten Generation aufgedeckt werden könnten.

Contents

List of Figures

Chapter 1

Foreword

Astronomy is a branch of natural science, which aims at studying celestial objects, and the phenomena surrounding them. Why have humans been looking up at the sky since the dawn of time? Why are we interested in studying the galaxies far far away, and what can we learn from them?

Curiosity is an essential part of human nature, and is the main driving force that moves us forward. Through astronomic research, we can learn more about our origin in the Universe, and about the future of our Solar system. Astronomy has provided us with several paradigm-changing results (see Ch. 4.1), from the discovery that we are, indeed, not the center of the Universe, through the first detection of the cosmic microwave background to the observation of the first exoplanet, these results expanded our view on how the Universe works and how our existence fits in this picture. The vastness of what surrounds us teaches us about humility, as our Pale Blue Dot (Sagan 1994) is merely one of the many planets in the Milky Way, which in turn is just a typical spiral galaxy among the billions of galaxies in the Cosmos. From this perspective, my upcoming thesis defense does not look as consequential as it feels while writing these lines.

These thoughts reflect the more abstract aspects of astronomy, but there are tangible inventions that we can thank astronomy for. Tracking celestial objects aided people for centuries to keep track of time, the passing of seasons, navigation, and determining times for planting or hunting seasons. Nowadays, tangible uses of astronomy are connected to technological and medical developments. Charge-coupled devices used to capture astronomical images, are now commonly utilized in cameras and mobiles. Tomography, developed by Larry Altschuler, is a technique used to image sections via a penetrating wave. Magnetic resonance imaging is a non-invasive medical imaging technique commonly used to detect tumors. The relevance of geodetic very long baseline interferometry (VLBI) is seen in the Global Positioning System, which relies on the position of distant quasars for determining the Earth orientation parameters. Probably the most well-known example is

the wireless local area network, which was initially developed to sharpen images coming from a radio telescope. These are only a few examples as how astronomy is present in our everyday lives, without us noticing it.

My journey in radio astronomy started with quasars. I saw the BSc thesis topics offered at my university's chair of astronomy, and after quickly checking the Wikipedia page on quasars – disputed as the most reliable source of information –, I thought that these are the most fascinating objects I have ever heard of, and I would like to learn more about them. I learned about very long baseline interferometry for the first time through this project, an observation technique which I have been sticking by ever since.

In this dissertation, I present my research on VLBI observations of active galactic nuclei (AGN) jets, covering a broad range of topics from galaxy evolution to the nature of multiwavelength variability in these radio sources. To reflect this, the following chapters (Ch. 2-4) will provide an introduction on these subjects, as well as on the observation technique, VLBI, itself. Consecutive chapters (Ch. 5-8) include my published or submitted papers, each with a short summary on the research question and the results.

Chapter 2

Introduction

2.1 The goal of this thesis

AGN, powered by accretion to a supermassive black hole, which is the most powerful engine in nature, are one of the most luminous sources in the Universe. About 10% of them exhibit collimated, relativistic outflows known as jets. These interesting objects still present us with many open questions, such as the mechanisms responsible for the launching, acceleration and collimation of jets, the location of the emission regions at different wavelength regimes, the evolution of AGN across cosmic timescales, and so on. This thesis work covers several of these open questions by studying individual and non-complete samples of AGN.

In the ΛCDM model (see e.g., for an overview, Perivolaropoulos & Skara 2022), galaxy formation is a hierarchical process governed by mergers. Supermassive black holes are thought to reside in the centers of all massive galaxies, and binary supermassive black holes are also expected to be abundant objects. Observing them can help better understand the merger history of galaxies, the growth of black holes, as well as AGN activity related to mergers. However, supermassive black hole binaries (SMBHBs) are quite elusive to detect with our current instruments, and direct detection of these sources is only possible in nearby galaxies. As a result of this, indirect methods such as periodic flux density variations and jet precession, are the primary way of identifying binary candidates, and any new addition to this class can significantly increase the current sample available. In Ch. 7 I discuss my study of a binary candidate AGN, PSO J334.2028+1.4075, looking for signs of precession of its kiloparsec-scale jets.

If we take a step further in galaxy evolution, AGN jets are launched when part of the matter falling to the central engine is ejected through the poles along the magnetic field lines. However, the exact mechanism behind this process is still unknown. The

collimation of the outflow also presents us with many unknowns, as it is a result of a complex relationship between the jet, the magnetic fields threading it, and the ambient medium. 3C 84, a radio galaxy at the heart of the Perseus cluster, located at $z = 0.0176$, 75.7 Mpc from us (Strauss et al. 1992). It is an ideal candidate to study jet evolution, as 3C 84 is a nearby, bright source with short, decade-long phases of activity. To learn more about the evolution of a new jet feature (hereafter component) which emerged in 2003 (Suzuki et al. 2012), in Chapter 8 I investigate the jet characteristics, kinematics and the jet width profile at the highest angular resolution provided by the space VLBI telescope *RadioAstron* (Kardashev et al. 2013) with data taken three years after the first such observation by Giovannini et al. (2018).

Blazars are a subclass of AGN whose jets are pointed towards the observer's line of sight. Their emission is Doppler boosted, which makes them bright and highly variable through the full electromagnetic spectrum. With its unbeaten resolution, VLBI imaging is well-equipped to study the properties and the temporal evolution in parsec-scale jets in connection to the γ-ray activity. Such a work is detailed in Chapter 6, where I investigate how a bright γ-ray flare affects the brightness, spectrum and opacity of the jet in the early Universe blazar TXS 1508+572. Many AGN have also been detected at high and very high energies, often showing minute-scale flux density variability (Mannheim 1998). Focusing on the connection between the γ-ray and radio variability, in this thesis I investigate the characteristics of southern-sky blazars detected in the TeV range, as they on average exhibit slower jet speeds and lower core brightness temperatures than non-TeV-emitter AGN (see Ch. 5).

In this thesis, I present a broad range of studies covering VLBI observations of AGN jets. These works are preludes to topics that are becoming increasingly important with the upcoming new instruments, such as the Square Kilometer Array (SKA), the Black Hole Explorer (BHEX), the Cherenkov Telescope Array (CTA), and the Laser Interferometer Space Antenna (LISA), and while it is still challenging for us today to answer the open questions related to AGN, these future arrays will help us better explore these fascinating objects.

Chapter 3

Active galactic nuclei

3.1 The structure and taxonomy of AGN[1]

Active galactic nuclei are one of the most energetic sources in the Universe. They are powered by accretion onto the central supermassive black hole (SMBH) of $10^6 - 10^9$ $M_\odot$. Accretion is the most efficient energy source, as it converts the gravitational energy of the infalling gas to radiation with a ~ 10 % efficiency. AGN are characterized by a spectral energy distribution (SED) that is not only comprised by the stellar radiation of the galaxy, but has an additional component extending from the radio to the γ-rays. This emission originates from the central kiloparsec region of the AGN (Shakura & Sunyaev 1973). AGN also exhibit strong emission lines, which are not characteristic of stellar spectra that show absorption lines. These objects are strongly variable on scales of minutes to years, and this rapid variability suggests a small emission region in the vicinity of the SMBH.

The central SMBH, whose evolution I will discuss in the next section (Sect. 3.2), is surrounded by an accretion disk formed by the outward transfer of angular momentum of the accreting matter and due to friction in a collapsing sphere of matter onto a strong gravitational well. This region gives rise to ultraviolet – the blue bump in the SED– and X-ray radiation, where the high-energy radiation originates from the gas located close to the central engine (Shakura & Sunyaev 1973). Gas from the accretion disk feeds the black hole, as it first spirals inward due to the loss of angular momentum, then falls into the black hole due to its gravitational pull. Clouds of matter around this region show emission lines which can be broadened by high rotation speeds. The broad- and narrow-line regions (BLR and NLR), depending on how deep they are located in the potential well of the black hole, show broad or narrow emission lines. The BLR consists of photoionized gas heated by radiation from the black hole and the accretion disk, and it re-emits this radia-

[1]This section is primarily based on (Urry & Padovani 1995).

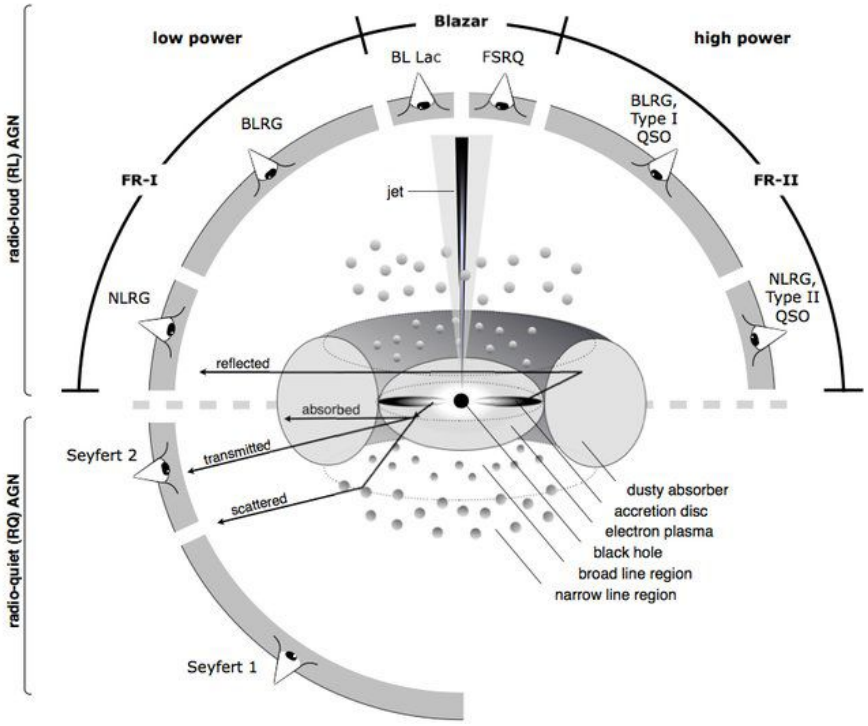

Figure 3.1: Schematic structure of AGN and different AGN types based on viewing angle and radio loudness (Beckmann & Shrader 2012).

tion in the optical and ultraviolet. The NLR is comprised of slowly moving gas clouds extending beyond the dusty torus. The torus re-radiates the emission of the accretion disk in the infrared regime between 1 μm and a few tens of μm. In the case the torus obscures the accretion disk and BLR, we talk about Type 2 AGN, while if these regions are visible in the line of sight, the sources are classified as Type 1. In radio-loud AGN, collimated beams of plasma, jets (see Sect. 3.2.2), emerge perpendicular to the plane of the accretion disk and the torus. Only about 10% of AGN are radio-loud, meaning that the ratio of the 5-GHz radio and B-band optical flux density (W m^{-2} Hz^{-1}) is larger than 10 (Kellermann et al. 1989), and these sources show jets. They emit non-thermal synchrotron radiation (see Sect. 3.4) from relativistic electrons gyrating around the magnetic field lines.

While the structure of these sources is thought to be the same, they appear as distinct types of AGN because they are observed under different viewing angles (see Fig. 3.1). As mentioned earlier, Type 1 AGN are un-obscured, therefore it is possible to observe their BLR. Radio-quiet sources in this group are nearby, low-luminosity Seyfert 1 galaxies, and more distant, luminous radio-quiet quasars (QSO). Their radio-loud counterparts are low-luminosity broad-line radio galaxies (BLRG) and steep spectrum (SSRQ), and flat spectrum (FSRQ) radio-loud quasars at higher redshift, distinguished by their radio spectra.

Table 3.1: Unified model of AGN based on Urry & Padovani (1995), see the text for more details and the abbreviations.

	Type 0	Type 1	Type 2
Radio-quiet	BAL	Seyfert 1	Seyfert 2
		QSO	
Radio-loud	BL Lacs	BLRG	FR I NLRG
	FSRQ	SSRQ	FR II NLRG
		FSRQ	

In Type 2 AGN, the line-of-sight to the BLR is obscured, so there are only narrow lines present in the spectra, if detectable. Low-luminosity Seyfert 2 galaxies and narrow-emission-line X-ray galaxies are the radio-quiet, and narrow-line radio galaxies (NLRG) are the radio-loud sources falling in this category. NLRGs are divided to two morphological subclasses, based on the most luminous parts of their radio jets and their power (Fanaroff & Riley 1974). Fanaroff-Riley class I (FR I) sources show higher intensity regions near their nucleus, and are less luminous, while FR II galaxies are brighter at the jet termination, lobes with hotspots, and are more luminous. The division in jet power, $P_{1.4\,\mathrm{GHz}}$, between these classes is $P_{1.4\,\mathrm{GHz}} \geq 10^{25}$ W Hz^{-1}, with FR I sources showing lower jet powers than this value.

Type 0 AGN include sources with unusual spectral characteristics caused by their orientation towards our line of sight. Broad-absorption-line quasars (BAL) are radio-quiet AGN which show a P-Cygni absorption profile (Beals 1934) in their optical and ultraviolet spectra, probably caused by bi-polar outflows. Blazars are the radio-loud objects in this class. Their jets are oriented at only a few degrees to our line of sight, as a result of which their emission is strongly boosted, they appear brighter, show superluminal motion and fast variability (see Sect. 3.3 for details). Their subclasses, BL Lacs and FSRQs are distinguished via the equivalent with of the emission lines, where BL Lacs show no or narrow emission lines with equivalent width < 5 Å. According to the unification scheme, BL Lacs are the beamed versions of FR I, and FSRQ are the beamed equivalents of FR II radio galaxies, because they have similar host galaxies with similar average half-light radius and absolute magnitude, as well as radio power.

In the next sections, I will give more details on AGN-related phenomena. I discuss the evolution of SMBHs via merger events, the mechanisms responsible for the creation of jets, and the radiation processes that are responsible for the broadband emission of these sources.

3.2 Galaxy evolution[2]

Currently the ΛCDM cosmological model is the most successful to explain the structure formation and evolution of the Universe. The main components of the model are dark energy, dark matter and baryonic matter, whose contributions to the total energy density, $\Omega_{\rm tot} = 1$, that is a flat Universe, are $\Omega_\Lambda = 0.73$, $\Omega_{\rm DM} = 0.27$ and $\Omega_{\rm M} = 0.04$. In this model, structure formation happens in a hierarchical manner. Small density fluctuations grew via gravitational instabilities after the recombination era, and collapsed to form small, gravitationally bound objects. Dark matter haloes then form as these objects merge, and form galaxies via radiative cooling of hot baryons in the dark matter halo. The galaxy is affected by feedback from star formation, supernovae, AGN, et cetera. The properties of black holes residing in the center of galaxies correlate with that of their hosts. The black hole mass in early-type galaxies is correlated with the stellar velocity dispersion, with the mass of the bulge of the host, and the total stellar mass. These relations suggest that the evolution of black holes and their host galaxies are tied together.

3.2.1 Galaxy mergers and binary supermassive black holes

As mentioned before, structure formation happens in a hierarchical manner in the ΛCDM Universe, and galaxy mergers are responsible for the growth and structure of galaxies. Supermassive black holes are thought to reside in the centers of all massive galaxies. During a major merger of galaxies with comparable masses, the gas contained in the galaxies loses angular momentum, and falls into to center, stellar orbits are disrupted, star formation is quenched or enhanced, accretion of the perturbed gas may lead to AGN activity, and the final phase of this violent process is characterized by the interaction of the SMBHs (see e.g., Van Wassenhove et al. 2012).

Mergers of SMBHs can be divided into three major steps. The first stage of the merger is driven by dynamical friction as the two black holes loose angular momentum and fall towards the center. In the next phase, three-body interactions with stars help the binary to loose orbital energy. Finally, the decay of the binary separation progresses through the emission of gravitational waves, until their eventual coalescence. The gravitational waves emitted during the coalescence are the object of study of the European Space Agency's LISA mission, expected to be launched in the mid-2030s (Amaro-Seoane et al. 2017). If the merging SMBHs differ in mass, the merger event will create a non-zero momentum that is carried away by gravitational waves, and causes a recoil which moves the new SMBH out from the center of the galaxy. Depending on the recoil velocity, the black hole

[2]This section is based on (Netzer 2013; Schneider 2006).

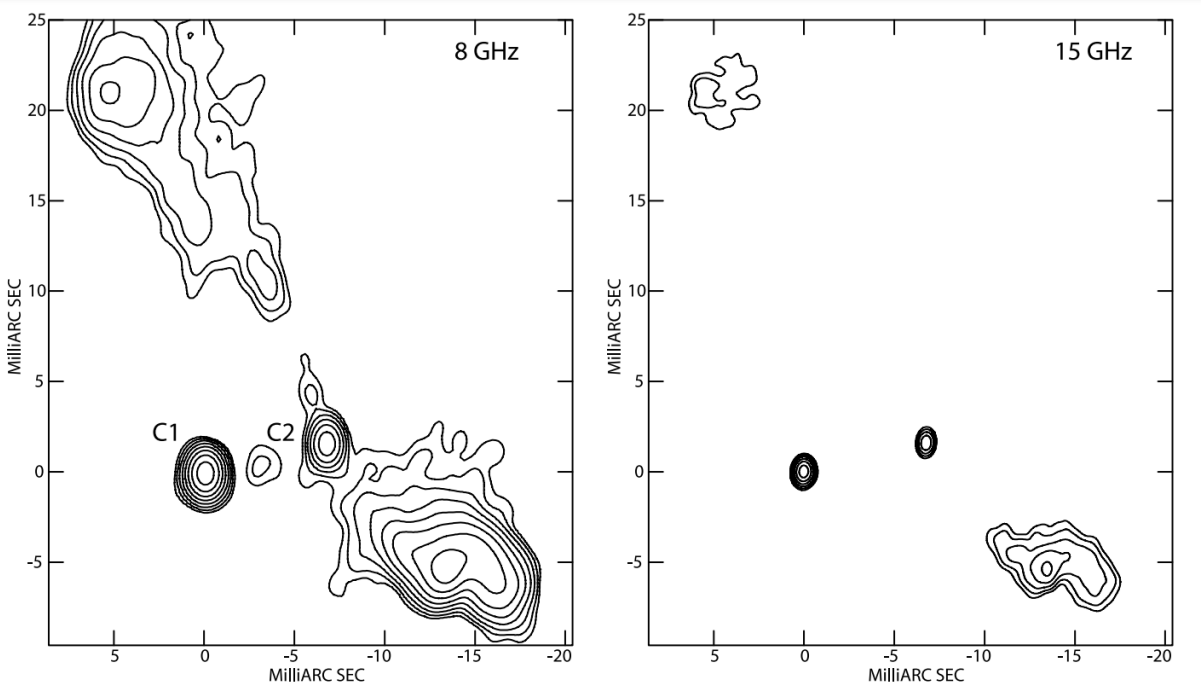

Figure 3.2: The binary AGN 0402+379 as seen by the VLBA at parsec scales (Rodriguez et al. 2006).

either returns to the nucleus in a few dynamical timescales or it is ejected, and continues its existence as an intergalactic black hole.

Observing SMBHBs can help understand the merger history of galaxies, black hole growth and AGN activity related to mergers. However, these objects are quite elusive to detect with our current instruments. The direct detection of these sources is only possible in nearby galaxies. The ultraluminous infrared galaxy, NGC 6240, harbors a dual AGN whose components have been resolved with the *Chandra* X-ray space observatory (Komossa et al. 2003). A similar discovery was made by *Chandra* in Mrk 739, where the two nuclei's projected separation is 3.4 kpc (Koss et al. 2011). VLBI makes it possible to observe SMBHBs at even smaller separations. For example, the binary with a 7.3-pc separation in the radio galaxy 0402+379 (Fig. 3.2) was resolved with the Very Long Baseline Array (Maness et al. 2004; Rodriguez et al. 2006).

Indirect methods aimed at discovering SMBHBs include periodic variations in the light curve, double-peaked emission lines, jet precession, and a double-double or an X-shaped jet morphology. The most famous candidate, OJ 287 exhibits outbursts in the optical every $\sim$ 12 yrs, when a possible companion black hole crosses the accretion disk of the primary SMBH (Lehto & Valtonen 1996).

When the components of a binary orbiting a common center of mass are still far away ($1-10$ kpc) from each other and the the gas clouds of the NLR are still independent from

each other, the clouds' line-of-sight velocity differs. As a result of this, emission lines of, for example O[III], will appear with double peaks. This effect can also be caused by for example a jet interacting with clouds of a single NLR, so this method alone is not reliable to identify binary candidates (Frey et al. 2012).

Jet precession, revealed by a helical jet pattern, can be indicative of the perturbing effects of a secondary SMBH (Caproni & Abraham 2004) or Lense–Thirring precession (Lense & Thirring 1918; Liska et al. 2018). These external drivers of jet precession cause a helical jet shape with a constant pitch angle, that reflects the periodic change in the direction of the component ejection, and components move on ballistic paths. Internal drivers, such as jet instabilities (Perucho et al. 2006) create helices with increasing pitch angles where components move in helical patterns.

Finally, double-double and X-shaped sources are thought to be products of galaxy mergers. In X-shaped sources, the legs of the "X" are comprised of the jets of past and present active phases, and are oriented at large angles because the spin of the two original AGN and the merger product SMBH are different from each other, hence the jets are ejected in different directions (Gergely & Biermann 2009). In double-double sources, however, this spin-flip does not happen during the merger, and both the relic and recent outflows lay in the same direction (Roettiger et al. 1994). The break in jet activity might be caused by the merger sweeping out the accreting material from the vicinity of the newly formed black hole. It is also possible that double-double AGN are X-shaped sources, however their orientation to our line of sight makes the outflows appear in the same direction.

3.2.2 Launching and evolution of AGN jets

While several models have been proposed to explain the launching mechanism of AGN jets, none of them have been proven as the ultimate one. In this section, I discuss the two most commonly invoked processes, namely, the Blandford–Znajek (Blandford & Znajek 1977) and Blandford–Payne mechanisms (Blandford & Payne 1982).

The Blandford–Znajek mechanism is a type of Penrose process (Penrose & Floyd 1971) that extracts the rotational energy from the black hole ergosphere via force-free electromagnetic fields that are supported by the accretion disk. Additionally, jets can be launched from the accretion disk surrounding the SMBH via the Blandford–Payne mechanism. In this instance, the magnetic field is anchored in the accretion disk. The plasma attached to the field lines is accelerated analogously to the bead-on-a-wire scenario, whereby the centrifugal force along the field line increases as they move away from the axis. Once this force exceeds the gravitational force, the plasma along the line is accelerated

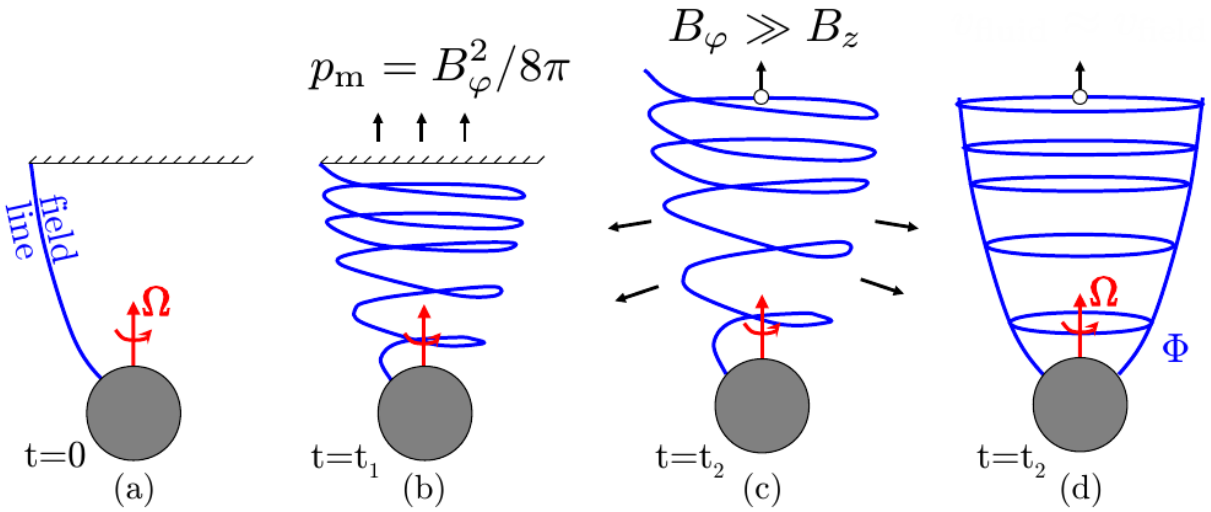

Figure 3.3: Schematic drawing of jet launching represented at three time intervals. First, the magnetic field is dominated by its poloidal component which coils up as the black hole rotates to form toroidal field lines. At some point, the forming pressure, $p_{\rm m} = B_\phi^2/(8\pi)$, where B_ϕ is the magnetic field strength of the toroidal field lines, becomes large enough to accelerate plasma attached to the toroidal field lines that slide down the poloidal ones, whose magnetic field strength is denoted by B_z. The slightly modified figure originates from Tchekhovskoy (2015).

outwards (Spruit 1996). In both launching mechanisms, once the acceleration cannot be maintained, the field lines get wound up due to the gas lagging behind the field line rotation. Each rotation adds a new loop of the field line in a spiral formation. The schematic of these processes is shown in Fig. 3.3. It is currently impossible to observationally distinguish which mechanism is responsible for the launching of AGN jets, and it is also possible that both of these processes are at play. Extremely high resolution observations, for example with *RadioAstron*, might shed some light on this question.

The exact way these outflows are collimated remains uncertain. It is hypothesized that helical magnetic fields play a pivotal role in this process, whereby the hoop stress of the toroidal magnetic field directs the poloidal field lines towards the jet axis (Spruit 1996). In the central region, winds from the accretion disk, cocoons inflated by the jet or the ambient medium can also play a part in confining the jet (Bogovalov & Tsinganos 2005; Globus & Levinson 2016). Apart from this, further away from the nucleus external pressure exerted by the ambient medium might also be necessary to sufficiently collimate relativistic outflows (Lyubarsky 2009). The collimation profile close to the central engine is cylindrical or parabolic, and at $\sim 10^4 - 10^6$ $r_{\rm S}$[3], where the collimation is less efficient, the profile transitions to conical (see e.g., Asada & Nakamura 2012; Kovalev et al. 2020).

[3] $r_{\rm S} = 2GMc^{-2}$ is the Schwarzschild radius, G is the gravitational constant, M is the black hole mass, and c is the speed of light

3.3 Relativistic effects

Relativistic photons originating from AGN jets are emitted in a narrow cone with a half-opening angle of Γ^{-1}. This beaming effect influences the brightness and variability timescales of the object. For a jet pointing towards the observer, time intervals that are measured in the frame of the observer (t) are shorter than in the AGN's rest frame t', $t = \delta^{-1}t'$, where δ is the Doppler factor. Intensity is enhanced as $I_\nu(\nu) = \delta^3 I'_{\nu'}(\nu')$, where primed quantities are measured in the object's rest frame, and non-primed quantities are measured in the frame of the observer. The broadband flux density, on the other hand, increases as $S = \delta^4 S'$ (Rybicki & Lightman 1979), which explains why one-sided AGN are more commonly observed compared to double-sided jets, as the emission from the approaching jet is boosted and from the receding one is dimmed. This also leads to a selection effect, where jets far away which are oriented toward us are detected, while other de-boosted jets at the same distances are not.

Superluminal apparent motion is a common characteristic of AGN (see e.g., Lister et al. 2021). It was first observed in 3C 273 by Cohen et al. (1977). Superluminal motion is essentially the result of a projection effect paired with the finite speed of light (Fig. 3.4). Two jet components ejected at t_1 and t_2, both traveling with velocity v along a line oriented at θ toward the observer. The distance between these components along the line of sight is $v\cos\theta\Delta t$, where Δt is the difference between the ejection of the components. Perpendicularly to this, the distance between the clumps is $c\Delta t - v\cos\theta\Delta t$. Based on this, the difference in arrival times between the two features is $\Delta t_{\rm meas} = (1 - \beta\cos\theta)\Delta t$. Then the distance traveled by the components in the plane of the sky is $d = v\sin\theta\Delta t$. The apparent speed in the plane of the sky is then given as:

$$\beta_{\rm app} = \frac{d}{c\Delta t_{\rm meas}} = \frac{\beta\sin\theta}{1 - \beta\cos\theta}. \tag{3.1}$$

This can lead to an observed apparent velocity faster than the speed of light when β is high and θ is small. However, it is difficult to distinguish based on observations which one of these two jet parameters gives rise to the superluminal apparent motion (see Fig. 3.4).

Relativistic effects, such as Doppler boosting, play an important role in variability studies, for example when researching TeV-emitter AGN affected by the Doppler crisis. I discuss the multiwavelength variability, including the Doppler crisis, in detail in Sect. 3.5, but first I explain the most important emission processes that give rise to the broadband SED of active galactic nuclei.

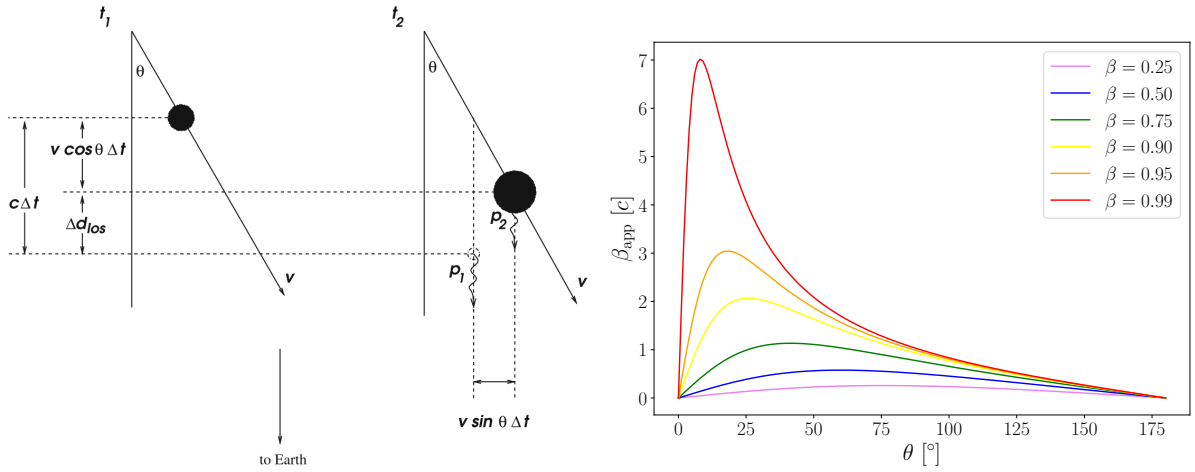

Figure 3.4: Relativistic effects in AGN. *Left:* superluminal motion based on Gabuzda (2015); *right:* $\beta_{\rm app}$ as a function of viewing angle and intrinsic jet velocity.

3.4 Emission processes in AGN jets[4]

AGN emit radiation throughout the whole electromagnetic spectrum. While there are several contributions to this emission from the different parts of the object, here I discuss the two main ones related to jet emission, synchrotron and inverse Compton radiation. Both of these processes will be important when I take a deeper look into the multiwavelength variability observed in AGN (Sect. 3.5).

3.4.1 Synchrotron radiation

Synchrotron emission is a type of free-free radiation created by relativistic electrons gyrating in a magnetic field. They produce non-thermal radiation from the radio up to the X-rays. For an electron with energy E moving in a uniform magnetic field with strength B, the power P of the electron is given as:

$$P = 2\sigma_{\rm T} c \gamma^2 \beta^2 u_B \sin^2 \alpha, \tag{3.2}$$

where $\sigma_{\rm T}$ is the Thomson cross section, $\gamma = E/mc^2$ is the electron Lorentz factor, $\beta = v/c$ with v being the speed of the electron, $u_B = B^2/8\pi$ is the magnetic energy density, and α is the pitch angle between the magnetic field line and the direction of motion. Averaging Eq. 3.2 over isotropic pitch angles, we get:

$$\overline{P} = \frac{4}{3}\sigma_{\rm T} c \gamma^2 \beta^2 u_B, \tag{3.3}$$

[4]This chapter is based on Rybicki & Lightman (1979).

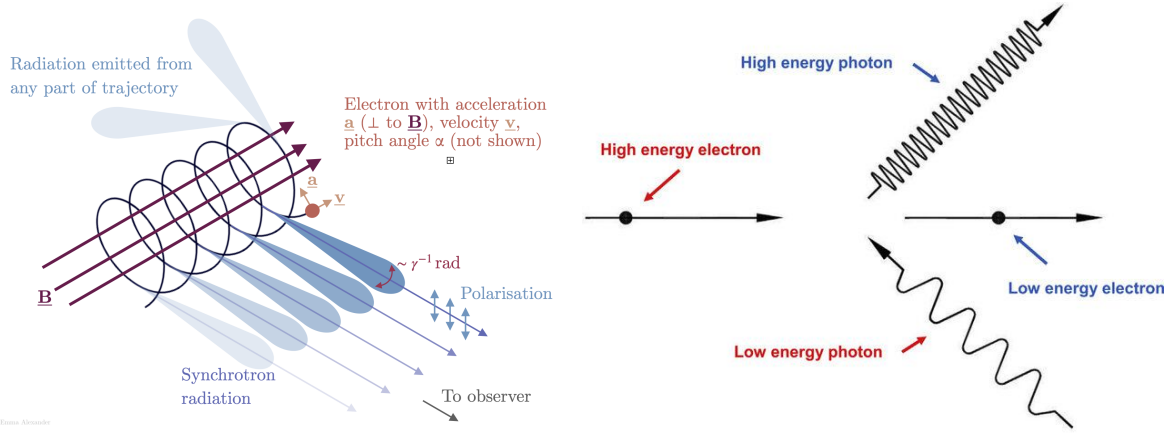

Figure 3.5: Sketches of synchrotron (left panel) and inverse Compton (right panel) radiation. Image credits: Emma Alexander and Michael D. Wright.

indicating that the electrons gyrating in the magnetic field lines emit radiation in the direction of their motion. The cooling time scale can be calculated based on the energy loss rate for a single electron as:

$$\tau_{\rm cool}[{\rm s}] = \frac{3mc}{4\sigma_{\rm T} u_B \gamma} \simeq 5 \times 10^8 B^{-1}[{\rm G}]\gamma^{-1}. \tag{3.4}$$

This means that high-energy electrons cool faster than their low-energy counterparts. The different parts of AGN are classified based on their characteristic cooling times and spectral properties. For example, extended lobes on kiloparsec-scales typically show cooling timescales of 10^7 yr, magnetic field strengths of 10^{-5} G with a turnover frequency of 1 GHz. While parsec-scale jets have their turnover in the same frequency range, magnetic field strengths are higher, approximately 0.1 G and electrons cool on shorter timescales of 10 yr.

The spectrum created by synchrotron photons with a power-law electron energy distribution of $N(E)dE \sim E^{-p}dE$, can be divided to an optically thin and optically thick part, separated by a break at the turnover frequency, $\nu_{\rm s}$. Integrating the photon energy distribution yields a spectrum that can be described as a power-law, ν^{α}, where the spectral index is given as $\alpha = -(p-1)/2$. The optically thick part of the spectrum below $\nu_{\rm s}$ is created by photons whose mean free path is smaller than the size of the emission region. At these frequencies, the absorption of photons by the synchrotron-emitting electrons, a process know as synchrotron self-absorption, gives rise to a spectrum with $\alpha = 2.5$. Although the radio core is usually partially optically thick, free-free absorption, when a free electron collides with an ion absorbs a photon, gaining energy in the process, can lead to higher spectral indices than $\alpha = 2.5$. In the optically thin components, generally represented by the jet in AGN, the photons can escape the emission region. Above $\nu_{\rm s}$, typical spectral indices fall around $\alpha \sim -0.5$ to -1.

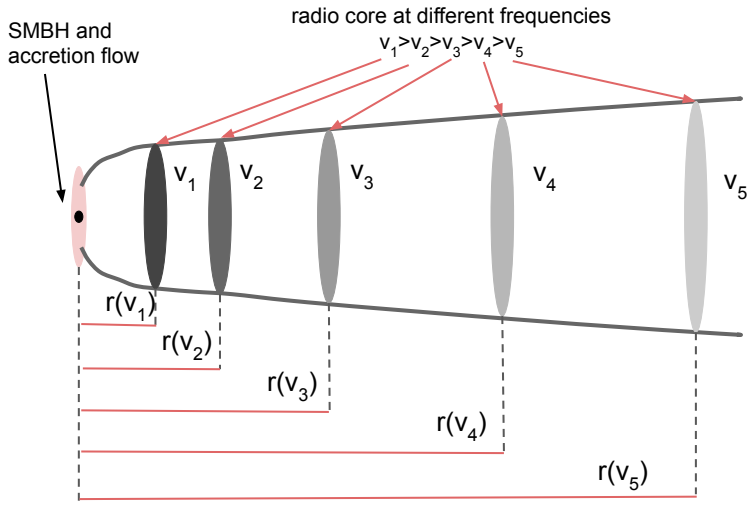

Figure 3.6: A schematic illustrating the frequency-dependent position of the radio core, that is the core shift.

Synchrotron radiation can be linearly polarized up to 70%. However, observations usually reveal a much lower degree of polarization around $\leq 15\%$, indicative of depolarization. AGN also exhibit correlated variability in polarization and total intensity. On kiloparsec scales, the lobes exhibit the largest fractional polarization, with electric vector polarization angles (EVPA) lined up parallel to the boundary, otherwise transverse to the jet direction, which indicates that the toroidal component of the magnetic field lines dominates in this region (Laing 1980). In parsec-scale jets, several tendencies have been identified for different AGN classes. Usually the core exhibits the highest polarized flux density, but the fractional polarization only reaches a few percent in blazars, and it is even weaker in radio galaxies. In general, fractional linear polarization grows downstream in the jet, suggestive of more ordered magnetic field lines in these regions. Radio galaxies exhibit a much smaller fractional polarization values than blazars in their jets as well. Out of the AGN subclasses, BL Lacs show the highest fractional polarization in their core and jet regions. They have stable EVPAs which are commonly aligned with the inner region of the jet, while EVPAs in the jet are aligned with its direction (Pushkarev et al. 2017). A similar trend has not been observed in other sources.

The standard theory describing the synchrotron-emitting regions of AGN is presented by (Blandford & Königl 1979). The model assumes that the optically thin jet is of conical shape, and that the optically thick core represents the region where the optical depth equals unity, thus its location is frequency-dependent (Fig. 3.6). While the absolute position of the source is lost during fringe fitting (see Sect. 4.5) the optically thin jet provides a basis for alignment, as this component represents the location across the observing

frequencies. The alignment then enables the approximation of the distance between the central engine and the highest-frequency core position, as well as the measurement of the magnetic field strength near the SMBH (see Sect. 6).

3.4.2 Inverse Compton radiation

During inverse Compton (IC) scattering, low-energy photons gain energy via collisions with fast electrons, as a result of which they can reach a frequency of $\nu' \approx \gamma^2\nu$. In jets, the typical Lorentz factor of synchrotron emitting electrons is $\gamma \sim 10^4$, meaning that the photons can be scattered up to the X-ray and γ-ray bands. Depending on the origin of the photons relative to the electrons scattering them, we talk about synchrotron self-Compton (SSC), when the synchrotron-photons are up-scattered by the electrons emitting them, and external Compton (EC) scattering, where the photon fields are external to the jet flow, for example the BLR, the dusty torus, or the cosmic microwave background.

The power emitted by IC photons can be calculated in a similar manner as for synchrotron radiation:

$$\overline{P} = \frac{4}{3}\sigma_{\mathrm{T}} c \gamma^2 \beta^2 u_{\mathrm{ph}}, \tag{3.5}$$

with the only difference that the energy density of the magnetic field, u_B, is replaced by that of the radiation field, u_{ph}. The electron energy distribution for IC is a power-law, and the spectral index of the scattered photons can be described similarly to the case of synchrotron emission as $P \propto \nu^{\alpha}$, where $\alpha = -(p-1)/2$.

IC catastrophe ensues when the number density of low-energy photons is so significant that energy loss is dominated by IC scattering rather than synchrotron radiation. This means that the ratio of the IC and synchrotron power should fall below unity:

$$\frac{\overline{P}_{\mathrm{IC}}}{\overline{P}_{\mathrm{synch}}} = \frac{u_{\mathrm{ph}}}{B^2/8\pi} > 1. \tag{3.6}$$

For a non-relativistic radio source, this puts a limit on the brightness temperature so that it should not exceed $\sim 10^{12}$ K (Kellermann & Pauliny-Toth 1969), and electrons which exceed this limit will swiftly cool by IC scattering below the 10^{12} K.

3.5 The radio-gamma connection in blazars

Blazars, as mentioned above, are AGN whose jets are pointed towards the observer's line of sight, which, for high Lorentz factors in the plasma fluid, leads to highly Doppler-boosted emission that makes them bright and variable through the full electromagnetic spectrum. Their SED consists of a low- (radio to UV/X-rays) and a high-energy (X-rays to γ-rays) component, the former produced by synchrotron emission (Sect. 3.4.1), while

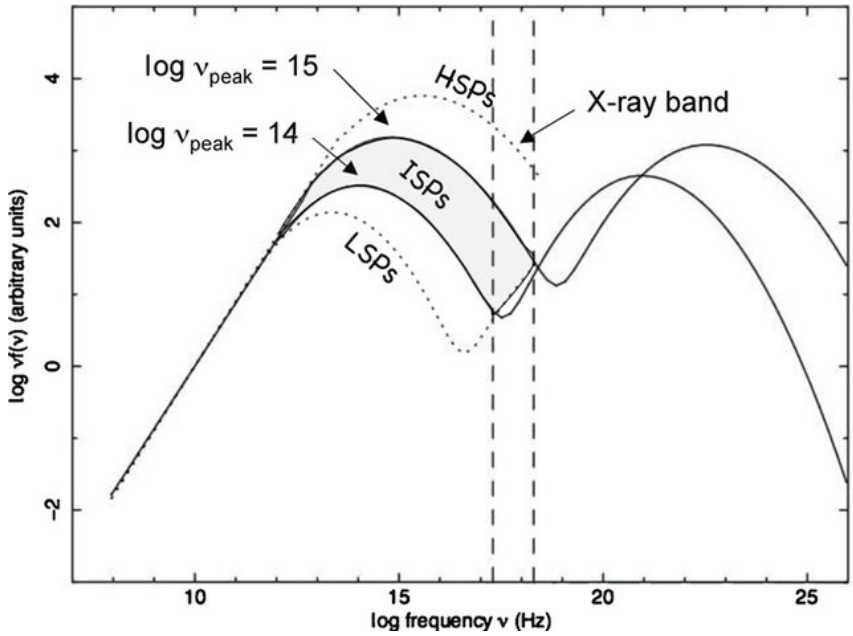

Figure 3.7: Model SED of different blazar classes. The low-frequency hump arises due to synchrotron emission, and the high-energy one due to leptonic and/or hadronic processes. Figure taken from (Abdo et al. 2010).

the origin of the latter is still disputed. In leptonic models, the high-energy hump originates from inverse Compton scattering (Sect. 3.4.2), which depending on the origin of the seed photon field, can be either SSC or EC scattering with seed photons from the broad-line region and/or the dusty torus.

Alternatively, hadronic models, such proton-synchrotron, can also explain the high-energy emission (e.g., Aharonian 2002; Böttcher et al. 2013). The definitive signal of hadronic processes would be the detection of neutrinos from blazars. Mannheim (1995) predicted that these objects would give a cumulative neutrino signal that exceeds the atmospheric background at energies of > 100 TeV. This is based on the assumption that both the neutrinos and the γ-ray photons are produced by accelerated protons in a relativistic jet. However, only neutrinos of PeV energies are certainly of astrophysical origin, since the steep spectra of atmospheric neutrinos do not extend to these energies. Although associations with AGN exist, such as with the γ-ray flaring blazar TXS 0506+056 (IceCube Collaboration et al. 2018), and PKS B1424−418 during a major outburst (Kadler et al. 2016), and there is growing evidence that neutrinos originate from AGN. However, unambiguous identifications have thus far eluded us (see e.g., Hovatta et al. 2021; Plavin et al. 2023).

Blazars can be further classified as FSRQs and BL Lac objects, which can be divided into four subclasses based on the location of the synchrotron peak, $\nu_{\rm peak}$, in their SED

(Abdo et al. 2010): low (LBL, $\nu_{\rm peak} < 10^{14}$ Hz), intermediate (IBL, $10^{14} < \nu_{\rm peak} < 10^{15}$ Hz), high (HBL, $10^{15} < \nu_{\rm peak} < 10^{17}$ Hz), and extremely high (EHBL, $\nu_{\rm peak} > 10^{17}$ Hz)- synchrotron-peaked objects. The blazar sequence, a trend that higher radio luminosity sources have lower SED peak frequencies, was first suggested by Fossati et al. (1998). This idea went through several incarnations, as contradicting sources for example with high luminosity and high peak frequency (e.g., Padovani et al. 2003) were found. The latest version of the blazar sequence presented by Ghisellini et al. (2017) proposes that the sequence only exists for BL Lac objects, while the SED peak remains constant for FSRQs in different radio luminosity bins. In addition, FSRQs are Compton dominated, that is the high-energy component peaks at higher luminosities. This is due to existence of a BLR and dusty torus in these sources surrounding the emission region, making radiative cooling more dominant for FSRQs than for BL Lacs.

Lister et al. (2011) found a correlation between γ-ray loudness and the synchrotron peak frequency for BL Lacs, suggesting a universal SED shape for this blazar class. HBL sources, which are the main TeV-emitters, exhibit lower than average core brightness temperatures, and unlike FSRQs, they do not show large amplitude radio variations nor high linear core polarization levels. Lister et al. (2011) concludes that HBL sources have lower Doppler factors than FSRQs, as well as LBL and IBL objects (see also Benke et al. 2024). These sources are also distinguished by kinematic characteristics, where HBLs show quasi-stationary jet knots, and FSRQs have jet components traveling at relativistic speeds, and finally LBL and IBL sources form a transition between these classes (Hervet et al. 2016). These source properties are more prevalent in VHE-detected blazars, which are more likely to show relatively low brightness temperatures on the order of $\sim 10^{10}$ K, and low apparent jet speeds despite the very high Doppler factors needed to fit the SED of these sources.

One of the widely studied open questions regarding the multiwavelength nature of blazars is known as the Doppler crisis (Piner & Edwards 2018b). Many blazars have been detected at high (HE; 100 MeV $< E <$ 300 GeV) and very high energies (VHE; $E >$ 100 GeV), and these show rapid variability, often on timescales of minutes (see e.g., 2155−304, Mannheim 1998). This suggests a small emission region and high Doppler factors, and indeed Doppler factors of $\delta \approx 50$ are required to reproduce their spectral energy distribution (SED) at high energies (Piner & Edwards 2018b). On the other hand, VLBI observations reveal slow component motions with Doppler factors of < 10 (Piner & Edwards 2018b). A prominent example of the Doppler crisis blazar is Mrk 421 (Aleksić et al. 2012; Lico et al. 2012).

Locating the origin of the HE emission, also known as the blazar zone, has also proven challenging. The observed short-time variability in the VHE band suggests that the TeV

emission originates from a small region. Under the assumption that the emission region fills the jet diameter, the VHE emission region must be located close to the central engine (Saito et al. 2013). The availability of seed photons for external Compton scattering also supports this scenario (Böttcher & Els 2016). However, this HE emission is expected to be absorbed by the dense photon fields of the broad line region, which would prevent us from detecting blazars at VHE. On the other hand, Marscher et al. (2012) and Jorstad et al. (2013) found that activity near the radio core at 43 GHz coincides with γ-ray flares, suggesting that the HE emission originates downstream from the central supermassive black hole.

Several models have been proposed to explain both the Doppler crisis and the location of the blazar zone, all of them invoking multiple Doppler factors for different emission processes in the parsec-scale jet. These models include a spine-sheath transverse velocity structure (Ghisellini et al. 2005), a decelerating jet with a slower moving plasma at the jet edge (Georganopoulos & Kazanas 2003), multizone models (Tavecchio et al. 2011), or minijets created via magnetic reconnection (Giannios et al. 2009). Currently, high-resolution VLBI observations are required to distinguish between these jet models.

Long-term, quasi-simultaneous multiwavelength campaigns are essential to capture AGN during their different phases of activity. They provide a complete picture on the spectral properties, polarization and structure of their targets. VLBI is essential in order to study parsec-scale jet parameters, such as the opening and inclination angles, the Doppler factor (Lister et al. 2018), as well as the underlying magnetic field configuration (Zobnina et al. 2023). In addition, it enables jet kinematic measurements (Lister et al. 2021), the localization of the emission region (Kramarenko et al. 2022), and investigating the correlation in component brightness and size with activity observed at other wavelengths (Angioni et al. 2019, 2020). These information are crucial to distinguish between the various possible blazar emission models, and to provide association for VHE photons and neutrino candidate sources. In the next section, I discuss TANAMI, the monitoring program I have been contributing to during my dissertation work.

3.5.1 TANAMI: Tracking Active Galactic Nuclei with Austral Milliarcsecond Interferometry

TANAMI is a multiwavelength AGN monitoring program targeting sources of the southern hemisphere. The program utilizes antennas of the Australian extended Long Baseline Array. VLBI observations are carried out since 2007 at 8.4 and 22 GHz (Ojha et al. 2010; Müller et al. 2018), and at 2.3 GHz since 2020 (Benke et al. 2024). In addition, multi-frequency monitoring is carried out with ATCA under the project code C1730. Multiwave-

length observations with REM, *Swift*, *XMM-Newton*, *Suzaku*, *INTEGRAL*, *Fermi* LAT and other telescopes are also part of the program. The TANAMI sample contains 183 AGN as of May 2024, including HE and VHE-detected sources, as well as astrophysical neutrino associations.

The first images of 43 sources from the 8.4-GHz TANAMI monitoring appeared in Ojha et al. (2010), which was appended with a catalog of additional sources by Müller et al. (2018). They obtained high dynamic range images for all sources, and for several objects, these were the first ever VLBI maps to be published at milliarcsecond resolution. Müller et al. (2018) also concluded the γ-ray loud objects on average are more compact and exhibit higher core brightness temperatures, meaning the the emission region is smaller and the radiation is Doppler boosted, hence Doppler factors also tend to be higher in these sources than in γ-ray faint AGN.

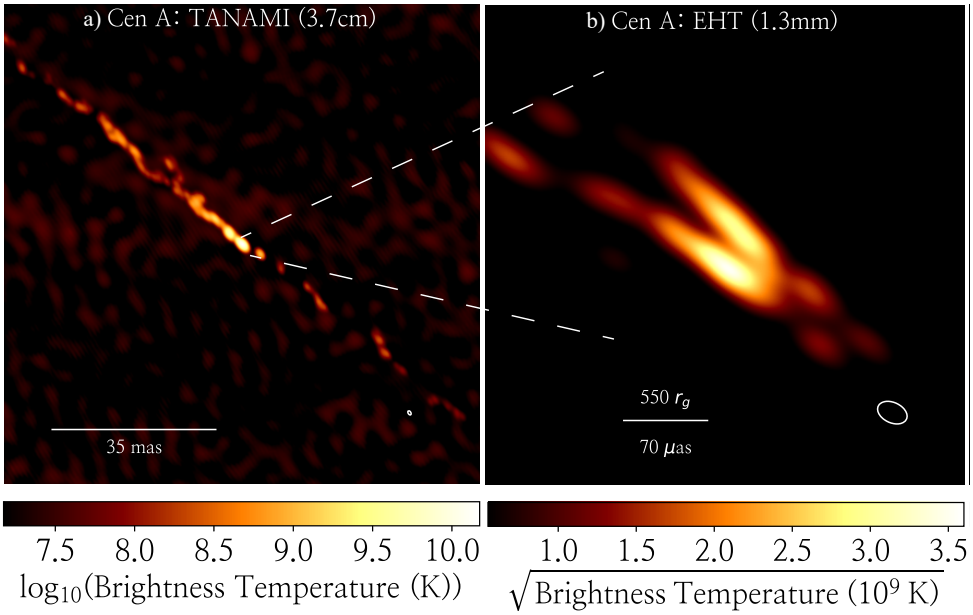

Figure 3.8: The 8.4-GHz TANAMI (Müller et al. 2014) and the 230-GHz EHT image (Janssen et al. 2021) Cen A. The lower frequency map reveals a double-sided structure of $\sim$ 100 mas along the northeast-southwest direction, while the EHT image shows a limb-brightened jet and counter-jet in the central $\sim$ 300 μas.

Centaurus A (hereafter Cen A, see Fig. 3.8), the closest AGN located at a distance of 3.8 Mpc (Harris et al. 2010), is an FR II class radio galaxy with spectacular lobes extending several kiloparsecs from the core. The 8.4-GHz and 22.3-GHz TANAMI maps published in Müller et al. (2014) revealed the milliarcsecond jet structure of Cen A. The authors found component speed ranging from 0.1 c to 0.3 c, with increasing component speed downstream in the jet, where it becomes optically thin. This differential motion is suggestive of a spine-sheath structure, detected as limb-brightening in the 230-GHz

EHT observations (Janssen et al. 2021). Based on the jet to counter-jet ratio, Müller et al. (2014) constrained the viewing angle to be $\theta \sim 20\,\mathrm{deg} - 45\,\mathrm{deg}$. The most interesting finding, however, was a decrease in surface brightness and circumfluent jet behavior at ~ 25 mas northeast from the core (see panel *a,* of Fig. 3.8) which was interpreted as an interaction between the jet flow and a star in the host galaxy.

The two main focuses of TANAMI are γ-ray detected AGN (Angioni et al. 2019, 2020) and neutrino associations (Rösch et al. 2023). As mentioned above in Section 3.5, while there is growing evidence for neutrinos associated with astrophysical sources (Hovatta et al. 2021; Plavin et al. 2023), unambiguous identification with individual AGN have not been made so far. One of the most energetic neutrinos nicknamed 'Big Bird' of 2 PeV, was detected by IceCube in December of 2012 (Aartsen et al. 2014). The uncertainty region also contained a γ-ray loud FSRQ, PKS B1424−418, which underwent a major outburst at several wavebands during the arrival time of the neutrino. The 8.4-GHz VLBI observations between November 2011 and March 2013, published by Kadler et al. (2016), revealed a significant brightening in the compact core region, with its flux density increasing from $\sim$ 1.5 Jy to $\sim$ 6 Jy. An association between the two events was thus established with a chance coincidence of about 5%.

The radio and γ-ray properties of γ-ray-detected and non-detected radio galaxies were studied in detail by Angioni et al. (2019, 2020). They found a correlation between the radio core and the γ-ray flux density, which has also been observed in samples dominated by blazars (see e.g., Kovalev et al. 2009). However, for radio galaxies there was no correlation detected between the core brightness temperature or core dominance, which are indicators of Doppler boosting, with respect to γ-ray luminosity. This finding is unlike what is observed for blazars, whose emission is highly Doppler beamed, and suggests that γ-ray loudness is not indicative of a Doppler-boosted jet flow.

In this thesis, I focus on studying the properties of the TeV-detected AGN included in the TANAMI monitoring. As mentioned in Sect. 3.5, the Doppler crisis has been puzzling radio and γ-ray astronomers for over a decade now. Among others (Piner & Edwards 2014, 2018a), our observations detailed in Ch. 5 aim to shed a light on this phenomenon.

Chapter 4

Very long baseline interferometry

4.1 The history of radio astronomy

Radio astronomy is the second branch of astronomy to appear after optical astronomy in the 1940s. The radio window stretching between 0.3 mm and 30 m enabled the development of ground-based radio astronomy, which was also supported by the emerging telecommunication facilities, such as radars.

Karl G. Jansky at the Bell Telephone Laboratories was researching weather phenomena interfering with intercontinental communication when he discovered a consistent increase in noise in a given direction that changed in azimuth angle by $\sim$ 4 min per day. He concluded that the source of the radiation is located outside the Solar system, and was later identified as the Galactic center black hole, Sgr A* (Jansky 1933). The pioneer of parabolic reflectors, Grote Reber, constructed his own antenna of 9.6 m in diameter in his backyard in Illinois. He mainly conducted long wavelength (160 MHz) observations mapping out the Galactic plane (Reber 1940). This non-thermal radiation was later discovered to be a type of free-free emission originating from electrons gyrating in the magnetic field lines, that is synchrotron radiation (see Sect. 3.4.1, Kiepenheuer 1950; Shklovskii 1952).

The first large radio antenna, the Dwingeloo Radio Observatory, was built in the Netherlands, and this 25-m dish began its operation in 1957. In the coming decades, other large telescopes followed, such as the 64-m Parkes telescope in Australia, the Arecibo Observatory with its 300-m filled-aperture telescope in 1963, and the Effelsberg 100-m telescope in 1972. The quest for resolution propelled radio astronomers to increase the size of our instruments via VLBI in the 1970s, even launching antennas to space, and to decrease the observing wavelength to the mm wavelength regime.

Figure 4.1: The three types of antennas used for astronomical observations: *a,* LOFAR dipole antennas; *b,* wire mesh antennas of CHIME; *c,* the Effelsberg 100-m parabola antenna. Image credits: ASTRON, CHIME, MPIfR/Norbert Tacken.

The first documented observation of AGN was carried out by Edward Fath who used the Lick 36-inch telescope to obtain the optical spectrum of seven spiral nebulae. Out of these objects, NGC 1068 exhibited a peculiar spectrum with forbidden emission lines of oxygen and neon, characteristic of planetary nebulae rather than stars (Fath 1909). Similar studies were carried out by Carl Seyfert, who described galaxies with „an exceedingly luminous stellar or semistellar nucleus which contains a relatively large percentage of the total light of the system", as well as wide emission lines with 10000 km s^{-1} (Seyfert 1943). Later, these galaxies were named after him. The first detection of an AGN jet is attributed to Heber Curtis in 1918, who described his observations of M 87 as the galaxy exhibits a „curious straight ray ... apparently connected with the nucleus by a thin line of matter" (Curtis 1918).

By the middle of the 20^{th}, century several radio sources, for example M 87, Cygnus A and Centaurus A, were identified with galaxies with extended jets (Bolton et al. 1949). In 1963, 3C 273 and 3C 48 have been observed as extragalactic sources at $z > 0.1$ (Hazard et al. 1963; Schmidt 1963). They were first identified as stellar objects, hence the name quasi-stellar object (QSO) or quasar. However, their extreme luminosities that are 10-30 times that of bright elliptical galaxies, and the emitted total energies $> 10^{60}$ erg s^{-1} (Greenstein 1963) could only be explained by compact objects, black holes.

The term "black hole" was coined by John Wheeler in 1968. The existence of black holes were first hinted at by the natural philosopher John Michell in 1784. Based on Newton's law of gravity and the escape velocity, he suggested the existence of 'dark stars' with enough mass that light could not escape them. This idea was published by Pierre-Simon Laplace in the 18^{th} century. The concept later coined as "black holes" gained more attention after Albert Einstein published his theory of general relativity in 1915. Solving these equations, Schwarzschild derived the formula for what is now known as the Schwarzschild radius defining the event horizon of a black hole. However, the existence of

a singularity concerned many of his contemporaries. Solutions for a rotating black hole were only found later by Kerr in 1963 (Kerr 1963). Spacetime around these objects was studied in detail from the 1970s, including the effects of gravitational lensing and Doppler boosting around black holes. The first image based on simulations also appeared around this time (Luminet 1979), depicting a spherical black hole with a thin accretion disk. VLBI observations have been developed since the 1990s in order to reach high enough frequencies to image the shadow of a black hole (Event Horizon Telescope Collaboration et al. 2019).

Radio astronomy has provided us with several ground-breaking discoveries. The Nobel prize in 1978 was awarded to Arno Penzias and Robert Wilson for their discovery of the cosmic microwave background. Pulsars were first observed by Jocelyn Bell in 1967, for which her supervisor, Antony Hewish, was awarded the Nobel prize in 1974. Martin Ryle was also given this prestigious award for the development of aperture synthesis (see Sect. 4.3). Recently, the Event Horizon Telescope (EHT) Collaboration dazzled the community with the first images of the black hole shadows of M 87* and Sgr A* (Event Horizon Telescope Collaboration et al. 2019, 2022), the former of which was recently confirmed based on 2018 EHT data (Event Horizon Telescope Collaboration et al. 2024), and independently with GMVA observations by Lu et al. (2023). For the first image of a SMBH, in 2020, the EHT Collaboration was awarded the Einstein Medal and the Breakthrough Prize. These results showcase the importance of radio astronomy research and the viability of VLBI.

4.2 The main elements of a radio antenna

Based on the wavelength at which the observations are carried out, radio astronomers use three types of antennas. At the longest wavelengths > 1 m, dipoles allow for a large collecting surface, and the phased array can observe in several directions at the same time. Wire mesh antennas observe at wavelengths ~ 1 m. Filled aperture parabolic antennas are the main instruments of cm- and mm-wavelength observations. They collect, focus and amplify the extremely weak signals arriving from astronomical objects.

Parabolic antennas, as all radio telescopes, are comprised of a frontend and a backend. The former is responsible for collecting light waves – reflector – and focusing it to the feed horn. This waveguide then transfers the incoming signal to the (usually cooled) receiver. The focus and receiver can be positioned above the dish in the primary focus, or the light can be directed to the secondary focus in the center of the dish, if a reflecting surface is placed in the primary focus.

The signal is processed in the backend. Bolometers are incoherent radiometers that do

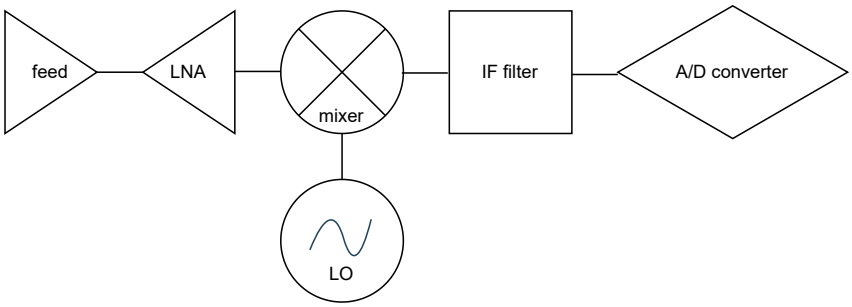

Figure 4.2: Signal path in a heterodyne receiver (from left to right).

not preserve the phase of the signal. These devices are used to carry out broadband total intensity and polarimetric observations at millimeter wavelengths. Bolometers measure the intensity of the incident radiation based on how much heat it generates, as resistance of a material is temperature-dependent. Heterodyne receivers, on the other hand, are coherent radiometers, that is they preserve the phase of the incoming wave. These radiometers transfer the frequency of the incoming radiation usually to a lower one for a more efficient processing.

Because of the low power of the incoming radio emission, low noise amplifiers (LNA) are used to amplify the signal without significantly degrading the signal-to-noise ratio (SNR). LNA are designed to introduce minimal noise related to the amplification. Mixers are devices performing the frequency shift in heterodyne receivers. This step is important in order to avoid power leakage into the frontend, and to shift the frequency of the signal to one that can be easily amplified. This is done by mixing the sky frequency with the monochromatic signal of the local oscillator, resulting in, among other outputs, a lower and an upper sideband, that are separated by the intermediate frequency (IF). Analog-to-digital converters digitize the signal. Their accuracy is determined by their speed, expressed in bits, meaning that higher bit quantization results in a smaller loss in SNR. The state-of-the-art recording rate in 2024 is 64 Gb s^{-1} for the EHT (Event Horizon Telescope Collaboration et al. 2019).

In order to convert the dimensionless signal to a physical quantity, one can use the Nyquist theorem to describe the total power per unit bandwidth as a brightness temperature distribution:

$$P_\nu = k_\mathrm{B} T_\mathrm{A}, \tag{4.1}$$

that relates the antenna power to that of a resistor, with the Boltzmann constant k_B. The antenna temperature can be expressed as:

$$T_\mathrm{A} = \frac{S A_\mathrm{eff}}{2 k_\mathrm{B}}, \tag{4.2}$$

where S is the flux density of the target source, and A_eff is the effective antenna surface

which is usually a fraction of the full surface of the dish. Larger, more efficient telescopes, as well as brighter sources yield larger $T_{\rm A}$. Radio antennas are not only sensitive to the radiation incoming from the direction of the pointing axis (main lobe), but also to radiation incident from other directions which is usually described by the beam pattern (sidelobes), the latter of which needs to be corrected for during calibration (see Sect. 4.5). The diffraction-limited resolution of the antenna is given as $\theta_{\rm HPBW} = 0.89\lambda/D$, where λ is the wavelength and D is the diameter of the dish, with the most sensitive parts contained within a small solid angle called the half power beam width (HPBW) or full width to half power (FWHP), the angle between the 0.5 and total normalized main lobe power. However, the resolution achievable even with the largest radio telescopes is insufficient to go beyond the resolution of the human eye in the optical. As it is not possible to build fully steerable filled-aperture antennas with a diameter above $\sim$ 100 m, nor fixed filled-aperture antennas equipped with steerable receivers above a few hundred meters in diameter, astronomers adopted the ingenious idea of aperture synthesis to achieve a resolution that beats any other observing method, as the present record is held be the space-VLBI mission, *RadioAstron*.

4.3 Aperture synthesis in a nutshell[1]

Aperture synthesis is a technique that aims to reproduce the imaging properties of a large antenna by combining the signal of multiple, smaller telescopes as an interferometer. In this instance, the interferometer response is derived by the multiplying and averaging of the outputs of the individual antennas. In the interferometer response pattern, both the main and the side lobes are referred to as fringes, as in an ideal case, there is no decrease in power with increasing angular offset from the antenna's axis. The fringes are centered around zero angular offset, which improves the dynamic range of the observations. However, this process results in the loss of total power information. The objective of aperture synthesis is to reduce the fringe spacing by increasing the separation between antennas, the baseline, in order to enhance the resolution.

For the purposes of this discussion, we consider a two-element quasi-monochromatic interferometer, whose telescopes are separated by a baseline vector $\mathbf{b}$ (see Fig. 4.3). The antennas are observing in a narrow frequency band, $d\nu$, centered on the frequency $\nu = \omega/(2\pi)$, in a direction described by the unit vector $\mathbf{s}$. The wavefront reaches the more distant telescope later, because the plane wave has to travel an additional distance of $\mathbf{b} \cdot \mathbf{s} = b\cos\Theta$ more to be observed at the second antenna. The corresponding so-called

[1]This section is based on Perley et al. (1989) and Wilson et al. (2013).

geometric delay can be expressed as:

$$\tau_{\rm g} = \frac{\mathbf{b}\cdot\mathbf{s}}{c}. \tag{4.3}$$

The voltage outputs of the first and second elements can be written as:

$$V_1 = A_1 \cos(\omega t) \tag{4.4}$$

and

$$V_2 = A_2 \cos(\omega(t-\tau_{\rm g})). \tag{4.5}$$

During correlation, the voltage outputs are multiplied and averaged, yielding the response:

$$R_{\rm c}(\tau) = P\cos(\omega\tau_{\rm g}) = P\cos\Big(\frac{2\pi\mathbf{b}\cdot\mathbf{s}}{\lambda}\Big), \tag{4.6}$$

where $P = A_1A_2/2$ is the received power after multiplication and averaging of the telescope signals. The mutual correlation function, $R_{\rm c}$, is dependent on the received power, which is determined in part by the antenna collecting area and gain. It varies as a function of the source and baseline orientation resulting from the rotation of the Earth. By introducing a 90°phase shift prior to the signal reaching the correlator, the following sinusoidal signal is generated:

$$R_{\rm s}(\tau) = P\sin(\omega\tau_{\rm g}) = P\sin\Big(\frac{2\pi\mathbf{b}\cdot\mathbf{s}}{\lambda}\Big). \tag{4.7}$$

This response is produced by summing the emission over the sky at each interferometer element, then multiplying and averaging the signal.

The coherence pattern projected onto the target by the cosine correlator is only sensitive to the even, $I_{\rm e}(s)$, part of the spatially incoherent emission originating from the target source:

$$R_{\rm c} = \int\int (I_{\rm o}(\mathbf{s}) + I_{\rm e}(\mathbf{s}))\cos(2\pi\nu\mathbf{b}\cdot\mathbf{s}/c)d\Omega = \int\int I_{\rm e}(\mathbf{s})\cos(2\pi\nu\mathbf{b}\cdot\mathbf{s}/c)d\Omega \tag{4.8}$$

The orientation of the coherence pattern is determined by the baseline geometry, while the fringe separation depends on the observing frequency and baseline length. In order to recover the source brightness distribution, $I(s) = I_{\rm e}(s) + I_{\rm o}(s)$, we need to introduce the sine correlator, which is sensitive to the odd, $I_{\rm o}(s)$, part of the coherence pattern:

$$R_{\rm s} = \int\int (I_{\rm o}(\mathbf{s}) + I_{\rm e}(\mathbf{s}))\cos(2\pi\nu\mathbf{b}\cdot\mathbf{s}/c)d\Omega = \int\int I_{\rm o}(\mathbf{s})\cos(2\pi\nu\mathbf{b}\cdot\mathbf{s}/c)d\Omega. \tag{4.9}$$

It is then possible to define the complex visibility function from the two independent correlator outputs, which describes the relationship between the sky brightness and the response of an interferometer:

$$V_\nu(\mathbf{b}) = R_{\rm c} - {\rm i}R_{\rm s} = Ie^{-{\rm i}\phi} = \int\int I_\nu(\mathbf{s})e^{-2\pi{\rm i}\nu\mathbf{b}\cdot\mathbf{s}/c}d\Omega. \tag{4.10}$$

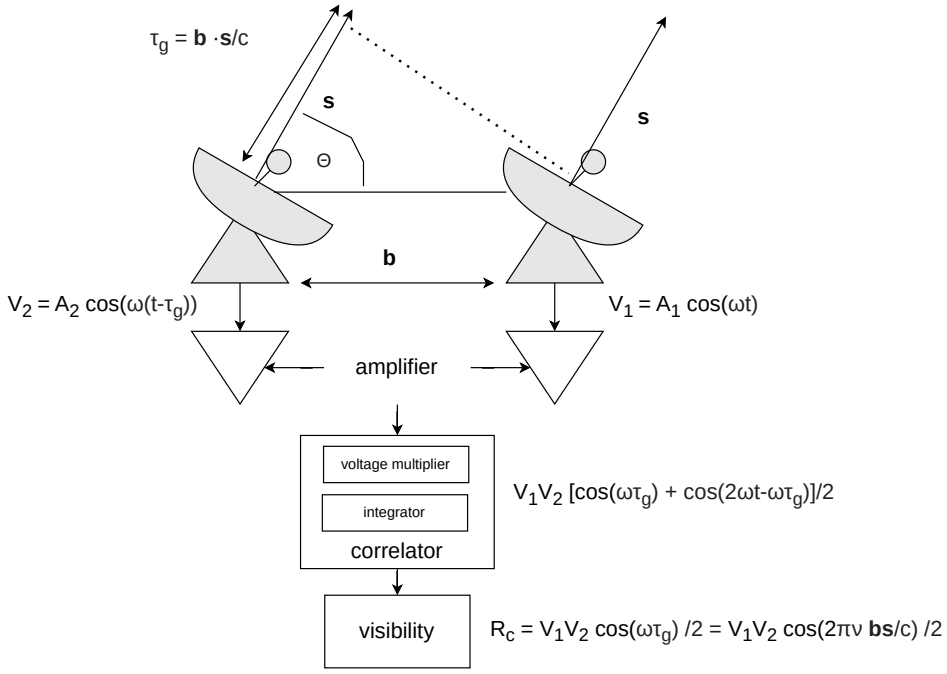

Figure 4.3: Schematic structure of a two-element radio interferometer. The voltage outputs of the individual antennas, V_1 and V_2, are go through a voltage multiplier and an integrator during the correlation, yielding a cosine signal, R_c.

Here $I = \sqrt{R_\mathrm{c}^2 + R_\mathrm{s}^2}$ is the visibility amplitude and $\phi = \tan^{-1}(R_\mathrm{s}/R_\mathrm{c})$ is the visibility phase. This equation is known as the van Cittert–Zernike theorem, which forms the basis of image reconstruction. It states that the visibility is the two-dimensional Fourier transform of the brightness distribution (see Sect. 4.5).

The first interferometers employed in radio astronomy were connected-element ones, exemplified by the Karl G. Jansky Very Large Array (VLA). In this configuration, the array elements are connected by optical cables in order to transmit the local oscillator signal. However, the advent of atomic clocks and phase-stable oscillators has rendered this requirement superfluous, enabling the antennas to conduct independent observations with baselines extending up to several thousands of kilometers, including satellites (see Sect. 8). The data were subsequently recorded and played back later at the correlator facility. In the present era, real-time correlation is made possible via data transmitted through rapid links during e-VLBI sessions.

We distinguish between two types of correlators, FX and XF, based on the order in which they Fourier transform (F) and perform cross-correlation (X) on the data (Titov et al. 2020). During the correlation process, the signals are aligned in time, and the local oscillator offsets, geometric delays, clock rate offsets and the differential Doppler shift re-

sulting from the rotation of the Earth are all accounted for. Subsequently, the coherence function, whose amplitude and phase represent the complex visibilities, is calculated for each baseline. Furthermore, the nature of VLBI observations introduces additional complication. The utilization of distinct clocks at each station results in an unquantifiable instrumental phase and phase drift at every station, in addition to the fact that the atmosphere and ionosphere are also distinct at each site. In contrast to connected-element interferometers, VLBI networks are characterized by heterogeneity, which presents a significant challenge in calibration. This is further compounded by the lack of suitable calibrators.

Despite the inherent difficulties in calibration, VLBI enables the to study of astrophysical sources of non-thermal emission, including AGN jets, pulsars, masers, supernova remnants, and even magnetically active stars. The flux density of these objects can be measured, their small-scale structure or precise location can be determined via astrometry, and the signal propagation through the interstellar medium and our atmosphere can be tested, along with antenna location and geodesy. In the case of AGN, kinematic measurements and studies of jet characteristics on parsec scales are only possible via VLBI observations (see Chapters 5 to 8).

4.4 Current cm-VLBI arrays and notable telescopes

4.4.1 Long Baseline Array

The Long Baseline Array (LBA, Tingay 2003) is a heterogeneous array comprised of the Australia Telescope National Facility dishes, Parkes, ATCA and Mopra, the antennas operated by the University of Tasmania, Hobart and Ceduna, as well as the Warkworth dishes of the Space Operations New Zealand Ltd. Many of the observations are supported by the 70-m and 34-m Deep Space Network dishes at Tidbinbilla, Hartebeesthoek in South Africa, as well as the International VLBI Service for Geodesy and Astrometry (IVS) telescopes Katherine and Yarragadee. The array has been in operation since 1997, and it is the only VLBI network targeting the southern sky. Observations are carried out between 1.3 and 22 GHz. The correlation is currently carried out at the Pawsey Centre for SKA Supercomputing using a DiFX software correlator (Deller et al. 2007, 2011). The TANAMI Collaboration utilizes this array for their AGN monitoring program to study the multiwavelength properties of jets. See more about the LBA in Ch. 5.

4.4.2 Very Long Baseline Array

The Very Long Baseline Array (VLBA, Zensus et al. 1995) is a homogeneous array of ten 25-m dishes, with the longest baseline spanning between Mauna Kea and St. Croix of 8611 km. This is the cm-VLBI array that provides the widest range of observing frequencies between 0.3 and 96 GHz. As can be seen in Ch. 6, the VLBA is occasionally supplemented by the Effelsberg 100-m telescope, the Green Bank Telescope, and the phased-up dishes of the VLA. The correlation is performed with a DiFX correlator (Deller et al. 2007, 2011). Because of its broad frequency coverage, and the fact that this array operates together throughout the whole year, the VLBA is perfectly suited for multiwavelength campaigns and target of opportunity follow-up observations.

4.4.3 European VLBI Network

Similarly to the LBA, the European VLBI Network (EVN, Zensus & Ros 2014) is a heterogeneous array that only observes together for a few months a year. The array consists of telescopes from South-Africa (Hartebeesthoek), Europe (Yebes, Robledo, Jodrell Bank Observatory, Medicina, Noto, Sardinia, Westerbork, Effelsberg, Onsala, Irbene, Toruń, Metsähovi, Zelenchukskaya, Badary, Svetloe) and Asia (Seshan, Urumqi, Tianma, Kunming). The Arecibo Observatory was part of the EVN until its collapse in 2020. The observing frequencies fall between 0.3 and 43 GHz. The EVN provides long north-south and east-west baselines of 9833 km and 9294 km, respectively, which is the main asset of the EVN compared to other cm-VLBI arrays. The correlation is carried out with the EVN software correlator (Keimpema et al. 2015), or alternatively at the MPIfR DiFX correlator.

4.4.4 *RadioAstron*

The second space-VLBI experiment, *RadioAstron* (Kardashev et al. 2013) was launched in 2011 with a 10-m radio antenna on board. The satellite was placed on an elliptical orbit that evolved due to the weak gravitational perturbations exerted on the satellite by the Moon and the Sun. Consequently, the perigee radius underwent a variation between 10,000 and 70,000 km, while the apogee radius fluctuated between 310,000 and 390,000 km. Observations were conducted at four frequencies, namely 0.327, 1.665, 4.830 and 18.392-25.112 GHz, which provided a maximum resolution of 500, 100, 35 and 7 μas, respectively. The scientific rationale of the mission was to study the central engine of AGN and physical processes occurring near supermassive black holes at extremely high resolution. Additionally, the mission aimed to investigate the structure and dynamics

of star- and planet-forming regions by observing maser and mega-maser radio emission. Despite the decommissioning of *RadioAstron* in May 2019 due to equipment failure, the mission has yielded numerous new and intriguing findings (Kardashev et al. 2017).

4.5 Calibration and imaging recipes for VLBI data sets

4.5.1 Standard data reduction

Calibration is a necessary procedure in order to correct for various instrumental and propagation effects that alter the measured visibility amplitudes and phases, as well as to convert the correlation coefficients to physical units. The calibration of VLBI data sets is traditionally carried out in the Astronomical Image Processing System (`AIPS`, Greisen 2003).

After loading the data, parallactic angle corrections are applied first, as feed rotation in circularly polarized receivers rotates cross hand visibilities. Subsequently, corrections for the loss of sensitivity resulting from quantization noise are calculated. Initial phase corrections are performed to align the instrumental phase along subbands (also referred to as intermediate frequencies or IFs) that have been offset due to delays arising from signal propagation through the antenna electronics. After this, system temperature measurements and gain curves provided by the participating stations are employed to calibrate amplitudes. However, during the TANAMI observations, most telescopes do not measure radiometry. For these antennas, `antab` files are generated assuming flat gain curves and constant system temperature based on the system equivalent flux densities. Although the manual phase calibration aligned the IFs, the data still contain residual frequency and time-dependent phase variations that must be account for. Fringe fitting determines the delay (the derivative of the phase with respect to frequency) and rate (phase derivative with respect to time) and applies them to the visibility data. Finally, the calibrated data is exported averaged in frequency (and eventually in time) and written out to a FITS (Flexible Image Transport System) file.

Imaging is typically carried out in `Difmap` (Shepherd 1997), an interactive software program designed for mapping and model fitting continuum VLBI data sets. Imaging is accomplished through iterating `clean` and self-calibration. The `clean` (Högbom 1974) algorithm deconvolves the sampling function, or dirty beam, from an observed brightness distribution known as the dirty map of a given radio source. This process results in the source being represented as a collection of delta functions. Self-calibration is employed to rectify station-based errors arising from, for example, atmospheric effects at the antenna site. The algorithm utilizes the source model generated via `clean` in order to compute

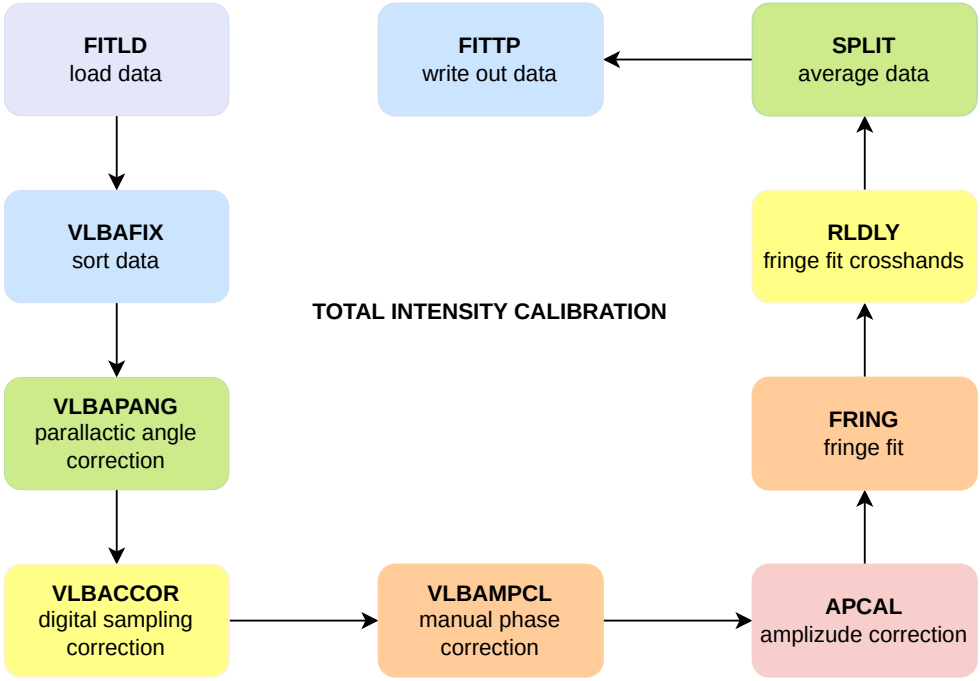

Figure 4.4: Schematic of the standard total intensity calibration procedure described in Sect. 4.5.1. `RLDLY` is used to prepare for the polarization calibration of dual-polarization data, and should be skipped otherwise.

time-dependent gain correction factors, thereby minimizing the discrepancy between the model and the observed visibilities.

First, data are edited by flagging outliers. Then we construct the first source model by iterating `clean` and phase self-calibration, until the model reaches the zero-baseline flux density. The first amplitude self-calibration determines a single gain correction factor for each antenna. To further improve the image, we continue iterating `clean` and phase self-calibration, performing amplitude self-calibration when the root mean square residual of the phase does not decrease anymore. The solution interval of the amplitude self-calibration is decreased at each step. Finally, the image is convolved with the clean beam (a Gaussian with the same properties as the main lobe of the dirty beam) and residuals are added to the map.

`modelfit` is a command to fit delta or 2D Gaussian functions (associated to so called components) to the self-calibrated data using a Levenberg-Marquardt least-squares approach. Model fitting is iterated by adding new and new components in order to minimize the χ^2 of the closure phase, and to create an image similar to the `clean` map. The model is then used to analyze the flux density, size, brightness temperature and speed of individual jet knots.

4.5.2 Special recipes

The above paragraphs detailed the standard calibration steps employed when reducing VLBI data. As this thesis work is based on data from various telescope arrays, here I discuss their peculiarities, as well as special recipes employed for some of these observations.

The LBA presents its users with several challenges. First, due to the geographical layout of the southern hemisphere continents, medium-length baselines are missing from the (u,v) coverage. East-west baselines between South-Africa and Australia, and north-south baselines within Australia create a highly elliptical beam, providing very diverging spatial resolutions in the east-west and in the north-south directions. The telescopes were primarily built to perform single-dish observations, meaning that their sizes, slewing times, receivers and backends were not homogenized. Larger antennas, such as Parkes, ATCA and the Deep Space Network dishes strongly improve the sensitivity of the array, as they are either large > 50 m dishes, or a phased up array consisting of several individual telescopes synthesizing a larger collecting surface. Several stations do not measure radiometry data, and it is up to the user to generate these ancillary files. This also makes the amplitude calibration difficult and unreliable, and on many occasions manual tuning in `AIPS` is needed to correct the flux density scale (Ros 2005).

Phase referencing (Beasley & Conway 1995) is a technique that allows for the phase calibration of a target source based on regular observations of a nearby $< 1°$calibrator. This method enables us to observe faint objects where fringe fitting cannot be applied directly. For these observations, the Earth orientation parameters and the ionospheric effects must be accounted for, especially when the observations were carried out at low frequencies and low elevations. Then the fringe solutions determined for the calibrator, also using the source model of this source, can be transferred to the target source.

Space VLBI observations with *RadioAstron* require special treatment because the 10-m antenna does not always have sufficient sensitivity to detect a source on single baselines due to its passively cooled receivers. If the ground array is phased, then the detection threshold can be lowered during the fringe search. The same effect can be obtained by global fringe fitting of the ground array using the source model, if the baselines between ground telescopes is more sensitive than between ground-space ones (Schwab & Cotton 1983). After this, one can proceed with fringe fitting the ground-space baselines (Kogan 1996). As for imaging practices, to recover the extremely high angular resolution provided by *RadioAstron*, the ground-array data is down-weighted by employing super-uniform weighting in `Difmap`. For the Space Radio Telescope, only the initial amplitude self-calibration is performed, and the solution interval of the phase self-calibration is never smaller than 1 min. This is an important postulation, because it is easy to create spurious

flux from the noisy data of *RadioAstron* (Martí-Vidal & Marcaide 2008).

In the last years, several developments have been made using novel automated data reduction and imaging algorithms (see e.g., Janssen et al. 2022) to mitigate challenges presented by for example the extremely high observing frequency and sparse (u,v) coverage of the EHT. Special data reduction recipes are utilized in nearly all the individual papers included in this dissertation work, highlighting what a laborious process VLBI data reduction is. However, one must keep in mind that VLBI observations provide the sharpest view on the Universe, making all these efforts worthwhile.

Chapter 5

TANAMI: III. First-epoch S band images

In 2020, the TANAMI monitoring program has been expanded to incorporate 2.3-GHz observations. This was necessary in order to follow up faint TeV-emitter AGN that could not be detected at 8.4 GHz. In addition, these observations enable us to study extended jet structures in bright sources.

In this paper, I present the first images form the 2.3-GHz monitoring that contain all TeV-detected AGN of the southern hemisphere as of 2021 December. Many of these sources have flux densities below 50 mJy, which hindered the detection of extended jet emission in these targets. These sources also yielded weak fringe detections on transoceanic baselines to Hartebeesthoek. This decreases both the angular resolution and the image fidelity, and strongly limits studies aimed at extremely-high- and high-synchrotron-peaked BL Lac populations. Therefore to improve our observations the TANAMI Collaboration advocates for the efforts to phase up the MeerKAT array, with which we could achieve three times better sensitivity on the long baselines.

Focusing on the sample of the twenty-four TeV-detected AGN of the southern hemisphere, I inspected the redshift, γ-ray photon flux, and core brightness temperature ($T_{\mathrm{b,core}}$) distribution of these sources. Biases of the source selection originate from the pointing mode observations and the limited sensitivity of Imaging Atmospheric Cherenkov Telescopes (IACTs) (Actis et al. 2011). In addition, VHE emission from high-redshift sources is attenuated by the extragalactic background light, so TeV-detected AGN are mostly found below $z < 1$. Selection biases towards lower redshifts also affect BL Lac objects, whose redshift, especially at high values, cannot be determined due to the lack of emission lines in their spectra (Sol 2018). This bias is also present in our sample, as the distribution of BL Lac objects peak around $z \sim 0.1$ while FSRQ are located between

$z \sim 0.36$ and 1.11. This distribution is consistent with the *Fermi* LAT γ-ray Bright AGN Source List (Abdo et al. 2009).

The logarithmic γ-ray photon flux distribution shows an inverse relation with the frequency of the synchrotron peak, that is, extremely-high- and high-synchrotron-peaked BL Lac sources are dimmer at high energies than FSRQ and low-synchrotron-peaked BL Lacs. This rather even distribution of TeV-detected sources contrasts the distribution of HE-detected blazars of Abdo et al. (2009), which shows a peak around 10^{-7} ph cm^{-2} s^{-1}. This difference may also originate from the selection biases affecting our sample.

Brightness temperature distributions reveal an inverse relation between the synchrotron peak frequency and $T_{\rm b,core}$, that is high-synchrotron-peaked objects, in general, have lower $T_{\rm b,core}$ values than low-frequency-peaked BL Lacs and FSRQs. This also suggests that the emission from high-frequency-peaked objects is not beamed as strongly as in FSRQs. Gamma-ray faint AGN also exhibit lower $T_{\rm b,core}$ values. The average and median $T_{\rm b,core}$ for the TANAMI TeV sample are 8.19×10^{10} K and 4.9×10^{9} K, respectively. As all sources except three have $T_{\rm b,core}$ values below the equipartition brightness temperature, $T_{\rm eq} \approx 5 \times 10^{10}$ K (**?**), and all except one of these fall below the inverse Compton catastrophe limit of $\approx 10^{12}$ K (Kellermann & Pauliny-Toth 1969), we propose that in most cases the emission from these sources is not beamed at 2.3 GHz. 15 GHz MOJAVE (**?**) and 8.4 GHz TANAMI observations (Böck et al. 2016), samples dominated by LBL and FSRQ objects, reveal a mean core brightness temperatures in the order of 10^{11} K, an order of magnitude higher than that of our TeV-sample. This has been shown as a characteristic of VHE-detected sources by Piner & Edwards (2018b).

In the future, the 2.3 and 8.4-GHz monitoring data will be used to perform quasi-simultaneous spectral studies, core-shift measurements, et cetera. Until the arrival of the SKA, TANAMI will remain the only VLBI AGN monitoring program targeting the southern sky. Since the frequency coverage of SKA coincides well with our survey, TANAMI will provide an additional two decades of time baselines for variability studies when the SKA comes online.

Conceptualization, R.O., M.K., E.R., P.G.E., C.P.; methodology, P.B., R.O.; formal analysis, P.B.; software, P.B.; validation, P.B., E.R., M.K.; writing-original draft preparation, P.B.; writing-review and editing, E.R. M.K., F.R., S.H., L.J.H., J.F.H.Q. J.S., A.K.T., S.W.; visualization, P.B.; supervision, E.R., M.K.

A&A, 681, A69 (2024)
https://doi.org/10.1051/0004-6361/202347823

Astronomy & Astrophysics

TANAMI: Tracking active galactic nuclei with austral milliarcsecond interferometry

III. First-epoch *S* band images★

P. Benke[1,2], F. Rösch[2], E. Ros[1], M. Kadler[2], R. Ojha[3], P. G. Edwards[4], S. Horiuchi[5], L. J. Hyland[6], C. Phillips[4], J. F. H. Quick[7], J. Stevens[4], A. K. Tzioumis[4], and S. Weston[8]

[1] Max Planck Institute for Radio Astronomy, Auf dem Hügel 69, 53121 Bonn, Germany
e-mail: pbenke@mpifr-bonn.mpg.de
[2] Julius Maximilians University Würzburg, Faculty of Physics and Astronomy, Institute for Theoretical Physics and Astrophysics, Chair of Astronomy, Emil-Fischer-Str. 31, 97074 Würzburg, Germany
[3] NASA HQ, 300 E St SW, Washington, DC 20546-0002, USA
[4] CSIRO Space and Astronomy, PO Box 76, Epping, NSW 1710, Australia
[5] CSIRO Space and Astronomy, Canberra Deep Space Communications Complex, PO Box 1035, Tuggeranong, ACT 2901, Australia
[6] School of Natural Sciences, University of Tasmania, Private Bag 37, Hobart, Tasmania 7001, Australia
[7] Hartebeesthoek Radio Astronomy Observatory, PO Box 443, 1740 Krugersdorp, South Africa
[8] Space Operations New Zealand Ltd, Hargest House, PO Box 1306, Invercargill 9840, New Zealand

Received 29 August 2023 / Accepted 14 October 2023

ABSTRACT

Context. With the emergence of very high energy astronomy (VHE; $E > 100$ GeV), new open questions were presented to astronomers studying the multi-wavelength emission from blazars. Answers to these open questions, such as the Doppler crisis, and finding the location of the high-energy activity have eluded us thus far. Recently, quasi-simultaneous multi-wavelength monitoring programs have shown considerable success in investigating blazar activity.
Aims. Such quasi-simultaneous observations across the electromagnetic spectrum became possible thanks to the launch of the *Fermi* Gamma-ray Space Telescope in 2008. In addition, with very long baseline interferometry (VLBI) observations, we can resolve the central parsec region of active galactic nuclei (AGN) and compare morphological changes to γ-ray activity in order to study high-energy-emitting blazars. To achieve our goals, we need sensitive, long-term VLBI monitoring of a complete sample of VHE-detected AGN.
Methods. We performed VLBI observations of TeV-detected AGN and high-likelihood neutrino associations as of December of 2021 with the Long Baseline Array (LBA) and other southern-hemisphere radio telescopes at 2.3 GHz.
Results. In this paper, we present first light TANAMI *S*-band images, focusing on the TeV-detected subsample of the full TANAMI sample. In addition to these VHE-detected sources, we show images of two flux density calibrators and two additional sources included in the observations. We study the redshift, 0.1–100 GeV photon flux, and *S*-band core brightness temperature distributions of the TeV-detected objects, and find that flat-spectrum radio quasars and low-synchrotron-peaked sources on average show higher brightness temperatures than high-synchrotron-peaked BL Lacs. Sources with bright GeV γ-ray emission also show higher brightness temperature values than γ-low sources.
Conclusions. Long-term monitoring programs are crucial for studying the multiwavelength properties of AGN. With the successful detection of even the faintest sources, with flux densities below 50 mJy, future work will entail kinematic analysis and spectral studies both at 2.3 and 8.4 GHz to investigate the connection between the radio and γ-ray activity of these objects.

Key words. galaxies: active – galaxies: jets – galaxies: nuclei – gamma rays: galaxies

1. Introduction

Blazars are active galactic nuclei (AGN) whose jets are oriented towards the line of sight of the observer. As a result of this orientation, their emission is highly beamed, and they often exhibit apparent superluminal jet motion. Their two-humped spectral energy distribution (SED) can be modeled with a lower energy synchrotron component and a high-energy component arising due to leptonic (Maraschi et al. 1992) and/or hadronic processes (Mannheim 1993). Blazars can be further classified as BL Lac objects and flat-spectrum radio quasars (FSRQs). The former can be divided into four subclasses based on the location of the synchrotron peak, $\nu_{\rm peak}$, in their SED (Abdo et al. 2010): low (LBL, $\nu_{\rm peak} < 10^{14}$ Hz)-, intermediate (IBL, $10^{14} < \nu_{\rm peak} < 10^{15}$ Hz)-, high (HBL, $10^{15} < \nu_{\rm peak} < 10^{17}$ Hz)-, and extremely high (EHBL, $\nu_{\rm peak} > 10^{17}$ Hz)-synchrotron-peaked objects. However, these objects still present us with many open questions, which refer to, for example, the launching mechanisms responsible for the creation of jets, the collimation and acceleration of jet material, and the origins of the multi-wavelength emission.

★ Figures 2, 3, A.1, as well as Tables A.1–A.3 are available at the CDS via anonymous ftp to cdsarc.cds.unistra.fr (130.79.128.5) or via https://cdsarc.cds.unistra.fr/viz-bin/cat/J/A+A/681/A69

Table 1. Antennas participating in the observations.

Telescope	Abbreviation	Diameter (m)	Location	Latitude	Longitude
Parkes	Pa	64	Parkes, New South Wales, Australia	32°59′52″ S	148°15′47″ E
ATCA	At	5 × 22	Narrabri, New South Wales, Australia	30°18′46″ S	149°33′01″ E
Mopra	Mp	22	Coonabarabran, New South Wales, Australia	31°16′04″ S	149°06′00″ E
Hobart	Ho	26	Mt. Pleasant, Tasmania, Australia	42°48′13″ S	147°26′26″ E
Ceduna	Cd	30	Ceduna, South Australia	31°52′04″ S	133°48′34″ E
DSS43 [(a)]	Ti	70	Tidbinbilla, Australia	35°24′05″ S	148°58′54″ E
DSS36 [(a)]	Td	34	Tidbinbilla, Australia	35°24′05″ S	148°58′54″ E
Hartebeesthoek	Hh	26	Gauteng, South Africa	25°53′25″ S	27°41′08″ E
Warkworth [(b,c)]	Ww	12	Auckland, New Zealand	36°26′00″ S	174°39′46″ E
Katherine [(c)]	Ke	12	Northern Territory, Australia	14°22′32″ S	132°09′09″ E
Yarragadee [(c)]	Yg	12	Western Australia	29°02′50″ S	115°20′44″ E

Notes. [(a)]Operated by the Deep Space Network of the USA National Aeronautics and Space Administration. [(b)]Operated by the Space Operations New Zealand Ltd. (Gulyaev et al. 2010). [(c)]International VLBI Service for Geodesy and Astrometry (IVS) station.

One of the widely studied open questions regarding the multiwavelength nature of blazars is known as the Doppler crisis (Piner & Edwards 2018b). Many blazars have been detected at high (HE; 100 MeV < E < 300 GeV) and very high energies (VHE; E > 100 GeV), and these show rapid variability, often on timescales of minutes (see e.g., 2155−304; Aharonian et al. 2007c). This suggests a small emission region and high Doppler factors, and indeed Doppler factors of $\delta \approx 50$ are required to reproduce the spectral energy distribution (SED) at high energies (Piner & Edwards 2018b). On the other hand, very long baseline interferometry (VLBI) observations reveal slow component motions with Doppler factors of < 10 (Piner & Edwards 2018b). A prominent example of the Doppler crisis blazar is Mrk 421 (Aleksić et al. 2012; Lico et al. 2012). Locating the origin of the HE emission, also known as the blazar zone, has also proven challenging. The observed short-time variability in the VHE band (see e.g., 2155−304; Rieger & Volpe 2010) suggests that the TeV emission originates from a small region. Under the assumption that the emission region fills the jet diameter, the VHE emission region must be located close to the central engine (Saito et al. 2013). The availability of seed photons for external Compton scattering also supports this scenario (Böttcher & Els 2016). However, this HE emission is expected to be absorbed by the dense photon fields of the broad line region, which would prevent us from detecting blazars at VHE. On the other hand, Marscher et al. (2012) and Jorstad et al. (2013) found that activity near the radio core at 43 GHz coincides with γ-ray flares, suggesting that the HE emission originates downstream from the central supermassive black hole.

Several models have been proposed to explain both the Doppler crisis and the location of the blazar zone, all of them invoking multiple Doppler factors for different emission processes in the parsec-scale jet. These models include a spine-sheath transverse velocity structure (Ghisellini et al. 2005), a decelerating jet with a slower moving plasma at the jet edge (Georganopoulos & Kazanas 2003), multizone models (Tavecchio et al. 2011), or minijets created via magnetic reconnection (Giannios et al. 2009). Currently, high-resolution VLBI observations are required to distinguish between these jet models.

To resolve these open questions, we need long-term quasi-simultaneous multiwavelength monitoring with high cadence. With the launch of *Fermi* in 2008 (Atwood et al. 2009), continuous GeV γ-ray monitoring became possible with the Large Area Telescope instrument on board the satellite. However, as HE telescopes lack the resolution to determine which part of the AGN is responsible for the γ-ray emission, we need additional high-resolution observations that can reveal the parsec-scale structure of these objects. Tracking Active Galactic Nuclei with Austral Milliarcsecond Interferometry (TANAMI) is a VLBI monitoring program designed to carry out long-term observations of the rarely exploited southern sky. TANAMI started X and K band (8.4 and 22 GHz, respectively) observations in 2007 (Ojha et al. 2010). The program uses telescopes of the extended Long Baseline Array (LBA; see Table 1). Monitoring programs such as TANAMI, MOJAVE, and the Boston University Blazar Group are needed to capture the different emission states of AGN and reveal their multiwavelength properties via tracking morphological and brightness changes of the targets. With the emergence of neutrino astronomy, the TANAMI sample has been expanded to include neutrino associations, and in 2020, TANAMI began observing in S band in order to study faint TeV sources and extended jet structures. Currently, TANAMI is the sole AGN monitoring program focusing on southern-hemisphere sources, and our multifrequency monitoring in the S and X bands (K-band observations were discontinued in 2020) will enable us to carry out spectral studies, core-shift measurements, and so on in the future.

In this paper, we present the first light S band (2.3 GHz) images of sources observed during the first three epochs in 2020–2021, focusing on the TeV-detected subsample of TANAMI. In Sect. 2, we describe the sample selection, observations, and data reduction, and in Sect. 3 we discuss the data analysis. In Sects. 4 and 5, we describe the clean images and properties of the sample, and finally we summarize our results in Sect. 6.

2. The source sample, observations, and data reduction

The TANAMI AGN sample currently consists of 183 sources below the J2000 declination of 0°. The original sample was defined as a radio- and γ-ray-selected sample below −30° declination in the X and K bands (Ojha et al. 2010). However, with the emergence of neutrino astronomy, the declination range of the observations was broadened, and the sample was expanded to accommodate new astrophysical neutrino associations, as well as newly discovered TeV-emitting AGN on the southern

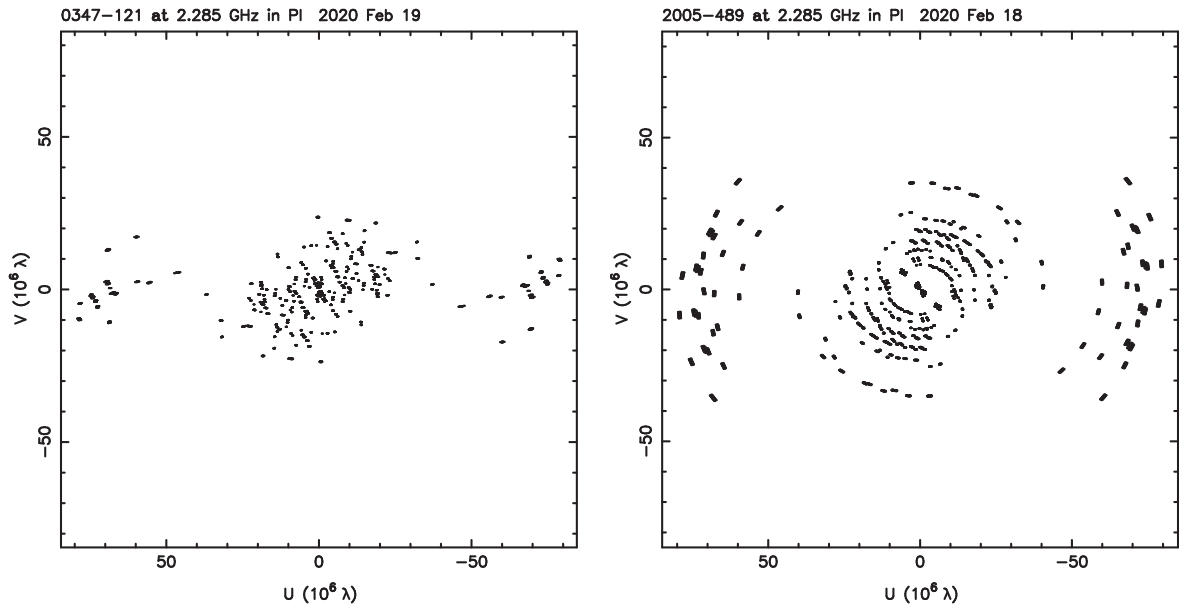

Fig. 1. TANAMI S band (u, v) coverage in the most extended array configuration for sources of low and high declination. Due to the geographical layout of the array at the southern hemisphere, we do not have antenna pairs that cover intermediate-length baselines.

Table 2. Summary of observing sessions and participating antennas.

Epoch	Participating telescopes [(a)]	Remarks
2020-02-18	Pa, At, Mp, Ho, Cd, Hh, Ke, Yg, Td, Ti, Ww	Td and Ti recorded single polarization at a time
2020-11-21	Pa, At, Mp, Ho, Cd, Hh, Yg, Ww	Cd only in the first half of the observations due to recording problems
2021-12-04	Pa, At, Mp, Hb, Cd, Hh, Ke, Yg, Ww	Yg experienced recording problems

Notes. [(a)]Telescopes are denoted as Parkes (Pa), ATCA (At), Mopra (Mp), Hobart (Ho), Ceduna (Cd), Hartebeesthoek (Hh), Katherine (Ke), Tidbinbilla 34 m (Td), Tidbinbilla 70 m (Ti), Warkworth (Ww), Yarragadee (Yg). See antenna characteristics in Table 1.

hemisphere. In 2020, S band observations were introduced to TANAMI in order to study extended jet structures and to monitor faint ($S_{2.3\,\mathrm{GHz}} < 50$ mJy) sources that were previously excluded from the sample. In this paper, we discuss the first light S band results in our TeV sample, which at the time of the observations (December, 2021) contained all known VHE-emitting AGN on the southern celestial hemisphere.

Observations were carried out in S band with the ad hoc TANAMI array, using Parkes, ATCA, Mopra, Hartebeesthoek, Ceduna, Hobart, and Tidbinbilla, as well as IVS stations, such as Katherine, Warkworth, and Yarragadee. Antenna parameters are summarized in Table 1. Each observing session lasts for about 24 h, and sources are observed in blocks of six 10-min scans throughout the session to better fill the (u, v) plane (see Fig. 1). Generally, we observe 24–30 sources per session. Here we report on the first three epochs of our S band observations (Table 2).

Data reduction was carried out in `AIPS` (Greisen 2003). Data were loaded using `FITLD` with `CLINT` set to 0.1 min and without applying digital corrections. Before fringe fitting, we applied digital sampling corrections, corrected the parallactic angles, and calibrated the amplitudes using `APCAL`. In the case of antennas where system temperatures were not available, we used nominal values to calibrate visibility amplitudes. Delay and rate solutions from `FRING` were applied using `CLCAL`. The data were then averaged in frequency, split, and written out for imaging in `Difmap` (Shepherd 1997).

After building a source model containing most of the zero-baseline flux, the first amplitude self-calibration was carried out with a solution interval larger than the observing time. After this, cleaning and self-calibration with decreasing solution intervals were iterated until we reached a good dynamic range, and finally, the residuals were added to the final, clean image. First-epoch S-band clean images are displayed in Figs. 2, 3, and A.1. The first two plots show the TeV-detected sample, while the latter displays calibrators and additional sources included in the observations. We then used the `modelfit` command in `Difmap` to model the source structure with circular Gaussian components.

3. Results

We have summarized the properties of the 26 targets and two calibrators included in the first three S-band observational epochs in Table A.1. The table displays the source designation and common name, the source class, and redshift. These observations are focused on the TeV sample, but one neutrino source, 1424–418, was also added to these sessions. Of the 26 sources, 10 have previously been studied in the X-band by the TANAMI team, and so references to these papers are also shown.

Based on the parameters of the `modelfit` components, we can calculate the brightness temperature, $T_{\mathrm{b,obs}}$, of the core components in the following way (Kovalev et al. 2005):

$$T_{\mathrm{b,obs}}[\mathrm{K}] = 1.22 \times 10^{12} \left(\frac{S_\nu}{\mathrm{Jy}}\right) \left(\frac{\nu}{\mathrm{GHz}}\right)^{-2} \left(\frac{b_{\mathrm{min}} \times b_{\mathrm{maj}}}{\mathrm{mas}^2}\right)^{-1} (1+z), \quad (1)$$

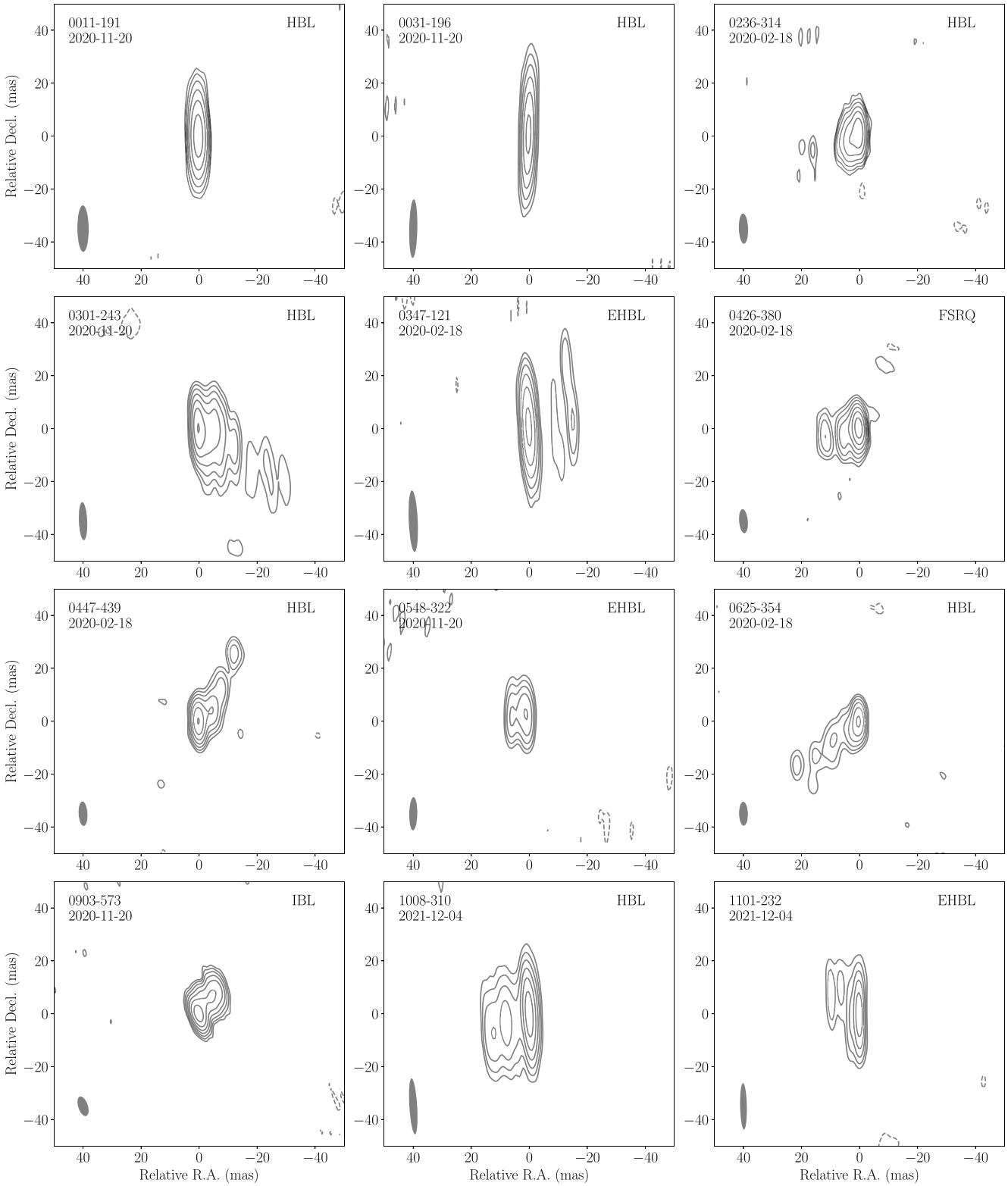

Fig. 2. Clean maps of the TANAMI TeV sample at 2.3 GHz. Image properties are summarized in Table A.3. Lowest contours are listed in Table A.3, and contour levels increase by a factor of two. The class is given in the top right corner of the image (see Table A.1).

where S_ν is the flux density of the component, ν is the observing frequency, and $b_{\rm min}$ and $b_{\rm maj}$ are the minor and major axes of the component. Errors in flux density are estimated to be 10% (Ojha et al. 2010) and errors of the component sizes are taken as one-fifth of the beam minor axis (Lister et al. 2009). We computed the resolution limit based on Eq. (2) of Kovalev et al. (2005), and found that all components are resolved (see Table A.3). The characteristics of the clean hybrid images are summarized in Table A.3 for the TeV sample and in Table A.2 for additional sources. The source structure is described in Col. 2; Col. 3 shows the observing epoch, and Cols. 4–8 show the clean image properties including beam major and minor axis,

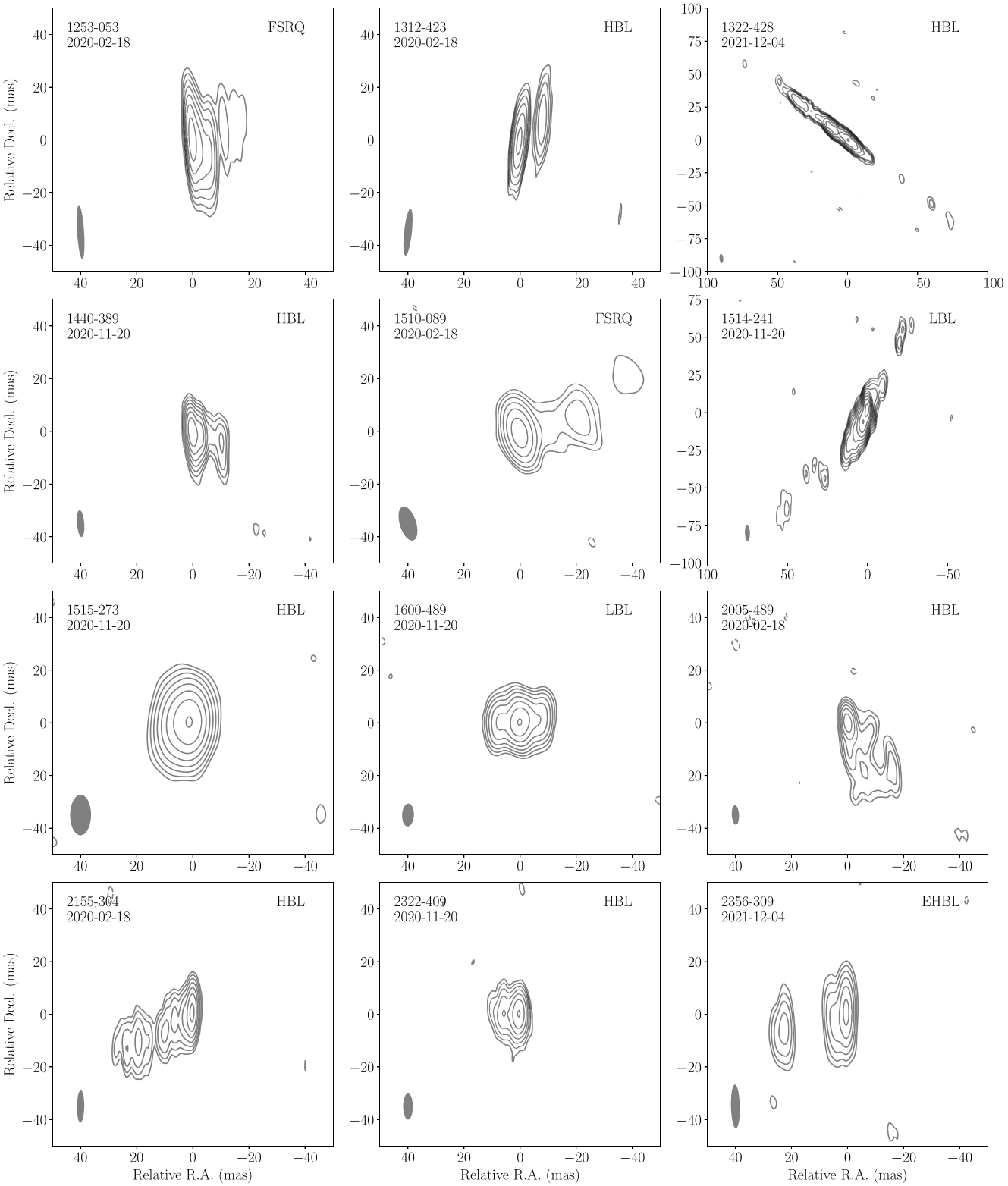

Fig. 3. Clean maps of the TANAMI TeV sample at 2.3 GHz, continuing Fig. 2. Lowest contours are listed in Table A.3, and contour levels increase by a factor of two. The class is given in the top right corner of the image (see Table A.1).

position angle, total flux density, rms noise level, and the lowest contours used in the clean images in Figs. 2 and 3. Columns 9–11 describe the flux density, size, and brightness temperature of the core components, and Cols. 12 and 13 display the HE properties of the source.

4. Notes on individual sources

In this section, we provide a short summary of previous results from the literature regarding each of the sources of our TeV-sample and describe the source morphology in our observations.

0011−191. 8.4 GHz observations of Piner & Edwards (2014) with the VLBA reveal a compact core−jet structure with an opening angle of 26.2°. The jet component is close to stationary at ∼1 mas (Piner & Edwards 2018a). Our 2.3 GHz images reveal a faint, compact core structure with a flux density of 140 mJy.

0031−196. This source is part of the HBL sample presented in Piner & Edwards (2014). It shows an extended jet on parsec scales that has a proper motion of 0.204 ± 0.071 mas yr^{-1} and an opening angle of 18.2°. The source was detected at VHE by H.E.S.S. (Abdalla et al. 2020). Our images show only a core with a flux density of 200 mJy, because we lack the sensitivity to detect the extended jet emission.

0236−314. This is an X-ray source from the ROSAT Bright Survey (Schwope et al. 2000), and has been detected by *Fermi* in 2FGL (Ackermann et al. 2011) and H.E.S.S. (Gaté et al. 2017) as well. The TANAMI *S* band image shows a single-sided core−jet structure.

0301−243. The source was monitored by MOJAVE at 15 GHz between 2010 and 2012. Superluminal apparent speeds of up to 2.3 ± 0.5 *c* were detected (Lister et al. 2019). Both the 15 GHz MOJAVE and 22 and 43 GHz (Piner & Edwards 2023) observations show an unresolved core and an extended jet towards the southwest. We recover a similar structure with an extended jet reaching ∼30 mas. The source is part of the *Fermi* Bright Source List (Abdo et al. 2009a), and has been detected by H.E.S.S. (H.E.S.S. Collaboration 2013b) with a 9.4σ significance and a flux of 1.4% of that of the Crab Nebula.

0347−121. This source shows a compact structure with a faint jet at 8.4 GHz (Piner & Edwards 2014), similar to what we see in the *S* band. The opening angle is measured to be 21.6°, and apparent speeds of 1.7 ± 1.2 *c* are detected by Piner & Edwards (2018a). A VHE detection by H.E.S.S. reveals an integral flux of 0.02 Crab units (CU) above 250 GeV and a power-law spectrum with Γ = 3.10 ± 0.33 between 250 GeV and 3 TeV (Aharonian et al. 2007b). The SED can be reasonably described by a one-zone model (Aharonian et al. 2007b).

0426−380. This source is currently the furthest known VHE-emitting FSRQ at z = 1.1 (Tanaka et al. 2013), and has been part of the TANAMI *X*-band sample since 2009; the first images were published in Müller et al. (2018). 0426−380 shows a core–jet structure with the jet pointing west–southwest.

0447−439. This source is a *Fermi* Bright Source List blazar (Abdo et al. 2009a) and has been detected at VHE (H.E.S.S. Collaboration 2013a) with an integrated flux density of 0.03 CU. 0447−439 shows a faint extended jet towards the northwest, both in *S* - and *X*-band (Müller et al. 2018).

0548−322. This source resides in a giant elliptical galaxy in the center of Abell S0549 (Falomo et al. 1995). 0548−322 has also been observed by Piner & Edwards (2013) and Piner & Edwards (2014) at 8 and 15 GHz. These observations reveal an unresolved core and a faint jet pointing towards the northeast with an opening angle of 13.4°. On the other hand, our 2.3 GHz observations show only the core – with a flux density of 30 mJy – due to the low image sensitivity.

0625−354. This is an FR I radio galaxy hosted by a giant elliptical galaxy in the center of Abell 3392. First TANAMI images of the source at 8.4 GHz were published in Ojha et al. (2010). Based on a kinematic analysis of nine epochs, Angioni et al. (2019) found superluminal motions with apparent speeds reaching ∼3 *c* from the radio core. In the *S* band, the jet extends ∼20 mas to the southeast, but tapered images of Ojha et al. (2010) reveal a jet up to 40 mas. Among many other FR I radio galaxies, 0625-354 has also been detected at VHE (H.E.S.S. Collaboration 2018) with an integral flux of 0.04 CU and a photon index of Γ = 2.8 ± 0.5.

0903−573. This source was first detected in the GeV range by *Fermi* LAT in 2015 (Carpenter & Ojha 2015). The source was considered a blazar candidate of unknown type until recently, when it was classified as a BL Lac object by Lefaucheur & Pita (2017). 0903−573 exhibited a complex γ-ray flaring activity during 2018 and 2020 (Mondal et al. 2021), which coincides with our first *S*-band observation. Our image reveals a core and an extended jet in the northwest direction.

1008−310. *X* band observations of Piner & Edwards (2014) and Piner & Edwards (2018a) show a compact core structure with a faint jet with an opening angle of 47.8°. Our 2.3 GHz image shows a slightly more extended jet towards the east–northeast. Integral flux above 0.2 TeV is 0.008 CU (H.E.S.S. Collaboration 2012).

1101−232. This source is hosted by an elliptical host galaxy. On kiloparsec scales, it shows a one-sided structure with a diffuse extension to the north (Laurent-Muehleisen et al. 1993). Observations at 5 and 8 GHz with the VLBA (Tiet et al. 2012), as well as our 2.3 GHz TANAMI observations, show a core with a faint, slightly extended jet to the northwest. Aharonian et al. (2007a) detected the source at VHE with H.E.S.S. Yan et al. (2012) showed that SED modeling can recover the observed TeV emission by using slightly beamed HE jet emission, but only the models with moderately high Doppler factors result in a jet in equipartition. Yan et al. (2012) suggest that inverse Compton scattering of the cosmic microwave background (CMB) photons in the extended jet is the main source of the TeV emission.

1253−053. 3C 279 is one of the most well-studied AGN in VLBI science and has been monitored by MOJAVE at 15 GHz since 1995, and by the Boston University Blazar Group at 43 GHz since 2007. On VLBI scales, the jet has a well-collimated one-sided structure, which is similar to our findings from *S*-band images, but on kiloparsec scales it shows a significant bend towards the east (Cheung 2002). RadioAstron observations at 22 GHz reveal a filamentary structure in the jet interpreted as Kelvin–Helmholtz instability (Fuentes et al., in prep.). Event Horizon Telescope (EHT) observations at 230 GHz show two components within the inner 150 μas of the 86 GHz core, with the upstream feature identified as the core oriented perpendicular to the downstream jet component (Kim et al. 2020). The core features show apparent speeds of ∼15–20 *c*, which are consistent with values measured at centimeter wavelengths. 3C 279 was the first blazar detected in the γ-rays (Hartman et al. 1992), and has since been detected at VHE by MAGIC as well (MAGIC Collaboration 2008). The source has also been noted as a possible source of astrophysical neutrinos (Plavin et al. 2020).

1312−423. This source was detected by H.E.S.S. (H.E.S.S. Collaboration 2013c) and shown to have an integral flux density of 0.5% of that of the Crab Nebula. With the careful modeling

of Cen A, these authors recover the source in the HE *Fermi* LAT data as well. Our *S*-band observations show a core and a slight extension of the jet towards the northeast.

1322−428. Cen A is an FR I radio galaxy (Tingay et al. 1998), and is the closest radio-loud AGN to the Earth. The source was detected early on by *Fermi* LAT and is part of the *Fermi* Bright Source List (Abdo et al. 2009a). The first *X*-band TANAMI image of Cen A was published in Ojha et al. (2010), which was followed by a detailed analysis of the source by Müller et al. (2014). The jet shows differential motion, that is to say, downstream features exhibit higher velocities than those closer to the VLBI core. This observation leads the authors to propose a spine-sheath structure present in the jet, which has been detected on subparsec scales at 230 GHz with the EHT (Janssen et al. 2021). Based on the jet–counterjet ratio, the viewing angle is constrained to fall between 12° and 45°. Our *S*-band images also show a double-sided structure with an extended, well-collimated jet.

1440−389. Müller et al. (2018) presented 8.4 GHz images of this source from TANAMI. The source shows a compact structure in *S* band with a jet that can be modeled by a single component. 1440−389 was first detected at VHE in 2012 (Abdalla et al. 2020), and was recently detected in a high γ-state by the *Fermi* LAT for the first time (Ciprini et al. 2022).

1510−089. This source has been part of the MOJAVE program since 1995, but observations were dropped in 2013, and then taken up again recently in 2021. On parsec scales, the jet shows a one-sided structure, which we also recover in our 2.3 GHz images. The MOJAVE kinematic analysis (Lister et al. 2019) shows maximum apparent speeds up to $28.0 \pm 0.6\,c$, which suggests highly beamed emission (Liodakis et al. 2017). Multifrequency radio observations during high states in 2015–2017 reveal the emergence of two new jet components almost cotemporal to the HE flares; during one of the flares, the jet showed a limb-brightened linear polarization structure in the core region (Park et al. 2019). The authors conclude that the passing of the new components through stationary shocks gives rise to the γ-ray emission, and that the jet shows a complex transverse velocity structure that changes with time (MacDonald et al. 2015; Casadio et al. 2017).

1514−241. AP Librae has been part of MOJAVE between 1997 and 2012. Observations at 15 GHz show a 30 mas extended jet with a complex structure. In *S* band, we recover a double-sided jet. The maximum jet speed from MOJAVE observations is $6.21 \pm 0.26\,c$ (Lister et al. 2019). If we assume Doppler factors above 10, this suggests the jet viewing angle falls below 5° (Lister et al. 2013). Given the superluminal apparent jet speed and the small viewing angle, the double-sided jet structure in the *S* band image is of interest. VHE detection was reported by H.E.S.S. Collaboration (2015) with H.E.S.S. The VHE emission has been proposed to originate from the extended jet – which is also detected in the X-rays – via inverse Compton scattering of the CMB photons (Zacharias & Wagner 2016).

1515−273. TXS 1515−273 was detected by MAGIC (Acciari et al. 2021) during a γ-ray flare by *Fermi* (Cutini 2019). MOJAVE images reveal a one-sided jet structure that can be modeled as one component with an apparent speed of $0.73 \pm 0.18\,c$ (Lister et al. 2021). Our *S*-band images also show a core–jet morphology pointing toward the east.

1600−489. First 8.4-GHz TANAMI observations of this object were published in Müller et al. (2014). The source shows a double-sided structure, and due to its nonblazar-like spectral properties, it is classified as a compact symmetric object (CSO). The source is bright in the γ-rays (Abdo et al. 2009a). Our new *S*-band images show a double-sided jet structure and bright central core, which is reminiscent of the CSO class.

2005−489. This source was the first blazar independently detected by H.E.S.S. at VHE, and the second source noted as a VHE emitter in the southern hemisphere (Aharonian et al. 2005b). The integral flux is 0.025 of that of the Crab Nebula and has a very soft spectrum with a photon index of $\Gamma = 4.0 \pm 0.4$. Both *X*-band TANAMI observations by Ojha et al. (2010) and our new 2.3 GHz image show an elongated core in the northeast–southwest direction and a diffuse jet emission to the southwest.

2155−304. 15 GHz VLBA (Piner & Edwards 2004; Piner et al. 2010), 8 GHz and 22 GHz TANAMI observations (Ojha et al. 2010), and our new 2.3 GHz image reveal an initially well-collimated jet on mas scales. The first polarimetric image published by (Piner et al. 2008) reveals polarization in the core region with a polarization fraction of 2.9% and EVPAs with a position angle of 131° misaligned with the jet position angle by 30°. The source 2155−304 was detected at VHE in 1999 by the University of Durham Mark 6 atmospheric Cherenkov telescope (Chadwick et al. 1999), and can exhibit integral fluxes of up to 60% of that of the Crab Nebula (Aharonian et al. 2005a). The source exhibited a high flaring activity during 2006, when Doppler factors over 100 were used to model the SED (Aharonian et al. 2007c), which is much higher than typical Doppler factors estimated from VLBI data.

2322−409. While observing PKS 2316−423, Abdalla et al. (2019) detected an excess in hard γ-rays at the position of 1ES 2322−409 with H.E.S.S. The VHE spectrum can be described with a power law with the soft photon index of $\Gamma = 3.40 \pm 0.86$. The only published VLBI image of the source is presented by Schinzel et al. (2017) with the VLBA at 7.62 GHz. The source has a jet extending ~ 4 mas towards the northeast. Our *S* band image shows a similar morphology, but the jet points towards east.

2356−309. This source has been reported as an extreme synchrotron peaked blazar because its low-energy SED component peaks in the X-rays (Costamante et al. 2001). VLBI observations of Tiet et al. (2012) at 5 and 8 GHz show a core and a jet extending a few mas from the core. Our new TANAMI images reveal a similar structure.

5. Discussion

The morphology of radio-loud AGN can be described as double-sided when we detect both the jet and the counter-jet, single-sided when we only see the jet, or as compact cores without jet emission (Kellermann et al. 1998). Of the sources in the sample, 25% show only the radio core, 62.5% are single-sided, and the rest only exhibit double-sided jets. Faint $S_{2.3\,\mathrm{GHz}} < 50$ mJy sources on average show no extended jet emission, because the low signal-to-noise ratio prohibits the robust detection of jet emission. With that said, nine targets have total flux densities below 50 mJy, and only five reach 1 Jy.

The upper left-hand panel of Fig. 4 shows the redshift distribution of the TANAMI TeV sources. While the distribution

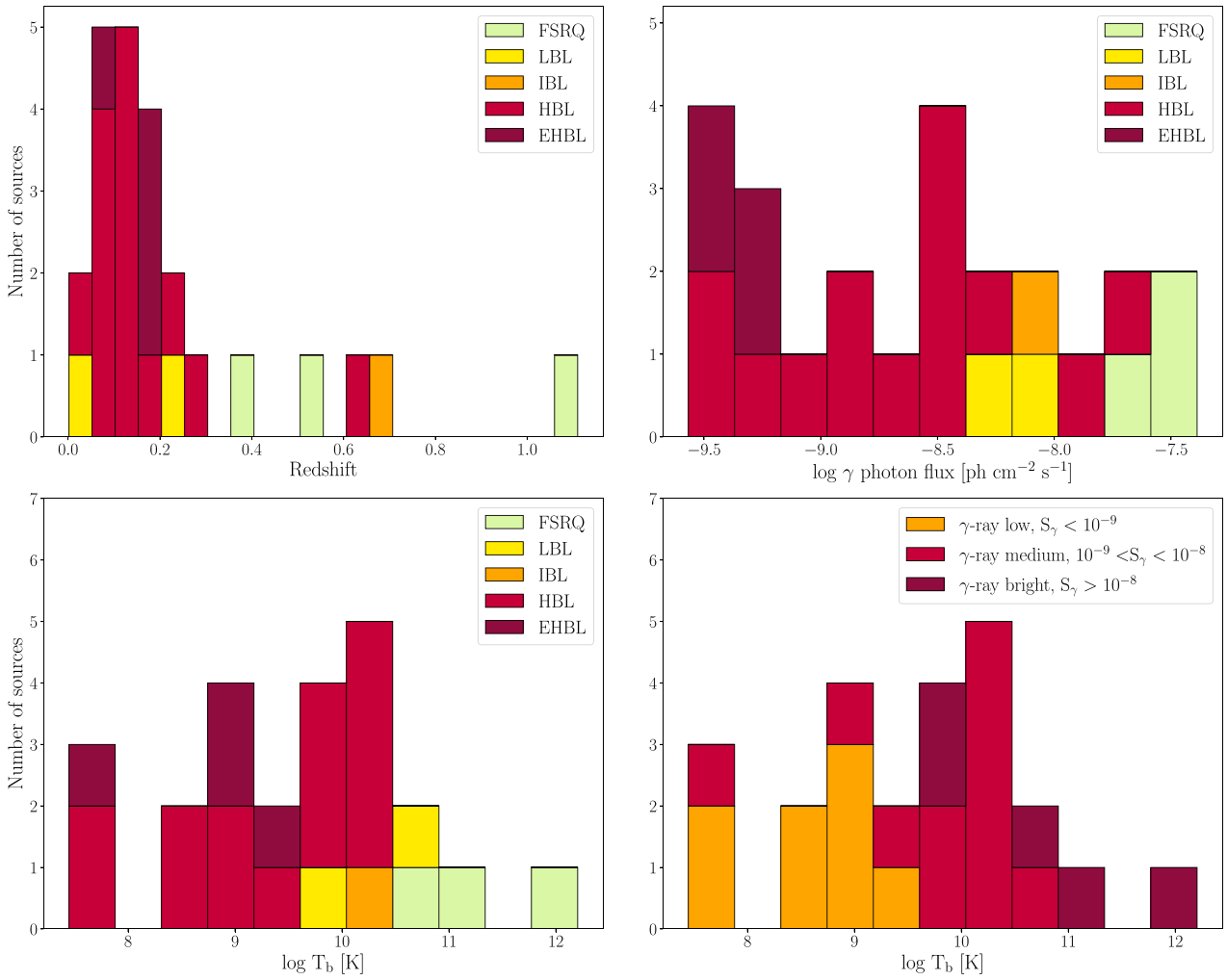

Fig. 4. Histogram showing the redshift (upper left panel), 0.1–100 GeV photon flux (upper right panel), and 2.3-GHz core brightness temperature (lower panels) distribution of sources in the TeV sample.

of HBL and EHBL objects peaks around $z \sim 0.1$, FSRQs in the sample fall between $z \sim 0.36$ and 1.11, and 0426−380 at $z = 1.11$ is the furthest known TeV emitter to date (Tanaka et al. 2013). The distribution of BL Lacs and FSRQs is consistent with the redshift distribution seen in the Bright AGN Source List (Abdo et al. 2009b) – which is a γ-ray-selected sample –, where BL Lacs are mainly located below a redshift of 0.5, and the distribution of FSRQs peaks around $z \sim 1$. However, the redshift distribution of TeV-detected AGN is biased for several reasons. The current generation of Imaging Atmospheric Cherenkov Telescopes (IACTs) operate in pointing mode, which means that they lack full-sky coverage. In addition, most AGN observed at VHE are only detected during high states of activity because of the lack of sensitivity of IACTs. Nevertheless, these issues will be overcome with the arrival of the Cherenkov Telescope Array (Actis et al. 2011). TeV emission from high-redshift sources is also affected by the attenuation from the extragalactic background light. In addition, many BL Lac objects have no redshifts available, which is due to the lack of detectable emission lines in their spectra, especially when considering high-redshift sources, further decreasing the number of known distant TeV-emitting AGN (Sol 2018).

The logarithmic GeV γ-ray photon flux distribution (Fig. 4, upper right panel) shows that BL Lac objects are distributed evenly, but mainly inhabit the fainter end of the sample. In addition, γ-ray brightness shows an inverse relation with the frequency of the synchrotron peak, that is, EHBL and HBL sources are dimmer at higher energies. The photon flux distribution of the *Fermi*-detected blazars from the above-mentioned Bright AGN Source List (Abdo et al. 2009b) peaks around 10^{-7} ph cm^{-2} s^{-1}. However, our TeV sample shows a rather uniform distribution, with a mean photon flux of 9.09×10^{-9} ph cm^{-2} s^{-1}.

The 2.3 GHz core brightness temperature distributions (Fig. 4, lower panels) show that BL Lac objects have the lowest $T_{\rm b,core}$ values, with a mean of 7.49×10^9 K, and FSRQs exhibit the highest $T_{\rm b,core}$ values, with an average of 1.52×10^{10} K. This is also seen in the study of a complete flux-limited sample of AGN (Lister et al. 2011), where HBL sources show lower brightness temperatures than other BL Lac objects and quasars. (Homan et al. 2021) reported that BL Lac objects in this flux-limited sample show the same trend that we find for our TeV-detected sample, namely that there is an inverse relation between the synchrotron peak frequency and the median core brightness temperature.

The $T_{\rm b,core}$ distribution with γ-ray flux classes marked shows that γ-ray-low ($S_\gamma < 10^{-9}$ ph cm^{-2} s^{-1}) objects tend to exhibit lower core brightness temperatures, while medium

($10^{-9} < S_\gamma < 10^{-8}$ ph cm^{-2} s^{-1}) and bright ($>10^{-8}$ ph cm^{-2} s^{-1}) sources have higher $T_{\rm b,core}$ values. A similar trend is recovered for the above-mentioned MOJAVE 1.5-Jy flux-limited sample, in which quasars show higher median core brightness temperatures and are more luminous at GeV energies than BL Lacs (Homan et al. 2021). These results suggest that the emission from low-synchrotron-peaked objects, like FSRQs and LBLs, is more strongly Doppler boosted than that from high-synchrotron-peaked objects, such as HBL and EHBL sources.

The average and median $T_{\rm b,core}$ for the TANAMI TeV sample are 8.19×10^{10} K and 4.9×10^9 K, respectively. Twenty-one $T_{\rm b,core}$ values are below the equipartition brightness temperature of $T_{\rm eq} \approx 5 \times 10^{10}$ K (Readhead 1994) and all but one of the values fall below the inverse Compton catastrophe limit of $\approx 10^{12}$ K (Kellermann & Pauliny-Toth 1969). This suggests that, in most cases, the emission from these sources is not beamed at 2.3 GHz. Observations at 15 GHz in MOJAVE, a sample dominated by LBL and FSRQ objects, reveal a mean core brightness temperature of 2.93×10^{11} K with a median of 3.66×10^{11} K (Homan et al. 2021), which is significantly higher than those observed in our sample. $T_{\rm b,core}$ values of the X-band TANAMI sample from Böck et al. (2016) have an average and median of 9.62×10^{11} K and 2.1×10^{11} K, respectively, which are consistent with those of the MOJAVE sample. The nearly one-order-of-magnitude lower average $T_{\rm b,core}$ for the TeV sample has been shown as a characteristic of VHE-detected sources (Piner & Edwards 2018b).

6. Conclusion

In this work, we present the first results of our new 2.3 GHz AGN monitoring, including all 24 TeV-detected sources at the southern hemisphere at the time of the observations. The 2.3 GHz band was added in our program to better study extended jet emission and to include TeV sources in our sample that would be too faint to detect at higher frequencies. With the inclusion of Parkes and ATCA, we were capable of detecting even the faintest ($S_{2.3\,\rm GHz} \approx 10$ mJy) target in the sample. While this was a success, the current long transoceanic baselines to the Hartebeesthoek antenna yield only limited sensitivity, which degrades the image fidelity and angular resolution in observations of faint targets. This is a strong limitation for studies of the bulk of the HBL and extreme-blazar population. In order to improve our observations, we support the efforts to phase up the MeerKAT array, with which we would be able to achieve three times better sensitivity on the long baselines.

We fitted circular Gaussian components to model the source structures and calculated the brightness temperatures for the radio core. Core brightness temperature distributions reveal that the FSRQs in the sample generally have higher core brightness temperatures than BL Lacs and radio galaxies. We also observe that, with increasing γ-ray photon flux, core brightness temperatures are higher as well. Comparing this sample to 8.4 GHz TANAMI and 15 GHz MOJAVE results, which are samples dominated by FSRQs and low-synchrotron-peaked objects, we find that the $T_{\rm b,core}$ values in the S band are up to one magnitude lower than average values in the other samples, which is consistent with previous results of Piner & Edwards (2018b), who noted that TeV-detected sources have lower $T_{\rm b,core}$. However, at low frequencies, it is also possible that we do not detect the optically thick VLBI core, but instead only a bright, optically thin jet component that we identify as the core. As brightness temperature measurements are heavily dependent on the maximum baseline length and the flux density of the component, bright jet features, like the core, can exhibit high $T_{\rm b}$ values.

Due to the success of the first three S band observing epochs, we continue to monitor VHE-detected AGN and perform kinematic and spectral studies once a sufficient number of observing epochs is reached. While the 2.3 GHz observations lack the resolution and sensitivity to determine the location of the γ-ray production or to differentiate between jet models suggested to resolve the Doppler crisis, they enable us to study the faintest TeV-emitters and to perform multi-frequency studies together with our 8.4 GHz monitoring. TANAMI is currently the only AGN monitoring program on the southern hemisphere, and forming complete samples to study these rarely observed targets is crucial in order to advance multiwavelength studies.

Acknowledgements. The authors would like to thank the anonymous referee for their valuable comments on the manuscript. We thank H. Müller for his constructive suggestions to improve our work. The Long Baseline Array is part of the Australia Telescope National Facility (https://ror.org/05qajvd42) which is funded by the Australian Government for operation as a National Facility managed by CSIRO. From the 2023 July 1, operation of Warkworth was transferred from AUT University to Space Operations New Zealand Ltd with new funding from Land Information New Zealand (LINZ). This research was supported through a PhD grant from the International Max Planck Research School (IMPRS) for Astronomy and Astrophysics at the Universities of Bonn and Cologne. M2FINDERS project has received funding from the European Research Council (ERC) under the European Union's Horizon 2020 research and innovation programme (grant agreement no. 101018682). M.K. and F.R. acknowledge funding by the Deutsche Forschungsgemeinschaft (DFG, German Research Foundation) – grant 434448349.

References

Abdalla, H., Aharonian, F., Ait Benkhali, F., et al. 2019, MNRAS, 482, 3011
Abdalla, H., Adam, R., Aharonian, F., et al. 2020, MNRAS, 494, 5590
Abdo, A. A., Ackermann, M., Ajello, M., et al. 2009a, ApJS, 183, 46
Abdo, A. A., Ackermann, M., Ajello, M., et al. 2009b, ApJ, 700, 597
Abdo, A. A., Ackermann, M., Agudo, I., et al. 2010, ApJ, 716, 30
Abdollahi, S., Acero, F., Baldini, L., et al. 2022, ApJS, 260, 53
Acciari, V. A., Ansoldi, S., Antonelli, L. A., et al. 2021, MNRAS, 507, 1528
Ackermann, M., Ajello, M., Allafort, A., et al. 2011, ApJ, 743, 171
Actis, M., Agnetta, G., Aharonian, F., et al. 2011, Exp. Astron., 32, 193
Aharonian, F., Akhperjanian, A. G., Aye, K.-M., et al. 2005a, A&A, 430, 865
Aharonian, F., Akhperjanian, A. G., Aye, K.-M., et al. 2005b, A&A, 436, L17
Aharonian, F., Akhperjanian, A. G., Bazer-Bachi, A. R., et al. 2007a, A&A, 470, 475
Aharonian, F., Akhperjanian, A. G., Barres de Almeida, U., et al. 2007b, A&A, 473, L25
Aharonian, F., Akhperjanian, A. G., Bazer-Bachi, A. R., et al. 2007c, ApJ, 664, L71
Aleksić, J., Alvarez, E. A., Antonelli, L. A., et al. 2012, A&A, 542, A100
Angioni, R., Ros, E., Kadler, M., et al. 2019, A&A, 627, A148
Arsioli, B., Fraga, B., Giommi, P., et al. 2015, A&A, 579, A34
Atwood, W. B., Abdo, A. A., Ackermann, M., et al. 2009, ApJ, 697, 1071
Böck, M., Kadler, M., Müller, C., et al. 2016, A&A, 590, A40
Böttcher, M., & Els, P. 2016, ApJ, 821, 102
Carpenter, B., & Ojha, R. 2015, ATel, 7704
Casadio, C., Krichbaum, T., Marscher, A., et al. 2017, Galaxies, 5, 67
Chadwick, P. M., Lyons, K., McComb, T. J. L., et al. 1999, ApJ, 513, 161
Chang, Y.-L., Arsioli, B., Giommi, P., et al. 2019, A&A, 632, A77
Cheung, C. C. 2002, ApJ, 581, L15
Ciprini, S., Cheung, C. C., & Fermi Large Area Telescope Collaboration 2022, ATel, 15635
Costamante, L., Ghisellini, G., Giommi, P., et al. 2001, A&A, 371, 512
Craig, N., & Fruscione, A., 1997, AJ, 114, 1356
Cutini, S. 2019, ATel, 12532
Falomo, R., Pesce, J. E., & Treves, A. 1995, ApJ, 438, L9
Ganguly, R., Lynch, R. S., Charlton, J. C., et al. 2013, MNRAS, 435, 1233
Gaté, F., H.E.S.S. Collaboration, & Fitoussi, T. 2017, 35th International Cosmic Ray Conference (ICRC2017), 301, 645
Georganopoulos, M., & Kazanas, D. 2003, ApJ, 594, L27
Ghisellini, G., Tavecchio, F., & Chiaberge, M. 2005, A&A, 432, 401
Giannios, D., Uzdensky, D. A., & Begelman, M. C. 2009, MNRAS, 395, L29
Goldoni, P., Pita, S., Boisson, C., et al. 2016, A&A, 586, A2
Greisen, E. W. 2003, Information Handling in Astronomy – Historical Vistas (Dordrecht: Kluwer Academic Publishers), 285, 109

Gulyaev, S., Natusch, T., & Wilson, D. 2010, Sixth International VLBI Service for Geodesy and Astronomy. Proceedings from the 2010 General Meeting, 113
Hartman, R. C., Bertsch, D. L., Fichtel, C. E., et al. 1992, ApJ, 385, L1
H.E.S.S. Collaboration (Abramowski, A., et al.) 2012, A&A, 542, A94
H.E.S.S. Collaboration (Abramowski, A., et al.) 2013a, A&A, 552, A118
H.E.S.S. Collaboration (Abramowski, A., et al.) 2013b, A&A, 559, A136
H.E.S.S. Collaboration (Abramowski, A., et al.) 2013c, MNRAS, 434, 1889
H.E.S.S. Collaboration (Abramowski, A., et al.) 2015, A&A, 573, A31
H.E.S.S. Collaboration (Abdalla, H., et al.) 2018, MNRAS, 476, 4187
Homan, D. C., Cohen, M. H., Hovatta, T., et al. 2021, ApJ, 923, 67
Jackson, C. A., Wall, J. V., Shaver, P. A., et al. 2002, A&A, 386, 97
Janssen, M., Falcke, H., Kadler, M., et al. 2021, Nat. Astron., 5, 1017
Jones, D. H., Read, M. A., Saunders, W., et al. 2009, MNRAS, 399, 683
Jorstad, S. G., Marscher, A. P., Smith, P. S., et al. 2013, ApJ, 773, 147
Keeney, B. A., Stocke, J. T., Pratt, C. T., et al. 2018, ApJS, 237, 11
Kellermann, K. I., & Pauliny-Toth, I. I. K. 1969, ApJ, 155, L71
Kellermann, K. I., Vermeulen, R. C., Zensus, J. A., et al. 1998, AJ, 115, 1295
Kim, J.-Y., Krichbaum, T. P., Broderick, A. E., et al. 2020, A&A, 640, A69
Kovalev, Y. Y., Kellermann, K. I., Lister, M. L., et al. 2005, AJ, 130, 2473
Lavaux, G., & Hudson, M. J. 2011, MNRAS, 416, 2840
Lauer, T. R., Postman, M., Strauss, M. A., et al. 2014, ApJ, 797, 82
Laurent-Muehleisen, S. A., Kollgaard, R. I., Moellenbrock, G. A., et al. 1993, AJ, 106, 875
Lefaucheur, J., & Pita, S. 2017, A&A, 602, A86
Lico, R., Giroletti, M., Orienti, M., et al. 2012, A&A, 545, A117
Liodakis, I., Zezas, A., Angelakis, E., et al. 2017, A&A, 602, A104
Lister, M. L., Cohen, M. H., Homan, D. C., et al. 2009, AJ, 138, 1874
Lister, M. L., Aller, M., Aller, H., et al. 2011, ApJ, 742, 27
Lister, M. L., Aller, M. F., Aller, H. D., et al. 2013, AJ, 146, 120
Lister, M. L., Homan, D. C., Hovatta, T., et al. 2019, ApJ, 874, 43
Lister, M. L., Homan, D. C., Kellermann, K. I., et al. 2021, ApJ, 923, 30
MacDonald, N. R., Marscher, A. P., Jorstad, S. G., et al. 2015, ApJ, 804, 111
MAGIC Collaboration (Albert, J., et al.) 2008, Science, 320, 1752
Mannheim, K. 1993, A&A, 269, 67
Mao, L. S. 2011, New Astron., 16, 503
Maraschi, L., Ghisellini, G., & Celotti, A. 1992, ApJ, 397, L5
Marscher, A. P., Jorstad, S. G., Agudo, I., et al. 2012, ArXiv e-prints [arXiv:1204.6707]
Mondal, S. K., Prince, R., Gupta, N., et al. 2021, ApJ, 922, 160
Müller, C., Kadler, M., Ojha, R., et al. 2014, A&A, 569, A115
Müller, C., Kadler, M., Ojha, R., et al. 2018, A&A, 610, A1
Neeleman, M., Prochaska, J. X., Ribaudo, J., et al. 2016, ApJ, 818, 113
Ojha, R., Fey, A. L., Johnston, K. J., et al. 2004, AJ, 127, 1977
Ojha, R., Kadler, M., Böck, M., et al. 2010, A&A, 519, A45
Park, J., Lee, S.-S., Kim, J.-Y., et al. 2019, ApJ, 877, 106
Paturel, G., Dubois, P., Petit, C., et al. 2002, LEDA
Piner, B. G., & Edwards, P. G. 2004, ApJ, 600, 115
Piner, B. G., & Edwards, P. G. 2013, Eur. Phys. J. Web Conf., 61, 04021
Piner, B. G., & Edwards, P. G. 2014, ApJ, 797, 25
Piner, B. G., & Edwards, P. G. 2018a, ApJ, 853, 68
Piner, B. G., & Edwards, P. G. 2018b, Fourteenth Marcel Grossmann Meeting – MG14 (World Scientific Publishing Co. Pte. Ltd.), 3074
Piner, B. G., & Edwards, P. G. 2023, https://whittierblazars.com/
Piner, B. G., Pant, N., & Edwards, P. G. 2008, ApJ, 678, 64
Piner, B. G., Pant, N., & Edwards, P. G. 2010, ApJ, 723, 1150
Plavin, A., Kovalev, Y. Y., Kovalev, Y. A., et al. 2020, ApJ, 894, 101
Readhead, A. C. S. 1994, ApJ, 426, 51
Rieger, F. M., & Volpe, F. 2010, A&A, 520, A23
Saito, S., Stawarz, Ł., Tanaka, Y. T., et al. 2013, ApJ, 766, L11
Schinzel, F. K., Petrov, L., Taylor, G. B., et al. 2017, ApJ, 838, 139
Schwope, A., Hasinger, G., Lehmann, I., et al. 2000, Astron. Nachr., 321, 1
Shepherd, M. C. 1997, Astronomical Data Analysis Software and Systems VI, A.S.P. Conference Series, 125, 77
Sol, H. 2018, J. Astrophys. Astron., 39, 52
Tanaka, Y. T., Cheung, C. C., Inoue, Y., et al. 2013, ApJ, 777, L18
Tavecchio, F., Becerra-Gonzalez, J., Ghisellini, G., et al. 2011, A&A, 534, A86
Thompson, D. J., Djorgovski, S., & de Carvalho, R. 1990, PASP, 102, 1235
Tiet, V. C., Piner, B. G., & Edwards, P. G. 2012, ArXiv e-prints [arXiv:1205.2399]
Tingay, S. J., Jauncey, D. L., Reynolds, J. E., et al. 1998, AJ, 115, 960
Truebenbach, A. E., & Darling, J. 2017, ApJS, 233, 3
Yan, D., Zeng, H., & Zhang, L. 2012, MNRAS, 424, 2173
Zacharias, M., & Wagner, S. J. 2016, A&A, 588, A110

Appendix A: Additional data

Table A.1: Sources observed during the first three S band epochs.

Name	Alternative name	Class [(a)]	z	X band first epoch	Association
0011−191	SHBL J001355.9−185406	HBL	0.095 (1)	-	TeV
0031−196	KUV 00311−1938	HBL	0.610 (2)	-	TeV
0236−314	1RXS J023833.1−311808	HBL	0.233 (3)	-	TeV
0301−243		HBL	0.260 (2)	-	TeV
0347−121	1ES 0347−121	EHBL	0.185 (2)	-	TeV
0426−380		FSRQ	1.111 (2)	(16)	TeV
0447−439		HBL	0.107 (4)	(16)	TeV
0548−322		EHBL	0.069 (2)	-	TeV
0625−354	OH−342	RG	0.056 (5)	(17)	TeV
0903−573		IBL	0.695 (6)	-	TeV
1008−310	1RXS J101015.9−311909	HBL	0.143 (1)	-	TeV
1101−232	1ES 1101−232	EHBL	0.186 (7)	-	TeV
1248−350		U	0.410 (8)	-	neutrino
1253−053	3C 279	FSRQ	0.538 (7)	-	neutrino/TeV
1312−423	1ES 1312−423	HBL	0.105 (2)	-	TeV
1322−428	Cen A, NGC 5128	RG	0.002 (9)	(17)	TeV
1424−418	[HB89] 1424−418	FSRQ	1.520 (10)	(17)	neutrino
1440−389		HBL	0.065 (11)	(16)	TeV
1510−089		FSRQ	0.360 (10)	-	TeV
1514−241	AP Librae	LBL	0.049 (1)	-	TeV
1515−273	TXS 1515−273	HBL	0.140 (11)	-	TeV
1600−489	PMN J1603−4904	CSO	0.232 (12)	(18)	TeV
1921−293		BL Lac	0.353 (1)	-	calibrator
1934−638		CSO	0.183 (13)	(19)	calibrator
2005−489	[HB89] 2005−489	HBL	0.071 (14)	(17)	TeV
2155−304	[HB89] 2155−304	HBL	0.116 (15)	(17)	TeV
2322−409	1ES 2322−409	HBL	0.174 (1)	-	TeV
2356−309		EHBL	0.165 (1)	-	TeV

Notes. [(a)] Source class abbreviations: LBL - low frequency peaked blazar; IBL - intermediate frequency peaked blazar; HBL - high frequency peaked blazar; EHBL - extremely high frequency peaked blazar; RG - radio galaxy; FSRQ - flat spectrum radio quasar; CSO - compact symmetric object; U - unidentified.

References. (1) Jones et al. (2009); (2) Mao (2011); (3) Arsioli et al. (2015); (4) Craig & Fruscione (1997); (5) Lauer et al. (2014); (6) Thompson et al. (1990); (7) Neeleman et al. (2016); (8) Jackson et al. (2002); (9) Lavaux & Hudson (2011); (10) Truebenbach & Darling (2017); (11) Chang et al. (2019); (12) Goldoni et al. (2016); (13) Paturel et al. (2002); (14) Keeney et al. (2018); (15) Ganguly et al. (2013); (16) Müller et al. (2018); (17) Ojha et al. (2010); (18) Müller et al. (2014); (19) Ojha et al. (2004).

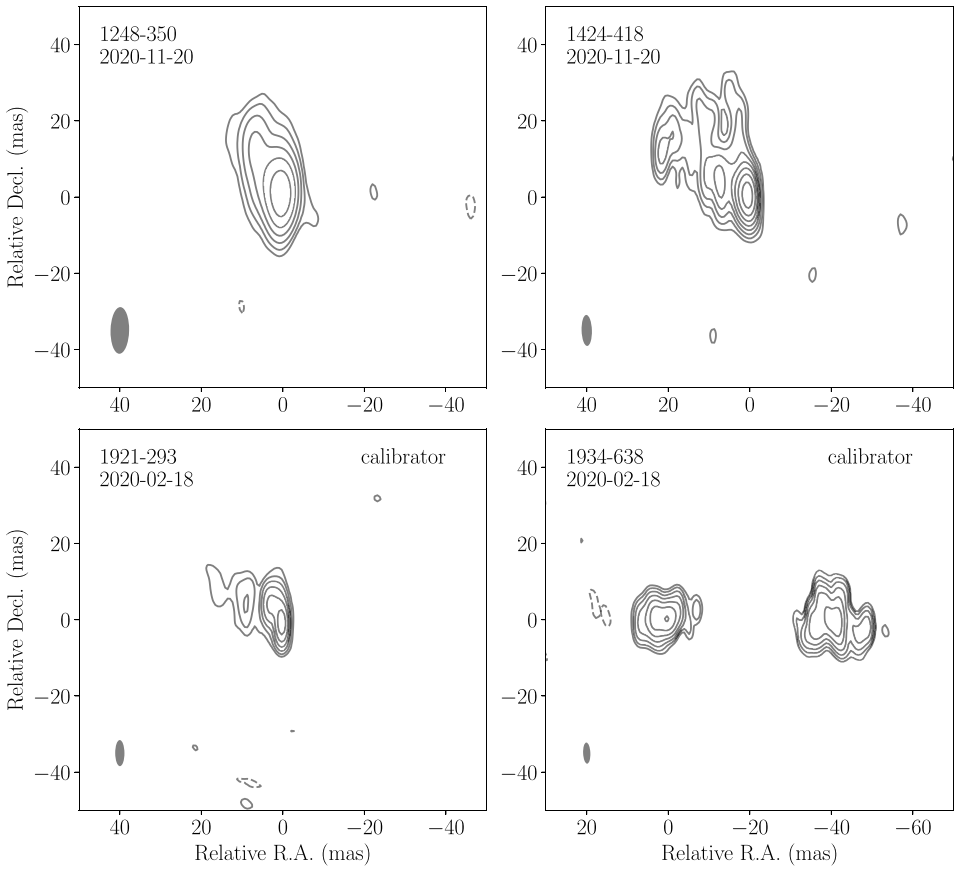

Fig. A.1. Clean maps of additional sources and calibrators included in the 2.3 GHz observations. Image parameters and lowest contours are listed in Table A.2. Contour levels increase by a factor of two.

Table A.2: Image properties of non-TeV sources and calibrators observed during 2020–2021 in S band.

Source	Morphology [a]	Epoch [yyyy-mm-dd]	b_{maj} [b] [mas]	b_{min} [c] [mas]	PA [d] [°]	S_{tot} [e] [mJy]	σ [f] [mJy/beam]	I_{base} [g] [mJy/beam]
1248−350	SS	2020-11-20	12.2	4.6	−1	200.8	0.6	2.2
1424−418	SS	2020-11-20	8.1	2.5	2	1988.0	1.6	5.1
1921−293	SS	2020-02-18	6.84	2.3	0	5087.7	14.9	47.3
1934−638	DS	2020-02-18	5.54	1.8	2	11194.5	5.2	17.9

Notes. [a] Source morphology: SS - single-sided; DS - double-sided jet morphology. [b] Beam major axis. [c] Beam minor axis. [d] Beam position angle. [e] Total flux density. [f] Rms noise of the image. [g] Lowest contour.

Table A.3: Image properties of the TeV-detected AGN in our observations.

Source	Morphology [a]	Epoch [yyyy-mm-dd]	b_{maj} [b] [mas]	b_{min} [c] [mas]	PA [d] [°]	S_{tot} [e] [mJy]	σ [f] [mJy/beam]	I_{base} [g] [mJy/beam]	S_{core} [h] [mJy]	Θ_{core} [i] [mas]	T_b [j] [K]	$S_{0.1-100GeV}$ [k] [ph/cm^2/s]	S_{TeV} [l] CU
0011−191	C	2020-11-20	17.6	3.9	1	16.4	0.1	0.3	16.6 ± 1.7	8.8 ± 0.8	$(5.5 \pm 1.1) \times 10^7$	$(2.71 \pm 0.33) \times 10^{-10}$	0.006
0031−196	C	2020-11-20	22.2	2.8	−1	19.1	0.2	0.4	19.1 ± 1.9	14.2 ± 0.6	$(3.6 \pm 0.5) \times 10^7$	$(2.69 \pm 0.08) \times 10^{-9}$	0.009
0236−314	SS	2020-02-18	11.4	3.2	2	24.9	0.1	0.3	14.9 ± 1.5	3.3 ± 0.6	$(4.0 \pm 1.6) \times 10^8$	$(9.13 \pm 0.48) \times 10^{-10}$	-
0301−243	SS	2020-11-20	14.4	2.9	2	170.5	0.5	1.1	91.9 ± 9.2	1.4 ± 0.6	$(1.4 \pm 1.2) \times 10^{10}$	$(4.79 \pm 0.11) \times 10^{-9}$	0.014
0347−121	SS	2020-02-18	23.3	3.1	2	10.4	0.1	0.2	10.0 ± 1.0	10.0 ± 0.6	$(2.8 \pm 0.4) \times 10^7$	$(3.69 \pm 0.37) \times 10^{-10}$	0.02
0426−380	SS	2020-02-18	9.1	3.0	4	761.1	1.6	5.3	599.1 ± 59.9	1.5 ± 0.6	$(1.4 \pm 1.1) \times 10^{11}$	$(2.14 \pm 0.02) \times 10^{-8}$	-
0447−439	SS	2020-02-18	9.3	3.1	3	89.9	0.3	0.8	58.2 ± 5.8	1.9 ± 0.6	$(4.3 \pm 2.9) \times 10^9$	$(1.25 \pm 0.02) \times 10^{-8}$	0.03
0548−322	C	2020-11-20	10.6	3.0	1	27.2	0.3	0.7	13.9 ± 1.4	1.0 ± 0.55	$(1.1 \pm 0.7) \times 10^9$	$(3.13 \pm 0.34) \times 10^{-10}$	0.013
0625−354	SS	2020-02-18	9.0	3.0	1	352.0	2.5	5.3	218.0 ± 21.8	1.8 ± 0.6	$(1.7 \pm 1.2) \times 10^{10}$	$1.26 \pm 0.06) \times 10^{-9}$	0.04
0903−573	SS	2020-11-20	7.6	3.4	16	346.8	0.8	1.8	196.8 ± 19.7	2.4 ± 0.7	$(1.4 \pm 0.8) \times 10^{10}$	$(9.09 \pm 0.15) \times 10^{-9}$	-
1008−310	C	2021-12-04	21.2	2.7	3	28.7	2.0	0.3	19.0 ± 1.9	2.3 ± 0.5	$(9.0 \pm 4.0) \times 10^8$	$(6.08 \pm 0.54) \times 10^{-10}$	0.008
1101−232	C	2021-12-04	17.6	2.3	1	38.3	0.3	0.9	30.3 ± 3.0	2.2 ± 0.5	$(1.7 \pm 0.7) \times 10^9$	$(4.29 \pm 0.44) \times 10^{-10}$	0.02
1253−053	SS	2020-02-18	20.6	2.5	3	8133.5	7.9	45.1	5220.1 ± 522.0	1.1 ± 0.5	$(1.6 \pm 1.4) \times 10^{12}$	$(4.09 \pm 0.03) \times 10^{-8}$	-
1312−423	C	2020-02-18	18.0	2.8	−6	11.9	0.1	0.2	8.3 ± 0.8	2.0 ± 0.6	$(5.1 \pm 2.8) \times 10^8$	$(3.85 \pm 0.47) \times 10^{-10}$	0.005
1322−428	DS	2021-12-04	7.1	2.7	5	3630.6	2.5	8.6	519.8 ± 52.0	2.3 ± 0.5	$(2.3 \pm 1.1) \times 10^{10}$	$(3.59 \pm 0.09) \times 10^{-9}$	0.08
1440−389	SS	2020-11-20	10.3	2.6	4	133.5	0.2	0.6	104.7 ± 10.5	1.7 ± 0.5	$(9.0 \pm 5.0) \times 10^9$	$(4.08 \pm 0.11) \times 10^{-9}$	0.054
1510−089	SS	2020-02-18	13.4	5.9	16	2445.4	7.9	30.5	1842.5 ± 184.3	3.6 ± 1.2	$(4.5 \pm 2.9) \times 10^{10}$	$(3.38 \pm 0.03) \times 10^{-8}$	0.03
1514−241	DS	2020-11-20	11.0	3.1	2	2571.3	0.9	2.9	993.7 ± 99.4	2.2 ± 0.6	$(5.0 \pm 2.9) \times 10^{10}$	$(6.67 \pm 0.13) \times 10^{-9}$	0.04
1515−273	SS	2020-11-20	15.4	7.5	0	120.6	0.3	0.7	81.0 ± 8.1	3.7 ± 1.5	$(1.5 \pm 1.2) \times 10^9$	$(1.71 \pm 0.07) \times 10^{-9}$	-
1600−489	DS	2020-11-20	8.7	4.2	−2	1282.9	1.1	3.8	581.4 ± 58.1	5.4 ± 0.8	$(5.7 \pm 1.9) \times 10^9$	$(5.62 \pm 0.20) \times 10^{-9}$	-
2005−489	SS	2020-02-18	7.4	2.6	3	751.7	2.1	5.4	235.1 ± 23.5	1.4 ± 0.5	$(2.9 \pm 2.1) \times 10^{10}$	$(2.90 \pm 0.09) \times 10^{-9}$	0.03
2155−304	SS	2020-02-18	12.3	2.6	−1	320.3	0.6	2.0	186.0 ± 18.6	3.0 ± 0.5	$(5.5 \pm 2.0) \times 10^9$	$(2.00 \pm 0.02) \times 10^{-8}$	0.15
2322−409	SS	2020-11-20	10.0	3.5	0	55.8	0.2	0.6	43.5 ± 4.4	2.3 ± 0.7	$(2.3 \pm 1.4) \times 10^9$	$(1.07 \pm 0.06) \times 10^{-9}$	0.011
2356−309	SS	2021-12-04	16.6	3.2	1	24.1	0.1	0.3	14.0 ± 1.4	2.6 ± 0.6	$(5.8 \pm 2.9) \times 10^8$	$(4.50 \pm 0.39) \times 10^{-10}$	0.02

Notes. [a]Source morphology: C - core only; SS - single-sided; DS - double-sided jet morphology. [b]Beam major axis. [c]Beam minor axis. [d]Beam position angle. [e]Total flux density. [f]Rms noise of the image. [g]Lowest contour. [h]Flux density of the core. [i]FWHM of the core. [j]Brightness temperature. [k]Photon flux from (Abdollahi et al. 2022). [l]Very high energy flux in Crab units.

Chapter 6

VLBI study of the flaring blazar TXS 1508+572 from the early Universe

Blazars are the most abundant sources of the γ-ray sky. While over half of the fourth catalog of the *Fermi* Large Area Telescope is comprised of these objects, only 33 or 0.65% of these blazars are high-redshift objects (Abdollahi et al. 2020, $z > 2.5$ cutoff set by the *Fermi* LAT). However, most of these high-redshift sources can only be detected by *Fermi* during flaring states (Paliya et al. 2019; Kreter et al. 2020), otherwise their steeply falling spectra prevents their detection at low states in the GeV energy range. This complicates obtaining quasi-simultaneous multi-wavelength observational data for studies of their broadband emission. The only example of such a quasi-simultaneous study to date is the case of the intermediate-redshift object TXS 0536+145 at $z = 2.69$ (Orienti et al. 2014).

When a strong γ-ray flare was detected in 1508+572 on the 4^{th} of February, 2022, (Gokus et al. 2022) within the γ-ray monitoring program described in Kreter et al. (2020), we started a multi-frequency campaign across the electromagnetic spectrum to follow up this event with quasi-simultaneous observations (Gokus et al. 2024). Since γ-ray observations lack the resolution required for determining the origin of the activity, we have initiated a multi-frequency VLBI monitoring campaign at 15, 22 and 43 GHz with the VLBA and the Effelsberg 100-m telescope to capture the evolution of the source morphology, spectral index and opacity variations and, possibly, relate VLBI structural components to the observed high-energy activity.

The hybrid images obtained from the VLBI observations reveal a change in source morphology, that is especially evident on the 43-GHz maps, where the jet propagates towards the southwest and becomes more diffuse with time. The jet feature moves with a proper motion of (0.12−0.27) mas yr^{-1}, which corresponds to a superluminal apparent

speed of $(14.3 - 32.2)$ c. The kinematic back-extrapolation suggests that the feature was ejected around 2016−2019. These proper motion values are consistent with the maximum apparent speed expected on the $(\mu - z)$ diagram with the assumption of a Lorentz factor of 20 (Zhang et al. 2022), the same value that was assumed to fit the broadband SED of TXS 1508+572 (Gokus et al. 2024).

The core shift measurement reveals no significant impact of the high-energy flare on the distance between the jet apex and the 43-GHz radio core. We determine the average projected distance to the central supermassive black hole to be (46.1 ± 2.3) μas or (0.32 ± 0.02) pc. However, there might be a traveling disturbance/density enhancement that affected the position of the apparent cores at different frequencies during the 2022.67 epoch, as the 15-GHz core lies closer to the 43-GHz core than the 22-GHz one. We estimate the equipartition and non-equipartition magnetic field strength 1 pc from the central engine (Zdziarski et al. 2015) to be on the order of 1.8 G and 257 G, respectively. The first are typical values for low and intermediate redshift AGN of the MOJAVE sample (Pushkarev et al. 2012) and Zamaninasab et al. (2014) for sources below redshift 2.43 and 2.37, respectively.

In conclusion, we propose that the γ-ray activity observed in February 2022 is caused by a shock-shock interaction between the jet of TXS 1508+572 and new plasma flowing through this components.

https://doi.org/10.1051/0004-6361/202450153

Conceptualization, A.G., M.L.; methodology, P.B., M.L.; formal analysis, P.B., M.L.; software, P.B.; validation, P.B., M.L., E.R., M.K.; writing-original draft preparation, P.B.; writing-review and editing, M.L., L.I.G, E.R., J.H., F.E., F.R.; visualization, P.B.; supervision, E.R.

A&A, 689, A43 (2024)
https://doi.org/10.1051/0004-6361/202450153

Astronomy & Astrophysics

Very-long-baseline interferometry study of the flaring blazar TXS 1508+572 in the early Universe

P. Benke[1,2], A. Gokus[3], M. Lisakov[4,5,1], L. I. Gurvits[6,7], F. Eppel[2,1], J. Heßdörfer[2,1], M. Kadler[2], Y. Y. Kovalev[1], E. Ros[1], and F. Rösch[2,1]

[1] Max-Planck-Institut für Radioastronomie, Auf dem Hügel 69, 53121 Bonn, Germany
e-mail: pbenke@mpifr-bonn.mpg.de
[2] Julius-Maximilians-Universität Würzburg, Fakultät für Physik und Astronomie, Institut für Theoretische Physik und Astrophysik, Lehrstuhl für Astronomie, Emil-Fischer-Str. 31, 97074 Würzburg, Germany
[3] Department of Physics & McDonnell Center for the Space Sciences, Washington University in St. Louis, One Brookings Drive, St. Louis, MO 63130, USA
[4] Instituto de Física, Pontificia Universidad Católica de Valparaíso, Casilla 4059, Valparaíso, Chile
[5] Astro Space Center of Lebedev Physical Institute, Profsouznaya 84/32, Moscow 117997, Russia
[6] Joint Institute for VLBI ERIC, Oude Hoogeveensedijk 4, 7991 PD Dwingeloo, The Netherlands
[7] Faculty of Aerospace Engineering, Delft University of Technology, Kluyverweg 1, 2629 HS Delft, The Netherlands

Received 27 March 2024 / Accepted 1 June 2024

ABSTRACT

Context. High-redshift blazars provide valuable input to studies of the evolution of active galactic nuclei (AGN) jets and provide constraints on cosmological models. Detections at high energies ($0.1 < E < 100$ GeV) of these distant sources are rare, but when they exhibit bright gamma-ray flares, we are able to study them. However, contemporaneous multi-wavelength observations of high-redshift objects ($z > 4$) during their different periods of activity have not been carried out so far. An excellent opportunity for such a study arose when the blazar TXS 1508+572 ($z = 4.31$) exhibited a γ-ray flare in 2022 February in the 0.1−300 GeV range with a flux 25 times brighter than the one reported in the in the fourth catalog of the *Fermi* Large Area Telescope.
Aims. Our goal is to monitor the morphological changes, spectral index and opacity variations that could be associated with the preceding γ-ray flare in TXS 1508+572 to find the origin of the high-energy emission in this source. We also plan to compare the source characteristics in the radio band to the blazars in the local Universe ($z < 0.1$). In addition, we aim to collect quasi-simultaneous data to our multi-wavelength observations of the object, making TXS 1508+572 the first blazar in the early Universe ($z > 4$) with contemporaneous multi-frequency data available in its high state.
Methods. In order to study the parsec-scale structure of the source, we performed three epochs of very-long-baseline interferometry (VLBI) follow-up observations with the Very Long Baseline Array (VLBA) supplemented with the Effelsberg 100-m Telescope at 15, 22, and 43 GHz, which corresponds to 80, 117, and 228 GHz in the rest frame of TXS 1508+572. In addition, one 86 GHz (456 GHz) measurement was performed by the VLBA and the Green Bank Telescope during the first epoch.
Results. We present total intensity images from our multi-wavelength VLBI monitoring that reveal significant morphological changes in the parsec-scale structure of TXS 1508+572. The jet proper motion values range from 0.12 mas yr^{-1} to 0.27 mas yr^{-1}, which corresponds to apparent superluminal motion $\beta_{\rm app} \approx 14.3-32.2\,c$. This is consistent with the high Lorentz factors inferred from the spectral energy distribution (SED) modeling for this source. The core shift measurement reveals no significant impact by the high-energy flare on the distance of the 43-GHz radio core with respect to the central engine, that means this region is probably not affected by e.g., injection of new plasma as seen in other well-studied sources like CTA 102. We determine the average distance from the 43-GHz radio core to the central supermassive black hole to be 46.1 ± 2.3 µas, that corresponds to a projected distance of 0.32 ± 0.02 pc. We estimate the equipartition magnetic field strength 1 pc from the central engine to be on the order of 1.8 G, and the non-equipartition magnetic field strength at the same distance to be about 257 G, the former of which values agrees well with the magnetic field strength measured in low to intermediate redshift AGN.
Conclusions. Based on our VLBI analysis, we propose that the γ-ray activity observed in February 2022 is caused by a shock-shock interaction between the jet of TXS 1508+572 and new plasma flowing through this component. Similar phenomena have been observed, for example, in CTA 102 in a shock-shock interaction between a stationary and newly emerging component. In this case, however, the core region was also affected by the flare as the core shift stays consistent throughout the observations.

Key words. techniques: high angular resolution – techniques: interferometric – galaxies: active – galaxies: jets – radio continuum: galaxies

1. Introduction

Blazars, a subclass of radio-loud active galactic nuclei (AGN) whose jets point toward the observer (Urry & Padovani 1995), are among the most luminous objects in the Universe. They emit radiation throughout the whole electromagnetic spectrum, and their spectral energy distribution (SED) shows a double-humped structure (Padovani & Giommi 1995). In leptonic models, the low-energy hump, stretching from the radio to the ultraviolet, and sometimes even to the X-ray band, arises from synchrotron and the high-energy hump (X-rays to γ-rays) originates from inverse Compton scattering (IC). Depending on the origin of

the seed photon field, the IC process can be either synchrotron self-Compton (SSC) or external Compton (EC) with seed photons from the broad-line region and/or the dusty torus. Alternatively, hadronic models (e.g., proton synchrotron) can also be responsible for the high-energy emission (e.g., Aharonian 2002; Böttcher et al. 2013). High-redshift blazars that existed when the Universe was only ∼1 Gyr old already harbored supermassive black holes (SMBHs, $M_{\rm BH} \geq 10^9\,M_\odot$) in their central engines (Bloemen et al. 1995; Ghisellini et al. 2010). However, it is not yet clear how these objects could have formed so early in the Universe, but studies by Jolley & Kuncic (2008) and Ghisellini et al. (2013) suggest that AGN feedback can boost accretion onto the central engine and accelerate black hole growth. Thus, investigating the properties of high-redshift blazars can help us to better understand SMBH and AGN evolution, as well as the intricacies of AGN feedback on their host galaxies (Volonteri 2010).

Blazars are the most abundant sources on the extragalactic γ-ray sky. While over half of the 5064 sources contained in the fourth catalog of the *Fermi* Large Area Telescope (LAT, Atwood et al. 2009) are blazars, only 33 of these sources are categorized as high redshift objects ($z > 2.5$ cutoff set by the LAT, Abdollahi et al. 2020). However, most of these high-redshift sources can only be detected by the LAT during flaring states (Paliya et al. 2019; Kreter et al. 2020), otherwise their steeply falling spectra prevent their detection at low states in the GeV energy range. This complicates obtaining quasi-simultaneous multi-wavelength observational data for studies of their broadband emission. The only example of such a quasi-simultaneous study to date is the case of the intermediate-redshift object TXS 0536+145 at $z = 2.69$ (Orienti et al. 2014).

TXS 1508+572 (also called GB6 B1508+5714, J1510+5702) is a high-redshift blazar at $z = 4.31$ (Hook et al. 1995; Schneider et al. 2007). On kiloparsec scales, the source shows a double-sided jet structure (Kappes et al. 2022) in the east-west direction. The first very-long-baseline interferometry (VLBI) image of TXS 1508+572 was published by Frey et al. (1997), and the resulting 5 GHz map shows an unresolved source structure with the synthesized beam of ∼5 mas. However, global VLBI observations at 5 and 8.4 GHz revealed an optically thin jet component at 5 GHz and 8.4 GHz about 2 mas south of the core (O'Sullivan et al. 2011). The AstroGeo Database[1] provides 8.7 GHz images of the source with a compact core-jet morphology and the jet oriented toward southwest. Kinematic analysis based on 4 years of 8.6 GHz observations reveals a jet proper motion of 0.117 ± 0.078 mas yr^{-1} (Titov et al. 2023).

A strong γ-ray flare was detected in TXS 1508+572 on 2022 February 4 (Gokus et al. 2022) with a γ-ray monitoring program following the high-z blazar detection method described in Kreter et al. (2020). We have started a multi-frequency campaign across the electromagnetic spectrum to follow up this event with quasi-simultaneous observations (see Paper I, Gokus et al. 2024). Since γ-ray observations lack the resolution required for determining the origin of the activity, we have initiated a multi-frequency VLBI monitoring to capture the evolution of the source morphology and, possibly, relate VLBI structural components to the observed high-energy activity. To the best of our knowledge, such an immediate follow-up observing campaign has never been carried before for any blazar at such a high redshift.

In Sect. 2 we describe VLBI observations aimed to trace the source's morphological evolution during its high state. Section 3 describes the analysis of the observing data. Our results are discussed in Sect. 4, and we summarize our findings in Sect. 5. In this work we assume a ΛCDM cosmology with $H_0 = 70.7\,{\rm km\,s^{-1}\,Mpc^{-1}}$, $\Omega_\Lambda = 0.73$, and $\Omega_{\rm M} = 0.27$ (Salvatelli et al. 2013). At the redshift of $z = 4.31$, this corresponds to a scale of 6.9 pc mas^{-1}, and a luminosity distance of $D_{\rm L} \approx 40$ Gpc.

2. Observations and data reduction

To correlate the γ-ray activity with possible parsec-scale morphological changes in TXS 1508+572, we requested three Very Long Baseline Array (VLBA) and Effelsberg observations at 15, 22, and 43 GHz, as well as an additional observation with the VLBA and the Green Bank Telescope (GBT) at 86 GHz (PIs: A. Gokus, M. Lisakov, project code: BG281).

Observations are summarized in Table 1. The correlation was carried out using the VLBA DiFX correlator (Deller et al. 2007, 2011), in 4 subbands (intermediate frequencies or IFs) and two circular polarizations, each with 256 spectral channels and a bandwidth of 128 MHz. The integration time was 0.5 s for the 86 GHz observations and 1 s for all other observations. The source 1803+784 was used as a fringe finder calibrator in all experiments.

We performed the calibration according to the standard recipes in the Astronomical Image Processing Software (`AIPS`, Greisen 2003). After loading the data to `AIPS` using `FITLD`, we applied parallactic angle and digital sampling corrections. Amplitude calibration was performed based on the system noise temperature and elevation dependent gain curves provided by the stations. Opacity corrections were also applied at this step based on the weather information recorded at each antenna site. We used `FRING` to determine phase delay and rate solutions, and applied them both to the calibrator and target using `CLCAL`. It is worthwhile to highlight the importance of the GBT in the 86-GHz observation, because sufficiently high signal-to-noise ratio (S/N) fringe detections ($S/N > 5$) were only found on GBT baselines. These solutions were applied to the data and the fringe fit was repeated setting delay and rate windows of 200 ns and 200 mHz, and lowering the S/N cutoff to 3.7.

We corrected the flux density scale based on the quasi-simultaneous single-dish observations at 20, 14, and 7 mm of TXS 1508+572 with the Effelsberg 100-m telescope[2] (see Fig. 1). Observations and data reduction was carried out as described in Eppel et al. (2024). The data was then averaged in frequency with `SPLIT` and written out for imaging.

Hybrid imaging was performed in `Difmap` (Shepherd 1997) with iterating `clean` and phase and amplitude self-calibration with decreasing solution interval ranging from 180 to 1 min. Due to the low quality of the 86-GHz data (see Fig. 2), the imaging was carried out in two ways: assuming the same source structure as seen at lower frequencies, that is loading the 43-GHz clean windows to image the 86-GHz data; and assuming a core-dominated source. The latter yields a better map, because we do not detect any significant emission at the location of the 43-GHz jet component. Resulting maps are displayed in Figs. 3 and 4 and their properties are tabulated in Table A.1.

[1] http://astrogeo.org/vlbi_images/

[2] The data is available at: https://telamon.astro.uni-wuerzburg.de/

Table 1. Summary of our VLBI observations.

Epoch	Array [a]	Frequencies [GHz]	Comments
2022.24	VLBA+Effelsberg	15, 22, 43	Pt only recorded RCP
2022.24	VLBA+GBT	86	Pt only recorded RCP
2022.67	VLBA+Effelsberg	15, 22, 43	No Kp
2023.05	VLBA+Effelsberg	15, 22, 43	No Hn, Kp

Notes. [a]Antenna names: Br – Brewster, Eb – Effelsberg, Fd – Fort Davis, Hn – Hancock, Kp – Kitt Peak, La – Los Alamos, Mk – Mauna Kea, Nl – North Liberty, Ov – Ovens Valley, Pt – Pie Town, Sc – Saint Croix, GBT – Green Bank Telescope.

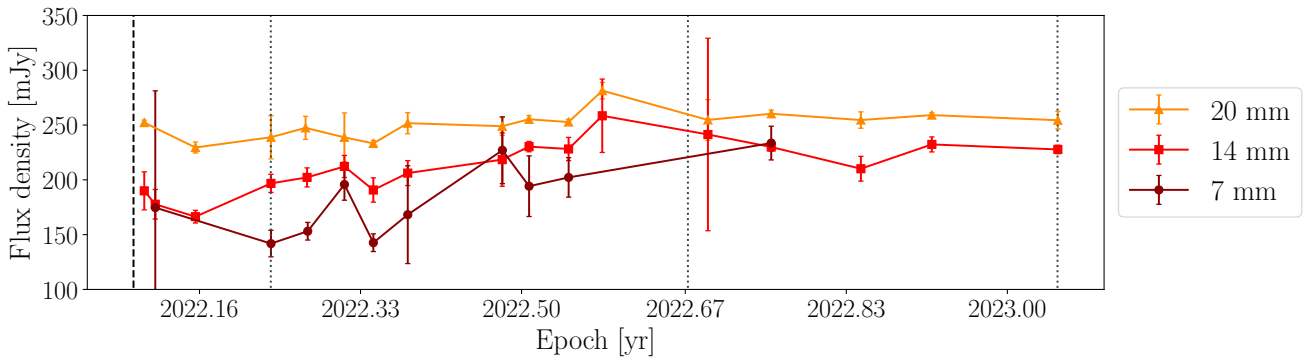

Fig. 1. Radio light curve of TXS 1508+572 observed with the Effelsberg 100-m telescope after the γ-ray flare (dashed black line). The VLBI observations are marked with black dotted lines.

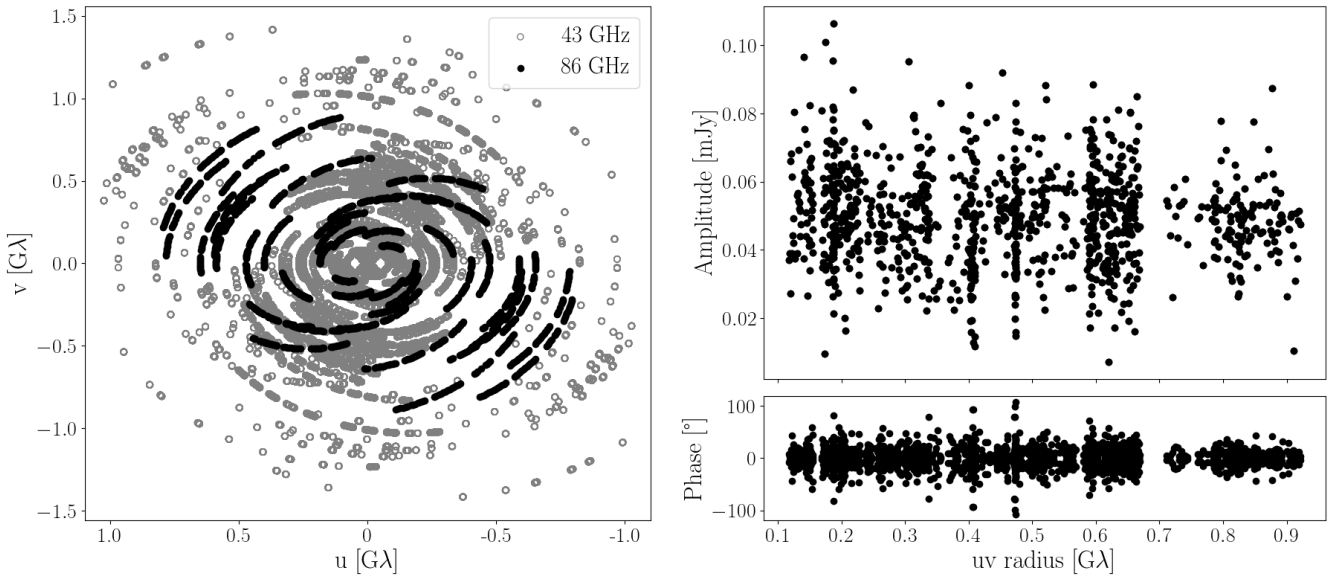

Fig. 2. Left panel: (u, v) coverage of the 43-GHz VLBA and EF (grey) and the 86-GHz VLBA and GBT (black) observations, plotting the fringe detections. Right panel: self-calibrated amplitude and phase of the 86-GHz data set.

3. Data analysis

3.1. Model fitting of individual source components

To be able to track individual components, as well as their brightness and kinematic evolution, we modeled the source structure with delta and elliptical Gaussian components using the `modelfit` command in `Difmap` (see Table A.2). The source is usually well modeled with four components representing the core, two jet components, and the lobe. To measure the jet components' proper motion, μ, we calculated the angular separation between the core and jet components and fitted the obtained values using linear regression. Results from our kinematic measurements are shown in Fig. 5. The obtained values of proper motion are $\mu_{15,C1} = 0.19 \pm 0.12\,\mathrm{mas\,yr^{-1}}$, $\mu_{15,C2} = 0.27 \pm 0.16\,\mathrm{mas\,yr^{-1}}$, $\mu_{22,C1} = 0.20 \pm 0.09\,\mathrm{mas\,yr^{-1}}$, $\mu_{22,C2} = 0.21 \pm 0.10\,\mathrm{mas\,yr^{-1}}$, $\mu_{43,C1} = 0.12 \pm 0.20$, and $\mu_{43,C2} = 0.15 \pm 0.29\,\mathrm{mas\,yr^{-1}}$ at 15, 22, and 43 GHz, respectively. These values are somewhat higher than the value $\mu_8 = 0.117 \pm 0.078\,\mathrm{mas\,yr^{-1}}$ from Titov et al. (2023) based on observations at 8 GHz (see Sect. 4.2). In Appendix B we discuss the multi-frequency kinematic analysis of the two jet components.

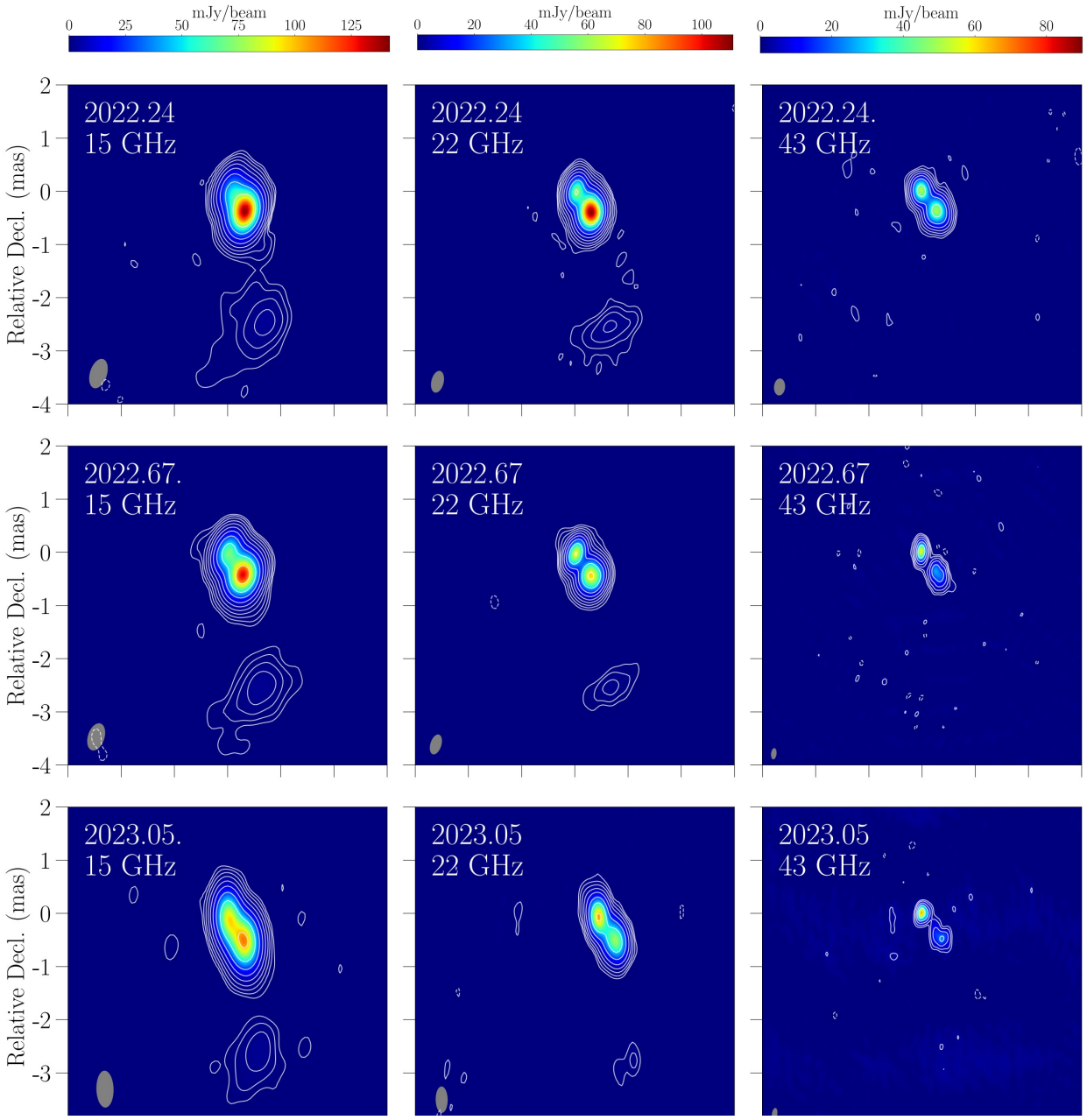

Fig. 3. Clean images of TXS 1508+572 at 15, 22, and 43 GHz. The observations were carried out in 2022 March, September, and in 2023 January (see Table 1). Image properties are summarized in Table A.1. Contours and colors represent the brightness distribution of the parsec-scale structure of the object. The images are aligned based on the core shift measurement.

We calculated the brightness temperature in the source frame, $T_{\rm b,obs}$, the following way:

$$T_{\rm b,obs}\,[{\rm K}] = 1.22\times10^{12}\left(\frac{S_\nu}{\rm Jy}\right)\left(\frac{\nu}{\rm GHz}\right)^{-2}\left(\frac{b_{\rm comp}}{\rm mas}\right)^{-2}(1+z), \quad (1)$$

where S_ν is the flux density of the components, ν is the observing frequency and $b_{\rm comp}$ is the size (full width at half maximum, FWHM) of the component. If a component is not resolved according to the resolution limit calculated based on Eq. (2) from Kovalev et al. (2005), we give an upper limit on the component size, and calculate a lower limit for $T_{\rm b,obs}$. These values are listed in Table A.2. Taking Doppler boosting into account with a Doppler factor of $\delta \approx 20$, all values are below the equipartition brightness temperature of $T_{\rm eq} \approx 5\times10^{10}$ K (Readhead 1994).

3.2. Spectral index maps and core shift measurements

To create spectral index maps, we re-mapped the image pairs in order for them to have a similar (u, v) range, pixel size, and restoring beam size. Images were then aligned on the optically thin jet components using 2D cross-correlation. Spectral index maps are displayed in Fig. A.2, and spectra of the core and jet components are shown in Fig. A.1. In the Blandford–Königl jet model (Blandford & Königl 1979), the VLBI core represents the $\tau = 1$ optical depth to synchrotron radiation, whose geometry is frequency dependent. As a result of this, higher frequency observations probe the regions closer to the central engine, and one can extrapolate the location of the SMBH based on the relative frequency-dependent shifts of the optically thick core determined from pairs of images at different frequencies

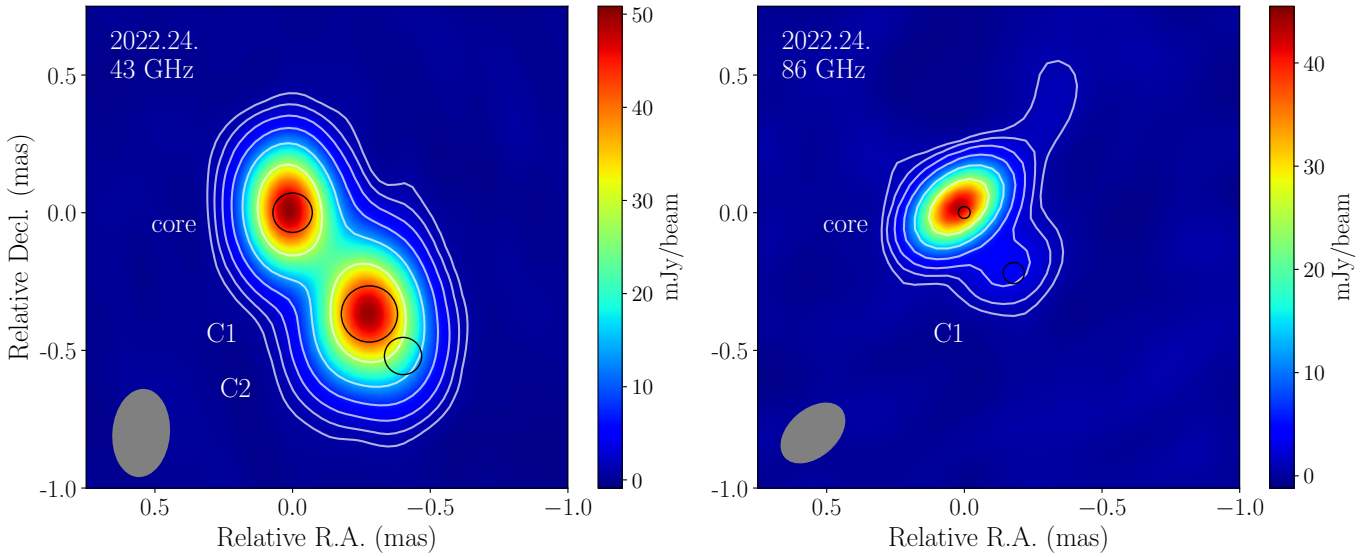

Fig. 4. 43 and 86 GHz image of TXS 1508+572 observed with the VLBA+EF (43 GHz, left) and VLBA+GBT (86 GHz, right). Lowest contours are at 0.53 and 1.37 mJy beam^{-1}, and increase as a factor of two. Positions of the `modelfit` components are overlaid as black circles.

(Marcaide & Shapiro 1984; Lobanov 1998). For our analysis, we use the 43 GHz core as a reference. Our core shift measurement is carried out the same way as described in Pushkarev et al. (2012), aligning the images using the shifts obtained from 2D cross-correlation, and measuring the difference between the core positions of consecutive frequency pairs. The alignment error was assumed to be half of the pixel size of a given frequency pair, and the core position errors were estimated based on the χ^2 minimization method described in Lampton et al. (1976). Under the assumption of equipartition, conserved magnetic flux, as well as that both the particle density and the magnetic field decrease with the distance from the central engine (Lobanov 1998), we can then measure the apparent distance between the VLBI core and the jet apex as:

$$\Delta r_{\rm core}\,[\mu{\rm as}] = r_0\left[\left(\frac{\nu}{43\,{\rm GHz}}\right)^{-1/k_{\rm r}} - 1\right], \tag{2}$$

where r_0 is the distance between the jet apex and the 43 GHz core. $k_{\rm r} = 1$ corresponds to a conical jet width profile. The results of our core shift analysis are shown in Fig. 6.

Based on the core shift measurement, we estimate the magnetic field strength using the methods described in Lobanov (1998), Hirotani (2005), Zdziarski et al. (2015) and Lisakov et al. (2017). First, we calculate $\Omega_{{\rm r},\nu}$, the shift in parsec per unit $1/\nu$ difference:

$$\Omega_{{\rm r}\nu}[{\rm pc\,GHz^{k_r}}] = 4.85\times10^{-9}\frac{\Delta r_{\rm core} D_{\rm L}}{(1+z)^2}\frac{\nu_1^{1/k_{\rm r}}\nu_2^{1/k_{\rm r}}}{\nu_2^{1/k_{\rm r}}-\nu_1^{1/k_{\rm r}}}, \tag{3}$$

where $\Delta r_{\rm core}$ is the core shift between frequencies ν_1 and ν_2. To derive an upper limit on the magnetic field strength, we calculate the core shift and $\Omega_{{\rm r}\nu}$ between 15 and 43 GHz.

The magnetic field strength 1 pc from the jet apex under the equipartition assumption is calculated as (Zdziarski et al. 2015):

$$B^{\rm eq}_{1\,{\rm pc}}[{\rm G}] \approx 0.025\left[\frac{\Omega_{r\nu}^{3k_{\rm r}}(1+z)^3}{\delta^2\phi\sin^{3k_{\rm r}-1}\theta}\right]^{\frac{1}{4}}, \tag{4}$$

where ϕ is the intrinsic opening angle and θ is the viewing angle. For the viewing angle we adopted the same value as the one used for the SED fit in Paper I, $\theta = 1/20$ rad. We calculated the apparent half opening angle based on the size of the `modelfit` components as $\phi_{\rm app} = \arctan[(b_{\rm jet} - b_{\rm core})/d]$, which are the sizes of the jet, $b_{\rm jet}$, and core components, $b_{\rm core}$, and the distance between these components, d. We did this for all observations and adopted $\phi_{\rm app}$ as the average of these values, $(9 \pm 2)^\circ$. The intrinsic full opening angle was calculated as $\phi = 2\arctan(\tan\phi_{\rm app}\sin\theta)$, which is $(0.9 \pm 0.2)^\circ$.

We also calculate the magnetic field strength 1 pc from the central SMBH, without assuming equipartition (Zdziarski et al. 2015):

$$B^{\rm non-eq}_{1\,{\rm pc}}[{\rm G}] \approx \frac{3.35\times10^{-11}\,D_{\rm L}\Delta r_{\rm core}\delta\tan\phi}{(\nu_1^{-1}-\nu_2^{-1})^5[(1+z)\sin\theta]^3F_\nu^2}, \tag{5}$$

where F_ν is the flux density in the flat part of the spectrum.

The equipartition magnetic field strengths, $B^{\rm eq}_{1\,{\rm pc}}$, derived for the three considered epochs are the following: 1.91 ± 0.11 G, 1.57 ± 0.17 G, and 1.79 ± 0.16 G. The $B^{\rm non-eq}_{1\,{\rm pc}}$ values for the same epochs are 324.7 ± 156.3 G, 104.9 ± 82.7 G, and 341.9 ± 225.2 G, respectively.

In order to compare $B^{\rm eq}$ to that of M 87 on horizon scales (Event Horizon Telescope Collaboration 2021), we extrapolate the average $B^{\rm eq,aver} = 0.79 \pm 0.04$ G to 5 $r_{\rm g}$ or 0.0036 pc projected distance. The gravitational radius is calculated as $r_{\rm g} = GM_{\rm BH}/c^2$, where G is the gravitational constant and $M_{\rm BH}$ is the black hole mass assumed to be $1.5\times10^{10}\,M_\odot$ based on the SED fit parameters in Gokus et al. (2024). We measure $B^{\rm eq}_{5\,r_{\rm g}} = 487.4 \pm 33.0$ G, that is significantly larger than the $B \sim 1$–30 G reported for M 87 (Event Horizon Telescope Collaboration 2021).

4. Discussion

4.1. Change in source morphology related to the γ-ray flare

Our VLBI observing campaign on TXS 1508+572 started after the detection of a bright γ-ray flare on 2022 February 4. Our observations at 15, 22, and 43 GHz correspond to 80, 117, and 228 GHz in the rest frame of the source

given its redshift $z = 4.3$. Our observation at 86 GHz (456 GHz in the rest frame of the object) carried out with the VLBA and the GBT reaches frequency ranges similar to what is currently available with the Event Horizon Telescope (Event Horizon Telescope Collaboration 2019). At these observing frequencies we expect to probe the jet components in the optically thin regime.

Hybrid images from our multi-frequency observations are shown in Fig. 3. We identify the core to be the northeastern component, as it has a flat spectrum (see Fig. A.2), and it is more compact than the southwestern jet component (Table A.2). We denote the southernmost faint, diffuse component as the lobe. Its position coincides with the jet detected at 8.6 GHz by Titov et al. (2023), and it is most likely the remnant of previous activity of the blazar. 1.7 and 4.8-GHz very high resolution *RadioAstron* space VLBI observations reveal a similar source structure to what we observe in our images (L. I. Gurvits, priv. comm.). The 43 and 86 GHz images of TXS 1508+572 show only a compact core-jet morphology. Comparing the structure seen at 144 MHz with LOFAR (Kappes et al. 2022) and at 1.4 GHz with the VLA (Cheung 2004) to our high-frequency images, we note a difference in the jet orientation on kiloparsec and parsec scales. This projection effect, when the intrinsic bending of the jet is amplified via beaming, is commonly seen in AGN (Pearson & Readhead 1988; Conway & Murphy 1993).

4.2. Kinematics at high redshifts

While VLBI observations can measure intrinsic characteristics and kinematic properties of AGN jets, investigating high-redshift sources is challenging due to several reasons. As a result of their Doppler-boosted emission, blazars with compact core-jet structures tend to dominate flux limited AGN samples at any given redshift. In the case of AGN oriented at large angles to our line of sight, however, the steep-spectrum jet emission is too weak to be detected at high rest frame frequencies (Gurvits 2000). In addition, due to the time dilation caused by the expansion of the Universe, component movements are visible only on longer time intervals. The first jet proper motion measurements at $z > 5$ were performed by Frey et al. (2015) with the cadence of 7 yr or 1.17 yr in the rest frame of the target, J1026+2542. While high-redshift AGN are being targeted by VLBI observations more frequently (Krezinger et al. 2022, and references therein), kinematic analysis is only available for a small subset of them (Frey et al. 1997; Veres et al. 2010; Frey et al. 2015; Perger et al. 2018; An et al. 2020; Zhang et al. 2020, 2022; Gabányi et al. 2023; Gurvits et al. 2023, and references therein). Expanding this sample is crucial to widen our knowledge on the evolution of black hole jets. Kinematic analysis enable us to measure the bulk Lorentz factor and Doppler boosting factors, as well as the jet viewing angle. In addition, these observational data can be used to constrain SED model parameters (see Paper I), and can also be compared with the characteristics of local AGN. While high-redshift sources show only mildly relativistic apparent speeds (An et al. 2022), AGN in the local Universe exhibit a much wider range of jet speeds, and often show superluminal motion (Lister et al. 2021).

The follow-up of the flaring activity in TXS 1508+572 spans 0.82 yr (0.15 yr at $z = 4.31$), and reveals morphological changes on monthly timescales. This is most evident at 43 GHz, where the compact jet (southwest component in Fig. 3) observed at 2022.24 becomes fainter and more diffuse with time. Such changes on short timescales after a high-energy flare were not observed in high-redshift sources thus far. The results from our kinematic analysis, based on the `modelfit` parameters of the jet components in the three epochs of observations are shown in Fig. 5. The measured jet speeds ranging between $\mu = 0.12$ and $\mu = 0.27$ mas yr^{-1} correspond to apparent superluminal speeds of $\beta_{\rm app} \approx 14.3{-}32.2\,c$, where $\beta_{\rm app} = \mu D_{\rm L}/(1+z)$ is measured in the units of c. These jet speeds are higher than the value of $\mu_8 = 0.117 \pm 0.078$ mas yr^{-1} presented in Titov et al. (2023) based on 8-GHz observations between 2017 and 2021. The discrepancy between the two kinematic measurements can be explained not only by the different time range and frequency coverage, but essentially by the fact that our and the cited kinematic estimates by Titov et al. (2023) involve different structural components. Due to opacity effects (see Sect. 4.3) and a higher angular resolution achieved in our higher frequency observations, we detect innermost components not distinguishable at 8 GHz. The position of the jet component identified in Titov et al. (2023) corresponds to the lobe component in our observations. It is therefore not surprising that the diffuse southern component at about 2 mas from the core demonstrated a lower apparent velocity in the study by Titov et al. (2023) even if the jet did not change its orientation along the stream relative to the line of sight. However, the inner jet and the diffuse lobe might also be oriented at different angles to the line of sight, resulting in a different apparent speed.

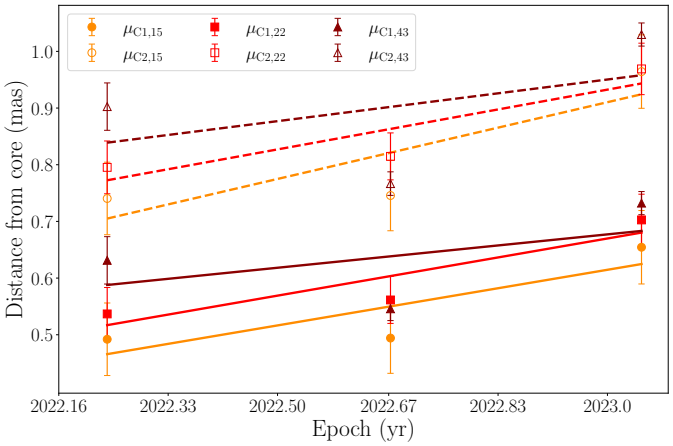

Fig. 5. Kinematics of the jet component at 15 (orange circles), 22 (red squares), and 43 GHz (dark red triangles) following the γ-ray flare. Jet speeds are listed in the text in Sect. 3. The positional errors are assumed to be one fifth of the beam minor axis. Note the systematic offset of the position of both jet components at the higher frequencies, which is roughly consistent with the core shift determined in Sect. 4.3.

Our kinematic measurement is consistent with the high Lorentz factor of $\Gamma = 11$ obtained from modeling the SED during a quiescent state of TXS 1508+572 (Ackermann et al. 2017), as well as a Lorentz factor of 20 used to model the source during the flaring state in our Paper I. Brightness temperatures on the order of $10^9{-}10^{12}$ K (see Table A.2 and the lower panel of Fig. A.1) also suggest Doppler-boosted emission. These values measured at high rest frame frequencies are comparable to the ones measured by *RadioAstron*, $(5.15 \pm 2.1) \times 10^{10}$ K at 1.67 GHz and $(2.15 \pm 3.3) \times 10^{12}$ at 4.84 GHz, at extremely high angular resolution (L. I. Gurvits, priv. comm.). In addition, apparent motion values agree well with expectations for high-redshift AGN based on the apparent proper-motion-redshift ($\mu{-}z$) relation (Cohen et al. 1988; Vermeulen & Cohen 1994; Kellermann et al. 1999; Frey et al. 2015; Zhang et al. 2022). Comparing our measurements to the ($\mu{-}z$) relation based on

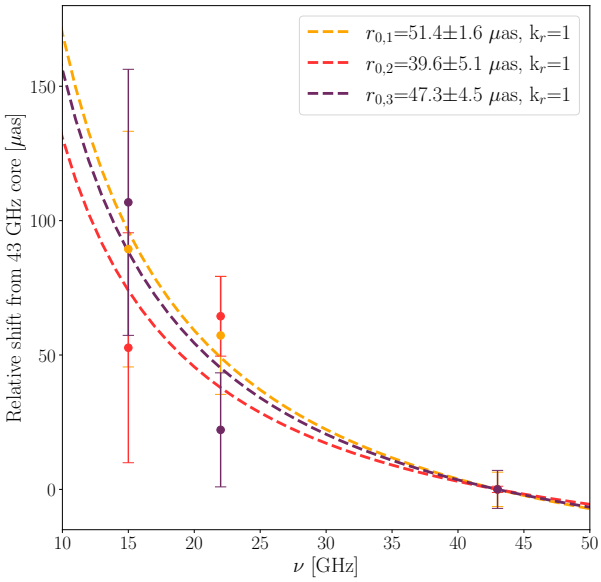

Fig. 6. Evolution of the core shift measured throughout the first (gold), second (red), and third (purple) VLBI epochs. The distance to the jet apex (r_0) is shown in the legend for each of the three epochs.

≤15 GHz VLBI data in Fig. 2 of Zhang et al. (2022), we find that all our jet proper motion values are consistent within the error bars with maximum apparent velocities assuming $\Gamma = 20$. However, proper motion measurements in the $z = 4.33$ (Péroux et al. 2001) quasar J2134−0419 reveal a significantly slower jet speed of $\mu = 0.035 \pm 0.023$ mas yr^{-1} at 5 GHz. The difference, again, might be explained with the different observing frequencies, or with the high state during which TXS 1508+572 was observed, while J2134−0419 shows no clear signs of flux density variability in the period studied.

Based on a simple linear fit to the distance from the radio core to the C1 and C2 components, we suggest that the ejection of the jet components fell around ~2016−2019. Indeed, the source showed an elevated state in the GeV range and was detected with about 3σ significance during 2018−2020. As a result of this, we suggest that the jet was not ejected during the current flaring activity. This, together with the cross-identification of the jet component in Titov et al. (2023) to the lobe component in our images, we suggest that the 8-GHz jet was ejected at an earlier epoch than the inner jet detected in our observations, which could explain the discrepancy in the proper motion values.

We have identified both components C1 and C2 at all frequencies and we also have measured the relative position of the apparent cores at different frequencies. Using these measurements together we have produced a combined kinematic plot presented in Fig. B.1. These combined data support a non-linear relation. However, with only three epochs it is impossible to distinguish between such options as accelerated motion (Homan et al. 2015; Weaver et al. 2022) and moving of the apparent jet base (Niinuma et al. 2015; Lisakov et al. 2017; Plavin et al. 2019).

One argument for the latter option comes from the coordinated motion of components C1 and C2, that is they both appear closer to the apparent core at the second epoch. At the same time, these two components are casually disconnected, since they are located tens of parsecs away from each other and unlikely experience the same variation of their apparent velocity simultaneously. It brings us to a conclusion, that the reference point, that is the apparent core, might be moving itself. Such movement, indeed, is expected for the apparent core if denser plasma is flowing through it.

In this case, the second epoch might showcase the apparent core to be located more downstream, which made the distance to components C1 and C2 shorter. This can be explained by an increase of plasma density in the jet in 2022.67, possibly associated with the preceding γ-ray flare.

4.3. Core shift evolution

The core shift measurements alone (see Fig. 6), described in Sect. 3.2, reveal no significant evolution in the distance to the jet apex subsequent to the high-energy flare. Our fits are consistent with a conical jet profile. The average distance of the 43-GHz core to the central engine is 46.1 ± 2.3 μas corresponding to a projected distance of 0.32 ± 0.02 pc (see Fig. 7). However, if we consider the core shift measurements together with the kinematics presented in Sect. 4.2, we see a coherent picture regarding the second epoch. Displacement of the apparent core not only affects single-frequency kinematics, but can also affect single-epoch core shift measurements. Indeed, since apparent cores at different frequencies are separated by several parsecs along the jet, a moving feature displaces them non-simultaneously and possibly by different amounts (Plavin et al. 2019). This behavior explains both kinematics and core shift measurements in a coherent manner. Unfortunately, large errors do not let us investigate this quantitatively.

Based on the core shift measurement, we derived the equipartition magnetic field strengths 1 pc from the SMBH (Zdziarski et al. 2015), which are 1.91 ± 0.11 G for the first, 1.57 ± 0.17 G for the second, and 1.79 ± 0.16 G for the third epoch. These magnetic field strengths are close to the ones derived for the MOJAVE sample (Pushkarev et al. 2012) and by Zamaninasab et al. (2014) for AGN below redshift 2.43 and 2.37, respectively. Non-equipartition magnetic field strengths 1 pc from the SMBH are 324.7 ± 156.3 G, 104.9 ± 82.7 G, and 341.9 ± 225.2 G for the first, second, and third epochs, respectively. Extrapolating the average $B^{\rm eq}_{\rm 1\,pc}$ to $5\,r_{\rm g}$, we measure $B^{\rm eq}_{5\,r_{\rm g}} = 487.4 \pm 33.0$ G, a value significantly larger than the $B \sim 1-30$ G reported for M 87 on horizon scales (Event Horizon Telescope Collaboration 2021).

Brightness temperatures as a function of the projected distance from the core can identify the dominant energy loss mechanism leading to the flux decay of jet components (Lobanov & Zensus 1999; Jorstad et al. 2005; Burd et al. 2022). According to the shock-in-jet model described by Marscher & Gear (1985), where an adiabatically expanding shock travels downstream in the jet, the main evolutionary stages the component goes through are characterized by Compton, synchrotron and adiabatic losses. In this scenario, brightness temperatures decay as power-laws, $T_{\rm b,jet} \propto d^{-\epsilon}$, where d is the distance of the jet component from the core, and ϵ is the power-law index, as the shock moves further away from the core (Schinzel et al. 2012; Kravchenko et al. 2016). In the case of TXS 1508+572, jet brightness temperatures can be described with power-law indices of 3.1 ± 0.6 at 15 GHz, −0.3 ± 1.11 at 22 GHz, and −1.7 ± 0.3 at 43 GHz (see Fig. 8). $T_{\rm b}$ gradients derived for 28 sources at 43 GHz by Burd et al. (2022) range from −3.19 to −1.23, with an average of −2.07, so our 43-GHz power-law index is consistent with these values. This $T_{\rm b}$ gradient places the jet of TXS 1508+572 in the Compton loss stage. The

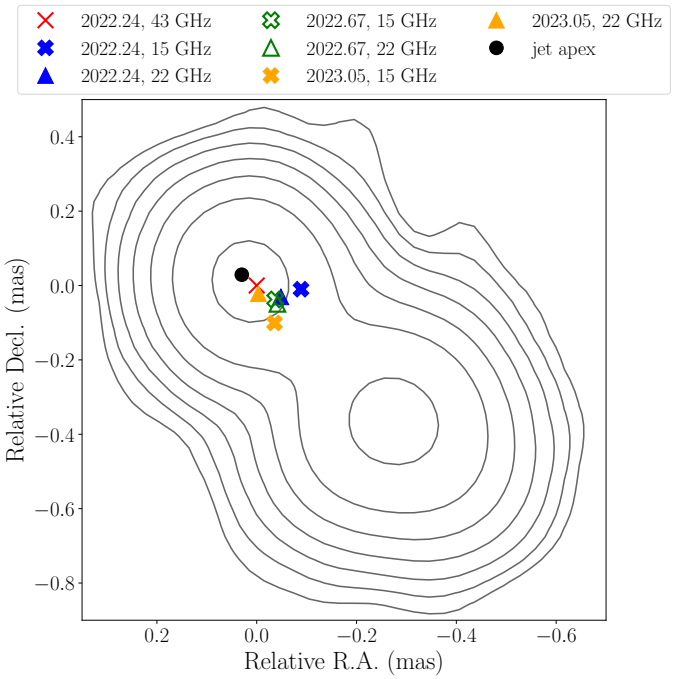

Fig. 7. Location of the radio core with respect to the 43-GHz one, overlaid on the 43-GHz map from the first observing epoch. Error bars are omitted for clarity. The average location to the central supermassive black hole is marked with a black dot.

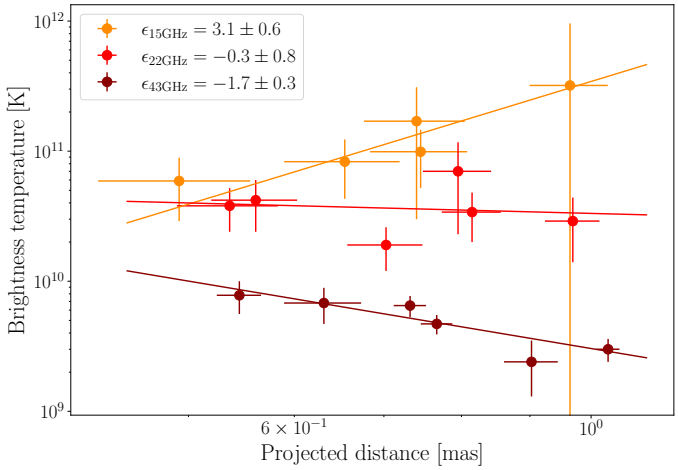

Fig. 8. Jet brightness temperature as a function of projected distance from the core. Solid lines represent power-law fits to the $T_{\mathrm{b,obs}}$ measurements at each frequency.

inverted and flat gradients at 15 and 22 GHz might be explained via the ongoing activity in the source. We suggest that the γ-ray activity observed in February 2022 is caused by a shock-shock interaction in the jet region of TXS 1508+572 and new plasma flowing through the C1 and C2 components. A similar phenomenon was observed in the blazar CTA 102 by Fromm et al. (2011) when a new shock wave traveled through a stationary recollimation shock.

5. Summary

After exhibiting a bright γ-ray flare, we started an intensive multi-wavelength follow-up campaign of the early-Universe blazar TXS 1508+572. To our knowledge, this is the first attempt at such observations of a flaring high-redshift AGN. While Paper I discusses the multi-wavelength properties of the source based on the quasi-simultaneous data we collected, here we focused on the VLBI observations included in our monitoring.

The present study of TXS 1508+572 extends our knowledge on the evolution of jet geometry and kinematics in high-redshift AGN. Our hybrid images reveal a compact core-jet structure on parsec scales (see Fig. 3). This morphology is affected by the γ-ray flare, as we recover changes in source structure and brightness on the timescale of months. Jet proper motion values of $0.12-0.27$ mas yr^{-1} are recovered, corresponding to superluminal speeds of $14.3-32.2\,c$. This result is comparable to the high Lorentz factors of 20 used to model the SED in Paper I, and is consistent with maximum apparent speeds assuming $\Gamma = 20$ in the $(\mu-z)$ relation for high-redshift AGN (Zhang et al. 2022). We trace back the ejection time of the jet component to be between 2016 and 2019, during which TXS 1508+572 was in an elevated state in the γ-rays. This means that the jet component was not ejected as a result of the high-energy flare in 2022 February.

Using our multi-frequency data, we measured the distance to the central engine based on the core shift. The distance to the jet apex stays consistent within the measurement errors throughout our observations. On average, the central engine is located 46.1 ± 2.3 µas or 0.32 ± 0.02 pc from the 43-GHz VLBI core. Under the equipartition assumption, which is supported by our brightness temperature measurements in the presence of Doppler boosting, we measure $B^{\mathrm{eq}}_{1\,\mathrm{pc}}$ of 1.91 ± 0.11 G, 1.57 ± 0.17 G, and 1.79 ± 0.16 G for the three epochs. Low to intermediate redshift AGN also exhibit similar values of $B^{\mathrm{eq}}_{1\,\mathrm{pc}}$ (Pushkarev et al. 2012; Zamaninasab et al. 2014). $B^{\mathrm{non-eq}}_{1\,\mathrm{pc}}$ values are significantly higher than this, with 324.7 ± 156.3 G, 104.9 ± 82.7 G, and 341.9 ± 225.2 G for the consecutive epochs.

We note that even though we do not observe any brightening in the jet that would be clearly associated with the γ-ray flare of 2022, there might be a traveling disturbance, such as a density enhancement, that was not emitting much at radio waves but affected the position of the apparent cores at different frequencies during the 2022.67 epoch. This scenario coherently explains our kinematics and core shift measurements. Based on our analysis, we propose that the activity was caused by a shock-shock interaction between the already existing jet component of TXS 1508+572 and new plasma flowing through this region.

Acknowledgements. The authors thank the anonymous referee for useful comments that helped to improve the manuscript. The data were obtained at VLBA within the proposal BG281. The National Radio Astronomy Observatory is a facility of the National Science Foundation operated under cooperative agreement by Associated Universities, Inc. This work made use of the Swinburne University of Technology software correlator, developed as part of the Australian Major National Research Facilities Programme and operated under license. This research was supported through a PhD grant from the International Max Planck Research School (IMPRS) for Astronomy and Astrophysics at the Universities of Bonn and Cologne. This publication is part of the M2FINDERS project which has received funding from the European Research Council (ERC) under the European Union's Horizon2020 Research and Innovation Programme (grant agreement No. 101018682). F.E., J.H., M.K., and F.R. acknowledge support from the Deutsche Forschungsgemeinschaft (DFG, grants 447572188, 434448349, 465409577).

References

Abdollahi, S., Acero, F., Ackermann, M., et al. 2020, ApJS, 247, 33
Ackermann, M., Ajello, M., Baldini, L., et al. 2017, ApJ, 837, L5

Aharonian, F. A. 2002, MNRAS, 332, 215
An, T., Mohan, P., Zhang, Y., et al. 2020, Nat. Commun., 11, 143
An, T., Wang, A., Zhang, Y., et al. 2022, MNRAS, 511, 4572
Atwood, W. B., Abdo, A. A., Ackermann, M., et al. 2009, ApJ, 697, 1071
Blandford, R. D., & Königl, A. 1979, ApJ, 232, 34
Bloemen, H., Bennett, K., Blom, J. J., et al. 1995, A&A, 293, L1
Böttcher, M., Reimer, A., Sweeney, K., et al. 2013, ApJ, 768, 54
Burd, P. R., Kadler, M., Mannheim, K., et al. 2022, A&A, 660, A1
Cheung, C. C. 2004, ApJ, 600, L23
Cohen, M. H., Barthel, P. D., Pearson, T. J., et al. 1988, ApJ, 329, 1
Conway, J. E., & Murphy, D. W. 1993, ApJ, 411, 89
Deller, A. T., Tingay, S. J., Bailes, M., et al. 2007, PASP, 119, 318
Deller, A. T., Brisken, W. F., Phillips, C. J., et al. 2011, PASP, 123, 275
Eppel, F., Kadler, M., Heßdörfer, J., et al. 2024, A&A, 684, A11
Event Horizon Telescope Collaboration (Akiyama, K., et al.) 2019, ApJ, 875, L1
Event Horizon Telescope Collaboration (Akiyama, K., et al.) 2021, ApJ, 910, L13
Frey, S., Gurvits, L. I., Kellermann, K. I., et al. 1997, A&A, 325, 511
Frey, S., Paragi, Z., Fogasy, J. O., et al. 2015, MNRAS, 446, 2921
Fromm, C. M., Perucho, M., Ros, E., et al. 2011, A&A, 531, A95
Gabányi, K. É., Belladitta, S., Frey, S., et al. 2023, PASA, 40, e004
Ghisellini, G., Della Ceca, R., Volonteri, M., et al. 2010, MNRAS, 405, 387
Ghisellini, G., Haardt, F., Della Ceca, R., et al. 2013, MNRAS, 432, 2818
Gokus, A., Kreter, M., Kadler, M., et al. 2022, ATel, 15202, 1
Gokus, A., Böttcher, M., Errando, M., et al. 2024, ApJ, Accepted [arXiv:2406.07635]
Greisen, E. W. 2003, Astrophys. Space Sci. Lib., 285, 109
Gurvits, L. I. 2000, Perspectives on Radio Astronomy: Science with Large Antenna Arrays, 183
Gurvits, L. I., Frey, S., Krezinger, M., et al. 2023, IAU Symp., 375, 86
Hirotani, K. 2005, ApJ, 619, 73
Homan, D. C., Kadler, M., Kellermann, K. I., et al. 2009, ApJ, 706, 1253
Homan, D. C., Lister, M. L., Kovalev, Y. Y., et al. 2015, ApJ, 798, 134
Hook, I. M., McMahon, R. G., Patnaik, A. R., et al. 1995, MNRAS, 273, L63
Jolley, E. J. D., & Kuncic, Z. 2008, MNRAS, 386, 989
Jorstad, S. G., Marscher, A. P., Lister, M. L., et al. 2005, AJ, 130, 1418
Kappes, A., Burd, P. R., Kadler, M., et al. 2022, A&A, 663, A44
Kellermann, K. I., Vermeulen, R. C., Zensus, J. A., et al. 1999, New Astron. Rev., 43, 757
Kovalev, Y. Y., Kellermann, K. I., Lister, M. L., et al. 2005, AJ, 130, 2473
Kravchenko, E. V., Kovalev, Y. Y., Hovatta, T., & Ramakrishnan, V. 2016, MNRAS, 462, 2747
Kreter, M., Gokus, A., Krauss, F., et al. 2020, ApJ, 903, 128
Krezinger, M., Perger, K., Gabányi, K. É., et al. 2022, ApJS, 260, 49
Lampton, M., Margon, B., & Bowyer, S. 1976, ApJ, 208, 177
Lisakov, M. M., Kovalev, Y. Y., Savolainen, T., et al. 2017, MNRAS, 468, 4478
Lister, M. L., Homan, D. C., Kellermann, K. I., et al. 2021, ApJ, 923, 30
Lobanov, A. P. 1998, A&A, 330, 79
Lobanov, A. P., & Zensus, J. A. 1999, ApJ, 521, 509
Marcaide, J. M., & Shapiro, I. I. 1984, ApJ, 276, 56
Marscher, A. P., & Gear, W. K. 1985, ApJ, 298, 114
Niinuma, K., Kino, M., Doi, A., et al. 2015, ApJ, 807, L14
Orienti, M., D'Ammando, F., Giroletti, M., et al. 2014, MNRAS, 444, 3040
O'Sullivan, S. P., Gabuzda, D. C., & Gurvits, L. I. 2011, MNRAS, 415, 3049
Padovani, P., & Giommi, P. 1995, ApJ, 444, 567
Paliya, V. S., Ajello, M., Ojha, R., et al. 2019, ApJ, 871, 211
Pearson, T. J., & Readhead, A. C. S. 1988, ApJ, 328, 114
Perger, K., Frey, S., Gabányi, K. É., et al. 2018, MNRAS, 477, 1065
Péroux, C., Storrie-Lombardi, L. J., McMahon, R. G., et al. 2001, AJ, 121, 1799
Plavin, A. V., Kovalev, Y. Y., Pushkarev, A. B., et al. 2019, MNRAS, 485, 1822
Pushkarev, A. B., Hovatta, T., Kovalev, Y. Y., et al. 2012, A&A, 545, A113
Readhead, A. C. S. 1994, ApJ, 426, 51
Salvatelli, V., Marchini, A., Lopez-Honorez, L., et al. 2013, Phys. Rev. D, 88, 023531
Schinzel, F. K., Lobanov, A. P., Taylor, G. B., et al. 2012, A&A, 537, A70
Schneider, D. P., Hall, P. B., Richards, G. T., et al. 2007, AJ, 134, 102
Shepherd, M. C. 1997, ASP Conf. Ser., 125, 77
Titov, O., Frey, S., Melnikov, A., et al. 2023, AJ, 165, 69
Urry, C. M., & Padovani, P. 1995, PASP, 107, 803
Veres, P., Frey, S., Paragi, Z., et al. 2010, A&A, 521, A6
Vermeulen, R. C., & Cohen, M. H. 1994, ApJ, 430, 467
Volonteri, M. 2010, A&ARv, 18, 279
Weaver, Z. R., Jorstad, S. G., Marscher, A. P., et al. 2022, ApJS, 260, 12
Zamaninasab, M., Clausen-Brown, E., Savolainen, T., et al. 2014, Nature, 510, 126
Zdziarski, A. A., Sikora, M., Pjanka, P., et al. 2015, MNRAS, 451, 927
Zhang, Y., An, T., & Frey, S. 2020, Sci. Bull., 65, 525
Zhang, Y., An, T., Frey, S., et al. 2022, ApJ, 937, 19

Appendix A: Additional figures and tables

Table A.1. Summary of image parameters.

Epoch	ν^a [GHz]	$S_{\rm tot}{}^b$ [mJy]	$S_{\rm peak}{}^c$ [mJy beam^{-1}]	σ^d [mJy beam^{-1}]	$I_{\rm low}{}^e$ [mJy beam^{-1}]	$b_{\rm maj}{}^f$ [mas]	$b_{\rm min}{}^g$ [mas]	PA^h [°]
2022.24	15	240.5	141.8	0.08	0.28	0.57	0.32	−18
	22	252.1	110.8	0.07	0.22	0.42	0.23	−13
	43	154.0	50.7	0.19	0.53	0.32	0.21	−5
	86	51.2	45.5	0.30	1.37	0.27	0.18	−49
2022.67	15	258.5	131.4	0.06	0.20	0.53	0.31	−18
	22	220.5	76.5	0.07	0.19	0.39	0.21	−17
	43	179.3	57.6	0.31	0.92	0.22	0.10	−6
2023.05	15	234.5	112.1	0.12	0.39	0.70	0.32	2
	22	192.6	84.4	0.19	0.59	0.50	0.23	1
	43	188.6	67.6	0.81	2.37	0.23	0.10	−9

Notes. [a]Observing frequency. [b]Total flux density. [c]Peak brightness. [d]Rms noise of the image. [e]Lowest contour level. [f]Beam major axis. [g]Beam minor axis. [h]Beam position angle.

Table A.2. Properties of `modelfit` components.

ν [GHz]^a	Component	Epoch	$S_{\rm comp}$ [mJy]^b	$b_{\rm maj}$ [mas]^c	$b_{\rm min}$ [mas]^d	$T_{\rm b}$ [K]^e
15	core	2022.24	38.6 ± 3.9	< 0.01	< 0.01	$> 1.2 \times 10^{13}$
		2022.67	72.8 ± 7.3	0.09 ± 0.06	0.09 ± 0.06	$(2.3 \pm 2.2) \times 10^{11}$
		2023.05	85.1 ± 8.5	0.05 ± 0.06	0.05 ± 0.06	$(1.1 \pm 2.1) \times 10^{12}$
	C1	2022.24	97.6 ± 9.8	0.32 ± 0.06	0.14 ± 0.06	$(5.9 \pm 3.0) \times 10^{10}$
		2022.67	49.4 ± 4.9	< 0.01	< 0.01	$> 2.0 \times 10^{13}$
		2023.05	116.1 ± 11.6	0.20 ± 0.06	0.20 ± 0.06	$(8.3 \pm 4.0) \times 10^{10}$
	C2	2022.24	94.7 ± 9.5	0.18 ± 0.06	0.09 ± 0.06	$(1.7 \pm 1.4) \times 10^{11}$
		2022.67	127.1 ± 12.7	0.19 ± 0.06	0.19 ± 0.06	$(9.9 \pm 4.7) \times 10^{10}$
		2023.05	24.6 ± 2.5	0.05 ± 0.06	0.05 ± 0.06	$(3.2 \pm 6.7) \times 10^{11}$
	lobe	2022.24	6.6 ± 0.7	0.38 ± 0.06	0.38 ± 0.06	$(1.2 \pm 0.3) \times 10^{9}$
		2022.67	6.7 ± 0.7	0.48 ± 0.06	0.48 ± 0.06	$(8.1 \pm 1.7) \times 10^{8}$
		2023.05	6.4 ± 0.6	0.60 ± 0.06	0.60 ± 0.06	$(4.8 \pm 1.0) \times 10^{8}$
22	core	2022.24	62.0 ± 6.2	0.07 ± 0.05	0.07 ± 0.05	$(1.4 \pm 1.3) \times 10^{11}$
		2022.67	81.7 ± 8.2	0.08 ± 0.04	0.08 ± 0.04	$(1.3 \pm 1.0) \times 10^{11}$
		2023.05	95.2 ± 9.5	0.10 ± 0.05	0.10 ± 0.05	$(1.1 \pm 0.7) \times 10^{11}$
	C1	2022.24	117.9 ± 11.8	0.25 ± 0.05	0.15 ± 0.05	$(3.8 \pm 1.4) \times 10^{10}$
		2022.67	70.1 ± 7.0	0.14 ± 0.04	0.14 ± 0.04	$(4.2 \pm 1.8) \times 10^{10}$
		2023.05	51.6 ± 5.2	0.18 ± 0.05	0.18 ± 0.05	$(1.9 \pm 0.7) \times 10^{10}$
	C2	2022.24	64.8 ± 6.5	0.13 ± 0.05	0.09 ± 0.05	$(7.0 \pm 4.7) \times 10^{10}$
		2022.67	63.8 ± 6.4	0.15 ± 0.04	0.15 ± 0.04	$(3.4 \pm 1.4) \times 10^{10}$
		2023.05	41.3 ± 4.1	0.13 ± 0.05	0.13 ± 0.05	$(2.9 \pm 1.5) \times 10^{10}$
	lobe	2022.24	6.3 ± 0.6	0.55 ± 0.05	0.55 ± 0.05	$(2.4 \pm 0.4) \times 10^{8}$
		2022.67	4.8 ± 0.5	0.51 ± 0.04	0.51 ± 0.04	$(2.2 \pm 0.3) \times 10^{8}$
		2023.05	8.0 ± 0.8	1.86 ± 0.05	1.86 ± 0.05	$(2.7 \pm 0.3) \times 10^{7}$
43	core	2022.24	67.6 ± 6.8	0.14 ± 0.04	0.14 ± 0.04	$(1.1 \pm 0.5) \times 10^{10}$
		2022.67	89.2 ± 8.9	0.09 ± 0.02	0.09 ± 0.02	$(3.7 \pm 1.2) \times 10^{10}$
		2023.05	82.2 ± 8.2	0.09 ± 0.02	0.09 ± 0.02	$(3.8 \pm 1.3) \times 10^{10}$
	C1	2022.24	77.3 ± 7.7	0.20 ± 0.04	0.19 ± 0.04	$(6.8 \pm 2.1) \times 10^{9}$
		2022.67	27.0 ± 2.7	0.11 ± 0.02	0.11 ± 0.02	$(7.8 \pm 2.2) \times 10^{9}$
		2023.05	59.4 ± 5.9	0.18 ± 0.02	0.18 ± 0.02	$(6.5 \pm 1.2) \times 10^{9}$
	C2	2022.24	11.7 ± 1.2	0.14 ± 0.04	0.13 ± 0.04	$(2.4 \pm 1.1) \times 10^{9}$
		2022.67	72.2 ± 7.2	0.23 ± 0.02	0.23 ± 0.02	$(4.7 \pm 0.8) \times 10^{9}$
		2023.05	22.45 ± 2.2	0.16 ± 0.02	0.16 ± 0.02	$(3.0 \pm 0.6) \times 10^{9}$
86	core	2022.24	47.7 ± 4.8	0.04 ± 0.04	0.04 ± 0.04	$(3.0 \pm 5.0) \times 10^{13}$
	C1	2022.24	4.7 ± 0.5	0.08 ± 0.04	0.08 ± 0.04	$(6.0 \pm 6.0) \times 10^{11}$

Notes. [a]Observing frequency. [b]Flux density. [c]Component major axis. [d]Component minor axis. [e]Brightness temperature corrected for redshift.

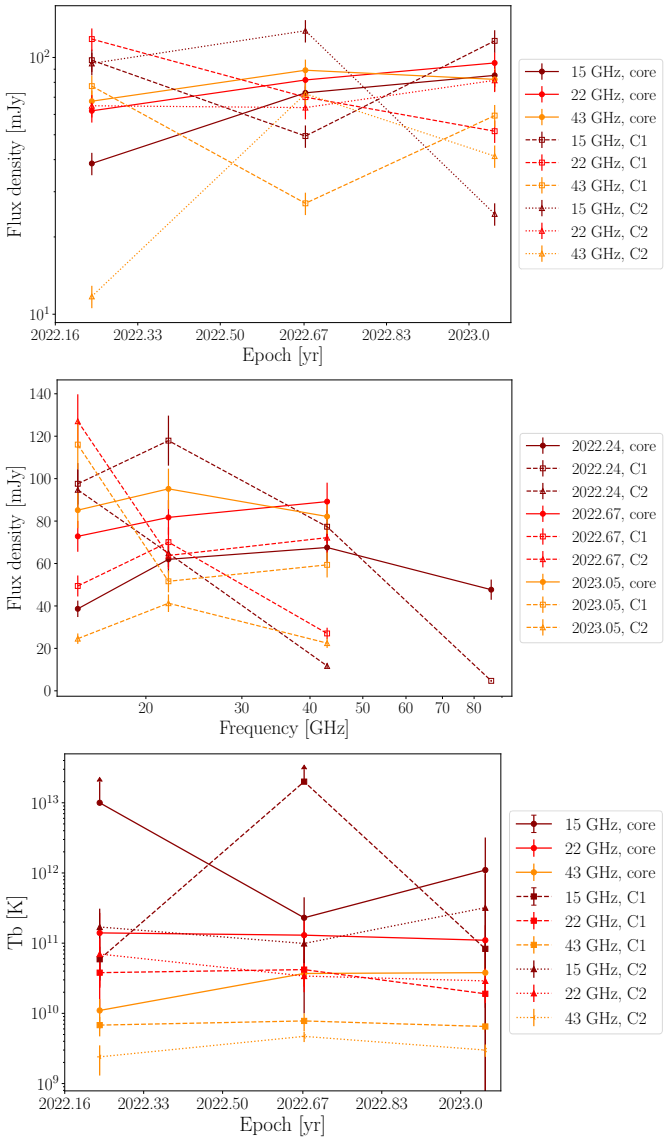

Fig. A.1. Light curves, spectra, and brightness temperatures of the core and jet components of TXS 1508+572.

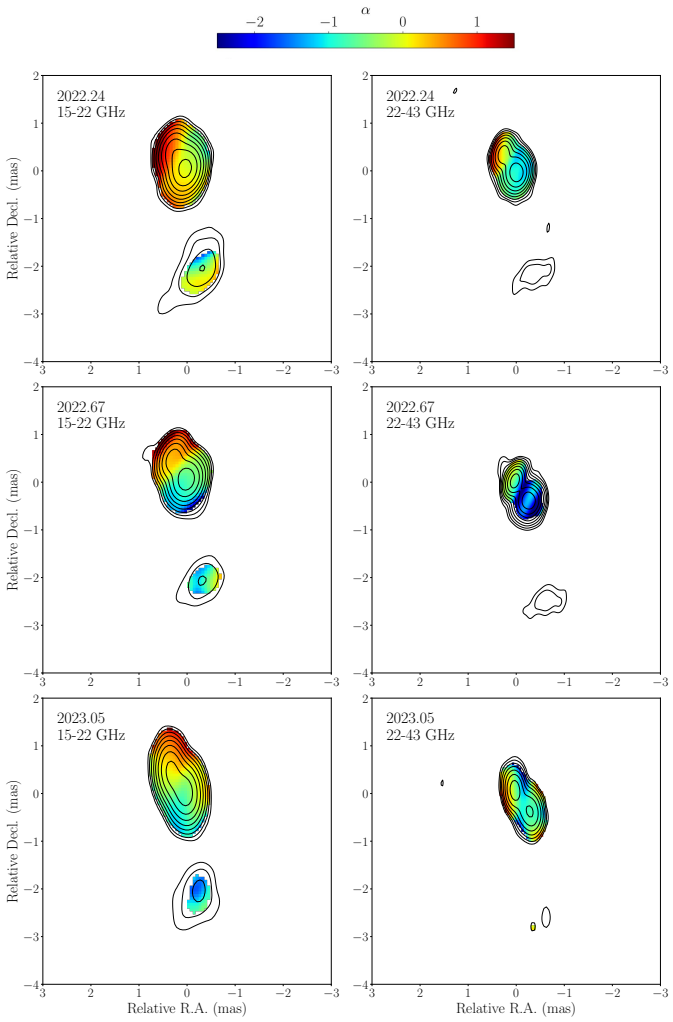

Fig. A.2. Spectral index maps between 15, 22 and 43 GHz.

Appendix B: Multi-frequency kinematic fit

Here we present a multi-frequency kinematic analysis of the two jet components whose positions were aligned based on the core shift measurement (see Sect. 3.2). The component distances and the best fit functions are shown in Fig. B.1. Our data is well described with a linear fit which reveals apparent component speed of $\mu_{C1} = 0.16 \pm 0.07$ mas/yr and $\mu_{C2} = 0.20 \pm 0.08$ mas/yr.

However, the amount of data available for kinematic estimates is not sufficient to justify higher orders of trajectory fit, and our overall conclusions are not strongly dependent on the linearity of the apparent trajectory. In addition, according to the methodology established for AGN monitoring data Homan et al. (2009), component acceleration is only analyzed if a given jet feature is robustly detected in at least ten observing epochs. Linear fits are more suitable to determine the component speed and ejection time. Nevertheless, our data presented here would be a useful set of future study of kinematics which might favor a higher order of trajectory fit.

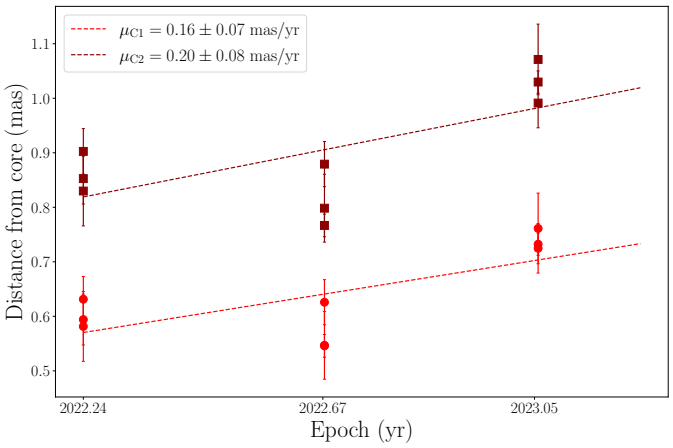

Fig. B.1. Kinematics of the jet components C1 (red circles) and C2 (dark red squares), with their positions aligned based on the core shift measurement.

Chapter 7

From binary to singular: The AGN PSO J334.2028+1.4075 under the high-resolution VLBI scope

Binary AGN are the products of hierarchical structure formation, that is galaxy mergers, and are expected to be common occurrences in the Universe (An et al. 2018). The evolution of a binary system can be separated into three stages. First, dynamical friction (Chandrasekhar 1943) decreases the binary separation via extracting effective angular momentum and energy from the system through stellar encounters (Milosavljević & Merritt 2001, 2003). The separation of these dual AGN (DAGN) is measured on kiloparsec scales. During the next evolutionary stage, the merger is driven by three-body gravitational interactions with stars (Begelman et al. 1980). The separation of the bound SMBHB is a few parsecs. Finally, at sub-parsec separations the energy loss of the binary happens through the emission of gravitational waves until the merger.

Observations of binary AGN can help us better understand the mechanisms driving galaxy mergers, as well as to study their contribution to the low-frequency gravitational wave background. However, so far only the existence of a few dual AGN (NGC 6240, Komossa et al. 2003), (Mrk 739, Koss et al. 2011) and SMBHB (0402+379, Rodriguez et al. 2006) have been confirmed via direct methods. VLBI plays a key role in the direct confirmation of DAGN and SMBHB, since with baseline lengths of a few thousand kilometers we are capable of reaching milliarcsecond resolution and capture closely separated AGN systems.

PSO J334.2028+01.4075 (hereafter PSO J334) is a binary AGN candidate at $z = 2.06$. It was discovered via a systematic search in the Pan-STARRS1 Medium Deep Survey shoving an optical flux density variation with the period of 542 days (Liu et al. 2015).

This was interpreted as the orbital period of a secondary SMBH passing through the accretion disk of the primary black hole. Based on the period of the variability, their coalescence would happen in $\sim$ 7 yrs in the rest frame of the object, placing them in the gravitational wave emitting phase of the merger. This rare type of object garnished considerable interest, but multiwavelength studies did not find any evidence to support the binary nature of PSO J334 (Liu et al. 2016; Foord et al. 2017). That is until a VLBI study by Mooley et al. (2018) revealed a 39°difference between the parsec- and kiloparsec-scale structures of the source, hinting at the presence of a precessing jet, possibly due to the perturbing effects of a secondary black hole in the system.

In this work, we expand on our previous study (Benke et al. 2018) on the source that included a 1.7-GHz EVN map of PSO J334. Our new 1.5 and 6.2-GHz images observed with the VLA, that have a higher resolution than the 2.8-GHz one presented in Mooley et al. (2018), show a lobe-dominated quasar with an asymmetric morphology and straight jets at 6.2 GHz at kiloparsec scales. Polarimetric signals in the lobes suggest that the source structure is influenced by interaction with the ambient medium rather than by a companion SMBH. Thus, our study disfavors the last remaining argument that supported the binary nature of PSO J334.

Conceptualization, S.F., K.É.G.; methodology, P.B., S.F., K.É.G.; formal analysis, P.B., S.F.; software, P.B.; validation, P.B., S.F.; writing-original draft preparation, P.B., S.F.; writing-review and editing, K.É.G, L.I.G, E.K., T.A., P.M., Z.P., E.R.; visualization, P.B.; supervision, S.F., E.R.

A&A 677, A1 (2023)
https://doi.org/10.1051/0004-6361/202346904

Astronomy & Astrophysics

From binary to singular: The AGN PSO J334.2028+1.4075 under the high-resolution scope

P. Benke[1,2], K. É. Gabányi[3,4,5,6], S. Frey[5,6,7], T. An[8,14], L. I. Gurvits[9,10], E. Kun[11,12,13,5,6], P. Mohan[8], Z. Paragi[9], and E. Ros[1]

[1] Max-Planck-Institut für Radioastronomie, Auf dem Hügel 69, 53121 Bonn, Germany
e-mail: pbenke@mpifr-bonn.mpg.de
[2] Institut für Theoretische Physik und Astrophysik, Universität Würzburg, Emil-Fischer-Str. 31, 97074 Würzburg, Germany
[3] Department of Astronomy, Institute of Physics and Astronomy, ELTE Eötvös Loránd University, Pázmány Péter sétány 1/A, 1117 Budapest, Hungary
[4] ELKH-ELTE Extragalactic Astrophysics Research Group, Eötvös Loránd University, Pázmány Péter sétány 1/A, 1117 Budapest, Hungary
[5] Konkoly Observatory, ELKH Research Centre for Astronomy and Earth Sciences, Konkoly Thege Miklós út 15-17, 1121 Budapest, Hungary
[6] CSFK, MTA Centre of Excellence, Konkoly Thege Miklós út 15-17, 1121 Budapest, Hungary
[7] Institute of Physics and Astronomy, ELTE Eötvös Loránd University, Pázmány Péter sétány 1/A, 1117 Budapest, Hungary
[8] Shanghai Astronomical Observatory, Chinese Academy of Sciences, Shanghai 200030, PR China
[9] Joint Institute for VLBI ERIC, Oude Hoogeveensedijk 4, 7991 PD Dwingeloo, The Netherlands
[10] Faculty of Aerospace Engineering, Delft University of Technology, Kluyverweg 1, 2629 HS Delft, The Netherlands
[11] Theoretical Physics IV, Faculty for Physics and Astronomy, Ruhr University Bochum, 44780 Bochum, Germany
[12] Astronomical Institute, Faculty for Physics and Astronomy, Ruhr University Bochum, 44780 Bochum, Germany
[13] Ruhr Astroparticle and Plasma Physics Center, Ruhr-Universität Bochum, 44780 Bochum, Germany
[14] Key Laboratory of Radio Astronomy and Technology, Chinese Academy of Sciences, A20 Datun Road, Chaoyang District, Beijing 100101, PR China

Received 15 May 2023 / Accepted 28 June 2023

ABSTRACT

Context. PSO J334.2028+1.4075 (PSO J334) is a luminous quasar located at redshift $z = 2.06$. The source gained attention when periodic flux density variations were discovered in its optical light curve. These variations were initially interpreted as the variability due to the orbital motion of a supermassive black hole binary (SMBHB) residing in a single circumbinary accretion disk. The orbital separation was determined to be 0.006 pc with an in-spiral time of 7 yr in the rest frame of PSO J334. These findings suggested the quasar could be in the gravitational wave emitting phase of its merger and so extended multiwavelength observations were commenced. However, subsequent observations provided evidence against the binary hypothesis as no optical periodicity was found on extended time baselines. On the other hand, detailed radio analysis with the *Karl G. Jansky* Very Large Array (VLA) and the Very Long Baseline Array (VLBA) revealed a lobe-dominated quasar at kiloparsec scales, and possibly a precessing jet, which could retain PSO J334 as a binary SMBH candidate.
Aims. We aim to study both the large- and small-scale radio structures in PSO J334 to provide additional evidence for or against the binary scenario.
Methods. We observed the source at 1.7 GHz with the European Very Long Baseline Interferometry Network (EVN), and at 1.5 and 6.2 GHz with the VLA, at frequencies that complement the previous radio interferometric study.
Results. Our images reveal a single component at parsec scales slightly resolved in the southeast-northwest direction and a lobe-dominated quasar at kiloparsec scales with a complex structure. The source morphology and polarization in our VLA maps suggest that the jet is interacting with dense clumps of the ambient medium. While we also observe a misalignment between the inner jet and the outer lobes, we suggest that this is due to the restarted nature of the radio jet activity and the possible presence of a warped accretion disk rather than due to the perturbing effects of a companion SMBH.
Conclusions. Our analysis suggests that PSO J334 is most likely a jetted active galactic nucleus with a single SMBH, and there is no clear evidence of a binary SMBH system in its central engine.

Key words. galaxies: jets – galaxies: active – techniques: interferometric – techniques: high angular resolution – polarization

1. Introduction

The discovery of PSO J334.2028+1.4075 (FBQS J2216+0124; hereafter denoted as PSO J334; Liu et al. 2015) as a supermassive black hole binary (SMBHB) candidate attracted significant interest due to the rarity of confirmed SMBHBs. Supermassive black holes are expected to be at the center of most galaxies. Since galaxies evolve hierarchically, SMBHBs are believed to be abundant, especially at small separations (An et al. 2018). However, confirming the existence of such objects has so far been mostly unsuccessful, with a few exceptions. The most notable examples are the dual active galactic nucleus (AGN) system in NGC 6240 (Komossa et al. 2003), which resides in an ultraluminous infrared galaxy, and 0402+379, which was detected with

the Very Long Baseline Array (VLBA) and has two radio cores separated by a projected distance of 7.3 pc (Rodriguez et al. 2006).

The SMBHB candidate quasar PSO J334 was discovered through a systematic search in the Pan-STARSS1 Medium Deep Survey (Liu et al. 2015). Based on an observed 542 ± 15 day period in the variation of the optical flux density and an estimated total black hole mass of $10^{9.97\pm0.5}\,M_{\odot}$ (with a mass ratio between 0.05 and 0.25), an orbital separation of 0.006 pc was inferred. According to this, the coalescence of the SMBHB would occur in approximately 7 yr in the rest frame of the quasar. Unfortunately, current astronomical instruments are not capable of resolving the two components at such a small separation, so evidence for the existence of a second component could only be indirect, such as the detected periodic variability in the optical flux density. This variability could be caused by a secondary black hole passing through the primary black hole's accretion disk, as proposed for OJ 287 (Lehto & Valtonen 1996). A similar explanation has been suggested in the case of the recently discovered SMBHB candidate SDSS J143016.05+230344.4 as well, which shows a periodic optical variability with a decay in both period and amplitude (Jiang et al. 2022; An et al. 2022). However, the detected 2.6 cycles of the putative periodicity are likely insufficient to claim sinusoidal variations (Vaughan et al. 2016), and other processes, such as quasi-periodic eruptions (Miniutti et al. 2019) and quasi-periodic oscillations (Gierliński et al. 2008) may also explain the periodic flux density variability observed in PSO J334. Indeed, subsequent observations with extended time baselines of the optical monitoring failed to find any evidence of periodic variability in PSO J334 (Liu et al. 2016).

The radio structure of PSO J334 has been investigated in a multifrequency study with the *Karl G. Jansky* Very Large Array (VLA) and the VLBA by Mooley et al. (2018). In the VLBA images obtained at four frequencies from 4.4 to 15.4 GHz, the quasar is resolved into two components, a compact core and a jet. Their separation is 3.6 milliarcsec (mas), corresponding to a projected linear separation of 30 pc. The VLA images at 2.8 and 4.38 GHz reveal a lobe-dominated structure extending 66 kpc from opposite sides of the core. In addition, the 39° difference between the position angles of the outer lobes and the inner jet is significant enough to suggest a perturbation of the jet by the second SMBH (Begelman et al. 1980), or alternatively a restarted double-double source. Thus, despite the results from the recent optical light curve, PSO J334 can still be considered as a SMBHB candidate (Mooley et al. 2018). Multiwavelength observations aimed at determining the accretion mode of the quasar by Foord et al. (2017) have not found any feature that would convincingly distinguish PSO J334 from a single AGN. However, there are still untested scenarios that would allow the object to retain its SMBHB status.

We studied the radio structure of PSO J334 using the technique of very long baseline interferometry (VLBI) with the European VLBI Network (EVN) at 1.7 GHz and with the VLA at 1.5 and 6.2 GHz. Here we present our results and compare them with those obtained with the VLBA at higher frequencies by Mooley et al. (2018). In Sect. 2, we describe the observations and the data reduction process. We then discuss our results in Sect. 3. Finally, a summary is given in Sect. 4. In this paper we assume a ΛCDM cosmological model with $H_0 = 70\,\mathrm{km\,s^{-1}\,Mpc^{-1}}$, $\Omega_\Lambda = 0.73$, and $\Omega_\mathrm{M} = 0.27$. At the redshift of the object, $z = 2.06$ (Becker et al. 2001), 1″ of angular distance in the sky corresponds to 8.569 kpc of projected linear distance (Wright 2006).

2. Observations and data reduction

2.1. VLA data

Observations with the VLA (project code AG980, PI: K. É. Gabányi) were carried out at 1.5 and 6.2 GHz (L and S/C bands) on 2016 October 28 and 2016 October 26, respectively. The VLA was observing in its most extended A configuration with 27 antennas. The on-source time was 0.5 h in both bands. The primary flux density calibrator in both experiments was 3C 48, and the polarization D-term calibrator was J2355+4950. The secondary calibrators were J2212+0152 (1.5 GHz) and J2218−0335 (6.2 GHz). The 1.5 GHz data were recorded in 16 spectral windows between 1.008 and 1.968 GHz with 64 channels, each with a bandwidth of 64 MHz. The 6.2 GHz data contained 48 spectral windows, but the first 16 were only used to set up the observations, so the target and calibrators were observed between 4.226 and 8.096 GHz frequencies in 32 spectral windows, each with 64 channels and a bandwidth of 128 MHz.

Data reduction was performed in the Common Astronomy Software Applications (`CASA`, McMullin et al. 2007; CASA Team 2022) package version 7.15.0. First, phase, delay, bandpass, and gain calibrations were derived for the primary calibrator. Then, to calibrate polarization, we determined cross-hand delays, solved antenna-based D terms for the unpolarized calibrator, and finally calibrated the polarization angle for the primary calibrator. We then used the calibration tables generated in the previous steps to transfer the solutions to the secondary calibrator and then to our target source[1]. As 3C 48 was undergoing an active phase during 2016[2], we inspected the polarimetric calibration carefully, imaged all calibrators to determine the polarization angle and fractional polarization values, and compared them to those available in the literature. In the case of the D-term calibrators, we found no significant polarization signatures and fractional polarization values were close to 0. In the case of 3C 48, polarization angles and fractional polarization values in the two bands differ by less than 15% compared to the values in the literature[2].

Hybrid imaging was performed by iterating `tclean` and self-calibration, while imaging all four Stokes parameters together, and then deriving polarized intensity and polarization fraction images from the total intensity (Stokes I) and linearly polarized (Stokes Q and U) images. The 1.5 and 6.2 GHz VLA images are shown in Fig. 1, and the polarized intensity and electric vector position angle (EVPA) images are shown in Fig. 2.

2.2. EVN data

Our EVN observation (project code RSG08, PI: S. Frey) at 1.7 GHz was performed on 2015 October 18, with the participation of eleven radio telescopes: Jodrell Bank Lovell Telescope (United Kingdom), Westerbork (single dish; the Netherlands), Effelsberg (Germany), Medicina (Italy), Onsala (Sweden), Sheshan (China), Toruń (Poland), Hartebeesthoek (South Africa), Svetloe, Zelenchukskaya, and Badary (Russia). The data were recorded at a $1\,\mathrm{Gbit\,s^{-1}}$ rate in left and right circular polarizations, with eight basebands (IFs) per polarization, each divided into thirty-two 500-kHz wide spectral channels. The total bandwidth was 128 MHz per polarization. The correlation was

[1] For the calibration, we followed this VLA tutorial: https://casaguides.nrao.edu/index.php/VLA_Continuum_Tutorial_3C391-CASA5.5.0

[2] https://science.nrao.edu/facilities/vla/docs/manuals/obsguide/modes/pol

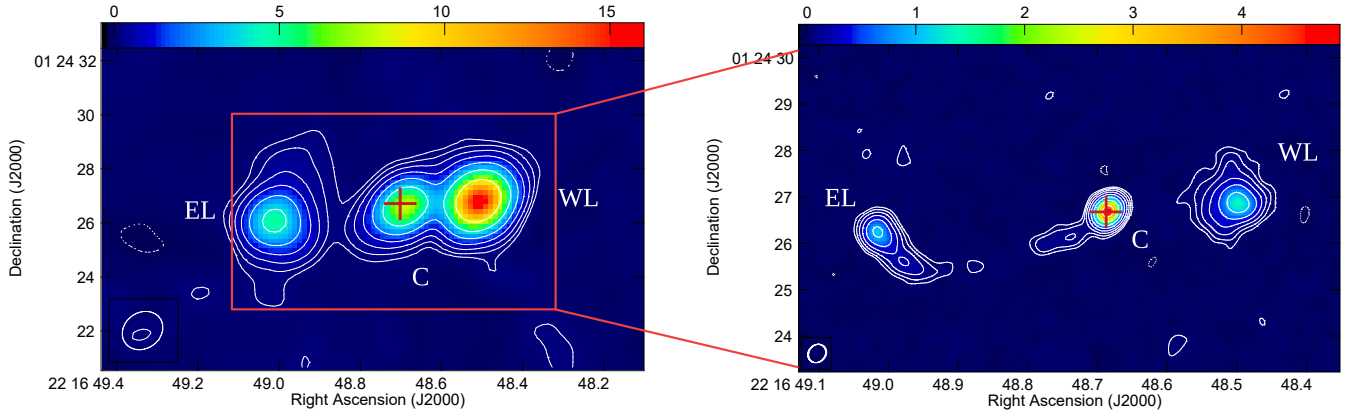

Fig. 1. VLA images of PSO J334 at 1.5 and 6.2 GHz. Each color bar represents the total intensity in mJy beam^{-1}. Restoring beam sizes (FWHM) are 1218 mas × 1665 mas at the major axis position angle PA = −30.5° at 1.5 GHz, and 340.6 mas × 422.4 mas at PA = −25.4° at 6.2 GHz. The lowest contours are at 0.12 and 0.03 mJy beam^{-1}, and further contour levels increase by a factor of two. The eastern and western lobes are marked as EL and WL, and the core is denoted as C. The red cross marks the position of the VLBI core at 1.7 GHz.

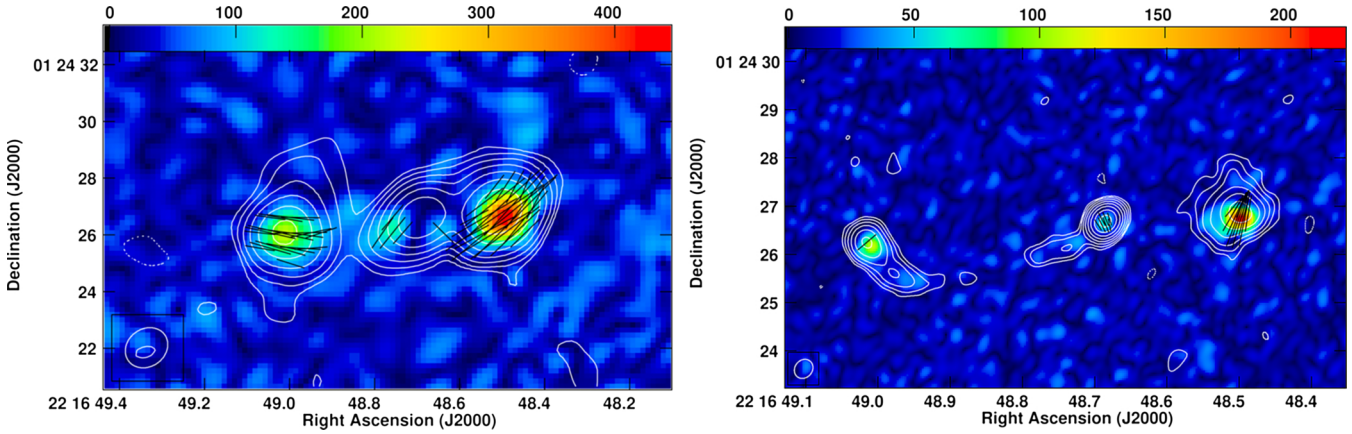

Fig. 2. VLA 1.5 GHz (*left panel*) and 6.2 GHz (*right panel*) polarimetric images of PSO J334. The colors represent the polarized intensity in μJy beam^{-1}, while the contours are the same as in the total intensity map in Fig. 1. EVPAs are represented by the black ticks in the image.

performed at the Joint Institute for VLBI ERIC (Dwingeloo, The Netherlands) with a 4 s integration time. The observation lasted for a total of 2 h.

We used phase referencing to a nearby (separated by 0.°96) compact calibrator source, J2217+0220, with duty cycles of 6.5 min, including 3 min 20 s scans spent on the target. The total accumulated observing time on PSO J334 was 1 h.

The data were calibrated with the US National Radio Astronomy Observatory (NRAO) Astronomical Image Processing System (`AIPS`, Greisen 2003), following the usual procedures. The amplitudes of the raw correlated visibility data were calibrated using the antenna gain curves and measured system temperatures (where available), as provided by the participating stations. Nominal system temperature values were used for Jodrell Bank, Sheshan, Svetloe, Zelenchukskaya, and Badary. The data were then corrected for the dispersive ionospheric delay by invoking the task `TECOR`, which uses total electron content maps derived from global navigation satellite systems' data. Phase changes due to the time variation of the source parallactic angle were also corrected for azimuth–elevation-mounted radio telescopes in the network. Global fringe-fitting was performed using the task `FRING` on the phase-reference calibrator J2217+0220 and the bright fringe-finder source J2148+0657 also observed for a 12-min scan at the beginning of the experiment. These calibrated visibility data were exported to `Difmap` (Shepherd 1997) for imaging. Conventional hybrid mapping with several iterations of the `clean` algorithm (Högbom 1974) and phase-only self-calibration was performed. Then antenna-based gain correction factors were determined. These values were within ±5% for the compact bright fringe-finder source, suggesting a reliable initial amplitude calibration. The `clean` component model obtained for the phase-reference source J2217+0220 in `Difmap` was fed back to `AIPS`, before repeating fringe-fitting, then taking the calibrator source structure into account for determining visibility phases. The fringe-fit solutions obtained for J2217+0220 were interpolated to the target source, PSO J334, within the atmospheric coherence time using the task `CLCAL`. The final calibrated visibility data file for PSO J334 was then transferred to `Difmap` for imaging and brightness distribution modeling.

The peak of the dirty image was offset by about 1.″1 from the center because of an inaccurate a priori position used for radio telescope pointing. Therefore we started the imaging by shifting the phase center to the actual brightness peak. Because PSO J334 is relatively weak with ∼7 mJy total flux density, and it appeared slightly resolved at 1.7 GHz with the EVN, self-calibration in general was not attempted during hybrid imaging in `Difmap`, except for phase self-calibration for the European stations (Effelsberg, Jodrell Bank, Onsala, Westerbork, Medicina, and Toruń). We used gradually decreasing solution intervals from 60 to 1 min. Amplitude self-calibration was not carried

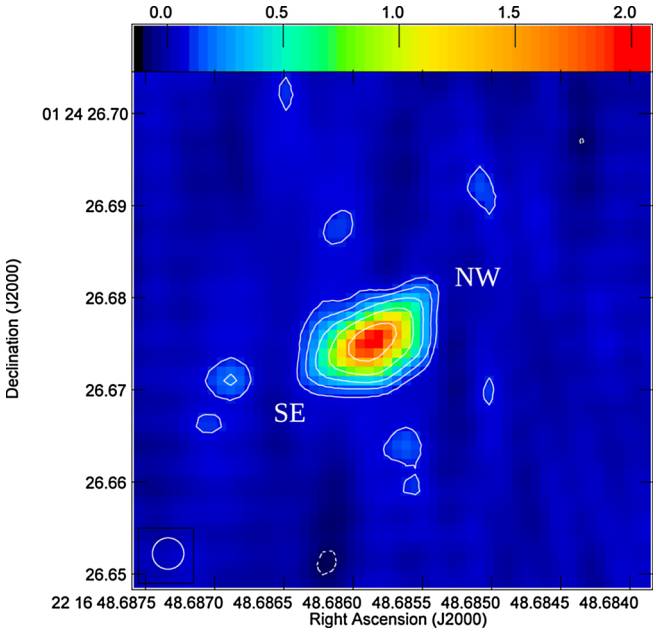

Fig. 3. 1.7-GHz EVN image of PSO J334. The image was restored with a 3.4-mas circular Gaussian beam. The lowest contours are at 0.09 mJy beam^{-1} and increase by a factor of two. The source shows an elongated shape in the southeast–northwest direction, which is consistent with the structure reported in Mooley et al. (2018).

out at all. The naturally weighted `clean` image of PSO J334 is shown in Fig. 3. A circular two-dimensional Gaussian brightness distribution model component fitted directly to the self-calibrated visibility data in `Difmap` can adequately describe the source, allowing us to quantitatively characterize its size and flux density (Table 2). Neither an elliptical Gaussian, nor a two-component circular Gaussian model could significantly improve the goodness of fit.

2.3. Archival VLBA data

To be able to perform brightness distribution model fitting in the visibility domain, from the NRAO data archive[3], we downloaded, recalibrated, and imaged the VLBA data of Mooley et al. (2018) measured at 4.38, 7.40, 8.67, and 15.37 GHz (project code BM438, PI: K. P. Mooley). For details on the observations, we refer readers to the original paper (Mooley et al. 2018). Calibration was carried out in `AIPS`. After loading the data with `FITLD`, we performed parallactic angle and digital sampling corrections, corrected for the Earth orientation parameters, and we applied ionospheric corrections that are especially important for phase-referenced observations performed at low frequencies and low source declination. At first, fringe-fitting was performed on the phase-reference calibrator, J2217+0220, using the task `FRING`. After applying the calibration tables and writing the data out of `AIPS`, we performed hybrid imaging in `Difmap`, in a similar way as described in Sect. 2.2 for the EVN data. Since the gain corrections for all the VLBA antennas were within ±5%, we did not perform any additional antenna-based amplitude correction in `AIPS`. The `clean` image of J2217+0220 was then loaded into `AIPS` and used during the second round of fringe-fitting. Delay and rate solutions were applied to both the calibrator and the target, PSO J334. The calibrated visibility data of the target source were written out. Imaging again was carried out in `Difmap` by only using `clean` iterations without self-calibration. The total flux densities, that is to say the sum of the individual clean components, and peak brightnesses agree with the values published in Mooley et al. (2018) within 10% (see image properties in Table 1). Gaussian brightness distribution model components (Table 2) were fit to the visibility data using the `modelfit` command in `Difmap`.

[3] https://data.nrao.edu/

3. Results and discussion

3.1. Source structure and polarization

The 1.7-GHz EVN image of PSO J334 (Fig. 3) restored with a 3.4-mas circular Gaussian beam – full width at half maximum (FWHM) – shows a single component that is slightly resolved in roughly the southeast–northwest direction. The structure is consistent with the higher-frequency VLBA images (Mooley et al. 2018), where two components – a southeastern synchrotron self-absorbed core and a northwestern jet – were identified with a 3.6 mas separation along the position angle of 139°. (Position angles are conventionally measured from north to east.) The 39° misalignment in position angles between the VLA and VLBA jets led Mooley et al. (2018) to restore the SMBHB status of PSO J334; however, alternative interpretations are still viable to explain the observations. Double-double radio sources, such as B0925+420 and B1450+333 (Schoenmakers et al. 2000), that retain signs of several active phases show a similar morphology to PSO J334. In this case, the lobes seen on kiloparsec scales with the VLA would be relics of past activity, and the compact, mas-scale core–jet morphology was formed more recently. The change in jet position angle can be interpreted as precession either due to an interaction with a companion SMBH (Begelman et al. 1980) or caused by a warped accretion disk changing the orientation of the jet (Pringle 1997).

Our VLA observations at 1.5 and 6.2 GHz show details of the complex structure of PSO J334 (Fig. 1). The source, as shown in the 2.8-GHz VLA B-configuration Caltech–NRAO Stripe 82 Survey (CNSS) image of Mooley et al. (2018), is a lobe-dominated quasar oriented at a large angle with respect to our line of sight. The projected linear size of the object is approximately 79 kpc, which is typical of $z = 2$ AGN (Blundell et al. 1999). The lengths of the arms are unequal, with the eastern arm being longer at both frequencies. However, contrary to expectations that the longer arm is pointing toward the observer and is brighter due to Doppler boosting (Longair & Riley 1979), here the western, shorter arm appears brighter in both images. In addition, the eastern arm shows a sharp turn before ending in a hotspot, which suggests an interaction with the surrounding interstellar medium (ISM), similarly as, in the high-redshift radio galaxy 4C 41.17 for instance (Gurvits et al. 1997). However, we do not detect polarized emission at the turning point as, for example, in PKS 0637−752 (Lovell et al. 2000), where the highly polarized bent jet region also gives rise to bright X-ray emission (Schwartz et al. 2000). By inspecting the polarimetric images, we also see that the polarized intensity is higher in the western lobe and that EVPAs are close to perpendicular to the jet propagation on both sides, indicating the presence of a termination shock where the lobe material interacts with the ambient medium. The asymmetric structure together with the polarimetric results suggest that PSO J334 is embedded in a large-scale environment that is not intrinsically symmetric, and the jet interacts with clumps of the ISM that are disrupted upon contact with the jet material.

Table 1. Map properties of the clean images shown in Figs. 1 and 3, as well as the reanalyzed VLBA images from Mooley et al. (2018).

ν [GHz] [a]	Array [b]	$S_{\rm tot}$ [mJy] [c]	$S_{\rm peak}$ [mJy beam^{-1}] [d]	σ [mJy beam^{-1}] [e]	$b_{\rm maj}$ [mas] [f]	$b_{\rm min}$ [mas] [g]	PA [°] [h]
1.5	VLA	35.41	14.7	0.04	1665	1218	−30.5
6.2	VLA	11.48	4.52	0.01	422.4	340.6	−35.4
1.7	EVN	6.8	2.1	0.035	3.4	3.4	0
4.38	VLBA	4.83	2.54	0.049	5.86	2.46	11.2
7.40	VLBA	3.24	1.41	0.036	3.48	1.46	12.1
8.67	VLBA	3.45	1.56	0.06	2.13	0.86	−0.27
15.37	VLBA	1.19	0.85	0.036	1.29	0.48	−3.99

Notes. [a]Observing frequency. [b]Interferometer array performing the observation. [c]Total flux density. [d]Peak brightness. [e]rms noise. [f]Beam major axis. [g]Beam minor axis. [h]Beam position angle.

Table 2. Characteristics of `modelfit` components.

ν [GHz] [a]	Array	Component	$S_{\rm comp}$ [mJy] [b]	$b_{\rm comp}$ [mas] [c]	$T_{\rm b}$ [10^8 K] [d]
1.7	EVN		7.15 ± 0.72	6.58 ± 0.68	2.2 ± 0.5
4.38	VLBA	SE	2.43 ± 0.24	1.53 ± 0.49	2.0 ± 1.3
		NW	2.64 ± 0.26	1.23 ± 0.49	3.4 ± 2.7
7.40	VLBA	SE	1.71 ± 0.17	0.8 ± 0.29	1.8 ± 1.4
		NW	1.75 ± 0.18	0.9 ± 0.29	1.5 ± 1.0
8.67	VLBA	SE	1.97 ± 0.2	0.59 ± 0.17	2.8 ± 1.6
		NW	2.03 ± 0.2	0.83 ± 0.17	1.5 ± 0.6
15.37	VLBA	SE	0.95 ± 0.1	0.16 [*]	>6.0 [*]
		NW	0.8 ± 0.08	0.38 ± 0.1	0.9 ± 0.4

Notes. [a]Frequency of the observation. [b]Flux density of the component. [c]Size of the component (FWHM). [d]Brightness temperature. [*]Component is unresolved based on Eq. (2) from Kovalev et al. (2005).

Inspecting the inner 2″−3″ in our 6.2-GHz VLA image (Fig. 1), we see a remarkably straight jet that cannot be described with any precession model. Jet precession itself would be revealed by a helical jet shape that is physically external or intrinsic to the jet. In the first case, the main driver might be, for example, binary motion (e.g. Kun et al. 2014), Lense–Thirring precession (e.g. Lense & Thirring 1918; Liska et al. 2018), or disk precession induced by a secondary black hole (e.g. Caproni & Abraham 2004). In this case, the jet components move more or less on straight or ballistic paths, and the pitch of the jet is constant. The helical pattern simply reflects the periodic ejection direction of the newborn jet components. The second case appears, for example, due to instabilities in the jet (e.g. Perucho et al. 2006) and components actually move along a helical path. In this case, the spatial wavelength of the jet along its symmetry axis is increasing with increasing core separation. The jet appearing in the 6.2-GHz VLA image (Fig. 1) has no resemblance to any of these scenarios. However, we cannot rule out the possibility that more sensitive images with a higher angular resolution could recover jet structures indicative of precession or the presence of instabilities (see, e.g., the case of 3C 279, Fuentes et al., in prep.). This structure seems hard to reconcile with the jet precession suggested by Mooley et al. (2018) based on lower-resolution VLA data, and rules out the last argument supporting the binary nature of the source.

3.2. Spectral analysis

Spectral index maps ($S_\nu \propto \nu^\alpha$) were created between our two VLA images at 1.5 and 6.2 GHz, as well as between our 1.7-GHz EVN image and the 4.38-GHz VLBA image of Mooley et al. (2018), plotted with black contours in Fig. 6. To align the images on the optically thin jet components, we used 2D cross-correlation.

The image pairs had the same restoring beam, map, and pixel size, as well as the same minimum and maximum (u, v) distance. The resulting spectral index maps are shown in Fig. 4. Due to the low signal-to-noise ratio outside of the peaks of the core and lobe regions, we do not recover spectral index solutions there.

Spectra are flat in the VLA core, that is to say the central component, and the eastern lobe; however, α values indicating a steeper spectrum are measured in the western lobe (Fig. 4). The flat spectrum of the eastern lobe might indicate a shock region, which is supported by the bending seen in the 6.2-GHz VLA image (Fig. 1), possibly happening due to the interaction with the ISM. The steeper spectrum of the western lobe, however, can be explained by an older population of electrons present in this region. The VLBI spectral index map created between 1.7 and 4.38 GHz shows a flat spectrum for both the core and the northwestern jet component. Since we assume that the amplitude calibration is accurate within 10%, spectral index errors are estimated to be ±0.15. Readers can also refer to Fig. 3 of Mooley et al. (2018) for the spectral index map between 8.67 and 15.37 GHz, showing steep spectra in both VLBI components. We also plotted the spectra of the core and jet components of the VLBI images in Fig. 5, where both the core and the jet components show a steep spectrum between 1.7 and 4.38 GHz. In addition, the steepening toward the jet edge might be an artifact due to the low brightness of the component. While our results confirm the southeastern component as the core (Mooley et al. 2018), here we must note that the observations used to create the spectral index map were made half a year

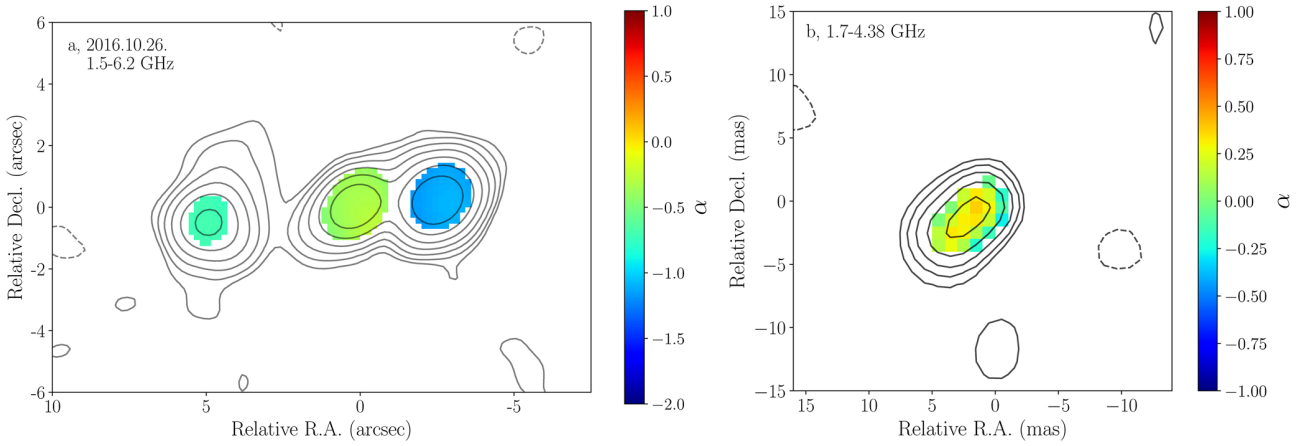

Fig. 4. Two-point spectral index distribution maps of PSO J334 based on: *a* quasi-simultaneous VLA images at 1.5 and 6.2 GHz, and *b* 1.7-GHz EVN and 4.38-GHz VLBA images. The lowest contours are at 0.12 and 0.14 mJy beam^{-1}, and contour levels increase by a factor of two. Colors represent spectral index values. We note that the VLBI images were taken half a year apart, so flux density variability cannot be excluded and therefore the spectral index map in *panel b* should be treated with caution.

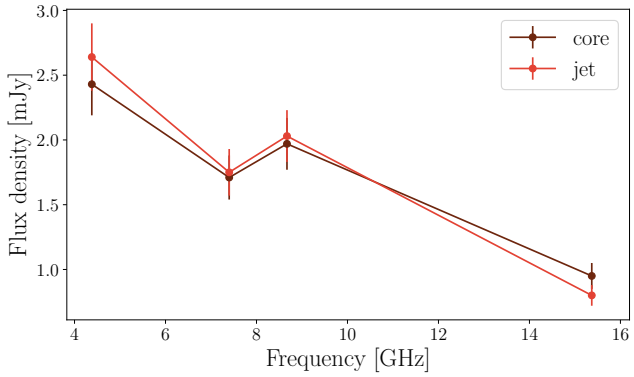

Fig. 5. Spectra of the core (southeast) and jet (northwest) components of the VLBA images.

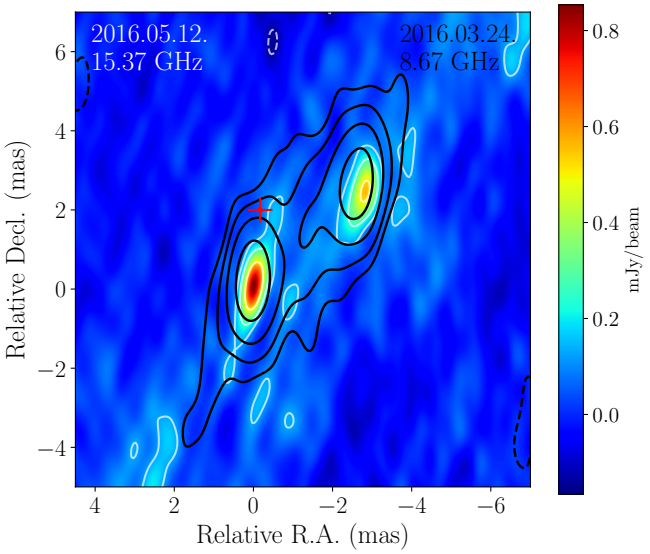

Fig. 6. 15.37-GHz VLBA image overplotted with the *Gaia* position and its uncertainty (red cross). White contours are at 0.83 mJy beam^{-1} × (−15, 15, 30, 60)%, and the restoring beam size is 1.29 mas × 0.48 mas at PA = −3.96°. Black contours representing the 8.67 GHz source structure are at 1.56 mJy beam^{-1} × (−7.5, 7.5, 15, 30, 60)%, and the FWHM of the restoring beam is 2.13 mas × 0.86 mas at PA = −3.99°.

apart, so these results must be interpreted cautiously because of possible flux density variability.

The radio spectrum compiled in Benke et al. (2018), as well as the broadband spectral energy distribution (SED) in Foord et al. (2017) show no deviation from single AGN spectra. The two models investigated by Foord et al. (2017) are the mini-disk and cavity models, which represent different stages of the binary evolution and manifest in the SED as missing emission at different frequencies. However, they found that the optical to X-ray bands are well modeled with a composite nonblazar SED (Shang et al. 2011) and the radio emission falls between what is expected from radio-loud and radio-quiet sources.

3.3. Brightness temperatures

To study the brightness temperature of the compact radio emitting features in the VLBI images (Figs. 3 and 6, also Mooley et al. 2018), we fit circular Gaussian components in the visibility domain with `modelfit` in `Difmap`. Characteristics of the `modelfit` components are summarized in Table 2. We assume flux density errors to be 10% and the error in component size to be 20% (Lister et al. 2009). We calculated the observed brightness temperature as

$$T_{\rm b,obs}[{\rm K}] = 1.22{\times}10^{12}\left(\frac{S_\nu}{\rm Jy}\right)\left(\frac{\nu}{\rm GHz}\right)^{-2}\left(\frac{b_{\rm min}\times b_{\rm maj}}{\rm mas^2}\right)^{-1}(1{+}z), \quad (1)$$

where $b_{\rm min}$ and $b_{\rm maj}$ are the minor and major axis (FWHM) of the component. The resolution limit was computed based on Eq. (2) in Kovalev et al. (2005). For the one component for which the size fell below this limit, we could only calculate a lower limit of its brightness temperature. The $T_{\rm b,obs}$ values fall between 10^7 and 10^9 K. This confirms that the emission originates from AGN activity and not from spatially extended star formation in the host galaxy (Condon et al. 1991). The measured brightness temperatures are lower than the average core brightness temperatures of blazars in the MOJAVE sample[4] of 1.39×10^{11} K (Homan et al. 2021). This indicates that the emission of PSO J334 is likely not beamed and the jets are probably inclined at a large angle to our line of sight.

[4] https://www.cv.nrao.edu/MOJAVE/

3.4. VLBI and Gaia astrometry

Both the EVN and VLBA observations were carried out in phase-referencing mode, enabling precise relative astrometric measurements. We determined the position of the brightness peak in the VLBI images using `MAXFIT` in `AIPS`. Since we expect that the optical emission originates from the vicinity of the central engine, that is the accretion disk and the inner jet (Kovalev et al. 2017), we can use *Gaia* data (Gaia Collaboration 2016) from the third data release (DR3, Gaia Collaboration 2023) to identify the nucleus position. The standard error of the optical position is 0.27 mas in right ascension and 0.32 mas in declination based on *Gaia* DR3. VLBI astrometric errors are comparable and estimated to be 0.3 mas for low declinations with the VLBA based on the analysis of Pradel et al. (2006). We also take the uncertainty of the position of the calibrator, J2217+0220, into account. The source is in the third realization of the International Celestial Reference Frame (ICRF3, Charlot et al. 2020), and the formal position errors are 0.0765 mas and 0.1137 mas in right ascension and declination, respectively. We added these error estimates in quadrature, and estimate errors to be 0.31 mas in right ascension and 0.32 mas in declination. We find that the southeastern component at 8.67 GHz is closer to the optical position of the source (see black contours in Fig. 6). We also see that the differences in right ascension are within the expected uncertainties, except at 4.38 GHz where ∼2 mas offset was found between the *Gaia* and the VLBI core positions. However, the optical–radio differences in declination reach up to ∼4 mas, but show no frequency dependence.

We suspect that these differences in declination arise from uncorrected tropospheric and ionospheric effects. The contribution of the ionosphere to phase errors is significant at low frequencies, and since its rapid changes are difficult to model, we expect that this affects the measurement of the source position considerably. Based on 22 GHz VLBA observations, Petrov (2023) determined that the ionospheric effects contribute around 0.1 mas to the error budget both in right ascension and declination for northern hemisphere sources. However, for southern hemisphere targets, the accuracy of ionospheric corrections in declination is only 0.3 mas. In addition, at low elevations, errors from the wet tropospheric component were shown to dominate over other systematic errors, and affect the precise measurement of source declination far more seriously than of right ascension (Pradel et al. 2006). In order to be able to account for the ionospheric and tropospheric effects on VLBI astrometry more accurately, we need more extended studies similar to Brisken et al. (2002), Pradel et al. (2006), and Petrov (2023), to explore how these effects influence the error budget of our measurements for various VLBI arrays (see e.g. the Long Basline Array and the VLBI Exploration of Radio Astrometry, Petrov et al. 2019; Honma et al. 2008) and to develop methods to correct for them in the most effective way.

4. Summary

Liu et al. (2015) originally proposed that PSO J334 might be a SMBHB based on the periodic variability observed in the optical light curves. The scenario was later disfavored as extended time baselines revealed no sinusoidal periodicity in the optical flux (Liu et al. 2016), and SED reconstruction did not show any signatures expected from a binary AGN system (Foord et al. 2017). The only remaining indication of a companion SMBH was the possible precession inferred from multi-frequency radio observations of Mooley et al. (2018), where the large misalignment of 39° between the parsec- and kiloparsec-scale structures led the authors to reinstate PSO J334 as a SMBHB candidate.

Our high-resolution radio observations carried out with the VLA at 1.5 and 6.2 GHz reveal a lobe-dominated quasar (in agreement with the findings of Mooley et al. 2018), which is likely oriented at a large angle to our line of sight. Based on polarimetric imaging and the analysis of the arm length and brightness ratios, we suggest that the source is embedded in an asymmetric environment and, similarly to the high-redshift radio galaxy 4C 41.17 (Gurvits et al. 1997), its morphology is affected by the surrounding ISM, creating a bend in the eastern jet. PSO J334 also shows remarkably straight jets at 6.2 GHz, which disfavor jet precession, and this is the only argument left to support the SMBHB status of the object. In addition, our 1.7 GHz EVN observations confirm the significant misalignment between the outer lobes and the inner jet observed by Mooley et al. (2018). We suggest that this misalignment can be explained by a newer phase of AGN activity where the orientation of the component ejection has changed. In conclusion, we find no evidence to support the binary nature of PSO J334, and it should be considered an ordinary quasar.

Acknowledgements. The authors would like to thank the anonymous referee for their useful suggestions. We thank J. Livingston for his valuable comments to the manuscript. The EVN is a joint facility of independent European, African, Asian, and North American radio astronomy institutes. Scientific results from data presented in this publication are derived from the following EVN project code: RSF08. The National Radio Astronomy Observatory is a facility of the National Science Foundation operated under cooperative agreement by Associated Universities, Inc. This research was supported through a PhD grant from the International Max Planck Research School (IMPRS) for Astronomy and Astrophysics at the Universities of Bonn and Cologne. This work was supported by the Hungarian National Research, Development and Innovation Office (NKFIH, grant number OTKA K134213).

References

An, T., Mohan, P., & Frey, S. 2018, Radio Sci., 53, 1211
An, T., Zhang, Y., Wang, A., et al. 2022, A&A, 663, A139
Becker, R. H., White, R. L., Gregg, M. D., et al. 2001, ApJS, 135, 227
Begelman, M. C., Blandford, R. D., & Rees, M. J. 1980, Nature, 287, 307
Benke, P., Frey, S., Gabányi, K., et al. 2018, 14th European VLBI Network Symposium & Users Meeting (EVN 2018), 98
Blundell, K. M., Rawlings, S., & Willott, C. J. 1999, AJ, 117, 677
Brisken, W. F., Benson, J. M., Goss, W. M., et al. 2002, ApJ, 571, 906
Caproni, A., & Abraham, Z. 2004, MNRAS, 349, 1218
CASA Team (Bean, B., et al.) 2022, PASP, 134, 114501
Charlot, P., Jacobs, C. S., Gordon, D., et al. 2020, A&A, 644, A159
Condon, J. J., Huang, Z.-P., Yin, Q. F., et al. 1991, ApJ, 378, 65
Foord, A., Gültekin, K., Reynolds, M., et al. 2017, ApJ, 851, 106
Gaia Collaboration (Prusti, T., et al.) 2016, A&A, 595, A1
Gaia Collaboration (Vallenari, A., et al.) 2023, A&A, 674, A1
Gierliński, M., Middleton, M., Ward, M., et al. 2008, Nature, 455, 369
Greisen, E. W. 2003, Astrophys. Space Sci. Lib., 285, 109
Gurvits, L. I., Schilizzi, R. T., Miley, G. K., et al. 1997, A&A, 318, 11
Homan, D. C., Cohen, M. H., Hovatta, T., et al. 2021, ApJ, 923, 67
Honma, M., Tamura, Y., & Reid, M. J. 2008, PASJ, 60, 951
Högbom, J. A. 1974, A&AS, 15, 417
Jiang, N., Yang, H., Wang, T., et al. 2022, arXiv e-prints [arXiv:2201.11633]
Komossa, S., Burwitz, V., Hasinger, G., et al. 2003, ApJ, 582, L15
Kovalev, Y. Y., Kellermann, K. I., Lister, M. L., et al. 2005, AJ, 130, 2473
Kovalev, Y. Y., Petrov, L., & Plavin, A. V. 2017, A&A, 598, L1
Kun, E., Gabányi, K. É., Karouzos, M., et al. 2014, MNRAS, 445, 1370
Lense, J., & Thirring, H. 1918, Phys. Z., 19, 156
Liska, M., Hesp, C., Tchekhovskoy, A., et al. 2018, MNRAS, 474, 81
Lehto, H. J., & Valtonen, M. J. 1996, ApJ, 460, 207
Liu, T., Gezari, S., Heinis, S., et al. 2015, ApJ, 803, L16
Liu, T., Gezari, S., Burgett, W., et al. 2016, ApJ, 833, 6

Lister, M. L., Cohen, M. H., Homan, D. C., et al. 2009, AJ, 138, 1874
Longair, M. S., & Riley, J. M. 1979, MNRAS, 188, 625
Lovell, J. E. J., Tingay, S. J., Piner, B. G., et al. 2000, Astrophysical Phenomena Revealed by Space VLBI, 215
McMullin, J. P., Waters, B., Schiebel, D., et al. 2007, ASP Conf. Ser., 376, 127
Miniutti, G., Saxton, R. D., Giustini, M., et al. 2019, Nature, 573, 381
Mooley, K. P., Wrobel, J. M., Anderson, M. M., et al. 2018, MNRAS, 473, 1388
Perucho, M., Lobanov, A. P., Martí, J. M., et al. 2006, A&A, 456, 493
Petrov, L. 2023, AJ, 165, 183
Petrov, L., de Witt, A., Sadler, E. M., et al. 2019, MNRAS, 485, 88
Pradel, N., Charlot, P., & Lestrade, J.-F. 2006, A&A, 452, 1099
Pringle, J. E. 1997, MNRAS, 292, 136
Rodriguez, C., Taylor, G. B., Zavala, R. T., et al. 2006, ApJ, 646, 49
Schoenmakers, A. P., de Bruyn, A. G., Röttgering, H. J. A., et al. 2000, MNRAS, 315, 371
Schwartz, D. A., Marshall, H. L., Lovell, J. E. J., et al. 2000, ApJ, 540, 69
Shang, Z., Brotherton, M. S., Wills, B. J., et al. 2011, ApJS, 196, 2
Shepherd, M. C. 1997, ASP Conf. Ser., 125, 77
Vaughan, S., Uttley, P., Markowitz, A. G., et al. 2016, MNRAS, 461, 3145
Wright, E. L. 2006, PASP, 118, 1711

Chapter 8

RadioAstron reveals a change in the jet collimation profile of 3C 84

3C 84 is a Fanaroff-Riley class I radio galaxy at $z = 0.0176$, at a distance of 75.7 Mpc from us (Strauss et al. 1992), located in the center of the Perseus cluster. Its brightness and proximity, as well as the short phases of activity exhibited by this object, make it one of the best studied AGN of the radio sky. It garnered a lot of attention when a new, powerful jet feature emerged from the radio core in 2003 (Suzuki et al. 2012), which provided an excellent opportunity to test theoretical models of jet launching, collimation and evolution.

As *RadioAstron* produces extremely high resolution images, we can probe the jet launching region with space-VLBI. 3C 84 has been targeted by *RadioAstron* previously in 2013, as part of the Nearby AGN Key Science Program. This earlier observation revealed an edge-brightened jet and counter-jet, as well as a quasi-cylindrical jet width profile of $r \propto z^{0.17\pm0.01}$ (Giovannini et al. 2018). This was explained as the collimation effect from the pressure of the mini-cocoon inflated by the jet (Savolainen et al. 2023). These works gave insights on the launching mechanism as well, because the measured wide jet base of 250 $r_{\rm g}$ at a 350 $r_{\rm g}$ distance from the core could be explained either by a quickly expanding jet, or by a composite jet, whose sheath originates from the accretion disk (Blandford & Payne 1982), and the spine is launched from the ergosphere of the central supermassive black hole (Blandford & Znajek 1977).

In this work, I present 22-GHz *RadioAstron* observations from 2016 targeting 3C 84. The aim of this paper is to analyze the evolution of the re-started jet between the two *RadioAstron* observations by tracking changes in the brightness distribution and measuring the collimation profile. In addition, I use quasi-simultaneous multiwavelength VLBA (supplemented by the Effelsberg 100-m telescope) data to measure the core shift and

study the spectra of the core and hotspot.

Our observations confirm the presence of a limb-brightened jet and counter-jet. We find that the jet has swinged towards the west by $(32 \pm 1)^\circ$, and is now more aligned with the downstream hotspot. This precession has been observed before by Britzen et al. (2019) and Dominik et al. (2021) with a period of (25−40) yrs, and can be indicative of the perturbing effect of a warped accretion disk (Pringle 1997) or a SMBHB. The jet has propagated south by ~ 1 mas with a de-projected speed of (0.56 ± 0.03) c. In addition, the hotspot has flipped from the middle of the lobe to the jet head, that is indicative of a termination shock as the jet hits dense clumps of the ambient medium (Kino et al. 2018). This interaction results in an enhanced polarized emission (Nagai et al. 2017) in the hotspot region.

We find that the collimation profile changes from quasi-cylindrical to parabolic, with a power-law width profile of $z^{0.44\pm0.11}$, suggesting that the mini-cocoon cannot collimate the jet efficiently as it propagates further south from the core. Because the resolution of our observations is lower than that from 2013, we can only resolve the two jet rails at ~ 1560 $r_{\rm g}$ from the core, meaning that we cannot confirm nor refute the findings of Giovannini et al. (2018) concerning the jet launching mechanism.

Using the multi-frequency ground-based data at 4.8, 8, 15, and 43 GHz, observed quasi-simultaneously with the *RadioAstron* observations, we study the spectra of the core and hotspot, and the distance to the jet apex in 3C 84. The latter is a debated topic, as the 2013 *RadioAstron* observation and a high-frequency analysis by Paraschos et al. (2021) measure contradicting core shift values. The first constrains the core shift based on the counter-jet detection to be smaller than 30 μas from the 22-GHz core, while the data of Paraschos et al. (2021) pinpoints the jet apex to be (83 ± 7) μas from the 86-GHz core. In our case, I measure the distance from the 43 GHz to the jet apex to be (76.0 ± 3.9) μas when the shift is proportional to the inverse of the frequency, $k_{\rm r} = 1$, and (59.6 ± 34.2) μas when the frequency-dependence of the shift is fitted, $k_{\rm r} = 0.9 \pm 0.2$. From the 22 GHz core these values correspond to (215.2 ± 33.5) μas and (198.8 ± 47.7) μas, that are significantly larger than the 30 μas constraint placed by Giovannini et al. (2018), but are similar to the values obtained by Paraschos et al. (2021). The equipartition magnetic fields strength at 1 pc measured based on the core shift is (0.05 ± 0.01) G, which is a typical value for radio galaxies (Zamaninasab et al. 2014).

I fit the synchrotron self-absorbed spectra (Pacholczyk 1970) to the spectra of the core and hotspot constructed from `modelfit` components. In this case, I measure magnetic field strength for the core and hotspot components based on their SSA spectrum properties, and i find that the magnetic field at the turnover frequency in the core is on the order of $(0.2 - 0.6)$ G, and for the hotspot components it falls between 7 mG and 76 mG.

Conceptualization, T.S., G.G.; methodology, T.S.; formal analysis, P.B.; software, T.S., P.B., M.L.; validation, P.B., T.S.; writing-original draft preparation, P.B.; writing-review and editing, T.S., Y.Y.K., E.R., G.B., M.G.; visualization, P.B.; supervision, T.S.

Astronomy & Astrophysics manuscript no. output
June 27, 2024

RadioAstron reveals a change in the jet collimation profile of 3C 84

P. Benke[1,2], T. Savolainen[3,4,1], G. Giovannini[5,6], Y. Y. Kovalev[1,7], G. Bruni[8], M. M. Lisakov[9,7,1], M. Giroletti[6], and E. Ros[1]

[1] Max Planck Institute for Radio Astronomy, Auf dem Hügel 69, D–53121 Bonn, Germany
[2] Julius Maximilians University Würzburg, Faculty of Physics and Astronomy, Institute for Theoretical Physics and Astrophysics, Chair of Astronomy, Emil-Fischer-Str. 31, D-97074 Würzburg, Germany
[3] Aalto University Department of Electronics and Nanoengineering, PL 15500, FI–00076 Aalto, Finland
[4] Aalto University Metsähovi Radio Observatory, Metsähovintie 114, FI–02540 Kylmälä, Finland
[5] Dipartimento di Fisica e Astronomia, Università di Bologna, via Gobetti 93/2, I–40129 Bologna, Italy
[6] INAF–IRA, Via Gobetti 101, I-40129 Bologna, Italy
[7] Astro Space Center of Lebedev Physical Institute, Profsoyuznaya Street 84/32, Moscow, 117997, Russia
[8] INAF – Institute for Space Astrophysics and Planetology, via del Fosso del Cavaliere, 100, I-00133 Rome, Italy
[9] Instituto de Física, Pontificia Universidad Católica de Valparaíso, Casilla 4059, Valparaíso, Chile

Received / Accepted

ABSTRACT

Context. Due to the brightness and proximity, the radio galaxy 3C 84 (optical counterpart: NGC 1275 in the Perseus cluster) has been the target for extensive studies to investigate the central parsec region of its active galactic nucleus. Its most recent active phase resulted in plasma ejection visible in the southern jet in 2003, which presented a unique opportunity to study jet formation and evolution at high angular resolution with very long baseline interferometry (VLBI).
Aims. We aim to study the morphology, evolution and spectral properties of the re-started jet three years after the first ultra-high angular resolution observations with the RadioAstron space-VLBI satellite in 2013.
Methods. We use space-VLBI observations carried out with the Global VLBI Network and the 10-m Spektr-R radio telescope in orbit at 22 GHz, as well as quasi-simultaneous multi-frequency observations at 4.8, 8, 15, and 43 GHz from the Very Long Baseline Array (VLBA) including the Effelsberg 100-m telescope to study 3C 84.
Results. Here we present a new 22 GHz *RadioAstron* image of 3C 84 that reveals its central region at a 58 μas effective resolution. During the three years that elapsed between this and the previous space-VLBI observation, the source has undergone significant morphological changes. We confirm the existence of the limb-brightened jet and counter-jet reported earlier, as well as a flip in the position of the hotspot discovered via KaVA monitoring at 43 GHz. We measure the collimation profile and find that it has evolved from quasi-cylindrical to parabolic, most likely as a result of the decreased pressure of the cocoon that cannot confine the jet efficiently as it propagates further away from the core.

Key words. Galaxies: jets – Galaxies: active – Galaxies: individual: 3C 84 – Techniques: interferometric – Techniques: high angular resolution – Radio continuum: galaxies

1. Introduction

Although the first active galaxy was discovered more than a hundred years ago (Curtis 1918), several aspects of these powerful and luminous sources are still not well understood. Radio-loud active galactic nuclei (AGN, Zensus 1997) exhibit collimated outflows of relativistic plasma, called jets, whose launching, acceleration and collimation mechanisms still pose open questions for us to investigate (Blandford et al. 2019). Due to the synchrotron radiation of relativistic electrons, jets can be studied at very high angular resolution in the radio domain, using very-long-baseline interferometry (VLBI) either at short wavelengths (Boccardi et al. 2017) or with extremely long baselines. 1.3 mm observations of the central region of M 87 with the Event Horizon Telescope (Event Horizon Telescope Collaboration et al. 2019) were capable of reaching an angular resolution of 20 μas, and detecting the shadow of the central black hole. The angular resolution using space VLBI observations with the *RadioAstron* telescope could exceed even this extraordinary resolution and resolve structures with 11 μas size while observing the maser galaxy NGC 4258 (Baan et al. 2022), and 12 μas when observing the blazar OJ 287 (Gómez et al. 2022).

The low-power radio galaxy, 3C 84 (NGC 1275, Perseus A) is located at the center of the Perseus cluster at $z = 0.0176$, 75.7 Mpc from us (Strauss et al. 1992). 3C 84 is not only a favourable target because of its proximity, but also because early VLBI observations have already revealed the variable nature of this source: Pauliny-Toth & Kellermann (1966) have reported an increase in flux density and angular diameter in the 1960s. 3C 84 has exhibited several periods of activity during the past decades (e.g., Nesterov et al. 1995). Its latest activity started in 2003 when a new component emerged from the radio core (Suzuki et al. 2012). This years-long activity coincided with the first detection of γ-ray emission from 3C 84 by the *Fermi* Gamma-ray Space Telescope (Abdo et al. 2009) in 2008. The source was detected at very high energies (VHE, $E > 100$ GeV) by the MAGIC telescopes in August 2010 (Aleksić et al. 2012), and a bright flare was observed on the night of December 31, 2016 (MAGIC Collaboration et al. 2018). While the γ-ray emission of 3C 84 is variable, it is regularly detected by the *Fermi* LAT.

However, VHE detections are only limited to the flaring episodes exhibited by the source. While no significant correlation was found between the radio and γ-ray activity and the location of the emission regions in these two energy regimes, a common trend is clearly present (Hodgson et al. 2021). Nevertheless, this recently emerged bright component provides an ideal case study to investigate the launching mechanism and evolution of parsec-scale scale jets at extremely high resolution with *RadioAstron*.

RadioAstron was a space VLBI project led by the Astro Space Center of Lebedev Physical Institute. The 10-m Space Radio Telescope (SRT) was launched in 2011 on board the Spektr-R spacecraft designed by the Lavochkin Association. The telescope was decommissioned after 7 years of operation on May 30, 2019. The orbit of *RadioAstron* could reach an apogee height of 370, 000 km. The telescope operated in the K (1.19 – 1.63 cm), C (6.2 cm), L (18 cm), and P bands (92 cm), and could reach the nominal resolution of 7 μas at the highest frequency and longest baselines (Kardashev et al. 2013). This extraordinary resolution, which is three times better than what the EHT can reach at 230 GHz (Event Horizon Telescope Collaboration et al. 2019), enabled the investigation of AGN jets close to their launching region in nearby AGN like 3C 84.

First observations of 3C 84 with *RadioAstron* at 22 GHz and 5 GHz were carried out in 2013, and the results were published in Giovannini et al. (2018) and Savolainen et al. (2023), respectively. Giovannini et al. (2018) reported the existence of a limb-brightened jet that had been also observed by Nagai et al. (2014) and a limb-brightened counter-jet. The collimation profile ($r \propto z^a$, where r is the jet width, z is the de-projected distance from the core, and a is a power-law index) measurement revealed a quasi-cylindrical jet with a power-law index of 0.17 ± 0.01. Another important finding of this observation was the measured wide jet base: the re-started jet is $r \approx 250 r_g$ wide at only $z \approx 350 r_g$ from the radio core. This suggests that the jet or its sheath was launched from the accretion disk, or the jet expanded laterally rather quickly on the first few hundred gravitational radii from the core.

In this paper, our goal was to study the morphology, evolution and spectral properties of the re-started jet of 3C 84 three years after the first 22 GHz *RadioAstron* observations in 2013. We present imaging results from the 2016 *RadioAstron* observations as well as a collimation profile measurement. Using the quasi-simultaneous multi-frequency VLBA data recorded together with the *RadioAstron* observations, we performed spectral analysis of the core and hotspot regions and measured the core-shift. First, we present the observations and the methods used for data reduction in Sect. 2. Then we proceed with the discussion of our analysis and results on the evolution of the re-started jet in Sect. 3 and Sect. 4. We present our collimation profile measurement, spectral analysis and core-shift estimation in Sect. 5, Sect. 7 and Sect. 6. Finally, we summarize our work in Sect. 8.

In this work we assume a ΛCDM cosmology with $H_0 = 70.7$ km s^{-1} Mpc^{-1}, $\Omega_\Lambda = 0.73$, and $\Omega_M = 0.27$. At $z = 0.0176$ this corresponds to a scale of 0.354 pc/mas. While there is a wide range of black hole masses and jet inclination angle estimates for 3C 84 (see for example Scharwächter et al. 2013; Lister et al. 2009; Fujita & Nagai 2017), in order to be compatible with Giovannini et al. (2018), we use a black hole mass of 2×10^9 M$_\odot$ and inclination angle of 18°. See Giovannini et al. (2018) for the discussion of this choice. This means that 1 mas $\approx 3.58 \times 10^3$ r$_g$.

2. Observations and data reduction

2.1. Calibration and imaging of RadioAstron space VLBI data

Space-VLBI observations at 22 GHz were carried out using Global VLBI Network of 23 ground-based antennas and the Space Radio Telescope, *RadioAstron*. The 23 ground-based antennas include the 10 VLBA stations (Brewster, Fort Davis, Hancock, Kitt Peak, Los Alamos, Mauna Kea, North Liberty, Owens Valley, Pie Town, and St. Croix), the 3 KVN stations (Tamna, Ulsan, and Yonsei), as well as Badary, the Effelsberg 100-m telescope, Hartebeesthoek, Medicina, Metsähovi, Noto, Onsala, Svetloe, Yebes, and Zelenchukskaya. Apart from the 24 antennas that provided data, the observation failed at Shanghai, Toruń, Urumqi, and Robledo. The observations started on September 11, 2016, at 13 UT, and finished after 30 hours on September 12, 2016. In addition to the target, 0300+470 and 1823+568 were observed, the first source as a D-term and amplitude calibrator, and the second one as an electric vector polarization angle (EVPA) calibrator. The correlation was performed at the Max-Planck-Institut für Radioastronomie in Bonn, Germany with a DiFX software correlator modified to allow correctly calculating the path delays for an orbiting antenna taking into account special and general relativistic effects (Deller et al. 2007, 2011; Bruni et al. 2016). The integration time was 0.25 s. The correlation was carried out with dual circular polarization at two sub-bands (intermediate frequencies/IFs) with 16 MHz bandwidth. Similarly to the 2013 observations, the recording rate of *RadioAstron* was 128 Mbps, while the ground array antennas recorded data at a 256 Mbps rate. *RadioAstron* used a 1 bit sampling, while the ground array telescopes used 2 bit sampling, resulting in a difference in the bit rate between the ground and space antennas.

Since the Space Radio Telescope is a 10-m antenna with passively cooled receivers, its sensitivity is not always sufficient to detect the source on single baselines between a ground-based antenna and *RadioAstron*. In principle, the detection threshold in fringe search on ground-space baselines can be lowered by phasing up the antennas in the ground array. However, according to Kogan (1996) the same increase in the fringe search sensitivity on the ground-space baselines can be obtained by employing global fringe fitting (Schwab & Cotton 1983) if the ground-ground baselines are much more sensitive than the ground-space baselines. In global fringe fitting, we use all the available data and determine delay, rate, and phase residuals per antenna, not per baseline.

The calibration was carried out in the National Radio Astronomy Observatory's Astronomical Image Processing System (`AIPS`), and imaging of the data was performed in `Difmap` (Shepherd et al. 1994). Data reduction was first performed for the ground array only, and the resulting source model (see the left panel of Fig. 1) was used to correct for the resolved source structure while fringe fitting the ground array data for the second time. After this, the ground-array data are self-calibrated and we could proceed to find a signal on the ground-space baselines. Since we have removed most of the atmospheric phase fluctuations in self-calibration, the solution intervals could be increased significantly, and further enhance the sensitivity on the ground-space baselines (for more discussion about the coherence times on the ground-space baselines, see Savolainen et al. (2023)). In the `AIPS` task `FRING` we used a weighted average of up to three baseline combinations in the initial coarse fringe search stage to improve the sensitivity. While the SNR cutoff in the initial fringe search is generally set to 5, the low signal-to-noise (S/N) space VLBI data often requires examining lower detection thresholds

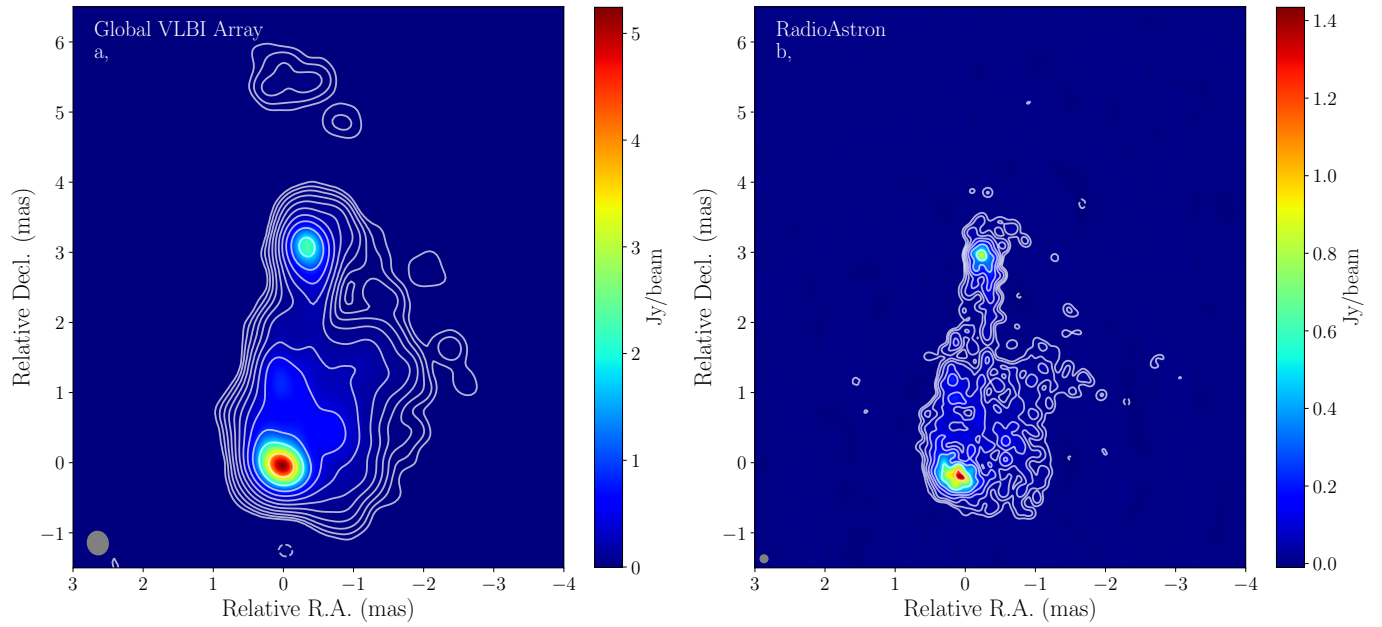

Fig. 1: Hybrid images of 3C 84 from the 2016 *RadioAstron* data. Panel *a* shows the image obtained from the ground array data, whereas panel *b,* contains data from the SRT as well. The lowest contours are at 3.7 mJy/beam for panel *a,* and 8.6 mJy/beam for panel *b,* and further contours increase as a factor of two. The image of the global array data has a total flux density of 27.8 ± 1.4 Jy, and the half-power beam width of the restoring beam is 0.35 × 0.32 mas at PA of 10.8°. The rms noise level is 0.7 mJy/beam. The *RadioAstron* image has a half power beam width of 0.13 × 0.13 mas. The rms noise level is 1.9 mJy/beam, and the total flux density is 23.0 ± 2.3 Jy.

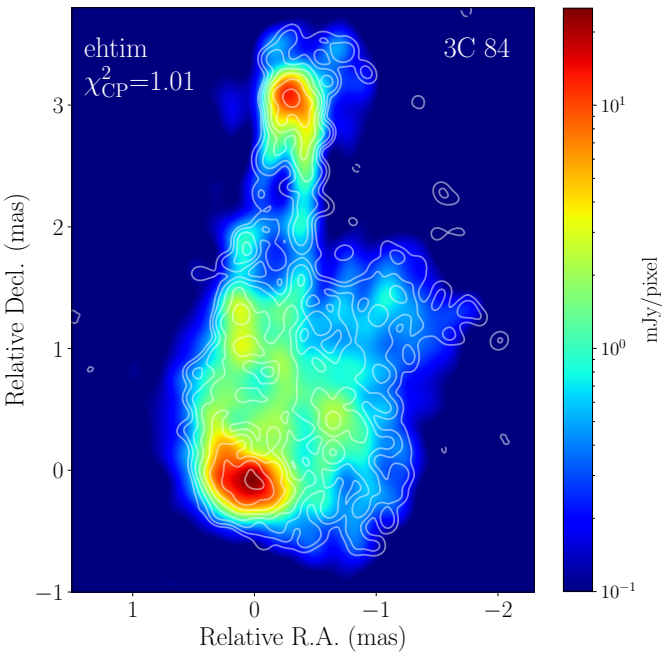

Fig. 2: The final image obtained via `ehtim` from the 22 GHz *RadioAstron* dataset, overlaid with the contours of the `clean` image for comparison. The reduced χ^2 of the closure phases is indicated in the upper left corner.

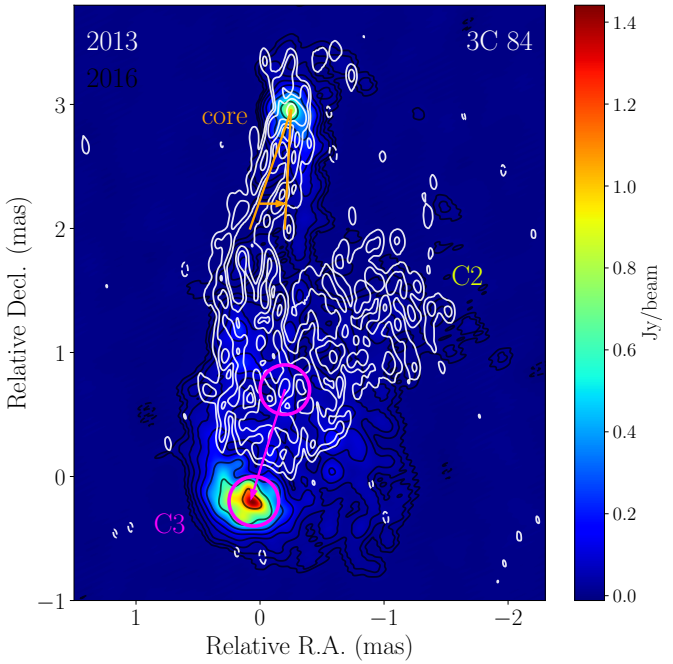

Fig. 3: *RadioAstron* images of 3C 84 from 2013 (white contours) and 2016 (color map and black contours). Black contours are the same as in Fig. 1 panel *b*, and white contours start from 0.75 Jy/beam and increase with the factor of four. Magenta circles mark the change in the hotspot (C3) position between the two epochs, and orange lines indicate the 32 ± 1°change in the jet position angle.

(Savolainen et al. 2023). This makes false detections more likely (see Appendix A) unless one limits the size of the search window

in the delay and rate space. Limiting the search window size requires that at least some fringe detections on space-ground baselines exist and the fringes have been shifted close to zero rate and delay. Frequency averaging in sub-bands after removing instrumental delays and combining left and right circular polarizations can also increase the chances of finding the signal.

During the fringe search at the correlator, the `PIMA` software (Petrov et al. 2011) found fringes between the Effelsberg 100 m telescope and *RadioAstron* in four scans, between 23:15-00:15 UT with S/N ratios in the range of 7.6 to 8.4. During these fringe detections, the SRT was far away from the perigee of its orbit, so acceleration was not fit. We could recover the signal in `FRING` in all four scans, but had no fringe detections in the rest of the scans including *RadioAstron*. However, two of the four fringe detections had a rather low signal-to-noise ratio. These two detections were justified by the smoothly changing rates and delays, and the `PIMA` detection.

Imaging *RadioAstron* data requires a careful treatment. To fully utilize the high angular resolution provided by *RadioAstron*, the ground array is down-weighted by using super-uniform weighting (`uvweight 5,-1`) in `Difmap`. In order not to create spurious flux from the noisy data of the Space Radio Telescope (Savolainen et al. 2023; Martí-Vidal & Marcaide 2008), the solution interval for phase self-calibration for *RadioAstron* was kept at 1 min. Since *RadioAstron* is not affected by the atmosphere, only a single gain correction factor was determined for the SRT, and further steps of amplitude self-calibration with decreasing solution intervals were only performed for the ground array. The final hybrid images are displayed if Fig. 1.

Since the (u, v) coverage of space baselines is very limited making it easy to create spurious features in the imaging process, we tested the significance of the image features by imaging the data also with the `ehtim` package (Chael et al. 2016) using a regularized maximum likelihood method. The image is solved pixel by pixel, and the final image, $\mathbf{I}$, is obtained by minimizing the objective function

$$J(\mathbf{I}) = \Sigma_{\rm dataterms}\alpha_{\rm D}\chi^2_{\rm D}(\mathbf{I},\mathbf{d}) - \Sigma_{\rm regularizers}\beta_{\rm R}S_{\rm R}(\mathbf{I}), \quad (1)$$

where $\chi^2_{\rm D}$ are the goodness-of-fit terms for the vector $\mathbf{d}$ and image $\mathbf{I}$, $S_{\rm R}(\mathbf{I})$ are the regularize terms, and the weights of data and regularizer terms are specified by $\alpha_{\rm D}$ and $\beta_{\rm R}$. As a prior image, we used the ground array `CLEAN` image restored with a 0.5 mas circular beam. We performed the imaging similarly as described in Savolainen et al. (2023), first including data terms of closure phases, log closure amplitudes and visibility amplitudes with low weights. After this, we self-calibrated the phases with a solution interval of 10 s for the ground-based telescopes, and 1 min for *RadioAstron*. In the second round of imaging we used both closure quantities and complex visibilities, then self-calibrated visibility amplitudes with a solution interval of 30 s for the ground array telescopes, and in the case of *RadioAstron* for the whole length of the observation. The final imaging round was performed using the same data terms as before but with updated weights. We used the maximum entropy, total variation, total squared variation regularizer terms, as well as a regularizer of the total flux density with the respective weights of 100, 1, 1, and 10^4. We performed no parameter survey, as we found that variations in the regularizer weights did not significantly affect the final image nor the χ^2 values of the data terms. The final image is shown in Fig. 2.

Comparing the `CLEAN` map in Fig. 1 with the maximum likelihood image made with `ehtim` in Fig. 2, note the latter produces smoother features than `CLEAN` does. As shown recently in Fuentes et al. (2023), `ehtim` is better at recovering filamentary structures, such as limb-brightening in jet and counter-jet. Apart from general differences arising from the distinct nature of these two algorithms, the source shows similar structures (and fits the observed data) on both maps, supporting the robustness of the existence of the edge-brightened features.

2.2. Reduction of the ground-based multi-frequency data

Simultaneous multi-frequency data at 4.8, 8, 15, and 43 GHz were observed with the VLBA and the Effelsberg 100-m Telescope on September 12, 2016, between 05:00 and 18:30 UT. The Medicina 32 m telescope also joined the 4.8 GHz observations. The data were correlated with the DiFX software correlator (Deller et al. 2007, 2011) at the Max-Planck-Institut für Radioastronomie, with dual circular polarization at sub-bands of 16 MHz bandwidth each and a recording rate of 256 Mbps. The data reduction was performed in `AIPS`, where we applied a priori amplitude calibration based on the system noise temperature, $T_{\rm sys}$ and elevation-dependent gain curves provided by the stations. This step also applied opacity corrections based on the weather tables recorded at each antenna. Residual delay and rate fitting were performed with the task `FRING`. Bandpass corrections were not applied. Effelsberg data were lost at 43 GHz due to technical issues. Imaging was performed in a hybrid manner in `Difmap` (Shepherd et al. 1994), iterating the deconvolution method `clean` and self-calibration, shortening the solution interval for each amplitude calibration step. The resulting hybrid images are displayed in Fig. B.1.

3. Jet parameters

The main components of 3C 84, marked in Fig. 3, are the core, connected to the hotspot denoted as C3, with a limb-brightened jet. The faint, diffuse feature, C2, to the southwest is a remnant of previous activity in the source.

Brightness temperatures of the core and hotspot in the *RadioAstron* data were measured via two methods. First, the self-calibrated dataset was fitted with circular and elliptical Gaussian components using the `Difmap` command `modelfit`. However, because of the sparse (u, v) coverage on large distances and the complex structure of 3C 84, we also use the method described in Lobanov (2015), where the minimum and maximum brightness temperature is estimated from the interferometric visibilities and their errors alone, under the assumption that the brightness distribution is circular or axially symmetric and for the maximum brightness temperature we also suppose that the observed structure is marginally resolved. Here we measure the minimum brightness temperature, $T_{\rm b,min}$ as (Lobanov 2015):

$$T_{\rm b,min}[{\rm K}] = 3.09\left(\frac{B}{\rm km}\right)^2\left(\frac{V_{\rm q}}{\rm mJy}\right), \quad (2)$$

where B is the baseline length, and $V_{\rm q}$ is the visibility amplitude. Brightness temperature measurements from this method are shown in Fig 4. The average $T_{\rm b,min}$ on the space baselines is 6.4×10^{12} K.

From the fitted Gaussian components the brightness temperature ($T_{\rm b,obs}$, see Tab. 1) is obtained as:

$$T_{\rm b,obs}[{\rm K}] = 1.22\times10^{12}\left(\frac{S_\nu}{\rm Jy}\right)\left(\frac{\nu}{\rm GHz}\right)^{-2}\left(\frac{b_{\rm min}\times b_{\rm maj}}{\rm mas^2}\right)^{-1}(1+z), \quad (3)$$

where S_ν is the flux density of the components, ν is the frequency of the observation and $b_{\rm min}$ and $b_{\rm maj}$ are the minor and

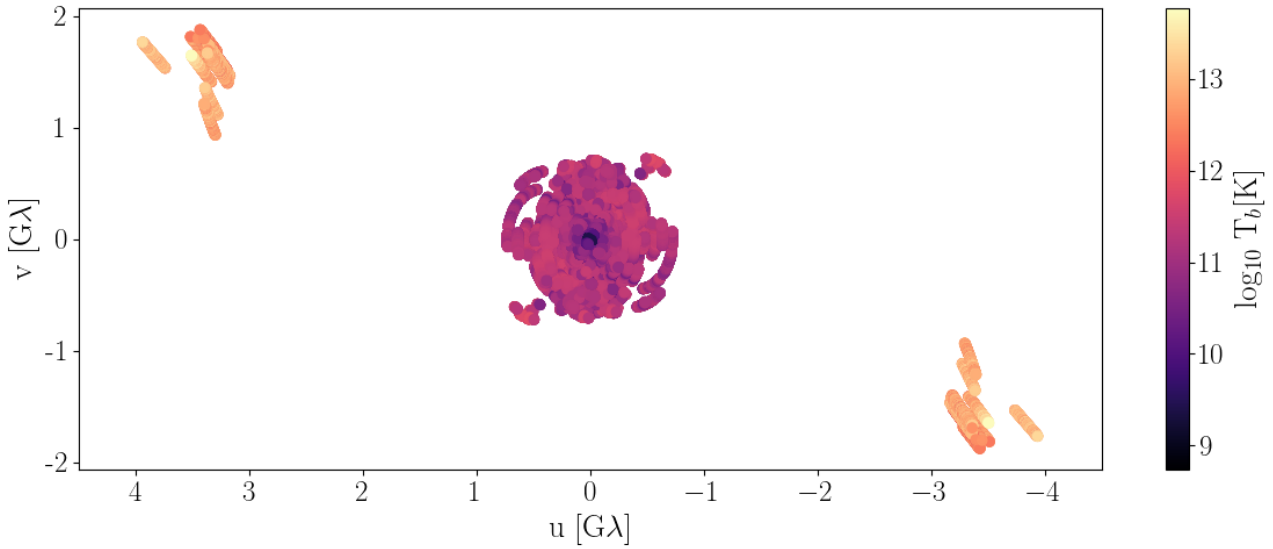

Fig. 4: (u,v) coverage and minimum brightness temperatures estimated from the interferometric visibilities as described in Sect. 3 Eq. 2. (Lobanov 2015).

Table 1: Brightness temperature, Lorentz and Doppler factor measurements for the core and hotspot.

Component	$T_{b,obs}$ [K][a]	Γ_{T_b}[b]	δ_{T_b}[c]	Γ_{kin}[d]	δ_{kin}[e]
Core	$(1.9 \pm 3.1) \times 10^{12}$	4.9 ± 0.5	9.5 ± 1.0	-	-
Hotspot	$(6.7 \pm 0.7) \times 10^{11}$	1.8 ± 0.2	3.3 ± 0.3	1.2 ± 0.1	1.8 ± 0.1

Notes. [(a)] Brightness temperature. [(b)] Lorentz factor determined from the brightness temperature. [(c)] Doppler factor determined from the brightness temperature. [(d)] Lorentz factor determined from kinematics of the jet. [(e)] Doppler factor determined from kinematics of the jet.

major axis of the component. All component sizes are above the resolution limit (Kovalev et al. 2005). Intrinsic brightness temperature, $T_{b,int}$ of a radio-emitting component is calculated as:

$$T_{b,int} = \frac{T_{b,obs}}{\delta(1+z)}, \quad (4)$$

where $\delta = (1-\beta^2)^{-1/2}/(1-\beta\cos\theta)$ is the Doppler factor, β is the component speed in the units of c, and θ is the jet viewing angle. Hence, by assuming an intrinsic brightness temperature value, we can obtain an estimate of the Doppler factor. Instead of the equipartition brightness temperature, $T_{eq} \approx 5 \times 10^{10}$ K (Readhead 1994), we adopt $T_{b,int} = 2 \times 10^{11}$ K suggested by Cohen et al. (2007) for sources in their highest brightness states, which applies to 3C 84 after the ejection of the re-started jet. This value, however, should be taken as a lower limit, since AGN during high states often exhibit intrinsic brightness temperatures greater than 2×10^{11} K (Homan et al. 2006). We infer the Doppler factors for the radio core and the hotspot, and the bulk Lorentz factor, $\Gamma = (1-\beta^2)^{-1/2}$ for the hotspot.

Kinematic analysis was performed by several groups since the emergence of the jet in 2003. In the first few years after its appearance, the jet has accelerated to $\beta \approx 0.2\ c$ (Nagai et al. 2010; Suzuki et al. 2012). The 15 GHz monitoring of the MOJAVE team report a maximum jet speed of $0.409 \pm 0.046\ c$, and significantly accelerating components in the re-started jet of 3C 84 (Lister et al. 2021). The apparent advance speed, β_{app} of the re-started jet was measured between the two *RadioAstron* observations by fitting circular Gaussian components in the image plane of the 2013 observations with the `AIPS` task `JMFIT`, and in the (u, v) plane of the 2016 observations with `Difmap` `modelfit`. The apparent speed is $\beta_{app} = 0.37 \pm 0.05\ c$, corresponding to the advance speed of $\beta = 0.56 \pm 0.03$ assuming $\theta = 18°$. However, viewing angle estimates up to 65° (Fujita & Nagai 2017) exist of the 3C 84 jet, so β ranges from 0.56 ± 0.03 to 0.35 ± 0.04. The bulk Lorentz factor, $\Gamma_{kin} = 1.2 \pm 0.1$, and the Doppler boosting factor, $\delta_{kin} = 1.8 \pm 0.1$, are significantly lower than the ones obtained from the brightness temperature measurements, $\Gamma_{T_b} = 4.9 \pm 0.5$ and $\delta_{T_b} = 1.8 \pm 0.2$ for the core, and $\Gamma_{T_b} = 4.9 \pm 0.5$ and $\delta_{T_b} = 3.4 \pm 0.3$ for the hotspot. The difference between the Doppler factor obtained from kinematics and the brightness temperature suggest that the high $T_{b,obs}$ in the hotspot is not the result of relativistic beaming, but is due to the interaction with the ambient medium (see Sect. 4 and Kino et al. 2021). The high Γ_{T_b} and δ_{T_b} values measured for the hotspot suggest viewing angles smaller than our initial assumption of 18°, with $\theta_{T_b} = 4.1 \pm 1.0°$. The measured brightness temperatures as well as the estimated Lorentz and Doppler factors are shown in Table 1.

4. Evolution of the parsec-scale jet

The 22 GHz *RadioAstron* high-resolution observation presented in this work allows us to investigate the evolution of the re-started jet that emerged in 2003 (Suzuki et al. 2012) at very high resolution. The results were compared with previous observations (see Fig. 3) carried out with *RadioAstron* by Giovannini et al. (2018). The most noticeable changes between the two epochs are the shift of the hotspot's position and the change in the jet base's direction. The new image confirms the existence of the

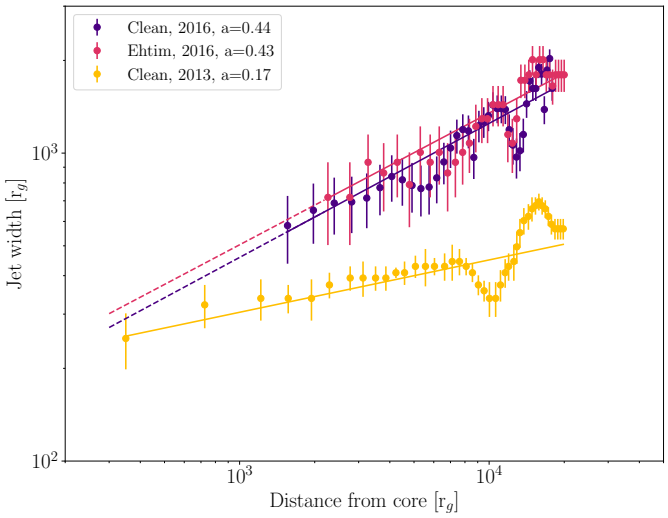

Fig. 5: Collimation profile of 3C 84, showing the jet width as a function of de-projected distance from the core for the 2013 and 2016 measurements. For the latter, we plot the collimation profiles obtained from the hybrid clean and the `ehtim` image as well. The jet width is measured as the separation between the edge-brightened structures of the jet. The closest measurement to the core is at $\sim$ 1560 r_g, where the jet width is $\sim$ 580 r_g. We fitted the profiles with a power-law, and the resulting power-law index is $a = 0.44 \pm 0.11$, indicating a parabolic profile similar to that of M 87.

limb-brightened jet, as well as the limb-brightened counter-jet that was seen on the 2013 map (see Fig. 1 and 2). This confirmation is important, because although the detection of the edge-brightened jet was robust, the same was not true for the limb-brightened counter-jet. The (u,v) coverage on the space baselines is very one-dimensional both in 2013 and 2016, which could have created image artefacts that affected the structure visible on the image. However, the orientation of the space baselines is orthogonal in the two observations, which makes the detection of the counter-jet more robust, as it is recovered in both data sets with different (u,v) coverage.

In the 2016 image (Fig. 3) we see a change in the jet direction. In 2016, the jet is more aligned towards the hotspot at 3 mas to the south. The base of the jet has changed direction by $32° \pm 1$ between the two observations, corresponding to a $\sim 11°$ change per year. Jet precession has been suggested previously by Britzen et al. (2019) and Dominik et al. (2021) with a period of 25 to 30 years based on the 43 GHz VLBA maps from the Boston University Blazar Group's monitoring program between 2010 November and 2020 January. Britzen et al. (2019) suggests two explanations for the jet precession. There may be a binary black hole residing in the centre of NGC 1275, which could cause a precession of the accretion disc, similarly as suggested for OJ 287 by Katz (1997), and recently for M 81 (Jiang et al. 2023). On the other hand, both an instability warping the accretion disk (Pringle 1997), and a misaligned disk with respect to the black hole spin (Liska et al. 2018; Kaaz et al. 2023) can lead to a precessing jet.

AGN jets are expected to interact with the interstellar medium, and even with stars in their host galaxies (e.g, in Centaurus A; Müller et al. 2014), especially in gas-rich galaxies like 3C 84. Kino et al. (2021) recently reported a transition from FR type II to FR type I morphology in the re-started jet. Kino et al. (2018) suggests that due to an interaction with a cold, dense clump of the interstellar medium, the position of the hotspot flipped during 2015 August-September while its peak intensity increased significantly during this period. This morphological change is also seen between the two *RadioAstron* epochs. Based on 43 GHz KaVA and VLBA light curves of the core and the hotspot presented in Kino et al. (2018), in the year following the flip the flux density of the hotspot has increased to four times its original value. It has also been shown by Hodgson et al. (2018) that there was a γ-ray flare originating from C3 around the time of the flip. Nagai et al. (2017) reported an enhanced polarized emission originating from the hotspot, which is expected in regions of the compressed magnetic field (Laing 1980). The authors also estimated the electron number density of the clump to fall between 4×10^3 cm^{-3} and 2×10^5 cm^{-3}, placing it in the narrow-line region of the AGN or in a denser part of an intergalactic molecular cloud. Kino et al. (2021) has shown that after the flip the jet has decelerated, and during the frustration period the position of the hotspot has moved in a counter-clockwise direction within the lobe. When it finally broke out of the ISM in 2018, thus transitioning from an FR II class morphology to an FR I class, it started to accelerate to velocities nearing the speed of light. During the frustration period the radio flux density of the hotspot was decreasing, which decrease stopped after the break–out of the jet. *Fermi* light curve (Hodgson et al. 2018) shows a steady increase in photon flux after the detection of the source in 2008, which culminated around the jet break-out in a flare, after which the flux remained constant. The data presented in this paper is taken at the beginning of the jet frustration period (Kino et al. 2021) of 2016.7 – 2018.0 when jet propagation was halted by a dense clump of the ambient medium. Due to this strong interaction, the position of the hotspot flipped from the center of the lobe to the leading edge around 2015 August-September (Kino et al. 2018).

Intrinsic brightness temperatures both in the core and hotspot significantly exceed the equipartition brightness temperature, $T_{\rm eq} \sim 5 \times 10^{10}$ K (Readhead 1994). However, the Doppler factor calculated from the kinematics, $\delta_{\rm kin} = 1.8 \pm 0.1$, indicates that the emission is weakly beamed. This suggests that the hotspot, which is associated with a termination shock at the jet head, is strongly particle dominated, probably due to the particle acceleration by the shock itself.

5. Collimation profile measurement

3C 84, similarly to nearby AGN, such as M 87 (Asada & Nakamura 2012), Mrk 421 (Giroletti et al. 2006), Mrk 501 (Giroletti et al. 2004), Cygnus A (Boccardi et al. 2016), or Centaurus A (Janssen et al. 2021), exhibits a limb-brightened structure in its jet. The structure was first observed on the 43 GHz VLBA image by Nagai et al. (2014), and it was also detected – together with a limb-brightened counter-jet – in both of the 22 GHz *RadioAstron* observations. The collimation profile can be described as $r \propto z^a$, for which the jet width, r, is a function of de-projected distance, z from the radio core, and a, the power-law index, implies: cylindrical for $a = 0$, parabolic for $a = 0.5$, and conical for $a = 1$. Collimation profile measurements by both Nagai et al. (2014) and Giovannini et al. (2018) report a quasi-cylindrical profile with power-law indices of 0.25 ± 0.03 and 0.17 ± 0.01, respectively. While the majority of AGN show a parabolic profile between the radio core and the transition zone to conical expansion at $\sim 10^4 - 10^6 r_g$ (Kovalev et al. 2020), a similar, cylindrical profile with power-law index of 0.16 was reported in the receding jet of NGC 1052 by Baczko et al. (2021). The quasi-cylindrical

profile of the re-started jet can be explained by the shallow pressure profile and almost constant density of a hot cocoon surrounding the re-started jet. The low-intensity cocoon emission was indeed discovered by Savolainen et al. (2023) in the 5 GHz *RadioAstron* data recorded simultaneously with the 22 GHz observations in 2013. Re-collimation by a surrounding cocoon has only been studied on kiloparsec scales previously (Komissarov & Falle 1998). The parsec-scale cocoon in 3C 84 was created by the re-started jet.

For our new 22 GHz *RadioAstron* data we measure the jet width profile in the manner similar to that used by Nagai et al. (2014) and Giovannini et al. (2018), by slicing the jet perpendicular to its direction and fitting 1D Gaussians on the limb-brightened edges to measure the separation of their peak positions. For the mass of the central SMBH and the jet inclination, we adopt the same values as Giovannini et al. (2018). The resulting collimation profile is parabolic with a power-law index of $a = 0.44 \pm 0.11$ (see Fig. 5). The closest measurement is located at $\sim$ 1560 r_g from the core. The width of the jet base at these distances is $\sim$ 580 r_g.

The parabolic profile, $r \propto z^{0.44\pm0.11}$ measured in this work is similar to the ones in the literature for M 87 ($r \propto z^{0.56\pm0.01}$, Nakamura et al. 2018), Cygnus A ($r \propto z^{0.55\pm0.07}$, Boccardi et al. 2016), and many other AGN in the MOJAVE sample (Kovalev et al. 2020). The profile suggests a decreasing pressure profile as a function of radius for the external medium, $p_{\rm ext} \propto z^{-4a} = z^{-1.76}$, and a density of the ambient medium decreasing as $\rho_{\rm ext} \propto z^{-k} = z^{1-4a} = z^{-0.76}$. The wider collimation profile is likely due to the decreasing pressure of the cocoon, which provides less confinement to the jet as it itself expands.

3D general relativistic magnetohydrodynamic simulations (GRMHD) presented in Rohoza et al. (2024) explore the collimation mechanisms which may result in a cylindrical jet width profile close to the black hole. They highlight the importance of accretion disk cooling, as such a disk collapses to the midplane as the simulation progresses and the resulting weaker disk winds allow for backflows to reach closer to the central engine than in accretion disks that do not cool efficiently. These backflows are capable of collimating the jet to a cylindrical shape closer to the BH. However, when the disk wind starts to dominate the jet power it will provide a stronger collimation, resulting in a smaller jet width and a quasi-parabolic collimation profile. It is possible that we are seeing this effect take place in our *RadioAstron* observations, when the collimation profile changes from quasi-cylindrical (Giovannini et al. 2018) to parabolic (Fig. 5).

The 2013 *RadioAstron* observations of Giovannini et al. (2018) also revealed a rather wide jet base of 250 r_g at merely 350 r_g from the core. This lead the authors to conclude that the jet is either launched from the accretion disk (Blandford & Payne 1982), or the jet sheath is launched from the accretion disk and the spine from the black hole ergosphere (Blandford & Znajek 1977). It is also possible that the jet is launched from the ergosphere, but expands quickly laterally in the first few hundred gravitational radii after launching. Unfortunately, we are only able to distinguish the limb-brightened edges at $\sim$ 1600 r_g from the core, so we cannot confirm nor refute their conclusions. However, extrapolating our jet width measurement down to 200 r_g, we get similar widths as measured by Giovannini et al. (2018) (see Fig. 5). A core-shift measurement (see next Section) is important to discuss this point.

6. Core-shift measurement

The location of the SMBH can be estimated by core-shift measurements. The detection of the counter-jet in the 22 GHz *RadioAstron* image by Giovannini et al. (2018) enabled the authors to constrain the distance between the SMBH and the 22 GHz core to be less than 30 μas. On the other hand, multi-frequency VLBI observations of Paraschos et al. (2021) place the jet apex farther out, 76−90 μas, from the 86 GHz core. Long-term GMVA measurements of Oh et al. (2022) are in agreement with this, placing the jet apex to fall between 54 and 215 μas upstream of the 86 GHz core. Placing the SMBH this far from the radio core would suggest a narrower jet base than measured in the 22 GHz *RadioAstron* image. However, the recent work by Park et al. (2023) measured a core shift of 14.1 μas between their 22 and 43 GHz maps, significantly smaller than Paraschos et al. (2021).

At a given frequency, the VLBI core represents the surface where the synchrotron self-absorption opacity $\tau = 1$, whose position therefore is frequency-dependent (Blandford & Königl 1979). Since higher frequencies probe regions closer to the central SMBH, we can extrapolate the location of the central engine based on the relative core position shifts, as a function of frequency, with respect to one of the maps if the jet stays self-similar down to the central engine (Marcaide & Shapiro 1984; Lobanov 1998). Here we estimate the distance to the jet apex with respect to the 43 GHz core position. For this, we followed the method described in O'Sullivan & Gabuzda (e.g., 2009), Pushkarev et al. (2012), and Fromm et al. (2013). First, we aligned the maps of two adjacent frequencies on the optically thin jet using 2D cross-correlation implemented in the software FITSalign. Before applying the cross-correlation, we matched the (u, v) range of the data sets to be similar, and the pixel and restoring beam sizes for the image pairs were chosen to be that of the lower-frequency map. As FITSalign allows for selecting the image area used for the cross-correlation, we tried to align the maps based on the optically thin lobe or jet emission, excluding the optically thick C3 component. Excluding the optically thick core region was difficult at 4.8 and 8 GHz, because the emission is dominated by the jet and the hotspot, and the core is not resolved at these frequencies. After the alignment, we measured the difference between the core component positions, obtained from `modelfit` in `Difmap`, between the different frequencies (see Tab. C.2). Errors in the image alignment were taken to be half of the pixel size of a given frequency pair, and `modelfit` error positions of the core were estimated based on the χ^2 minimization method described in Lampton et al. (1976).

If we assume that both the particle density and the magnetic field decrease with the distance, the magnetic flux is conserved, then the apparent distance between the VLBI core and the jet apex is given as (Lobanov 1998):

$$\Delta r_{\rm core}[\mu{\rm as}] = r_0 \left[\left(\frac{\nu}{43{\rm GHz}} \right)^{-1/k_{\rm r}} - 1 \right], \quad (5)$$

where r_0 is the distance to the jet apex from the 43 GHz core. In the case of a conical jet in equipartition, $k_{\rm r} = 1$. As the jet of 3C 84 is not conical but parabolic, we also fit $k_{\rm r}$. An additional motivation for this is the jump between the 22 and 43 GHz core distances that breaks the ν^{-1} dependency. The positions of the lower-frequency cores with respect to the 43 GHz one, as well as the fit results are are shown in Fig. 6.

With $k_{\rm r} = 1$ we obtain the jet apex location to be 76 ± 4 μas from the 43 GHz core, and 215 ± 34 μas from the 22 GHz core. When $k_{\rm r}$ is fitted, we obtain $k_{\rm r} = 0.9 \pm 0.2$ and a distance to the central SMBH from the 43 GHz core to be 60 ± 34 μas,

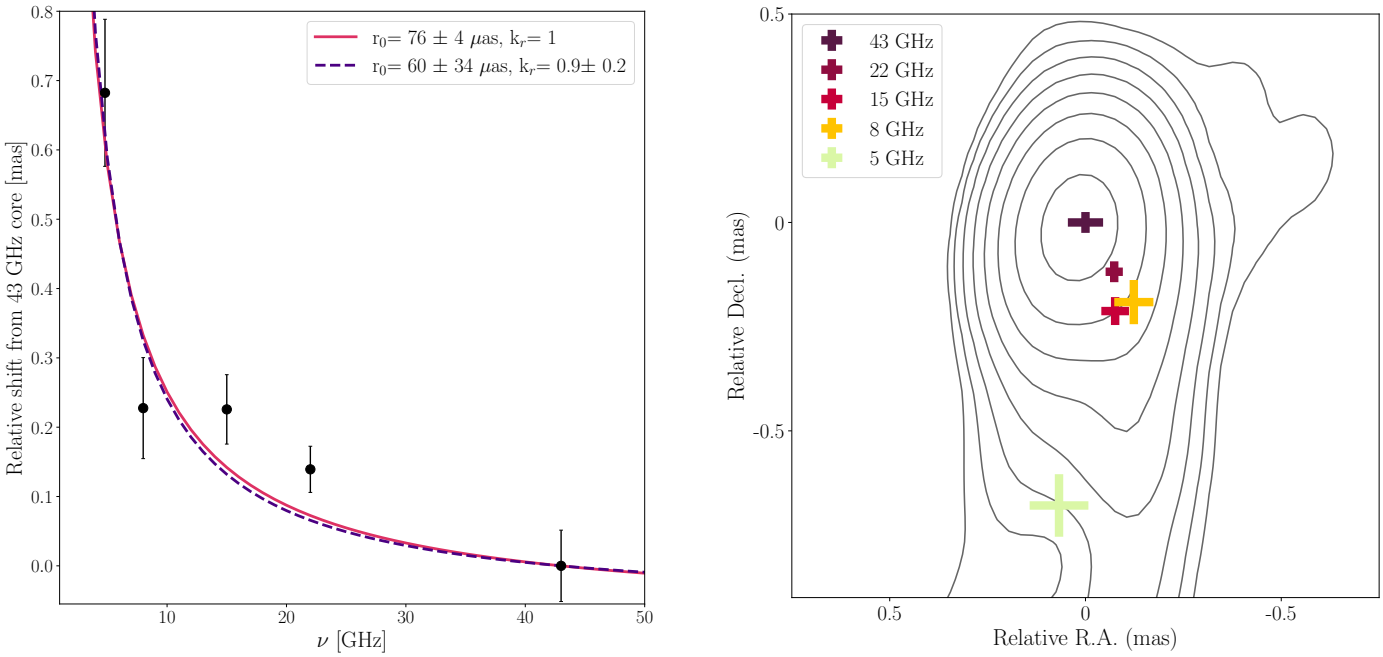

Fig. 6: *Left panel:* Positions of the lower-frequency cores with respect to the 43 GHz one. *Right panel:* Core-shift measurement with respect to the 43 GHz core position.

and 199 ± 48 μas from the 22 GHz core. These core shift values fall between what is reported in Giovannini et al. (2018) and Paraschos et al. (2021).

We can also estimate the magnetic field strength based on the coreshift measurement (Lobanov 1998; Hirotani 2005; Zdziarski et al. 2015; Lisakov et al. 2017), and compare them with the values obtained from our spectral fit (see Sect. 7). First, we calculate $\Omega_{\rm r}^{\nu}$ between $\nu_1 = 43$ GHz and $\nu_2 = 5$ GHz Lobanov (1998):

$$\Omega_{\rm r}^{\nu}[{\rm pcGHz}^{1/k_{\rm r}}] = 4.85\times10^{-9}\frac{\Delta r_{\rm core} D_{\rm L}}{(1+z)^2}\left(\frac{\nu_1^{1/k_{\rm r}}\nu_2^{1/k_{\rm r}}}{\nu_2^{1/k_{\rm r}}-\nu_1^{1/k_{\rm r}}}\right). \quad (6)$$

We use the following equation from Zdziarski et al. (2015) to calculate the equipartition magnetic field strength at 1 pc, or in this case, 2.82 mas, from the central engine:

$$B_{\rm 1pc}^{\rm eq}[{\rm G}] \approx 0.025\left[\frac{\Omega_{r\nu}^{3k_{\rm r}}(1+z)^3}{\delta^2\phi\sin^{3k_{\rm r}-1}\theta}\right]^{\frac{1}{4}}, \quad (7)$$

where ϕ is the intrinsic opening angle. We calculated ϕ based on the projected distance to the jet width measured closest to the core at the 22 GHz *RadioAstron* image, which are 0.131 ± 0.039 mas and 0.158 ± 0.039 mas, respectively. The apparent opening angle is $\phi_{\rm app} = 2\arctan(r/z) = 101\pm22°$, and the intrinsic opening angle $\phi = 2\arctan(\tan(\phi_{\rm app}/2)\sin\theta)$ which yields $\phi = 41 \pm 15°$.

We also calculate the non-equipartition magnetic field strength at 1 pc from the central engine Zdziarski et al. (2015):

$$B_{\rm 1pc}^{\rm non-eq}[{\rm G}] \approx \frac{3.35\times10^{-11} D_L \Delta r_{\rm core}\delta\tan\phi}{(\nu_1^{-1}-\nu_2^{-1})^5[(1+z)\sin\theta]^3 F_\nu^2}, \quad (8)$$

where F_ν is the flux density in the flat, $\propto \nu^0$, part of the spectrum. F_ν is the flux density of the inner jet which excludes the flux density contribution of the outer lobes. The optically thin spectrum of 3C 84 is not flat, but slightly steep with $\alpha = -0.84 \pm 0.11$ (see Tab. 2). As a result of this, we adopt F_ν as the flux density of the 22 GHz total flux density, as this measurement falls on the optically thin part of the spectrum and the source structure is only comprised of the core, jet and counter-jet at this frequency.

We measure $B_{\rm 1pc}^{\rm eq} = 0.05 \pm 0.01$ G and $B_{\rm 1pc}^{\rm non-eq} = 0.11 \pm 0.12$ G. The $B_{\rm 1pc}^{\rm eq}$ measured in 3C 84 is similar to the values measured in the radio galaxy sample of Zamaninasab et al. (2014). Extrapolating these values to the distance of the 22 GHz core and hotspot, which are 0.131 ± 0.039 mas and 3.331 ± 0.046 mas, under the $k_{\rm r} = 1$ assumption as $B = B_{\rm 1pc} r_{\rm 1pc}/r$, we obtain $B_{\rm core,22GHz} = 0.353 \pm 0.110$ G and $B_{\rm C3,22GHz} = 0.014 \pm 0.001$ G.

7. Spectral analysis of ground-based VLBI data

Using the quasi-simultaneous observations at 4.8, 8, 15 and 43 GHz, we were able to construct spectral index maps and perform a coreshift measurement. The spectral index maps were made between two adjacent frequencies using 2D cross-correlation on the optically thin jet, excluding the C3 optically thick hotspot region whenever possible, as described in Sect. 6.

In the spectral index maps shown in Fig. D.1, the inverted spectrum of the counter-jet is probably due to free-free absorption, which was previously reported both in the lobes originating from the component ejection in the 1990s (Walker et al. 2000) and for the re-started jet as well (Nagai et al. 2017). The spectral index of the hotspot between the lower frequency map pairs is inverted, but between 15 − 22 and 22 − 43 GHz pairs, it is flat, while the jet has a slightly steeper spectral index. Spectral index maps show a north-south gradient in the core, which can be explained by synchrotron self-absorption, and an inverted spectrum in the counter-jet, which is indicative of free-free absorption.

In order to ensure that we are extracting the spectra from the same source regions through our observing frequencies, we utilize the model transfer method described in Savolainen (2006). This method enabled us to measure the flux density of components smaller than the beam size at the lower frequencies. First,

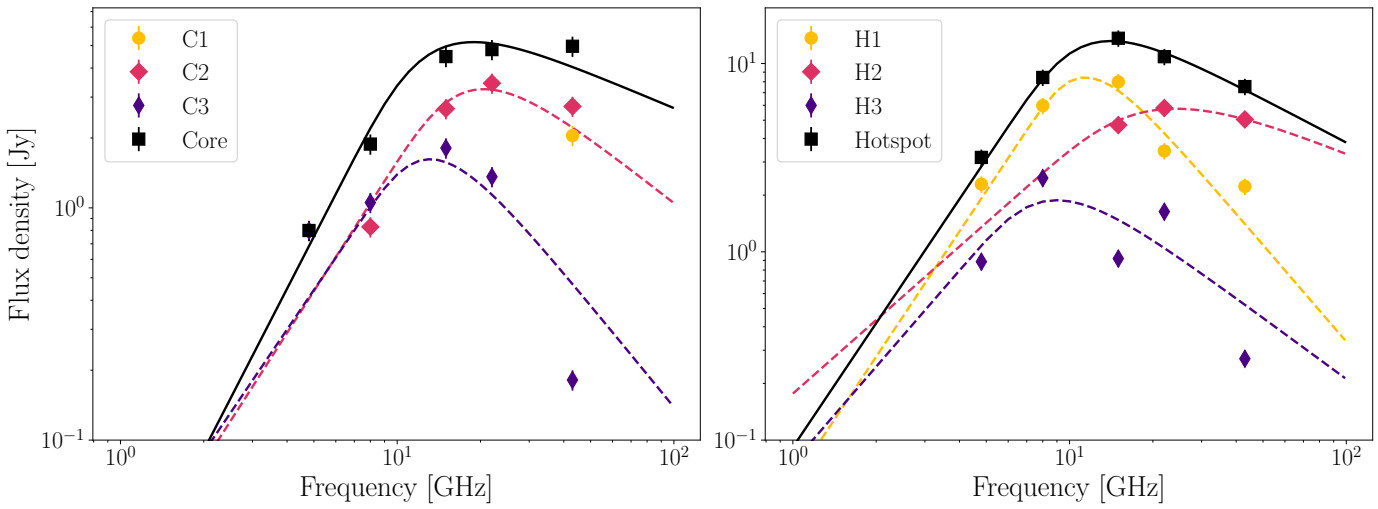

Fig. 7: Spectra of 3C 84 total flux density, core and jet emission, and best fit SSA models. Flux density errors are assumed to be 10%. Fit values are summarized in Tab. 2.

we obtained a simplified model of the 43 GHz map using circular Gaussian components. In order to transfer these components to the lower frequency maps, we used the shifts obtained from the 2D cross correlation to align the components between the frequencies. The assumption behind this is that there are no spectral index gradients along the components, thus they do not show positional changes with frequency.

In the first round we only fitted for the flux density and size of the components. While we assume that the size of the components is either constant or shows a smooth variation with frequency, this was not the case for the 5 and 8 GHz components that all showed a steep increase in size compared the smooth changes between 15 and 43 GHz. As a result of this, we only fit linear trends to the 15, 22 and 43 GHz component sizes to remove the low-frequency outliers. This step was important, because the component size is used for the magnetic field strength estimation, where it is assumed the components describe the same jet region. Finally, the angular sizes were fixed to the values derived from the linear fits, and only the flux density was allowed to vary in the subsequent model fitting step. The component characteristics are listed in Tab. C.3.

In general, the core region could be described with two (except at 43 GHz, where it consists of three), and the hotspot with three components, which we used to estimate the size and flux density contained within these regions. We study the spectrum of 3C 84 by fitting the total flux density, as well as the flux density of the individual core and hotspot components, as well as their sum, with a synchrotron self-absorbed spectrum (SSA, Pacholczyk 1970):

$$S_\nu(\nu) = S_\mathrm{m}\left(\frac{\nu}{\nu_\mathrm{m}}\right)^{\alpha_\mathrm{thick}} \frac{1-e^{-\tau_\mathrm{m}(\frac{\nu}{\nu_\mathrm{m}})^{\alpha-\alpha_\mathrm{thick}}}}{1-e^{-\tau_\mathrm{m}}} \tag{9}$$

where ν_m is the turnover frequency, S_m and τ_m are the maximum flux density and the optical depth at ν_m, α and α_thick are the spectral indices at the optically thin and thick parts of the spectrum. We approximate τ_m (Türler et al. 1999):

$$\tau_\mathrm{m} \approx \frac{3}{2}\left(\sqrt{1-\frac{8\alpha}{3\alpha_\mathrm{thick}}}-1\right). \tag{10}$$

Spectra are shown in Fig. 7, and fit parameters are summarized in Table 2.

If the components in questions are resolved, under the assumption that the emission region is homogeneous and spherical we can estimate the synchrotron self-absorption magnetic field based on Eq. 2 from Marscher (1983):

$$B_\mathrm{SSA}[G] = 10^{-5} b(\alpha) a(\nu_\mathrm{m})^4 \nu_\mathrm{m}^5 \left(\frac{S_\mathrm{m}\tau_\mathrm{m}}{1-e^{-\tau_\mathrm{m}}}\right)^{-2}\left(\frac{\delta}{1+z}\right), \tag{11}$$

where $b(\alpha)$ can be found in Marscher (1983) for typical spectral index values, $a(\nu_\mathrm{m})$ is the size of the emission region at the turnover, and can be estimated from linear interpolation based on the relation $a \propto \nu^{-1}$. In order to approximate the size of a partially opaque spherical source, the size of the fitted Gaussian components were multiplied by 1.6 as the components are (partially) optically thick. The size of the core and hotspot regions across the observing frequencies were measured as the sum of the distance between their most distant sub-components and their respective half widths, then these values were interpolated to the turnover frequency. For the total flux density magnetic field strength estimate, we used the same emission region sizes as for the core, interpolated to the turnover frequency estimated for the total flux density. The error of B_SSA was estimated by fitting 10000 realisations of the function, drawing from a Gaussian distribution whose mean corresponded to the value of a given parameter, with a standard deviation which corresponded to the error of said parameter.

The strength of the magnetic field at the turnover frequency in the core is on the order of 0.2-0.6 G, and for the hotspot components it falls between 7 and 76 mG. Given the generally low turnover frequencies of the C3, H1 and H3 components, these magnetic field strength estimates refer to components at a significant distance from the jet apex. As C2 and H2 have turnover frequencies of ~20 GHz, we compare them to the B_eq obtained from the core shift. As mentioned above, B_eq is 0.353 ± 0.110 G and 0.014 ± 0.001 G at the distance of the 22 GHz core and hotspot, respectively. This value agrees well with the $10^{-0.67\pm1.06} \approx 0.21$ G measured for the C2 component, and is about twice larger than the $10^{-1.08\pm1.58} \approx 0.08$ G measured in H2.

Paraschos et al. (2024) measured a magnetic field strength of 2.9 ± 1.6 G at the turnover frequency of 113 ± 4 GHz based on the total VLBI flux density between 15 and 228 GHz. They

report an equipartition magnetic field strength of 5.2 ± 0.6 G, which is consistent with our value measured in the core region, $B_{\rm SSA} \approx 5.1$ G at the turnover frequency of 23.7 ± 4.1 GHz.

8. Conclusions

We present new 22 GHz *RadioAstron* space VLBI observations of 3C 84 from 2016 that follow up the 2013 22 GHz *RadioAstron* results published by Giovannini et al. (2018). Our goal was to observe the evolution of the parsec-scale jet, whose latest phase of activity started when a new, bright jet component emerged from the core in 2003 (Suzuki et al. 2012). This, together with the proximity and brightness of the source, made 3C 84 a favourable target for *RadioAstron* to study the formation and evolution of parsec-scale jets.

We were able to detect fringes between the ground array and *RadioAstron* in four scans resulting in baselines reaching 4.32 Gλ or 4.4 Earth diameters. This corresponds to an equivalent resolution of 58 μas. Our high-resolution image displayed in Fig. 1 confirms the existence of the limb-brightened jet and counter-jet detected in 2013. We also see that the jet has swung by approximately 32° to the west, and is now more aligned with the hotspot. Britzen et al. (2019) and Dominik et al. (2021) inferred the period for the jet precession to be $\gtrsim$ 30 yr, and suggest that it could indicate the presence of a warped accretion disk (Pringle 1997) or a companion SMBH. Since 2013, the position of the hotspot has flipped to the leading edge of the jet, indicative of a termination shock as the jet hits dense clumps of the ambient medium (Kino et al. 2018). This interaction results in an enhanced polarized emission (Nagai et al. 2017) in the hotspot region.

The jet width profile of the re-started jet of 3C 84 has also evolved between the two *RadioAstron* observations. For the jet width, r as a power-law of the distance from the core, $r \sim z^a$, the quasi-cylindrical ($a = 0.17 \pm 0.01$, Giovannini et al. 2018) profile of 2013 has changed to parabolic ($a = 0.44 \pm 0.11$) by 2016. The parabolic profile suggests a rapidly decreasing pressure profile as a function of radius for the external medium, and its development can be attributed to the decreasing pressure of the hot cocoon (Savolainen et al. 2023) that cannot collimate the jet efficiently as the cocoon itself expands.

In addition, we have analysed the quasi-simultaneous multi-frequency dataset observed at 4.8, 8, 15 and 43 GHz with the VLBA and Effelsberg, as well as with Medicina at the lowest frequency (see hybrid maps in Fig. B.1). This multi-frequency dataset, together with the 22 GHz ground array image, made it possible to perform a spectral analysis (Fig. D.1 and 7) and measure the distance to the jet apex from the 43 GHz core. We measure the distance from the 43 GHz to the jet apex to be 76 ± 4 μas with $k_{\rm r} = 1$, and 60 ± 34 μas when $k_{\rm r} = 0.9 \pm 0.2$ is fitted. From the 22 GHz core these values correspond to 215 ± 34 μas and 199 ± 48 μas, that are significantly larger than the 20 μas constraint placed by Giovannini et al. (2018), but are much smaller than the values obtained by Paraschos et al. (2021). The equipartition magnetic fields strength at 1 pc measured based on the core shift is 0.05 ± 0.01 G, which is a typical value for radio galaxies (Zamaninasab et al. 2014).

We have also calculated the magnetic field strength for the core and hotspot components based on their SSA spectrum properties, and we find that the magnetic field at the turnover frequency in the core is on the order of 0.2-0.6 G, and for the hotspot components it falls between 7 and 76 mG. The $B_{\rm SSA}$ = 2.9 ± 1.6 G value reported by Paraschos et al. (2024) based on VLBI total flux density spectrum is in a good agreement with the $B_{\rm SSA} \approx 5.1$ G measured in the core region at the turnover frequency of 23.7 ± 4.1 GHz.

Acknowledgements. The RadioAstron project is led by the Astro Space Center of the Lebedev Physical Institute of the Russian Academy of Sciences and the Lavochkin Scientific and Production Association under a contract with the State Space Corporation ROSCOSMOS, in collaboration with partner organizations in Russia and other countries. Based on observations with the 100-m telescope of the MPIfR (Max-Planck-Institut für Radioastronomie) at Effelsberg. The National Radio Astronomy Observatory is a facility of the National Science Foundation operated under cooperative agreement by Associated Universities, Inc. The European VLBI Network is a joint facility of independent European, African, Asian, and North American radio astronomy institutes. This research is based on observations correlated at the Bonn Correlator, jointly operated by the Max Planck Institute for Radio Astronomy (MPIfR), and the Federal Agency for Cartography and Geodesy (BKG). This research was supported through a PhD grant from the International Max Planck Research School (IMPRS) for Astronomy and Astrophysics at the Universities of Bonn and Cologne. We acknowledge the M2FINDERS project from the European Research Council (ERC) under the European Union's Horizon 2020 research and innovation programme (grant agreement No 101018682). This research has made use of NASA's Astrophysics Data System Bibliographic Services.

References

Abdo, A. A., Ackermann, M., Ajello, M., et al. 2009, ApJ, 699, 31
Aleksić, J., Alvarez, E. A., Antonelli, L. A., et al. 2012, A&A, 539, L2
Asada, K. & Nakamura, M. 2012, ApJ, 745, L28
Baan, W. A., An, T., Henkel, C., et al. 2022, Nature Astronomy, 6, 976
Babul, A., Sharma, P., & Reynolds, C. S. 2013, ApJ, 768, 11
Baczko, A.-K., Ros, E., Kadler, M., et al. 2021, arXiv:2111.09850
Benke, P., Gabányi, K. É., Frey, S., et al. 2023, A&A, 677, A1
Blandford, R. D. & Königl, A. 1979, ApJ, 232, 34
Blandford, R. D. & Payne, D. G. 1982, MNRAS, 199, 883
Blandford, R. D. & Znajek, R. L. 1977, MNRAS, 179, 433
Blandford, R., Meier, D., & Readhead, A. 2019, ARA&A, 57, 467
Boccardi, B., Krichbaum, T. P., Bach, U., et al. 2016, A&A, 585, A33
Boccardi, B., Krichbaum, T. P., Ros, E., et al. 2017, A&A Rev., 25, 4
Britzen, S., Fendt, C., Zajaček, M., et al. 2019, Galaxies, 7, 72
Bruni, G., Anderson, J., Alef, W., et al. 2016, Galaxies, 4, 55
Chael, A. A., Johnson, M. D., Narayan, R., et al. 2016, ApJ, 829, 11
Chael, A. A., Johnson, M. D., Bouman, K. L., et al. 2018, ApJ, 857, 23
Cohen, M. H., Lister, M. L., Homan, D. C., et al. 2007, ApJ, 658, 232
Cotton, W. D 1992, Polarization Calibration of VLBI Data, AIPS Memo 79, NRAO
Curtis, H. D. 1918, Publications of Lick Observatory, 13, 9
Deller, A. T., Tingay, S. J., Bailes, M., et al. 2007, PASP, 119, 318
Deller, A. T., Brisken, W. F., Phillips, C. J., et al. 2011, PASP, 123, 275
Desai,K. M. 1998, The Calculation of SNR in KRING's FFT stage, AIPS Memo 101, NRAO
Dominik, R. M., Linhoff, L., Elsässer, D., et al. 2021, MNRAS, 503, 5448
Event Horizon Telescope Collaboration, Akiyama, K., Alberdi, A., et al. 2019, ApJ, 875, L1
Fromm, C. M., Ros, E., Perucho, M., et al. 2013, A&A, 557, A105
Fuentes, A., Gómez, J. L., Martí, J. M., et al. 2023, Nature Astronomy, 7, 1359
Fujita, Y. & Nagai, H. 2017, MNRAS, 465, L94
Giovannini, G., Savolainen, T., Orienti, M., et al. 2018, Nature Astronomy, 2, 472
Giroletti, M., Giovannini, G., Feretti, L., et al. 2004, ApJ, 600, 127
Giroletti, M., Giovannini, G., Taylor, G. B., et al. 2006, ApJ, 646, 801
Gómez, J. L., Traianou, E., Krichbaum, T. P., et al. 2022, ApJ, 924, 122
Hirotani, K. 2005, ApJ, 619, 73
Hodgson, J. A., Rani, B., Lee, S.-S., et al. 2018, MNRAS, 475, 368
Hodgson, J. A., Rani, B., Oh, J., et al. 2021, ApJ, 914, 43
Homan, D. C., Kovalev, Y. Y., Lister, M. L., et al. 2006, ApJ, 642, L115
Högbom, J. A. 1974, A&AS, 15, 417
Janssen, M., Falcke, H., Kadler, M., et al. 2021, Nature Astronomy, 5, 1017
Jiang, W., Shen, Z., Martí-Vidal, I., et al. 2023, ApJ, 959, 11
Kaaz, N., Liska, M. T. P., Jacquemin-Ide, J., et al. 2023, ApJ, 955, 72
Kardashev, N. S., Khartov, V. V., Abramov, V. V., et al. 2013, Astronomy Reports, 57, 153
Katz, J. I. 1997, ApJ, 478, 527
Kino, M., Wajima, K., Kawakatu, N., et al. 2018, ApJ, 864, 118
Kino, M., Niinuma, K., Kawakatu, N., et al. 2021, ApJ, 920, L24
Kogan, L. (1996): Global Ground VLBI Network as a Tied Array for Space VLBI. *VLBA Scientific Memo.*

Table 2: SSA spectrum fit parameters from Fig. 7.

Component	$S_{\rm m}$ [Jy][a]	$\nu_{\rm m}$ [GHz][b]	$\alpha_{\rm thick}$[c]	α[d]	$\tau_{\rm m}$[e]	$a(\nu_{\rm m})$ [mas][f]	$B_{\rm SSA}$ [G][g]
C2	3.2 ± 0.7	20.2 ± 2.5	1.9 ± 0.8	-0.9 ± 0.6	0.8 ± 0.5	0.43 ± 0.17	$10^{-0.67\pm1.06}$
C3	1.6 ± 0.6	13.1 ± 4.2	1.8 ± 0.9	-1.4 ± 0.8	1.2 ± 0.7	0.82 ± 0.50	$10^{-0.23\pm1.79}$
core	5.2 ± 0.6	18.7 ± 1.3	2.3 ± 0.8	-0.5 ± 0.2	0.4 ± 0.2	1.12 ± 0.06	$10^{0.70\pm0.22}$
H1	8.5 ± 0.8	11.2 ± 0.5	2.3 ± 0.5	-1.7 ± 0.3	1.1 ± 0.2	0.69 ± 0.36	$10^{-2.18\pm1.34}$
H2	5.7 ± 0.7	23.7 ± 4.1	1.3 ± 1.0	-0.6 ± 0.6	0.8 ± 0.7	0.42 ± 0.25	$10^{-1.12\pm1.61}$
H3	1.9 ± 0.5	8.7 ± 2.8	1.6 ± 1.0	-1.0 ± 0.6	1.0 ± 0.7	0.78 ± 0.41	$10^{-1.27\pm1.67}$
hotspot	13.2 ± 0.6	14.0 ± 0.9	2.2 ± 0.5	-0.8 ± 0.2	0.6 ± 0.2	1.34 ± 0.17	$10^{-0.46\pm0.28}$
total	38.4 ± 0.3	11.3 ± 0.1	1.4 ± 0.1	-0.9 ± 0.1	0.9 ± 0.1	1.18 ± 0.06	$10^{-2.18\pm0.10}$

Notes. [a] Flux density at the turnover. [b] Turnover frequency. [c] Optically thick spectral index. [d] Optically thin spectral index. [e] Optical depth. [f] Size of the emission region at the turnover [g] Magnetic field strength at the turnover.

Komissarov, S. S. & Falle, S. A. E. G. 1998, MNRAS, 297, 1087
Kovalev, Y. Y., Kellermann, K. I., Lister, M. L., et al. 2005, AJ, 130, 2473
Kovalev, Y. Y., Pushkarev, A. B., Nokhrina, E. E., et al. 2020, MNRAS, 495, 3576
Laing, R. A. 1980, MNRAS, 193, 439
Lampton, M., Margon, B., & Bowyer, S. 1976, ApJ, 208, 177
Leppanen, K. J., Zensus, J. A., & Diamond, P. J. 1995, AJ, 110, 2479
Lisakov, M. M., Kovalev, Y. Y., Savolainen, T., et al. 2017, MNRAS, 468, 4478
Liska, M., Hesp, C., Tchekhovskoy, A., et al. 2018, MNRAS, 474, L81
Lister, M. L., Cohen, M. H., Homan, D. C., et al. 2009, AJ, 138, 1874
Lister, M. L., Homan, D. C., Kellermann, K. I., et al. 2021, ApJ, 923, 30
Lobanov, A. P. 1998, A&A, 330, 79
Lobanov, A. 2015, A&A, 574, A84
MAGIC Collaboration, Ansoldi, S., Antonelli, L. A., et al. 2018, A&A, 617, A91
Marcaide, J. M. & Shapiro, I. I. 1984, ApJ, 276, 56
Marscher, A. P. 1977, ApJ, 216, 244
Marscher, A. P. 1983, ApJ, 264, 296
Martí-Vidal, I. & Marcaide, J. M. 2008, A&A, 480, 289
Müller, C., Kadler, M., Ojha, R., et al. 2014, A&A, 569, A115
Nagai, H., Suzuki, K., Asada, K., et al. 2010, PASJ, 62, L11
Nagai, H., Haga, T., Giovannini, G., et al. 2014, ApJ, 785, 53
Nagai, H., Fujita, Y., Nakamura, M., et al. 2017, ApJ, 849, 52
Nakamura, M., Asada, K., Hada, K., et al. 2018, ApJ, 868, 146
Nesterov, N. S., Lyuty, V. M., & Valtaoja, E. 1995, A&A, 296, 628
Oh, J., Hodgson, J. A., Trippe, S., et al. 2022, MNRAS, 509, 1024
O'Sullivan, S. P. & Gabuzda, D. C. 2009, MNRAS, 400, 26
Pacholczyk, A. G. 1970, Series of Books in Astronomy and Astrophysics, San Francisco: Freeman, 1970
Paraschos, G. F., Kim, J.-Y., Krichbaum, T. P., et al. 2021, A&A, 650, L18
Paraschos, G. F., Kim, J.-Y., Wielgus, M., et al. 2024, A&A, 682, L3
Park, J., Kino, M., Nagai, H., et al. 2023, arXiv:2311.08647
Pauliny-Toth, I. I. K. & Kellermann, K. I. 1966, ApJ, 146, 634
Petrov, L., Kovalev, Y. Y., Fomalont, E. B., et al. 2011, AJ, 142, 35
Pringle, J. E. 1997, MNRAS, 292, 136
Pushkarev, A. B., Hovatta, T., Kovalev, Y. Y., et al. 2012, A&A, 545, A113
Pushkarev, A. B., Kovalev, Y. Y., Lister, M. L., et al. 2017, MNRAS, 468, 4992
Readhead, A. C. S. 1994, ApJ, 426, 51
Reimer, O., Pohl, M., Sreekumar, P., et al. 2003, ApJ, 588, 155
Rohoza, V., Lalakos, A., Paik, M., et al. 2024, ApJ, 963, L29
Savolainen, T. 2006, Ph.D. Thesis
Savolainen, T., Giovannini, G., Kovalev, Y. Y., et al. 2023, A&A, 676, A114
Scharwächter, J., McGregor, P. J., Dopita, M. A., et al. 2013, MNRAS, 429, 2315
Schwab, F. R. & Cotton, W. D. 1983, AJ, 88, 688
Shepherd, M. C., Pearson, T. J., & Taylor, G. B. 1994, BAAS
Strauss, M. A., Huchra, J. P., Davis, M., et al. 1992, ApJS, 83, 29
Suzuki, K., Nagai, H., Kino, M., et al. 2012, ApJ, 746, 140
Türler, M., Courvoisier, T. J.-L., & Paltani, S. 1999, A&A, 349, 45
Walker, R. C., Dhawan, V., Romney, J. D., et al. 2000, ApJ, 530, 233
Zamaninasab, M., Clausen-Brown, E., Savolainen, T., et al. 2014, Nature, 510, 126
Zdziarski, A. A., Sikora, M., Pjanka, P., et al. 2015, MNRAS, 451, 927
Zensus, J. A. 1997, ARA&A, 35, 607

Appendix A: False detection probability of fringe solutions

Since baselines to *RadioAstron* have a low signal-to-noise ratio (S/N), we calculate the false detection rates of fringe fitting on the ground–space baselines in the fast Fourier transformation (FFT) step of `FRING`. A false detection may occur either when we pick up a strong noise peak as detection or find the wrong delay and rate solution of the signal (Desai 1998) during the FFT stage of the fringe fitting. To estimate the rate of false detection we use the following formula (Petrov et al. 2011; Savolainen et al. 2023):

$$p(s) = \frac{n_{\rm eff}}{\sigma_{\rm eff}} f_{\rm S/N}^2 s e^{-\frac{(f_{\rm S/N} s)^2}{2}} \left(1 - e^{-\frac{(f_{\rm S/N} s)^2}{2}}\right)^{n_{\rm eff}-1}, \quad \text{(A.1)}$$

where $n_{\rm eff}$ and $\sigma_{\rm eff}$ are the effective number of spectrum points in the search region and effective rms noise of the correlator output, and $f_{\rm S/N}$ the is a scaling factor since S/N estimates in `AIPS` are underestimated at the low S/N limit, and finally s is the maximum fringe amplitude. We perform the fringe search a hundred times, adding delays and rates far outside of our search windows of ±100 ns and ±100 mHz for delay and rate, respectively. The probability density of the fringe S/N is shown in Fig. A.1 and false detection rates at a given S/N are summarized in Tab. A.1. The S/N of the four *RadioAstron* fringe detections are 2.8, 3.4, 4.0, and 1.3. For the first three scans, the probability of false detection is below 1%, while for the last scan, it is ∼ 90%. We kept this detection because a signal was detected with `PIMA` as well, and the delay and rate changed smoothly from the previous scans (see Tab. A.2).

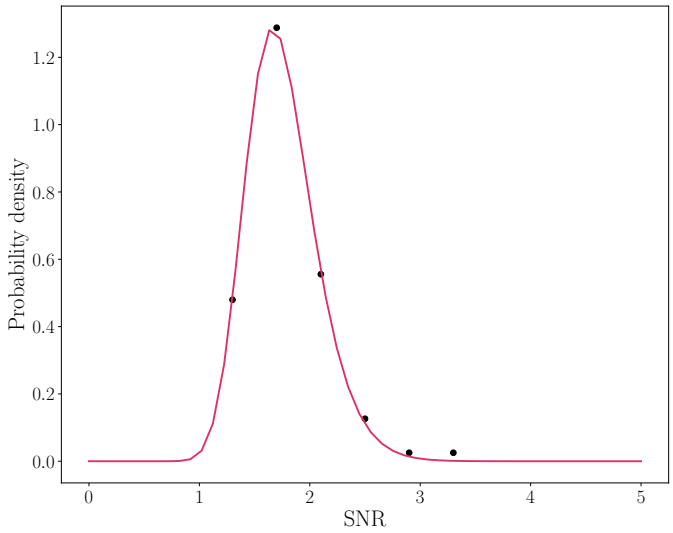

Fig. A.1: Distribution of the S/N of the fringe detections from one hundred fits. Search windows were ±100 ns for delay and ±100 mHz for rate.

Table A.1: Probability of false detection at a given S/N.

S/N	P_e
1.5	0.77
2.0	0.21
2.5	0.021
2.7	0.0073
3.0	0.0012
3.2	0.00033
3.5	4.0×10^{-5}
3.7	8.9×10^{-6}
4.0	8.0×10^{-7}

Table A.2: Delay, rate and S/N values of the *RadioAstron* fringe detections.

Scan [hh:mm:ss–hh:mm:ss]	Delay [ns]	Rate [mHz]	S/N
23:15:00–23:30:00	2.48	−0.27	2.9
23:30:30–23:45:00	0.00	−0.06	3.5
23:45:30–23:59:59	−7.81	−0.06	4.1
00:00:30–00:15:00	−9.77	0.00	1.4

Appendix B: Multi-frequency images of 3C 84

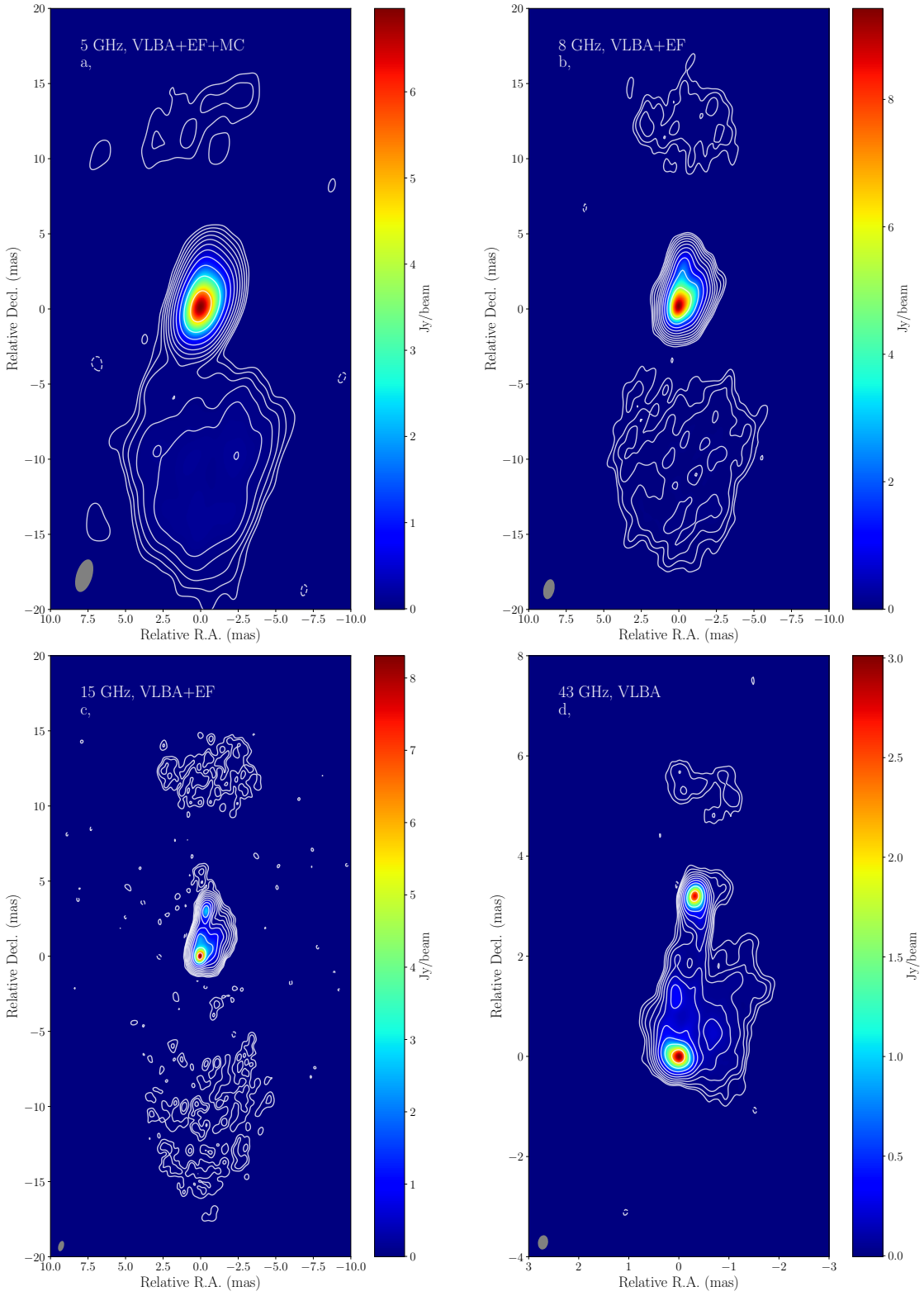

Fig. B.1: Clean images produced from the multi–frequency observations carried out simultaneously with the *RadioAstron* observations. Image properties are shown in Table B.1.

Table B.1: Map properties of the clean images shown Fig. B.1.

ν [GHz][a]	$S_{\rm tot}$ [Jy][b]	$S_{\rm peak}$ [Jy/beam][c]	σ [mJy/beam][d]	$S_{\rm low}$ [mJy/beam][e]	$b_{\rm maj}$ [mas][f]	$b_{\rm min}$ [mas][g]	PA [°][h]
4.8	19.6	6.97	1.8	4.9	2.25	1.06	−17.2
8	32.7	9.43	1.1	4.7	1.35	0.73	−12.4
15	38.3	8.31	0.9	3.3	0.71	0.37	−16.7
43	19.5	3.01	1.0	4.2	0.29	0.20	−10.0

Notes. [(a)] Observing frequency. [(b)] Total flux density. [(c)] Peak brightness. [(d)] Rms noise. [(e)] Lowest contour. [(f)] Beam major axis. [(g)] Beam minor axis. [(h)] Beam position angle.

Appendix C: Modelfit components

Table C.1: Characteristics of modelfit components fitted to the 22 GHz *RadioAstron* data sets. Flux density errors are assumed to be 10% of the flux density of the component, and errors in size are assumed to be 20% of the beam minor axis at the observing frequency. All components are above the resolution limit (Kovalev et al. 2005).

Year	Component	$S_{\rm comp}$ [Jy][a]	$b_{\rm maj}$ [μas][b]	$b_{\rm min}$ [μas][c]
2016	core	0.82 ± 0.08	32.7 ± 26.2	32.7 ± 26.2
	hotspot	1.59 ± 0.16	77.1 ± 26.2	77.1 ± 26.2

Notes. [(a)] Flux density of the component. [(b)] Major axis of the component. [(c)] Minor axis of the component.

Table C.2: Characteristics of the `modelfit` core components fitted to the ground array data, used to measure the core shift. All components are above the resolution limit (Kovalev et al. 2005).

Frequency [GHz][a]	$S_{\rm comp}$ [Jy][b]	FWHM [mas][c]	x [mas][d]	y [mas][e]
4.8	0.94 ± 0.09	0.843 ± 0.001	−0.266 ± 0.075	2.527 ± 0.075
8	1.42 ± 0.14	0.522 ± 0.001	−0.457 ± 0.050	3.014 ± 0.053
15	2.67 ± 0.27	0.254 ± 0.001	−0.410 ± 0.035	2.993 ± 0.036
22	2.74 ± 0.27	0.209 ± 0.001	−0.407 ± 0.022	3.087 ± 0.025
43	3.55 ± 0.36	0.155 ± 0.001	−0.334 ± 0.045	3.206 ± 0.025

Notes. [(a)] Observing frequency. [(b)] Flux density of the component. [(c)] Full width half maximum of the component. [(d)] Position in right ascension after alignment. [(e)] Position in declination after alignment.

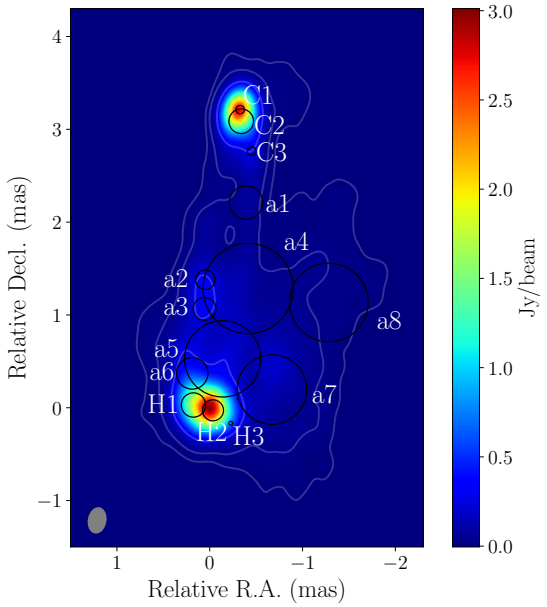

Fig. C.1: `modelfit` components used for the SSA fit at 43 GHz. Component characteristics are described in Table. C.3.

Appendix D: Spectral index maps

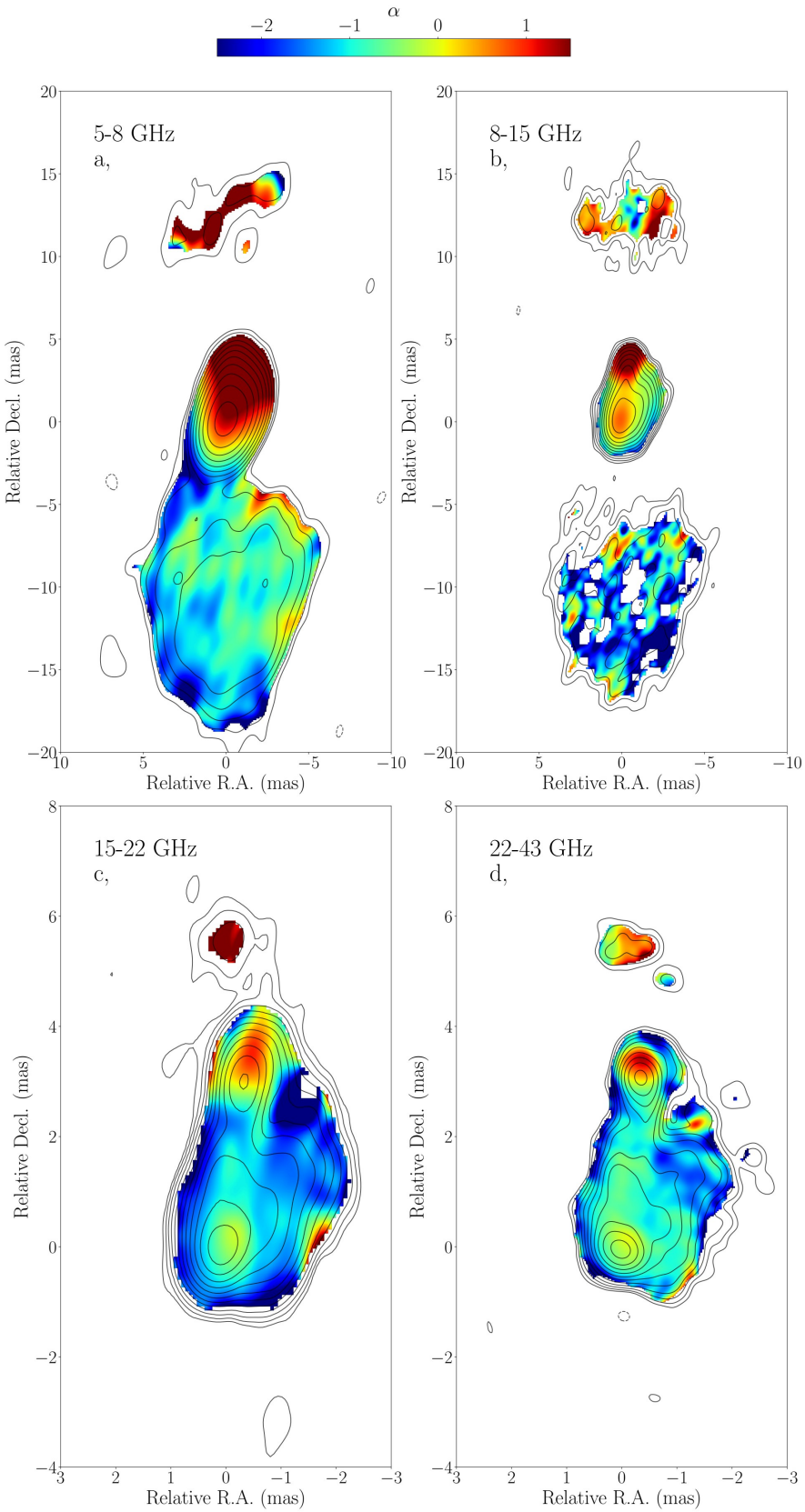

Fig. D.1: Spectral index maps of 3C 84 between adjacent observing frequencies. The description of the analysis and the results can be found in Sect. 7.

Table C.3: Characteristics of `modelfit` components fitted to the ground array data, used to perform the SSA fit. All components are above the resolution limit (Kovalev et al. 2005). Component flux density errors are assumed to be 10%, and size errors are calculated from the linear fit to the 15 to 43 GHz component sizes (see Sect. 7).

Frequency [GHz][a]	Component	S_{comp} [Jy][b]	FWHM [mas][c]	x [mas][d]	y [mas][e]
4.8	C2	0.80 ± 0.08	0.27 ± 0.11	−0.511	2.865
	H1	2.28 ± 0.23	0.47 ± 0.21	0.116	0.130
	H3	0.89 ± 0.09	0.54 ± 0.23	−0.286	−0.067
	a5	8.33 ± 0.83	1.48 ± 0.50	−0.199	0.627
	a7	1.62 ± 0.16	1.13 ± 0.49	−0.730	0.296
	a8	0.50 ± 0.05	0.92 ± 0.34	−1.343	1.234
8	C2	0.83 ± 0.08	0.27 ± 0.11	−0.399	3.087
	C3	1.05 ± 0.11	0.59 ± 0.28	−0.511	2.766
	H1	5.97 ± 0.60	0.44 ± 0.22	0.116	0.030
	H3	2.46 ± 0.25	0.50 ± 0.25	−0.286	−0.167
	a1	0.60 ± 0.06	0.37 ± 0.19	−0.452	2.210
	a2	1.04 ± 0.10	0.16 ± 0.12	0.012	1.379
	a3	0.58 ± 0.06	0.57 ± 0.34	0.004	1.065
	a4	4.06 ± 0.41	1.50 ± 0.45	−0.474	1.284
	a5	9.19 ± 0.92	1.43 ± 0.50	−0.198	0.527
	a7	3.07 ± 0.31	1.10 ± 0.37	−0.730	0.196
	a8	1.68 ± 0.17	0.91 ± 0.35	−1.343	1.134
15	C2	2.67 ± 0.27	0.27 ± 0.11	−0.399	3.087
	C3	1.81 ± 0.18	0.49 ± 0.32	−0.511	2.766
	H1	7.99 ± 0.80	0.41 ± 0.23	0.116	0.030
	H2	4.71 ± 0.47	0.28 ± 0.14	−0.095	−0.028
	H3	0.92 ± 0.09	0.41 ± 0.29	−0.286	−0.167
	a1	0.44 ± 0.04	0.37 ± 0.25	−0.452	2.210
	a2	0.49 ± 0.05	0.17 ± 0.20	0.012	1.379
	a3	2.30 ± 0.23	0.51 ± 0.38	0.004	1.065
	a4	5.76 ± 0.58	1.39 ± 0.48	−0.474	1.284
	a5	4.91 ± 0.49	1.31 ± 0.53	−0.199	0.527
	a6	0.28 ± 0.03	0.34 ± 0.07	1.291	0.370
	a7	4.39 ± 0.44	1.03 ± 0.40	−0.730	0.196
	a8	1.03 ± 0.10	0.90 ± 0.38	−1.343	1.134
22	C2	3.44 ± 0.34	0.27 ± 0.11	−0.339	3.087
	C3	1.36 ± 0.14	0.39 ± 0.38	−0.451	2.766
	H1	3.43 ± 0.34	0.38 ± 0.26	0.176	0.030
	H2	5.81 ± 0.58	0.27 ± 0.15	0.056	1.065
	H3	1.63 ± 0.16	0.31 ± 0.35	−0.226	−0.167
	a1	0.28 ± 0.03	0.37 ± 0.32	−0.392	2.210
	a2	0.25 ± 0.03	0.18 ± 0.28	0.048	1.379
	a3	1.34 ± 0.13	0.44 ± 0.42	0.056	1.065
	a4	3.36 ± 0.34	1.29 ± 0.52	−0.414	1.284
	a5	3.17 ± 0.32	1.19 ± 0.57	−0.139	0.527
	a6	0.56 ± 0.06	0.34 ± 0.07	0.189	0.370
	a7	2.72 ± 0.27	0.96 ± 0.45	−0.670	0.196
	a8	0.61 ± 0.06	0.89 ± 0.42	−1.283	1.134
43	C1	2.05 ± 0.20	0.09 ± 0.30	−0.327	3.212
	C2	2.74 ± 0.28	0.27 ± 0.11	−0.339	3.087
	C3	0.18 ± 0.02	0.09 ± 0.59	−0.451	2.766
	H1	2.23 ± 0.22	0.26 ± 0.36	0.176	0.030
	H2	5.05 ± 0.51	0.23 ± 0.20	−0.035	−0.028
	H3	0.27 ± 0.03	0.04 ± 0.58	−0.226	−0.167
	a1	0.22 ± 0.02	0.36 ± 0.55	−0.392	2.210
	a2	0.37 ± 0.04	0.21 ± 0.54	0.048	1.379
	a3	0.55 ± 0.05	0.25 ± 0.62	0.006	1.065
	a4	1.34 ± 0.13	0.97 ± 0.71	−0.414	1.284
	a5	1.70 ± 0.17	0.82 ± 0.74	−0.138	0.527
	a6	0.88 ± 0.09	0.34 ± 0.07	0.189	0.370
	a7	1.35 ± 0.14	0.75 ± 0.64	−0.670	0.196
	a8	0.24 ± 0.02	0.85 ± 0.62	−1.283	1.134

Notes. [a] Observing frequency. [b] Flux density of the component. [c] Full width half maximum of the component. [d] Position in right ascension after alignment. [e] Position in declination after alignment.

Chapter 9

Summary and outlook

This thesis addresses a range of questions related to AGN jets, including jet launching and collimation, and the connection between radio and γ-ray variability.

- In Chapter 5, I presented the first images from the 2.3-GHz monitoring of southern-sky TeV-emitter sources monitored by TANAMI. These images provide a broader view of the AGN jets as compared with earlier observations. Studying the properties of the twenty-four AGN included in this biased sample, I found that they exhibit an inverse relation between the synchrotron peak frequency and $T_{\rm b,core}$, that is high-synchrotron-peaked objects show lower $T_{\rm b,core}$ values, and that γ-ray faint AGN show lower $T_{\rm b,core}$ values than γ-loud objects. A similar trend has been observed in the MOJAVE sample as well (see e.g., Lister et al. 2011), and they suggest that the underlying parameter responsible for this is Doppler boosting, which is stronger in FSRQ than in HBL. In the future, the 2.3 and 8.4-GHz monitoring data will be used to perform quasi-simultaneous spectral studies and coreshift measurements for the monitored AGN.

- In Chapter 6, I discuss VLBI follow-up observations of the γ-ray flaring high-redshift blazar, TXS 1508+572. The images at 15, 22, and 43 GHz reveal the parsec-scale structure of the object to be comprised of the core, and a compact jet, as well as a diffuse lobe feature associated with the jet on the 8-GHz, lower resolution maps of Titov et al. (2023). The jet is moving with a superluminal apparent speed of $(14.3 - 32.2)$ c, and its proper motion is consistent with the maximum apparent speed expected on the $(\mu - z)$ diagram with the assumption of a Lorentz factor of 20 (Zhang et al. 2022). Based on the kinematics, the jet feature was ejected around 2016−2019. The core shift stays consistent through the monitoring, and we measure the average projected distance between the 43-GHz radio core and the jet apex to be (0.32 ± 0.02) pc. In this paper I conclude that the γ-ray flare is originating from

the shock-shock interaction between the jet component and new plasma flowing in this region.

- In Chapter 7, I studied the binary AGN candidate PSO J334 (Liu et al. 2015) in order to confirm its nature via VLBI observations. While multiwavelength observations found no evidence for a secondary BH residing in the center of this object (Liu et al. 2016; Foord et al. 2017), VLBI images presented by Mooley et al. (2018) showed evidence of possible jet precession. Our high-resolution VLBI images, however revealed remarkably straight jets on kiloparsec scales, and polarimetric data showed interaction between the jet and the ambient medium. My results suggest that PSO J334 is an ordinary jetted AGN and does not harbor a binary in its central engine.

- In Chapter 8, I investigate the morphology, collimation and spectral properties of the 3C 84 jet at extremely high resolution provided by the space radio telescope *RadioAstron*. Comparing the image from this 2016 observation with the 2013 one published by Giovannini et al. (2018), significant changes in the morphology of the limb-brightened jet and the hotspot become evident. Apart from confirming the fine structure morphology of the jet, the main finding of the paper is a change in the jet width profile from quasi-cylindrical in 2013 to parabolic on 2016. This change is attributed to the decreasing pressure of the mini-cocoon inflated by the jet (Savolainen et al. 2023) that cannot collimate the jet as efficiently as when it was closer to the core.

In this thesis work, I presented a broad range of studies covering VLBI observations of AGN jets, including topics that are becoming increasingly important with the upcoming new instruments. Southern sky monitoring will enter a new era once the SKA (see e.g, Paragi et al. 2015) launches its all-sky surveys below 15 GHz with its amazing sensitivity and increased resolution. While new populations of faint AGN will become observable this way, TANAMI will provide an extended time baseline up to ~ 20 yrs for the brightest sources to study their evolution and variability. Multi-messenger observations will flourish thanks to the KM3NeT (Adrián-Martínez et al. 2016), a neutrino detector planned to come online in the next years. Since the instrument is located in the Mediterranean Sea, it will also be sensitive to neutrinos originating from declinations below the celestial Equator. To detect any correlation between source activity and the incident neutrinos, AGN must be monitored on long timescales through their various phases of activity, and TANAMI will be able to provide such multi-frequency data for the astroparticle community. The same is true for VHE photons, as the increased sensitivity of the CTA (Actis et al. 2011)

will enable studies of complete samples of TeV-emitter AGN, as well as the detection of sources above $z \gtrsim 1$, that was only rarely possible with the current arrays.

When it comes to galaxy evolution, LISA (Amaro-Seoane et al. 2017), expected to launch in the mid-2030s, will explore the gravitational Universe, and hunt for gravitational waves originating from coalescing supermassive binary black holes. Establishing a sample of such objects via observations throughout the electromagnetic spectrum can enable astronomers to conduct multiwavelength studies and identifications of merging black holes. At this time, the ngVLA will be aligned to provide a new radio window to the Universe.

Astronomy, including radio astronomy, is an ever-evolving field of studies, which presents many ground-breaking and interesting results every year, uncovering new questions each and every turn. However, it seems we are only slowly inching towards possible explanations for phenomena that has been puzzling researchers for decades. As a community, we measure these great steps we achieve, but as individuals we contribute small, often personal victories by sharing our work with like-minded colleagues. I wish that the research presented in this dissertation may help others build on this work to uncover the secrets of one of the most fascinating phenomena in the Universe, active galactic nuclei.

„Manuscripts don't burn."
Mikhail Bulgakov: The Master and Margarita

Acknowledgments

First and foremost, I would like to thank my supervisor, Prof. Dr. Eduardo Ros for his guidance during my PhD work. He was always available to answer my questions and support me through my anxiety with giving talks. I am grateful to Prof. Dr. Zensus and Prof. Dr. Matthias Kadler for welcoming me in their groups at MPIfR and at the University of Würzburg, and for giving me the opportunity to learn from and collaborate with the experts in their groups. I would also like to thank Dr. Sándor Frey, Dr. Krisztina Gabányi and Dr. Tuomas Savolainen for getting me interested in radio astronomy and teaching me the fundamentals of VLBI, and for the continuing collaboration.

I am grateful for the PhD students of MPIfR, Joana, Hendrik, Luca, Aleksei, Jongseo, Saurabh and Cecilia, for the interesting discussions, and especially for their friendship through the years. I loved the trips and movie nights we organized, and they made my time in Bonn truly fun.

Szeretném megköszönni a családomnak a feltétlen szeretet és támogatást amit egész éltemben kaptam tőlük, és hogy lehetővé tették, hogy az álmaimat kövessem.

Szeretném megköszönni a férjemnek, Petinek, hogy kitartott mellettem a hosszú távkapcsolatunk alatt, és a türelméért a disszertáció leadását megelőző pár hónapban. A két héttel ezelőtti esküvőnk volt életem legboldogabb napja, és remélem még sok ilyen tökéletes napot fogunk együtt tölteni.

Bibliography

Aartsen, M. G., Ackermann, M., Adams, J., et al. (2014): Observation of High-Energy Astrophysical Neutrinos in Three Years of IceCube Data. *Physical Review Letters*, 113, 101101. https://doi.org/10.1103/PhysRevLett.113.101101

Abdo, A. A., Ackermann, M., Ajello, M., et al. (2009): Bright Active Galactic Nuclei Source List from the First Three Months of the Fermi Large Area Telescope All-Sky Survey. *ApJ*, 700, 597. https://doi.org/10.1088/0004-637X/716/1/30

Abdo, A. A., Ackermann, M., Agudo, I., et al. (2010):The Spectral Energy Distribution of Fermi Bright Blazars. *ApJ*, 716, 30. https://doi.org/10.3847/1538-4365/ab6bcb

Abdollahi, S., Acero, F., Ackermann, M., et al. (2020): Fermi Large Area Telescope Fourth Source Catalog. *ApJS*, 247, 33. https://doi.org/10.1007/s10686-011-9247-0

Actis, M., Agnetta, G., Aharonian, F., et al. (2011): Design concepts for the Cherenkov Telescope Array CTA: an advanced facility for ground-based high-energy gamma-ray astronomy. *Experimental Astronomy*, 32, 193. https://doi.org/10.1007/s10686-011-9247-0

Adrián-Martínez, S., Ageron, M., Aharonian, F., et al. (2016): Letter of intent for KM3NeT 2.0. *Journal of Physics G Nuclear Physics*, 43, 084001. https://doi.org/10.1088/0954-3899/43/8/084001

Aharonian, F. A. (2002): Proton-synchrotron radiation of large-scale jets in active galactic nuclei. *MNRAS*, 332, 215. https://doi.org/10.1046/j.1365-8711.2002.05292.x

Aleksić, J., Alvarez, E. A., Antonelli, L. A., et al. (2012): Mrk 421 active state in 2008: the MAGIC view, simultaneous multi-wavelength observations and SSC model constrained. *A&A*, 542, A100. https://doi.org/10.1051/0004-6361/201117442

Amaro-Seoane, P., Audley, H., Babak, S., et al. (2017): Laser Interferometer Space Antenna. *arXiv:1702.00786*. https://doi.org/10.48550/arXiv.1702.00786

An, T., Mohan, P., & Frey, S. (2018): VLBI Studies of DAGN and SMBHB Hosting Galaxies. *Radio Science*, 53, 1211. https://doi.org/10.1029/2018RS006647

Angioni, R., Ros, E., Kadler, M., et al. (2019): Gamma-ray emission in radio galaxies under the VLBI scope. I. Parsec-scale jet kinematics and high-energy properties of γ-ray-detected TANAMI radio galaxies. *A&A*, 627, A148. https://doi.org/10.1051/0004-6361/201935697

Angioni, R., Ros, E., Kadler, M., et al. (2020): γ-ray emission in radio galaxies under the VLBI scope. II. The relationship between γ-ray emission and parsec-scale jets in radio galaxies. *A&A*, 641, A152. https://doi.org/10.1051/0004-6361/202038236

Asada, K. & Nakamura, M. (2012): The Structure of the M87 Jet: A Transition from Parabolic to Conical Streamlines. *ApJL*, 745, L28. https://doi.org/10.1088/2041-8205/745/2/L28

Beals, C. S. (1934): P Cygni. *The Observatory*, 57, 319.

Beasley, A. J. & Conway, J. E. (1995): VLBI Phase-Referencing. *Very Long Baseline Interferometry and the VLBA*, 82, 327. Edited by Zensus, J. A., Diamond, P. J. and Napier, P. J.

Beckmann, V. & Shrader, C. R. (2012): Active Galactic Nuclei, ISBN-13: 978-3527410781. *Wiley-VCH Verlag GmbH*, Berlin.

Begelman, M. C., Blandford, R. D., & Rees, M. J. (1980): Massive black hole binaries in active galactic nuclei. *Nature*, 287, 307. https://doi.org/10.1038/287307a0

Benke, P., Frey, S., Gabanyi, K., et al. (2018): The rise and fall of a binary AGN candidate: the story of PSO J334.2028+1.4075. *14th European VLBI Network Symposium & Users Meeting*, 98. https://doi.org/10.22323/1.344.0098

Benke, P., Gabányi, K. É., Frey, S., et al. (2023): From binary to singular: The AGN PSO J334.2028+1.4075 under the high-resolution scope. *A&A*, 677, A1. https://doi.org/10.1051/0004-6361/202346904

Benke, P., Rösch, F., Ros, E., et al. (2024): TANAMI: Tracking active galactic nuclei with austral milliarcsecond interferometry. III. First-epoch S band images. *A&A*, 681, A69. https://doi.org/10.1051/0004-6361/202347823

Blandford, R. D. & Königl, A. (1979): Relativistic jets as compact radio sources. *ApJ*, 232, 34. https://doi.org/10.1086/157262

Blandford, R. D. & Payne, D. G. (1982): Hydromagnetic flows from accretion disks and the production of radio jets. *MNRAS*, 199, 883. https://doi.org/10.1093/mnras/199.4.883

Blandford, R. D. & Znajek, R. L. (1977): Electromagnetic extraction of energy from Kerr black holes. *MNRAS*, 179, 433. https://doi.org/10.1093/mnras/179.3.433

Bogovalov, S. & Tsinganos, K. (2005): Shock formation at the magnetic collimation of relativistic jets. *MNRAS*, 357, 918. https://doi.org/10.1111/j.1365-2966.2005.08671.x

Bolton, J. G., Stanley, G. J., & Slee, O. B. (1949): Positions of Three Discrete Sources of Galactic Radio-Frequency Radiation. *Nature*, 164, 101. https://doi.org/10.1038/164101b0

Böck, M., Kadler, M., Müller, C., et al. (2016): Radio and gamma-ray properties of extragalactic jets from the TANAMI sample. *A&A*, 590, A40. https://doi.org/10.1051/0004-6361/201424773

Böttcher, M., Reimer, A., Sweeney, K., et al. (2013): Leptonic and Hadronic Modeling of Fermi-detected Blazars. *ApJ*, 768, 54. https://doi.org/10.1088/0004-637X/768/1/54

Böttcher, M. & Els, P. (2016): Gamma-Gamma Absorption in the Broad Line Region Radiation Fields of Gamma-Ray Blazars. *ApJ*, 821, 102. https://doi.org/10.3847/0004-637X/821/2/102

Britzen, S., Fendt, C., Zajaček, M., et al. (2019): 3C 84: Observational Evidence for Precession and a Possible Relation to TeV Emission. *Galaxies*, 7, 72. https://doi.org/10.3390/galaxies7030072

Caproni, A. & Abraham, Z. (2004): Can long-term periodic variability and jet helicity in 3C 120 be explained by jet precession? *MNRAS*, 349, 1218. https://doi.org/10.1111/j.1365-2966.2004.07550.x

Chandrasekhar, S. (1943): Dynamical Friction. I. General Considerations: the Coefficient of Dynamical Friction. *ApJ*, 97, 255. https://doi.org/10.1086/144517

Cohen, M. H., Kellermann, K. I., Shaffer, D. B., et al. (1977): Radio sources with superluminal velocities. *Nature*, 268, 405. https://doi.org/10.1038/268405a0

Curtis, H. D. (1918): Descriptions of 762 Nebulae and Clusters Photographed with the Crossley Reflector. *Publications of Lick Observatory*, 13, 9.

Deller, A. T., Tingay, S. J., Bailes, M., et al. (2007): DiFX: A Software Correlator for Very Long Baseline Interferometry Using Multiprocessor Computing Environments. *PASP*, 119, 318. https://doi.org/10.1086/513572

Deller, A. T., Brisken, W. F., Phillips, C. J., et al. (2011): DiFX-2: A More Flexible, Efficient, Robust, and Powerful Software Correlator. *PASP*, 123, 275. https://doi.org/10.1086/658907

Dominik, R. M., Linhoff, L., Elsässer, D., et al. (2021): 3C 84: a possibly precessing jet in 43-GHz observations. *MNRAS*, 503, 5448. https://doi.org/10.1093/mnras/stab799

Event Horizon Telescope Collaboration, Akiyama, K., Alberdi, A., et al. (2019): First M87 Event Horizon Telescope Results. I. The Shadow of the Supermassive Black Hole. *ApJL*, 875, L1. https://doi.org/10.3847/2041-8213/ab0ec7

Event Horizon Telescope Collaboration, Akiyama, K., Alberdi, A., et al. (2019): First M87 Event Horizon Telescope Results. II. Array and Instrumentation. *ApJL*, 875, L2. https://doi.org/10.3847/2041-8213/ab0c96

Event Horizon Telescope Collaboration, Akiyama, K., Alberdi, A., et al. (2022): First Sagittarius A* Event Horizon Telescope Results. I. The Shadow of the Supermassive Black Hole in the Center of the Milky Way. *ApJL*, 930, L12. https://doi.org/10.3847/2041-8213/ac6674

Event Horizon Telescope Collaboration, Akiyama, K., Alberdi, A., et al. (2024): The persistent shadow of the supermassive black hole of M 87. I. Observations, calibration, imaging, and analysis. *A&A*, 681, A79. https://doi.org/10.1051/0004-6361/202347932

Fanaroff, B. L. & Riley, J. M. 81974): The morphology of extragalactic radio sources of high and low luminosity. *MNRAS*, 167, 31P. https://doi.org/10.1093/mnras/167.1.31P

Fath, E. A. (1909): The spectra of some spiral nebulae and globular star clusters. Lick Observatory Bulletin, 149, 71. https://doi.org/10.5479/ADS/bib/1909LicOB.5.71F

Foord, A., Gültekin, K., Reynolds, M., et al. (2017): A Multi-wavelength Analysis of Binary-AGN Candidate PSO J334.2028+01.4075. *ApJ*, 851, 106. https://doi.org/10.3847/1538-4357/aa9a39

Fossati, G., Maraschi, L., Celotti, A., et al. (1998): A unifying view of the spectral energy distributions of blazars. *MNRAS*, 299, 433. https://doi.org/10.1046/j.1365-8711.1998.01828.x

Frey, S., Paragi, Z., An, T., et al. (2012): Two in one? A possible dual radio-emitting nucleus in the quasar SDSS J1425+3231. *MNRAS*, 425, 1185. https://doi.org/10.1111/j.1365-2966.2012.21491.x

Gabuzda, D. C. (2015): Parsec-Scale Jets in Active Galactic Nuclei. *The Formation and Disruption of Black Hole Jets*, 414, 117. Edited by Contopoulos, I., Gabuzda, D., Kylafis, N. https://doi.org/10.1007/978-3-319-10356-3_5

Gawiser, E. (2006): Galaxy Formation. *New Horizons in Astronomy: Frank N. Bash Symposium, Astronomical Society of the Pacific Conference Series*, 352, 177. Edited by Kannappan, S. J., Redfield, S., Kessler-Silacci, J. E., Landriau, M. and Drory, N. https://doi.org/10.48550/arXiv.astro-ph/0512384

Georganopoulos, M. & Kazanas, D. (2003): Decelerating Flows in TeV Blazars: A Resolution to the BL Lacertae-FR I Unification Problem. *ApJL*, 594, L27. https://doi.org/10.1086/378557

Gergely, L. Á. & Biermann, P. L. (2009): The Spin-Flip Phenomenon in Supermassive Black hole binary mergers. *ApJ*, 697, 1621. https://doi.org/10.1088/0004-637X/697/2/1621

Ghisellini, G., Tavecchio, F., & Chiaberge, M. (2005): Structured jets in TeV BL Lac objects and radio galaxies. Implications for the observed properties. *A&A*, 432, 401. https://doi.org/10.1051/0004-6361:20041404

Ghisellini, G., Righi, C., Costamante, L., et al. (2017): The Fermi blazar sequence. *MNRAS*, 469, 255. https://doi.org/10.1093/mnras/stx806

Giannios, D., Uzdensky, D. A., & Begelman, M. C. (2009): Fast TeV variability in blazars: jets in a jet. *MNRAS*, 395, L29. https://doi.org/10.1111/j.1745-3933.2009.00635.x

Giovannini, G., Savolainen, T., Orienti, M., et al. (2018): A wide and collimated radio jet in 3C84 on the scale of a few hundred gravitational radii. *Nature Astronomy*, 2, 472. https://doi.org/10.1038/s41550-018-0431-2

Globus, N. & Levinson, A. (2016): The collimation of magnetic jets by disc winds. *MNRAS*, 461, 2605. https://doi.org/10.1093/mnras/stw1474

Gokus, A., Kreter, M., Kadler, M., et al. (2022): Gamma-ray flare of high-redshift blazar GB 1508+5714 detected by Fermi/LAT. *The Astronomer's Telegram*, 15202.

Gokus, A. et al. (2024): A gamma-ray flare from TXS 1508+572: characterizing the jet of a z=4.31 blazar in the early Universe. Submitted to *ApJ*.

Greenstein, J. L. (1963): Red-Shift of the Unusual Radio Source: 3C 48. *Nature*, 197, 1041. https://doi.org/10.1038/1971041a0

Greisen, E. W. (2003): AIPS, the VLA, and the VLBA. *Information Handling in Astronomy - Historical Vistas, Astrophysics and Space Science Library*, 285, 109. Kluwer Academic Publishers, Dordrecht. Edited by André Heck. https://doi.org/10.1007/0-306-48080-8_7

Harris, G. L. H., Rejkuba, M., & Harris, W. E. (2010): The Distance to NGC 5128 (Centaurus A). *PASA*, 27, 457. https://doi.org/10.1071/AS09061

Hazard, C., Mackey, M. B., & Shimmins, A. J. (1963): Investigation of the Radio Source 3C 273 By The Method of Lunar Occultations. *Nature*, 197, 1037. https://doi.org/10.1038/1971037a0

Hervet, O., Boisson, C., & Sol, H. (2016): An innovative blazar classification based on radio jet kinematics. *A&A*, 592, A22. https://doi.org/10.1051/0004-6361/201628117

Homan, D. C., Cohen, M. H., Hovatta, T., et al. (2021): MOJAVE. XIX. Brightness Temperatures and Intrinsic Properties of Blazar Jets. *ApJ*, 923, 67. https://doi.org/10.3847/1538-4357/ac27af

Hovatta, T., Lindfors, E., Kiehlmann, S., et al. (2021): Association of IceCube neutrinos with radio sources observed at Owens Valley and Metsähovi Radio Observatories. *A&A*, 650, A83. https://doi.org/10.1051/0004-6361/202039481

Högbom, J. A. (1974): Aperture Synthesis with a Non-Regular Distribution of Interferometer Baselines. *A&AS*, 15, 417.

IceCube Collaboration, Aartsen, M. G., Ackermann, M., et al. (2018): Multimessenger observations of a flaring blazar coincident with high-energy neutrino IceCube-170922A. *Science*, 361, eaat1378. https://doi.org/10.1126/science.aat1378

Jansky, K. G. (1933): Radio Waves from Outside the Solar System. *Nature*, 132, 66. https://doi.org/10.1038/132066a0

Janssen, M., Falcke, H., Kadler, M., et al. (2021): Event Horizon Telescope observations of the jet launching and collimation in Centaurus A. *Nature Astronomy*, 5, 1017. https://doi.org/10.1038/s41550-021-01417-w

Janssen, M., Radcliffe, J. F., & Wagner, J. (2022): Software and Techniques for VLBI Data Processing and Analysis. *Universe*, 8, 527. https://doi.org/10.3390/universe8100527

Jorstad, S. G., Marscher, A. P., Smith, P. S., et al. (2013): A Tight Connection between Gamma-Ray Outbursts and Parsec-scale Jet Activity in the Quasar 3C 454.3. *ApJ*, 773, 147. https://doi.org/10.1088/0004-637X/773/2/147

Kadler, M., Krauß, F., Mannheim, K., et al. (2016): Coincidence of a high-fluence blazar outburst with a PeV-energy neutrino event. *Nature Physics*, 12, 807. https://doi.org/10.1038/nphys3715

Kardashev, N. S., Khartov, V. V., Abramov, V. V., et al. (2013): "RadioAstron"-A telescope with a size of 300 000 km: Main parameters and first observational results. *Astronomy Reports*, 57, 153. https://doi.org/10.1134/S1063772913030025

Kardashev, N. S., Alakoz, A. V., Andrianov, A. S., et al. (2017): RadioAstron Science Program Five Years after Launch: Main Science Results. *Solar System Research*, 51, 535. https://doi.org/10.1134/S0038094617070085

Keimpema, A., Kettenis, M. M., Pogrebenko, S. V., et al. (2015): The SFXC software correlator for very long baseline interferometry: algorithms and implementation. *Experimental Astronomy*, 39, 259. https://doi.org/10.1007/s10686-015-9446-1

Kellermann, K. I. & Pauliny-Toth, I. I. K. (1969): The Spectra of Opaque Radio Sources. *ApJL*, 155, L71. https://doi.org/10.1086/180305

Kellermann, K. I., Sramek, R., Schmidt, M., et al. (1989): VLA Observations of Objects in the Palomar Bright Quasar Survey. *AJ*, 98, 1195. https://doi.org/10.1086/115207

Kerr, R. P. (1963): Gravitational Field of a Spinning Mass as an Example of Algebraically Special Metrics. *Physical Review Letters*, 11, 237. https://doi.org/10.1103/PhysRevLett.11.237

Kiepenheuer, K. O. (1950): Cosmic Rays as the Source of General Galactic Radio Emission. *Physical Review*, 79, 738. https://doi.org/10.1103/PhysRev.79.738

Kino, M., Wajima, K., Kawakatu, N., et al. (2018): Evidence of Jet-Clump Interaction: A Flip of the Radio Jet Head of 3C 84. *ApJ*, 864, 118. https://doi.org/10.3847/1538-4357/aad6e3

Kogan, L. (1996): Global Ground VLBI Network as a Tied Array for Space VLBI. *VLBA Scientific Memo* No. 13.

Komossa, S., Burwitz, V., Hasinger, G., et al. (2003): Discovery of a Binary Active Galactic Nucleus in the Ultraluminous Infrared Galaxy NGC 6240 Using Chandra. *ApJ*, 582, L15. https://doi.org/10.1086/346145

Koss, M., Mushotzky, R., Treister, E., et al. (2011): Chandra Discovery of a Binary Active Galactic Nucleus in Mrk 739. *ApJL*, 735, L42. https://doi.org/10.1088/2041-8205/735/2/L42

Kovalev, Y. Y., Aller, H. D., Aller, M. F., et al. (2009): The Relation Between AGN Gamma-Ray Emission and Parsec-Scale Radio Jets. *ApJL*, 696, L17. https://doi.org/10.1088/0004-637X/696/1/L17

Kovalev, Y. Y., Pushkarev, A. B., Nokhrina, E. E., et al. (2020): A transition from parabolic to conical shape as a common effect in nearby AGN jets. *MNRAS*, 495, 3576. https://doi.org/10.1093/mnras/staa1121

Kramarenko, I. G., Pushkarev, A. B., Kovalev, Y. Y., et al. (2022): A decade of joint MOJAVE-Fermi AGN monitoring: localization of the gamma-ray emission region. *MNRAS*, 510, 469. https://doi.org/10.1093/mnras/stab3358

Kreter, M., Gokus, A., Krauss, F., et al. (2020): Search for High-redshift Blazars with Fermi/LAT. *ApJ*, 903, 128. https://doi.org/10.3847/1538-4357/abb8da

Laing, R. A. (1980): A model for the magnetic-field structure in extended radio sources. *MNRAS*, 193, 439. https://doi.org/10.1093/mnras/193.3.439

Lehto, H. J. & Valtonen, M. J. (1996): OJ 287 Outburst Structure and a Binary Black Hole Model. *ApJ*, 460, 207. https://doi.org/10.1086/176962

Lense, J. & Thirring, H., (1918): Über den Einfluß der Eigenrotation der Zentralkörper auf die Bewegung der Planeten und Monde nach der Einsteinschen Gravitationstheorie. *Physikalische Zeitschrift*, 19, 156.

Lico, R., Giroletti, M., Orienti, M., et al. (2012): VLBA monitoring of Mrk 421 at 15 GHz and 24 GHz during 2011. *A&A*, 545, A117. https://doi.org/10.1051/0004-6361/201219870

Liska, M., Hesp, C., Tchekhovskoy, A., et al. (2018): Formation of precessing jets by tilted black hole discs in 3D general relativistic MHD simulations. *MNRAS*, 474, L81. https://doi.org/10.1093/mnrasl/slx174

Lister, M. L., Aller, M., Aller, H., et al. (2011): γ-Ray and Parsec-scale Jet Properties of a Complete Sample of Blazars From the MOJAVE Program. *ApJ*, 742, 27. https://doi.org/10.1088/0004-637X/742/1/27

Lister, M. L., Aller, M. F., Aller, H. D., et al. (2018): MOJAVE. XV. VLBA 15 GHz Total Intensity and Polarization Maps of 437 Parsec-scale AGN Jets from 1996 to 2017. *ApJS*, 234, 12. https://doi.org/10.3847/1538-4365/aa9c44

Lister, M. L., Homan, D. C., Kellermann, K. I., et al. (2021): Monitoring Of Jets in Active Galactic Nuclei with VLBA Experiments. XVIII. Kinematics and Inner Jet Evolution of Bright Radio-loud Active Galaxies. *ApJ*, 923, 30. https://doi.org/10.3847/1538-4357/ac230f

Liu, T., Gezari, S., Heinis, S., et al. (2015): A Periodically Varying Luminous Quasar at z = 2 from the Pan-STARRS1 Medium Deep Survey: A Candidate Supermassive Black Hole Binary in the Gravitational Wave-driven Regime. *ApJ*, 803, L16. https://doi.org/10.1088/2041-8205/803/2/L16

Liu, T., Gezari, S., Burgett, W., et al. (2016): A Systematic Search for Periodically Varying Quasars in Pan-STARRS1: An Extended Baseline Test in Medium Deep Survey Field MD09. *ApJ*, 833, 6. https://doi.org/10.3847/0004-637X/833/1/6

Lu, R.-S., Asada, K., Krichbaum, T. P., et al. (2023): A ring-like accretion structure in M87 connecting its black hole and jet. *Nature*, 616, 686. https://doi.org/10.1038/s41586-023-05843-w

Luminet, J.-P. (1979): Image of a spherical black hole with thin accretion disk. *A&A*, 75, 228. https://doi.org/

Lyubarsky, Y. (2009): Asymptotic Structure of Poynting-Dominated Jets. *ApJ*, 698, 1570. https://doi.org/10.1088/0004-637X/698/2/1570

Maness, H. L., Taylor, G. B., Zavala, R. T., et al. (2004): Breaking All the Rules: The Compact Symmetric Object 0402+379. ApJ, 602, 123. https://doi.org/10.1086/380919

Mannheim, K. (1995): High-energy neutrinos from extragalactic jets. *Astroparticle Physics*, 3, 295. https://doi.org/10.1016/0927-6505(94)00044-4

Mannheim, K. (1998): Possible Production of High-Energy Gamma Rays from Proton Acceleration in the Extragalactic Radio Source Markarian 501. *Science*, 279, 684. https://doi.org/10.1126/science.279.5351.684

Marscher, A. P., Jorstad, S. G., Agudo, I., et al. (2012): Relation between Events in the Millimeter-wave Core and Gamma-ray Outbursts in Blazar Jets. *arXiv:1204.6707*. https://doi.org/10.48550/arXiv.1204.6707

Martí-Vidal, I. & Marcaide, J. M. (2008): Spurious source generation in mapping from noisy phase-self-calibrated data. *A&A*, 480, 289. https://doi.org/10.1051/0004-6361:20078690

Milosavljević, M. & Merritt, D. (2001): Formation of Galactic Nuclei. *ApJ*, 563, 34. https://doi.org/10.1086/323830

Milosavljević, M. & Merritt, D. (2003): Long-Term Evolution of Massive Black Hole Binaries. *ApJ*, 596, 860. https://doi.org/10.1086/378086

Mooley, K. P., Wrobel, J. M., Anderson, M. M., et al. (2018): The twisted radio structure of PSO J334.2028+01.4075, still a supermassive binary black hole candidate. *MNRAS*, 473, 1388. https://doi.org/10.1093/mnras/stx2447

Müller, C., Kadler, M., Ojha, R., et al. (2014): TANAMI monitoring of Centaurus A: The complex dynamics in the inner parsec of an extragalactic jet. *A&A*, 569, A115. https://doi.org/10.1051/0004-6361/201423948

Müller, C., Kadler, M., Ojha, R., et al. (2018): TANAMI: Tracking Active Galactic Nuclei with Austral Milliarcsecond Interferometry. II. Additional sources. *A&A*, 610, A1. https://doi.org/10.1051/0004-6361/201731455

Nagai, H., Fujita, Y., Nakamura, M., et al. (2017): Enhanced Polarized Emission from the One-parsec-scale Hotspot of 3C 84 as a Result of the Interaction with the Clumpy Ambient Medium. *ApJ*, 849, 52. https://doi.org/10.3847/1538-4357/aa8e43

Netzer, H. (2013): The Physics and Evolution of Active Galactic Nuclei. *Cambridge University Press*, Cambridge, UK. https://doi.org/10.1017/CBO9781139109291

Ojha, R., Kadler, M., Böck, M., et al. (2010): TANAMI: tracking active galactic nuclei with austral milliarcsecond interferometry . I. First-epoch 8.4 GHz images. *A&A*, 519, A45. https://doi.org/10.1051/0004-6361/200912724

Orienti, M., D'Ammando, F., Giroletti, M., et al. (2014): Exploring the multiband emission of TXS 0536+145: the most distant γ-ray flaring blazar. *MNRAS*, 444, 3040. https://doi.org/10.1093/mnras/stu1644

Pacholczyk, A. G. (1970): Radio astrophysics. Nonthermal processes in galactic and extragalactic sources. *Series of Books in Astronomy and Astrophysics*, San Francisco: Freeman.

Padovani, P., Perlman, E. S., Landt, H., et al. (2003): What Types of Jets Does Nature Make? A New Population of Radio Quasars. *ApJ*, 588, 128. https://doi.org/10.1086/373899

Paliya, V. S., Ajello, M., Ojha, R., et al. (2019): Detection of a Gamma-Ray Flare from the High-redshift Blazar DA 193. *ApJ*, 871, 211. https://doi.org/10.3847/1538-4357/aafa10

Paragi, Z., Godfrey, L., Reynolds, C., et al. (2015): Very Long Baseline Interferometry with the SKA. *Advancing Astrophysics with the Square Kilometre Array*, 143. https://doi.org/10.22323/1.215.0143

Paraschos, G. F., Kim, J.-Y., Krichbaum, T. P., et al. (2021): Pinpointing the jet apex of 3C 84. *A&A*, 650, L18. https://doi.org/10.1051/0004-6361/202140776

Penrose, R. & Floyd, R. M. (1971): Extraction of Rotational Energy from a Black Hole. *Nature Physical Science*, 229, 177. https://doi.org/10.1038/physci229177a0

Perley, R. A., Schwab, F. R., & Bridle, A. H. (1989): Synthesis Imaging in Radio Astronomy. *Astronomical Society of the Pacific Conference Series*, 6. Astronomical Society of the Pacific, San Francisco, CA. Edited by Perley, R. A., Schwab, F. R. and Bridle, A. H.

Perivolaropoulos, L. & Skara, F. (2022): Challenges for ΛCDM: An update. *New Astronomy Reviews*, 95, 101659. doi:10.1016/j.newar.2022.101659

Perucho, M., Lobanov, A. P., Martí, J.-M., et al. (2006): The role of Kelvin-Helmholtz instability in the internal structure of relativistic outflows. The case of the jet in 3C 273. *A&A*, 456, 493. https://doi.org/10.1051/0004-6361:20065310

Piner, B. G. & Edwards, P. G. (2014): First-epoch VLBA Imaging of 20 New TeV Blazars. *ApJ*, 797, 25. https://doi.org/10.1088/0004-637X/797/1/25

Piner, B. G. & Edwards, P. G. (2018): Multi-epoch VLBA Imaging of 20 New TeV Blazars: Apparent Jet Speeds. *ApJ*, 853, 68. https://doi.org/10.3847/1538-4357/aaa425

Piner, B. G. & Edwards, P. G. (2018): The Doppler crisis in TeV blazars and its possible resolutions. *The Fourteenth Marcel Grossmann Meeting On Recent Developments in Theoretical and Experimental General Relativity, Astrophysics, and Relativistic Field Theories* World Scientific Publishing Co. Pte. Ltd. Edited b Bianchi, M., Jansen, R. T. and Ruffini, R. https://doi.org/10.1142/9789813226609_0389

Plavin, A. V., Kovalev, Y. Y., Kovalev, Y. A., et al. (2023): Growing evidence for high-energy neutrinos originating in radio blazars. *MNRAS*, 523, 1799. https://doi.org/10.1093/mnras/stad1467

Pringle, J. E. (1997): Self-induced warping of accretion discs: non-linear evolution and application to AGN. *MNRAS*, 292, 136. https://doi.org/10.1093/mnras/292.1.136

Pushkarev, A. B., Hovatta, T., Kovalev, Y. Y., et al. (2012): MOJAVE: Monitoring of Jets in Active galactic nuclei with VLBA Experiments. IX. Nuclear opacity. *A&A*, 545, A113. https://doi.org/10.1051/0004-6361/201219173

Pushkarev, A. B., Kovalev, Y. Y., Lister, M. L., et al. (2017): Linear Polarization Properties of Parsec-Scale AGN Jets. *Galaxies*, 5, 93. https://doi.org/10.3390/galaxies5040093

Readhead, A. C. S. (1994): Equipartition Brightness Temperature and the Inverse Compton Catastrophe. *ApJ*, 426, 51. https://doi.org/10.1086/174038

Reber, G. (1940): Cosmic Static. *Proceedings of the IRE*, 28, 68. https://doi.org/10.1109/JRPROC.1940.228921

Rybicki, G. B. & Lightman, A. P. (1979): Radiative processes in astrophysics. *A Wiley-Interscience Publication*, New York.

Rodriguez, C., Taylor, G. B., Zavala, R. T., et al. (2006): A Compact Supermassive Binary Black Hole System. *ApJ*, 646, 49. https://doi.org/10.1086/504825

Roettiger, K., Burns, J. O., Clarke, D. A., et al. (1994): Relic Radio Emission in 3C 388. *ApJL*, 421, L23. https://doi.org/10.1086/187178

Ros, E. (2005): High Precision Differential Astrometry. *Future Directions in High Resolution Astronomy: The 10th Anniversary of the VLBA, ASP Conference Proceedings*, 340, 482. Astronomical Society of the Pacific, San Francisco. Edited by Romney, J. and Reid M. https://doi.org/10.48550/arXiv.astro-ph/0308265

Rösch, F., Benke, P., Kadler, M., et al. (2023): The Impact of Southern-Hemisphere Radio Blazar Observations on Neutrino Astronomy. *arXiv:2310.07468*. https://doi.org/10.48550/arXiv.2310.07468

Sagan, C. (1994): Pale blue dot : a vision of the human future in space Sagan. *Random House*, New York. 1st ed.

Saito, S., Stawarz, Ł., Tanaka, Y. T., et al. (2013): Very Rapid High-amplitude Gamma-Ray Variability in Luminous Blazar PKS 1510-089 Studied with Fermi-LAT. *ApJL*, 766, L11. https://doi.org/10.1088/2041-8205/766/1/L11

Savolainen, T., Giovannini, G., Kovalev, Y. Y., et al. (2023): RadioAstron discovery of a mini-cocoon around the restarted parsec-scale jet in 3C 84. *A&A*, 676, A114. https://doi.org/10.1051/0004-6361/202142594

Schmidt, M. (1963): 3C 273 : A Star-Like Object with Large Red-Shift. *Nature*, 197, 1040. https://doi.org/10.1038/1971040a0

Schneider, P. 2006, Extragalactic Astronomy and Cosmology. Springer, Berlin. https://doi.org/10.1007/978-3-642-54083-7

Schwab, F. R. & Cotton, W. D. (1983): Global fringe search techniques for VLBI. *AJ*, 88, 688. https://doi.org/10.1086/113360

Seyfert, C. K. (1943): Nuclear Emission in Spiral Nebulae. *ApJ*, 97, 28. https://doi.org/10.1086/144488

Shakura, N. I. & Sunyaev, R. A. (1973): Black holes in binary systems. Observational appearance. *A&A*, 24, 337. https://doi.org/10.1007/978-94-010-2585-0_13

Shepherd, M. C. (1997): Difmap: an Interactive Program for Synthesis Imaging. *Astronomical Data Analysis Software and Systems VI, Astronomical Society of the Pacific Conference Series*, 125, 77. edited by Hunt, G. and Payne, H.

Shklovskii, I. S. (1952): O prirode radioizlučeniâ galaktikiO prirode radioizlučeniâ galaktikiOn the nature of the radioemission of the Galaxy. *Astronomicheskii Zhurnal*, 29, 418.

Sol, H. (2018): AGN at very high energies: Cosmic accelerators and probes of space-time. *Journal of Astrophysics and Astronomy*, 39, 52. https://doi.org/10.1007/s12036-018-9547-0

Spruit, H. C. (1996): Magnetohydrodynamic jets and winds from accretion disks. *Evolutionary Processes in Binary Stars, NATO ASI Series C.*, 477, 249. Kluwer academic publishers. Edited by Wijers, R. A. M. J., Davies, M. B., Tout, C. A. https://doi.org/

Strauss, M. A., Huchra, J. P., Davis, M., et al. (1992): A Redshift Survey of IRAS Galaxies. VII. The Infrared and Redshift Data for the 1.936 Jansky Sample. *ApJS*, 83, 29. https://doi.org/10.1086/191730

Suzuki, K., Nagai, H., Kino, M., et al. (2012): Exploring the Central Sub-parsec Region of the γ-Ray Bright Radio Galaxy 3C 84 with VLBA at 43 GHz in the Period of 2002-2008. *ApJ*, 746, 140. https://doi.org/10.1088/0004-637X/746/2/140

Tavecchio, F., Becerra-Gonzalez, J., Ghisellini, G., et al. (2011): On the origin of the γ-ray emission from the flaring blazar PKS 1222+216. *A&A*, 534, A86. https://doi.org/10.1051/0004-6361/201117204

Tchekhovskoy, A. (2015): Launching of Active Galactic Nuclei Jets. *The Formation and Disruption of Black Hole Jets, Astrophysics and Space Science Library*, 414, 45. Springer International Publishing Switzerland. Edited by Contopoulos, I., Gabuzda, D. and Kylafis, N. https://doi.org/10.1007/978-3-319-10356-3_3

Tingay, S. (2003): A Possible Upgrade Path for the Australian Long Baseline Array. *New technologies in VLBI, Astronomical Society of the Pacific Conference Series*, 306, 361. Astronomical Society of the Pacific, San Francisco. Edited by Minh, Y. C.

Titov, O., Melnikov, A., & Lopez, Y. (2020): Resolving VLBI correlator ambiguity in the time delay model improves precision of geodetic measurements. *PASA*, 37, e050. https://doi.org/10.1017/pasa.2020.43

Titov, O., Frey, S., Melnikov, A., et al. (2023): Astrometric Apparent Motion of High-redshift Radio Sources. *AJ*, 165, 69. https://doi.org/10.3847/1538-3881/aca964

Urry, C. M. & Padovani, P. (1995): Unified Schemes for Radio-Loud Active Galactic Nuclei. *PASP*, 107, 803. https://doi.org/10.1086/133630

Van Wassenhove, S., Volonteri, M., Mayer, L., et al. (2012): Observability of Dual Active Galactic Nuclei in Merging Galaxies. *ApJL*, 748, L7. https://doi.org/10.1088/2041-8205/748/1/L7

Wilson, T. L., Rohlfs, K., & Hüttemeister, S. (2013): Tools of Radio Astronomy. Springer Berlin Heidelberg, Berlin. OCLC: 922907410. ISBN: 3-642-39950-9. https://doi.org/10.1007/978-3-642-39950-3

Zamaninasab, M., Clausen-Brown, E., Savolainen, T., et al. (2014): Dynamically important magnetic fields near accreting supermassive black holes. *Nature*, 510, 126. https://doi.org/10.1038/nature13399

Zdziarski, A. A., Sikora, M., Pjanka, P., et al. (2015): Core shifts, magnetic fields and magnetization of extragalactic jets. *MNRAS*, 451, 927. https://doi.org/

Zensus, J. A., Diamond, P. J., & Napier, P. J. (1995): Very Long Baseline Interferometry and the VLBA. *Astronomical Society of the Pacific Conference Series*, 82. Astronomical Society of the Pacific, San Francisco. Edited by Zensus, J. A., Diamond, P. J. and Napier, P. J.

Zensus, J. S. & Ros, E. (2014): EVN: Present and Future. *Proceedings of the 12th European VLBI Network Symposium and Users Meeting*, id. 1. https://doi.org/10.22323/1.230.0001

Zhang, Y., An, T., Frey, S., et al. (2022): Radio Jet Proper-motion Analysis of Nine Distant Quasars above Redshift 3.5. *ApJ*, 937, 19. https://doi.org/10.3847/1538-4357/ac87f8

Zobnina, D. I., Aller, H. D., Aller, M. F., et al. (2023): MOJAVE - XXI. Decade-long linear polarization variability in AGN jets at parsec scales. *MNRAS*, 523, 3615. https://doi.org/10.1093/mnras/stad1481

PETRA BENKE

PhD candidate

Personal information:

Contact: +36202862051 pbenke@mpifr-bonn.mpg.de
Address: Burggartenstrasse 6, Bonn, Germany

Education:

2016-2019 Eötvös Loránd University, Budapest
BSc in Earth Sciences, Astronomy major
2019-2021 University of Helsinki, Helsinki
MSc in Astrophysics
2021- Max Planck Institute for Radio Astronomy, Bonn
PhD candidate

Skills:

- **Coding:** python
- **Data reduction software:** AIPS, CASA, Difmap
- Calibration and analysis of sparsely sampled VLBI data sets from RadioAstron, the Long Baseline Array (TANAMI collaboration), and the Event Horizon Telescope
- **Observations:** single-dish (TELAMON) and VLBI (GMVA) observations with the Effelsberg 100-m telescope
- Referee for A&A since 2024

Full list of publications:

2018 **Benke et al.:** The rise and fall of a binary AGN candidate: the story of PSO J334.2028+1.4075. *PoS(EVN2018)098*.
2023 **Benke et al.:** From binary to singular: The AGN PSO J334.2028+1.4075 under the high-resolution scope. *A&A* 677, A1.
2024 **Benke et al.:** TANAMI: Tracking Active Galactic Nuclei with Austral Milliarcsecond Interferometry. III. First-epoch S band images. *A&A* 681, A69.
2024 **Benke et al.:** VLBI study of the flaring blazar TXS 1508+572 in the early Universe. Accepted in *A&A*, AA50153-24.
2023 Rösch, Benke et al.: The Impact of Southern-Hemisphere Radio Blazar Observations on Neutrino Astronomy. *PoS ICRC2023* 1212.
2023 Eppel et al. (incl. Benke): VLBI Scrutiny of a New Neutrino-Blazar Multiwavelength-Flare Coincidence. *IAUS, 375, 91E.*
2023 Eppel, F. et al. (incl. Benke): VLBI Probes of Jet Physics in Neutrino Candidate Blazars. *PoS ICRC2023* 1199.
2023 Heßdörfer et al. (incl Benke): TELAMON: Effelsberg Monitoring of AGN Jets with Very-High-Energy Astroparticle Emissions - II. Polarization properties. *PoS ICRC2023* 1545.
2023 Nanci et al. (incl. Benke): A VLBI investigation of high-energy neutrino emitter candidates. *PoS(EVN2022)016*.

2024 Eppel et al. (incl. Benke): TELAMON: Effelsberg monitoring of AGN jets with very-high-energy astroparticle emission. I. Program description and sample characterization. *A&A* 684, A11.

2024 Frey et al. (incl. Benke): Revisiting a Core-Jet Laboratory at High Redshift: Analysis of the Radio Jet in the Quasar PKS 2215+020 at z = 3.572. *Universe* 10, 2, 97.

Astronomer's Telegrams:

2021 Kadler, M. et al. (incl. Benke): TELAMON, Metsahovi, Medicina, OVRO and RATAN-600 programs find a long-term radio flare in PKS 0735+17 coincident with IceCube-211208A. *ATel 15105*.

2022 Kadler, M. et al. (incl. Benke): TELAMON Radio Observations of Compact Radio Sources in the Overlap Field of IceCube220627A and IceCube220629A. *ATel 15503*.

2023 Eppel, F. et al. (incl. Benke): Radio Flaring of the Quasar Ton 599 (4C +29.45) on Historical Levels. *ATel 15872*.

2023 Kuberek, D. et al. (incl. Benke): Exceptionally high brightness of PG 1553+113 in the optical and radio range. *ATel 15915*.

2023 Rösch, F. et al. (incl. Benke): Radio Flaring of the Blazar S2 0109+22 on Historical Levels. *ATel 16093*.

2023 Heßdörfer et al. (incl Benke): High-Frequency Radio Flaring of the Blazar S4 0954+658. *ATel* 16388.

2024 Eppel et al. (incl. Benke): Ongoing High-Frequency Radio Flaring of the Blazar S4 0954+658. *ATel* 16491.